EFFICIENT REMOVAL OF NICKEL AND VANADIUM PORPHYRINS FROM PETROLEUM OIL USING CHITOSAN-MODIFIED ZEOLITE X COMPOSITE DERIVED FROM COAL FLY ASH

ASHRAFF AZIZ MARHOON

UNIVERSITI KEBANGSAAN MALAYSIA

EFFICIENT REMOVAL OF NICKEL AND VANADIUM PORPHYRINS FROM PETROLEUM OIL USING CHITOSAN-MODIFIED ZEOLITE X COMPOSITE DERIVED FROM COAL FLY ASH

ASHRAFF AZIZ MARHOON

THESIS SUBMITTED IN FULFILMENT FOR THE DEGREE OF DOCTOR OF PHILOSOPHY

FACULTY SCIENCE AND TECHNOLOGY
UNIVERSITI KEBANGSAAN MALAYSIA
BANGI
2024

PENYINGKIRAN NIKEL DAN VANADIUM PORFIRIN DARIPADA MINYAK PETROLEUM YANG EFEKTIF MENGGUNAKAN KOMPOSIT ZEOLITE X DIUBAHSUAI KITOSAN YANG DIHASILKAN DARIPADA ABU TERBANG ARANG BATU

ASHRAFF AZIZ MARHOON

TESIS YANG DIKEMUKAKAN UNTUK MEMPEROLEH
IJAZAH DOKTOR FALSAFAH

FAKULTI SAINS DAN TEKNOLOGI
UNIVERSITI KEBANGSAAN MALAYSIA
BANGI

2024

DECLARATION

I hereby declare that the work in this thesis is my own except for quotations and summaries which have been duly acknowledged.

15 February 2025

ASHRAFF AZIZ MARHOON
P103608

PERAKUAN TESIS SARJANA / DOKTOR FALSAFAH
(DECLARATION OF MASTER / DOCTOR OF PHILOSOPHY THESIS)

A. MAKLUMAT PELAJAR/*STUDENT DETAILS*

B. PERAKUAN / *DECLARATION*

tesis adalah hak milik UKM
thesis is the property of UKM

Sila tandakan (/) pada salah satu pilihan di bawah:
Please tick (/) one of the following:

RAHSIA
CONFIDENTIAL

TERHAD
RESTRICTED

Mengandungi maklumat TERHAD yang telah ditentukan oleh organisasi/
badan di mana penyelidikan dijalankan.
Consisting of RESTRICTED information as specified by the organisation/

AKSES TERBUKA/
TIDAK TERHAD
OPEN ACCESS/
NON-RESTRICTED

Saya membenarkan tesis ini disimpan di perpustakaan dengan syarat ia boleh diakses
atau dibuat salinan untuk tujuan pengajian sahaja dengan kebenaran bertulis
sahaja.
I give permission for this thesis to be kept in the library under the following
terms of access for study purposes only with written permission.

Bagi kategori Akses Terbuka/Tidak Terhad, saya membenarkan tesis (Sarjana/Doktor Falsafah) ini disimpan di Perpustakaan Universiti Kebangsaan Malaysia (UKM) dengan syarat-syarat kegunaan seperti berikut:

C. PENGESAHAN FAKULTI/INSTITUT | VERIFICATION OF FACULTY/INSTITUTE

Tandatangan / Signature

Nama / Name: PROF MADYA DR ABDUL MUNIR AB MURAD

Tarikh / Date: 15 Julai 2021

Cop Rasmi / Official Stamp

*** Laksana / 15 Julai 2021

ACKNOWLEDGEMENT

In the name of Allah, the Most Gracious, the Most Merciful. First and foremost, I owe my deepest gratitude to the overflow of divine generosity that has guided and sustained me throughout this journey. Without Allah's endless blessings and mercy, none of this would have been possible.

I am profoundly grateful to my main supervisor, Associate Professor Dr. Siti Aishah binti Hasbullah, whose unwavering support, insightful guidance, and constant encouragement have been instrumental in the completion of this thesis. Your wisdom and patience have inspired me to strive for excellence. Your dedication to my academic and personal growth has been beyond measure, and your willingness to always make time for my questions and concerns has been a source of great comfort. For all this and more, I am deeply thankful. My heartfelt thanks extend to my co-supervisors, Dr. Nurul Asikin-Mijan and Dr. Wan Nur Aini Wan Mokhtar. Your expertise, constructive feedback, and continuous support have been invaluable throughout this research.

I also wish to express my sincere appreciation to the Department of Chemical sciences, Faculty of Science and Technology, for providing me with the resources and environment conducive to conducting this research. The knowledge and experience gained here will forever be cherished.

To my beloved father, your love, sacrifices, and unwavering support have been my greatest source of strength. Your constant encouragement has given me the confidence to pursue my dreams.

To the cherished memory of my late mother, I dedicate this achievement to you. Your love, prayers, and guidance have always been with me, and I feel your presence in every step I take. I miss you dearly and hope to make you proud.

To my lovely wife, your unwavering support, patience, and encouragement have been my anchor. Your belief in me, even during the most challenging times, has been my motivation. To my children, your smiles and love have provided me with the energy to persevere.

To my sister, affection, and unwavering support have been a constant source of comfort and strength. Your faith in my abilities and your endless encouragement have been a beacon of hope and inspiration.

To everyone who accompanied me on this long journey friends, colleagues, and mentors your support, encouragement, and camaraderie have made this journey worthwhile.

Finally, this research journey has profoundly shaped me into a better person, enhancing both my personal and professional growth.

ABSTRAK

Peningkatan permintaan minyak sebagai sumber tenaga utama di seluruh dunia telah membawa kepada penurunan pesat dalam rizab minyak mentah ringan, menggalakkan penyelidikan terhadap minyak mentah berat sebagai alternatif lain. Salah satu cabaran kritikal yang dihadapi oleh industri minyak mentah berat ialah kandungan logam yang tinggi, terutamanya nikel dan vanadium. Kehadiran nikel dan vanadium porfirin menyebabkan kakisan peralatan dan keracunan pemangkin, selain kerosakan terhadap alam sekitar. Oleh itu, terdapat keperluan mendesak untuk menghapuskan unsur-unsur yang memudaratkan ini dan mencegah pembentukannya dalam bahan mentah. Kombinasi sinergi ciri-ciri unik zeolit dan kitosan menjanjikan peluang yang baik untuk pelbagai aplikasi, terutamanya dalam operasi penyingkiran logam daripada minyak mentah. Objektif utama kajian ini adalah untuk menyingkirkan nikel dan vanadium porfirin daripada minyak mentah menggunakan komposit kitosan (CHS) yang diubah suai dengan zeolit-X (ZX) yang berasal daripada abu terbang arang batu Malaysia (CFA) sebagai agen penyingkiran logam baharu. Sintesis ZX bermula dengan pra rawatan CFA. Proses ini termasuk memisahkan pecahan magnetik dan pencucian asid untuk menghilangkan kekotoran. Seterusnya, CFA yang dirawat diubah menjadi ZX melalui kaedah gabungan-hidroterma alkali di bawah pelbagai keadaan sintesis. ZX yang disintesis dicirikan menggunakan magnetometer sampel bergetar (VSM), pembelauan sinar-X (XRD), pendarfluor sinar-X (XRF), mikroskop elektron pengimbasan (SEM), isoterma penjerapan-penyahjerapan N_2, spektroskopi inframerah (FTIR), dan analisis termogravimetri (TGA). Di bawah keadaan optimum, ZX yang diperoleh daripada CFA yang dirawat berkesan menyingkirkan ion Ni^{2+} dan V^{5+} daripada larutan akueus, mencapai keupayaan penyerapan maksimum sebanyak 41.55 mg/g untuk Ni^{2+} dan 32.38 mg/g untuk V^{5+}. Walau bagaimanapun, zeolit yang dihasilkan mempamerkan keafinan yang rendah terhadap porfirin logam dalam medium organik. Komposit CHS/ZX telah difabrikasi dengan merendam zarah zeolit yang disintesis ke dalam larutan kitosan-gelasi, dan formulasi matriks telah dioptimumkan melalui kaedah gerak balas permukaan (RSM). Kebolehpercayaan model dalam meramalkan penyingkiran porfirin logam menggunakan pembolehubah yang ditetapkan telah disahkan dengan ralat ketepatan 0.5%. Pencirian sistematik menunjukkan bahawa komposit CHS/ZX yang disintesis berjaya menggabungkan struktur mesoporus dengan kedua-dua kumpulan berfungsi ZX dan CHS. Mekanisme penjerapan dan nyahjerapan porfirin logam oleh komposit CHS/ZX telah disiasat menggunakan larutan model yang mengandungi vanadil dan nikel tetrafenil porfirin (VO-TPP dan Ni-TPP) dalam toluena. Keberkesanan sebatian kitosan-zeolit dalam menyingkirkan porfirin logam meningkat dua kali ganda berbanding dengan kadar penyingkiran yang dicapai oleh komponen induk secara individu. Kesan pembolehubah kualitatif dan kuantitatif untuk mendapatkan semula porfirin logam daripada komposit CHS/ZX tepu telah diterokai.dikaji. Di bawah keadaan optimum, 27.07 mg/g daripada VO-TPP dan 28.02 mg/g daripada Ni-TPP yang diserap oleh komposit CHS/ZX telah berjaya didapatkan semula. Keputusan menunjukkan bahawa CHS/ZX berjaya menyingkirkan 3.00 mg/g nikel dan 7.68 mg/g vanadium daripada minyak mentah Basrah berat, serta 0.83 mg/g nikel dan 5.54 mg/g vanadium daripada minyak mentah Basrah sederhana dalam keadaan optimum. Secara keseluruhannya, komposit CHS/ZX menunjukkan potensi yang baik untuk dibangunkan sebagai bahan penyingkir logam minyak mentah, yang membawa kepada proses penapisan yang lebih baik dalam industri petrokimia.

ABSTRACT

The increasing worldwide demand for oil as a primary energy source has led to a rapid decline in light crude reserves, prompting the investigation of heavy crude as a viable alternative. One of the critical challenges facing the heavy crude oil industry is the high metal content, especially nickel and vanadium, which exist in the form of porphyrin complexes. The presence of nickel and vanadium porphyrins causes equipment corrosion and the poisoning of catalysts, in addition to environmental damage. Therefore, there is an urgent need to remove these detrimental elements and prevent their buildup in feedstocks. The synergistic combination of the unique characteristics of zeolite and chitosan presents promising opportunities for diverse applications, particularly in crude oil demetallization operations. The main objective of this study is to remove nickel and vanadium porphyrins from crude oil using a composite of chitosan (CHS) modified with zeolite-X (ZX) derived from Malaysian coal fly ash (CFA) as a new demetallization agent. The synthesis of ZX began with the pretreatment of CFA. This process included separating the magnetic fraction and acid washing to remove impurities. Next, the treated CFA was transformed into ZX through an alkaline fusion-hydrothermal method under different synthesis conditions. The synthesized ZX was characterized using a vibrating sample magnetometer (VSM), X-ray diffraction (XRD), X-ray fluorescence (XRF), scanning electron microscopy (SEM), N_2 adsorption-desorption isotherm, infrared spectroscopy (FTIR), and thermogravimetric analysis (TGA). Under optimal conditions, ZX derived from treated CFA efficiently eliminated Ni^{2+} and V^{5+} ions from aqueous solutions, achieving maximum adsorption capacities of 41.55 mg/g for Ni^{2+} and 32.38 mg/g for V^{5+}, respectively. However, the prepared zeolite exhibited a low affinity for metal porphyrins in the organic medium. The CHS/ZX composite was fabricated by immersing as-synthesized zeolite particles into the chitosan-gelling solution, and the matrix formulation was optimized via response surface methodology (RSM). The model's reliability in predicting the removal of metal porphyrins using the values of the established variables was excitedly validated with a reasonable accuracy error of 0.5%. The systematic characterization shows that synthesizing the CHS/ZX composite successfully combines the mesoporous structure with the functional groups of both ZX and CHS. The adsorption and desorption mechanisms of metal porphyrins by the CHS/ZX composite were investigated using a model solution containing vanadyl and nickel tetraphenyl porphyrin (VO-TPP and Ni-TPP) in toluene. The efficacy of CHS/ZX compounds in removing metal porphyrins doubled compared to the removal rates achieved by the parent components individually. The impact of qualitative and quantitative variables on the recovery of metal porphyrins from saturated CHS/ZX composites was explored and studied. Under optimized conditions, 27.07 mg/g of the VO-TPP and 28.02 mg/g of the Ni-TPP adsorbed by the CHS/ZX composite were successfully recovered. The results indicate that CHS/ZX effectively removed 3.00 mg/g nickel and 7.68 mg/g vanadium from heavy Basrah crude oil, and 0.83 mg/g nickel and 5.54 mg/g vanadium from medium Basrah crude oil under optimal conditions. Overall, CHS/ZX composites show promising potential to be developed for crude oil demetallization, leading to improved refining processes in the petrochemical industry.

TABLE OF CONTENTS

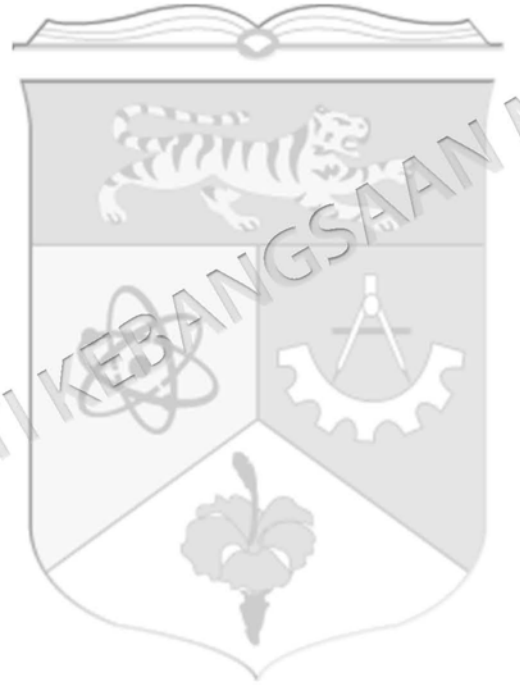

LIST OF TABLES

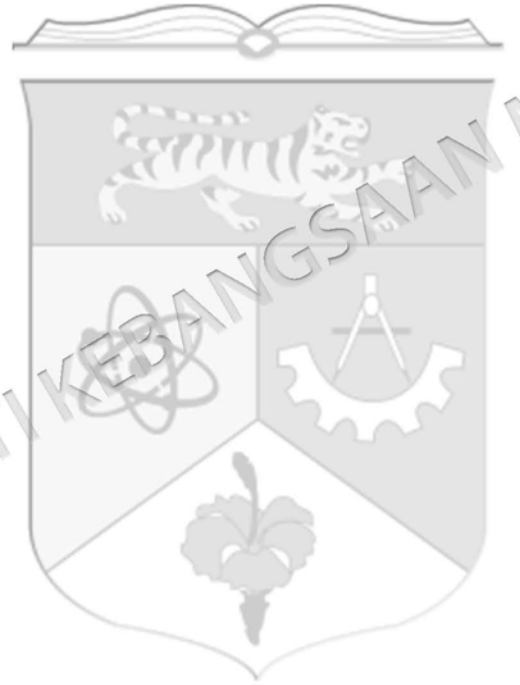

LIST OF ILLUSTRATIONS

LIST OF ABBREVIATIONS

%	Percentage
π	Pi
°C	Degree Celsius
°F	Degree Fahrenheit
Å	Angstrom
ADD	Adsorptive demetallization
API	American petroleum institute
Ar	Aromatic
ASTM	American society of testing and materials
BET	Brunauer-Emmett-Teller
CBA	Coal bottom ash
CEC	Cation exchange capacity
CFA	Coal fly ash
CHS	Chitosan
CNT	Carbon nanotube
DFT	Density functional theory
EDTA	Ethylenediaminetetraacetic acid
FAU	Faujasite
FCC	Fluid catalytic cracking
FESEM	Field emission scanning electron microscopy
FTIR	Fourier transform infrared
g	Gram
h	hour
HDM	Hydrodemetallation
Hz	Hertz
ICP-OES	Inductively coupled plasma-optical emission spectroscopy
L	Litre

LOD	Limit of detection
m	Metre
M	Molar
mboe	million barrels of oil equivalent
mg	milligram
min	minute
MP-AES	Microwave plasma atomic emission spectroscopy
NaOH	Sodium hydroxide
NCFA	Nonmagnetic fraction of raw coal fly ash
Ni^{2+}	Nickel ion
Ni-TPP	Nickel (II)-tetraphenylporphyrin
nm	nanometre
OPEC	Organization of the petroleum exporting countries
pH	Potential of hydrogen
ppm	Parts per million
RCFA	Raw coal fly ash
rpm	Revolutions per minute
RSM	Response surface methodology
TCFA	Treated coal fly ash
TEM	Transmission electron microscopy
TGA	Thermogravimetric analysis
UKM	Universiti Kebangsaan Malaysia
US EPA	United states environmental protection agency
UV-Vis	Ultraviolet-visible
V^{5+}	Vanadium ion
VO-TPP	Vanadyl (IV)-tetraphenylporphyrin
VSM	Vibrating sample magnetometer
W	Watt
XPS	Photoelectron spectroscopy

XRD	X-ray diffraction
XRF	X-ray fluorescence
ZX	Zeolite X
μ	Micro

CHAPTER I

INTRODUCTION

1.1 RESEARCH BACKGROUND

The increase in population and the continuous development of the global economy and industrialization have triggered a sharp growth in energy demand. Petroleum oil is the most used source of energy, and it is also the leading feedstock for various industries, including the manufacture of synthetic fibres, plastics, paints, fertilizers, insecticides, soaps, and synthetic rubber. Thus, the use of petroleum as a source of raw materials in manufacturing keeps the modern industry functioning. According to the organization of petroleum exporting countries, oil demand is expected to increase by 16.4 MB/D between 2015 and 2040, reaching 109.4 MB/D by 2040 (Tirado et al. 2023). As traditional light petroleum resources become scarce, there's a growing interest in using low-quality heavy oils and residues, derived from processing heavy crudes, as alternative sources for transportation fuels, energy, and petrochemicals. This shift could help meet the demands of our rapidly expanding population and advancing civilization. Moreover, many statistical studies have showed that reservoirs of heavy crude are much larger than those of conventional crude, which made the appropriate deep upgrading of heavy crude, for both refining and petrochemicals, more interesting and is attracting more and more attention from scientists and engineers (Corma et al. 2017). Heavy oil and residues are viscous with low API gravity ranging from seven up to twenty and contain very complex molecules and many impurities such as asphaltenes, metals such as nickel and vanadium, sulfur, and nitrogen that pose numerous problems during their up-gradation processes into high value-added products such as light olefins (Tirado et al. 2023).

The primary strategies for upgrading heavy oil involve the removal of excess carbon (through carbonization, cracking, and deasphaltization) or the addition of hydrogen (hydrorefining). The selection of hydrorefining technologies for heavy hydrocarbon crude is largely based on the content of metals, especially vanadium (V) and nickel (Ni) (Yakubov et al. 2021). Metallic constituents can be found in different chemical structures, such as organic metal complexes, inorganic salts, metal soaps, and metals attached to asphaltenes.

Organic metal complexes are mostly in the form of metal-porphyrins, that exist in native crude oil and mainly concentrate in heavy parts of petroleum. Metalloporphyrins in oils mainly consist of vanadium and nickel, which can associate with asphaltenes (Yakubov et al. 2021). The presence of these metals, even in a small percentage, is forming a significant concern and serious issue for both the oil industry and the environment. The effect of these metals is represented by the erosion of oil refinery equipment such as turbines, pumps, and distillation towers, poisoning the catalysts and reducing their efficiency via blocking the pores by accumulated carbon, rending the walls, and deformation of the reactors, as well as environmental pollution by this toxic and hazardous waste, disturbance of natural environmental balance, and other continuous problems (Groysman 2017; Tirado et al. 2023). The relative amount of metals (in all forms) to other major impurities present in crude is shown in Table 1.1.

Table 1.1 Typical concentration of some impurities in different types of petroleum feedstock

Petroleum type	**Impurity Concentration**		
	S (wt %)	**N (wt %)**	**Ni, V (ppm)**
Extra light	0.02-0.2	0-0.01	<10
Light	0.05-4	0.02-5	10-200
Heavy	0.1-5	0.2-0.8	50-500
Extra heavy	0.8-6	0.1-1.3	200-600

Source: Jenifer et al. 2015

A porphyrin is a symmetrical macrocyclic tetrapyrrole structure consisting of two di-pyrrolic units. Vanadium and nickel porphyrins are, in fact, the first biomarkers of petroleum (Tirado et al. 2023). The most common porphyrin compound is

metalloporphyrin, which is formed when a metal atom displaces two central hydrogen ions from the porphyrin ligand. Metals are strongly chelated or complexed in porphyrinic ligands that are completely stable and compatible with petroleum fractions, making metal removal from petroleum feedstocks extremely difficult (Chacon-Patino et al. 2021). The porphyrins are present in the most polar fractions of petroleum, asphaltenes, and resins (Jenifer et al. 2015). Owing to the detrimental effects of porphyrins on oil processing, it is strongly advisable to undertake the removal and identification of porphyrinic species, along with other nitrogen and sulfur contaminants, from their respective source oils (Saleh 2020). The qualitative and quantitative analyses of petroporphyrins become imperative for discerning oil properties and evaluating the potential impact on the refining process.

Metal porphyrins play a crucial role in the aggregation processes of asphaltenes in petroleum oils (Figure 1.1). These porphyrins are central to enhancing the aggregation of asphaltene molecules, even in the absence of polar lateral chains. The porphyrins achieve this through strong hydrogen bonding facilitated by the central metal and oxygen atoms (Santos Silva et al. 2018). This interaction is pivotal to the stability and formation of asphaltene aggregates, overshadowing the weaker π-π stacking interactions that occur due to aromaticity (Silva et al. 2017). Metal porphyrins are, therefore, integral to the intermolecular forces that drive asphaltene aggregation, influencing the structure and behaviour of these complex petroleum components (Musin et al. 2020).

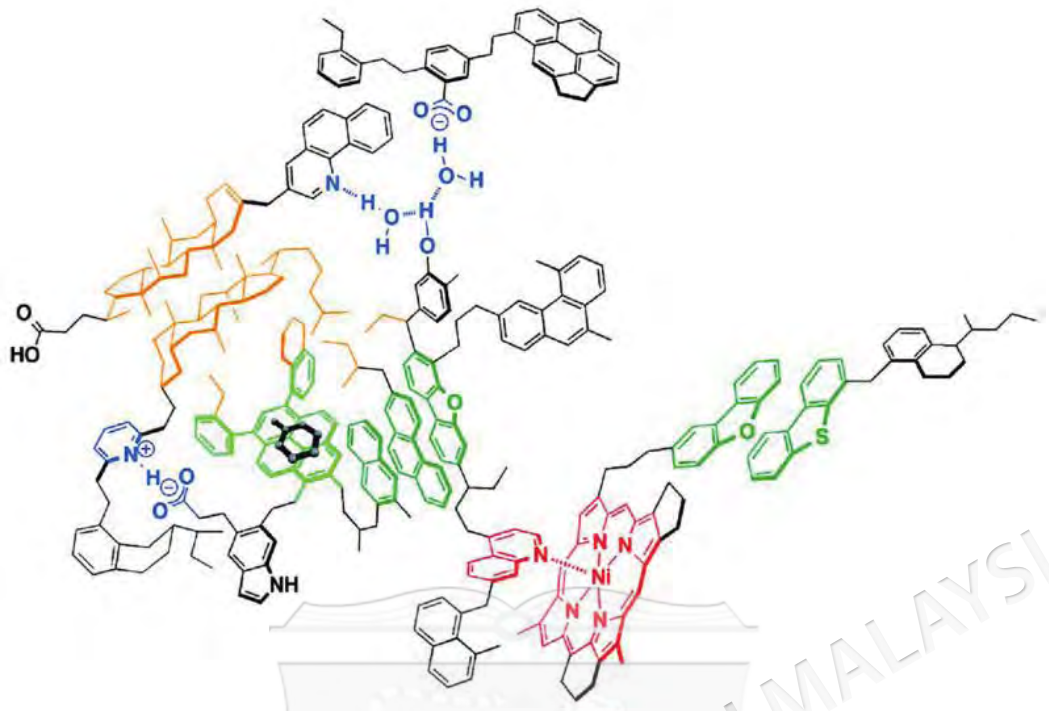

Figure 1.1. Diagrammatic representation of metal porphyrins interaction with asphaltene molecules in petroleum oil

Source: Zheng et al. 2020

Meanwhile, the recovery of porphyrins offers the opportunity to leverage their optical and electronic properties in various applications, as documented by several studies (W. Hipps & Mazur 2017). Synthetic porphyrins and metal porphyrins find application in surface science-related fields, particularly in catalysis (Kuzmin et al. 2020). Their photoelectronic properties make them valuable components for electronic devices like wires and diodes, contributing to advancements in energy transfer mechanisms (Milordov et al. 2021) establishes the feasibility of employing asphaltenes and resins, sourced from industrial vacuum oil residues, as precursors for extracting high-purity vanadyl porphyrins. The compositional integrity of the resultant vanadyl porphyrins is verified through MALDI-TOF and HPLC analyses. These compounds exhibit potential for catalytic roles across diverse chemical operations, presenting an eco-friendly alternative to conventional synthetic methodologies.

The hydrotreatment process for metals removal (HDM) is the only process widely used in the industrial sector. This conventional technique can remove up to 90% of the metals content from the oil. Although the HDM process effectively removes a

large portion of the metals and, it suffers from several issues. Most importantly, these issues include fast catalyst deactivation, high hydrogen consumption, which reaches 300-2000 Scf/bbl for light oil and 2000-10,000 Scf/bbl for heavy residual oil, an elevated temperature that ranges from 300 to 400°C for light distillate and from 340 to 425°C for heavy residual, and elevated pressure, which ranges from 30 to130 atmosphere (Attia et al. 2020).

Several unconventional methods are available to overcome the difficulties in crude upgradation due to the presence of vanadium and nickel complexes. The unconventional methods are categorized as physical and chemical methods. Chemical methods for demetallization involve deliberate chemical reactions or interactions that modify the chemical structure or phase of metal compounds, facilitating their removal (Jumina et al. 2021). Techniques like acid treatments, electrochemical removal, and the utilization of phosphorus compounds fall under this category. While chemical methods may offer more thorough removal of metal contaminants, such approaches come with the risk of side reactions and potential contamination of the final product. The environmental impact of chemical methods is a critical consideration, as these techniques may generate hazardous waste, necessitating meticulous management of reagents and by-products to prevent further environmental issues (Yang et al. 2022). Despite the potential for robust removal efficiencies, chemical methods must be judiciously applied, considering both effectiveness and environmental considerations.

In contrast, physical methods for demetallization are characterized by their reliance on non-chemical processes such as phase separation, extraction, or adsorption to extract metals from petroleum fractions. Employing techniques like solvent deasphalting (Speight 2016), ionic liquids (Chauhan & de Klerk 2020), core-shell materials (Geng et al. 2020), these methods capitalize on physical properties such as size, shape, and phase behavior for separation. The selectivity of physical methods is rooted in these inherent characteristics, aiming for precision in metal removal while minimally impacting the composition of crude oil. Notably, physical methods typically generate less hazardous waste, positioning them as more environmentally friendly alternatives in the demetallization process. Furthermore, these methods are

advantageous due to their cost-effectiveness, ease of operation, and potential for high removal efficiencies (Jenifer et al. 2015).

The adsorptive demetallization process offers an innovative approach to removing vanadium and nickel compounds from crude oil, utilizing energy-efficient adsorption techniques that are operable under ambient conditions. This method does not depend on catalysts or hydrogen gas, instead leveraging cost-effective solid adsorbents (Hammadou née Mesdour et al. 2022). Although the use of adsorption as a sustainable alternative has not been extensively investigated, it presents significant benefits, including adsorbent regeneration and reuse without the necessity for further chemical interventions (Caetano et al. 2023b). In this regard, zeolite is known to possess desirable physical properties like high surface area, large pore volume and chemical properties with the potential for a tunable surface with various metals/functional groups for selective metal removal.

Zeolites can be classified into two broad groups, namely, natural, and synthetic zeolites. Synthesizing zeolites offers advantages over natural zeolites due to the ability to control parameters, shorter production times, and superior adsorption properties. Despite associated costs, a focus on using low-cost or waste materials for synthesis, particularly fly ash from coal combustion, has gained attention. Fly ash, often considered hazardous, contributes to environmental pollution and toxicity. Leaching tests reveal the mobility of toxic elements from fly ash. Converting fly ash to zeolites proves effective in reducing heavy metal mobility, demonstrating both environmental and economic benefits. This approach, while alleviating environmental concerns, aligns with economic viability, providing a sustainable solution for waste management and zeolite synthesis (Szerement et al. 2021).

In the last twenty years, the use of zeolite-based composites in the forms of zeolite/inorganic and zeolite/polymer composites has been accelerated for multiple applications. Zeolite-based composites exhibited several advantages, such as high adsorption capability, high selectivity, better reusability, and fast adsorption compared to raw zeolites for the adsorption of adsorbates. The higher adsorption capability of zeolite-based composites for the adsorption of targeted matters from the studied

medium is caused by the various adsorption mechanisms such as hydrogen bonding, π-π interactions, ion-exchange, electrostatic interactions, van der Walls forces, chelation, and hydrophobic interactions (Rad & Anbia 2021).

Chitosan is among the most widely used natural polymers and is an economical, renewable, and abundant polysaccharide having unique molecular characteristics. Chitosan is derived by deacetylation of chitin, a natural polysaccharide existing in insects' exoskeleton, outer shells of crustaceans, and some fungi cell walls. Chitosan being a versatile bio-product and has been used for multiple applications in the petroleum industry, such as oil exploration, transportation, refining; and in petroleum products, along with the treatment of oil sludge and refinery wastewater; a frame diagram is shown in Figure 1.2.

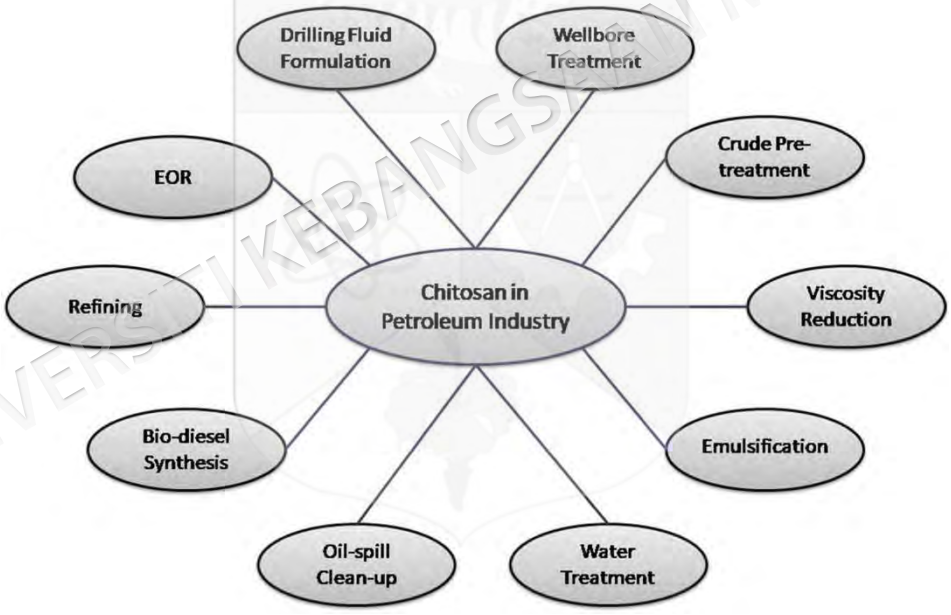

Figure 1.2 Different applications of chitosan in petroleum industry

Source: Negi et al. 2021

However, chitosan suffers from low mechanical strength and thermal resistance, weak stability and acid solubility, low surface area, and low total pore volume. Therefore, chitosan is modified to improve its properties and mitigate its disadvantages by organic-inorganic recombination and chemical cross-linking with high mechanical strength materials, such as zeolites (Ababneh & Hameed 2023; Sodha et al. 2022).

Chitosan/zeolite, as a biocompatible mesoporous material, possesses narrow pore size distributions and high surface areas that exhibit the appropriate biocompatibility and low toxicity. Environmental concerns have grown in recent years and industries endeavor to utilize bio-based and bio-compatible materials. Zeolite/chitosan composite can be attractive as a natural, cost-effective, and properties-controlled material. The tunable structure of zeolite/chitosan (zeolite pores diameter and around ions) enhances its usage in various applications such as adsorption, catalyst and biomedical. Moreover, zeolite composites can be utilized as polymerization substrates of conductive polymers, which yield unusual conductivity and can make frameworks in supercapacitors. The zeolite/chitosan properties, such composite can be used in various applications with desired and tunable properties. For instance, adding modified nanoparticles like zeolite and different polymers to the matrix of various substrates could improve their antifouling and abilities to selective filtration/adsorption. The physical and chemical characteristics of various zeolites can be carefully modified to select specific molecules for separation technology uses (Mahmodi et al. 2020).

1.2 PROBLEM STATEMENT

Crude oil is a complex mixture of hydrocarbons and impurities, including trace metals such as vanadium (V) and nickel (Ni). These metals, present in porphyrin forms, pose significant challenges to refining processes. Vanadium and nickel impurities deactivate desulphurization and cracking catalysts, leading to increased operational costs and equipment corrosion (Chacón-Patiño et al. 2022). The presence of vanadium compounds, in particular, can lead to the formation of toxic vanadium pentoxide during combustion, raising serious environmental and health concerns (Valencia 2023). These issues are exacerbated by the declining reserves of conventional light oils, which are being replaced by heavier feedstocks with higher concentrations of these metals. Therefore, the selective removal of these metal contaminants from crude oil is highly desirable.

Traditional methods for removing metallic impurities, such as solvent extraction, metal chelation, supercritical extraction, and hydrodemetallization, each have significant limitations. Solvent extraction is ineffective for crude oils with high

resin-asphaltene content, metal chelation can alter oil properties, supercritical extraction is economically unfeasible due to high temperature and pressure requirements, and hydrodemetallization consumes substantial energy and hydrogen, leading to catalyst fouling and high costs. Recent unconventional methods, such as oxidative, biological, electrolytic, ultrasonic, and photo-demetallation, have also proven inadequate due to undesirable alterations in the physicochemical properties of crude oil (Jumina et al. 2021).

Porphyrins are valuable in surface science and photodynamics; however, their industrial utilization is hindered by the high cost and complexity of synthetic preparation. Petroleum-derived porphyrins present a viable and cost-effective alternative to synthetic porphyrins (Yakubov et al. 2021). Given that most current methods rely on destroying porphyrin structures to demetallize crude oil (Nguyen et al. 2022), there is a critical need for a non-destructive approach that preserves these valuable complexes. Adsorption methods are particularly promising as they enable the recovery of porphyrins while maintaining their structural integrity.

Previous adsorbents for demetallization of crude oil have encountered significant limitations that reduce their effectiveness. The adsorbents have suffered from low porosity or rigid structures that limit the accessibility and movement of target molecules, thereby hindering metal removal efficiency (Jenifer et al. 2015). Additionally, the inability to regenerate certain adsorbents, along with issues like rapid deactivation, low mechanical strength, and poor diffusion, has further diminished their practicality (Iuzmukhametova et al. 2023). In some cases, adsorbents have interacted negatively with components in crude oil, creating interference that affects their performance (Caetano et al. 2023b). These limitations have highlighted the need for alternative adsorbents that can offer higher efficiency, better regeneration capabilities, and minimal interference with crude oil components. Furthermore, such adsorbents must be cost-effective and environmentally friendly to ensure practical application in large-scale refining processes and to minimize the environmental impact of demetallization efforts.

To address these challenges, this study focuses on developing a novel demetallization agent: a chitosan-modified zeolite X composite (CHS/ZX). This research aims to overcome the significant limitations observed with traditional adsorbents by optimizing the synthesis parameters using response surface methodology (RSM) and evaluating the composite's adsorption capacity under conditions simulating real crude oil environments. Additionally, this study explores recovery methods for metal porphyrins and introduces an innovative approach using proton-donating alcohol to enhance metal removal efficiency in crude oil samples. This comprehensive approach aims to provide an effective, non-destructive, cost-efficient, and eco-friendly solution for the removal of heavy metals from crude oil, contributing to more sustainable refining processes and the recovery of valuable porphyrins.

1.3 RESEARCH OBJECTIVES

This study embarks on the following objectives:

1. To synthesize and characterize high-purity zeolite X from Malaysian fly ash using the alkaline fusion-assisted hydrothermal process.
2. To evaluate the effectiveness of the synthesized zeolite in removing vanadium and nickel ions from aqueous solutions.
3. To synthesize and characterize the chitosan-modified zeolite X composite for efficiently removing vanadyl and nickel porphyrins from model solutions in toluene.
4. To study the performance of the synthesized CHS/ZX composite for the demetallization of real crude oil samples.

1.4 RESEARCH SCOPE

This work consists of several parts of the studies that have been focused on. The first part of the study encompasses the innovative synthesis and detailed characterization of high-purity, single-phase Zeolite-X from treated fly ash (TCFA) aimed at the efficient removal of nickel (Ni) and vanadium (V) ions from aqueous solutions.

Initially, the study delves into the pretreatment process of raw coal fly ash (RCFA), which includes magnetic fraction separation and acid washing to prepare the

ash for zeolite synthesis. The core of the research is focused on synthesizing zeolite-X via a fusion step followed by hydrothermal treatment, optimizing conditions to achieve a zeolite product of high crystallinity and purity. The characterization of the synthesized zeolite-X involves a comprehensive suite of analyses, including magnetic susceptibility via the vibrating sample magnetometer (VSM) test, chemical composition adjustments, particularly in undesirable oxides content through X-ray fluorescence (XRF), and crystallinity and phase purity assessments using X-Ray Diffraction (XRD) and scanning electron microscopy (SEM). Additionally, the study explores the surface and pore characteristics through Brunauer-Emmett-Teller (BET) analysis, functional groups via Fourier transform infrared spectroscopy (FTIR), and thermal stability through thermogravimetric Analysis (TGA). A significant part of the scope is dedicated to understanding the adsorption kinetics and isotherms for Ni and V ions on the synthesized zeolite, employing kinetic models and adsorption isotherms to elucidate the process.

The second part of the work is dedicated to the comprehensive exploration of the development, optimization, and thorough assessment of a novel composite material composed of chitosan and synthetic zeolite X, derived from coal fly ash (CH/ZX), investigating its utility as a demetallization agent targeting vanadyl and nickel porphyrins. The research trajectory includes fabricating the CH/ZX composite by integrating synthesized zeolite particles with a chitosan-gelling solution, meticulously optimizing this matrix through response surface methodology (RSM) to amplify metal porphyrin removal efficiency. The validity of a predictive model, designed to estimate metal porphyrin removal efficiency with a minimal error margin, is rigorously tested to ensure reliability. The synthesized composite was systematically characterized using X-ray photoelectron spectroscopy (XPS), SEM, BET, XRD, FTIR, TGA, and CHN analyses.

The study delves into the adsorption and desorption mechanisms of vanadyl and nickel tetraphenyl porphyrin (VO-TPP and Ni-TPP) in toluene, highlighting the superior removal capacity of the CH/ZX composite over its individual constituents. It further investigates the impact of various parameters including temperature, initial concentration of metal porphyrins, and composite dosage on the adsorption capacity to

delineate optimal process conditions. Kinetic analysis reveals that the adsorption behavior is best described by the pseudo-second-order model, with initial rapid adsorption stages underscoring the dominance of physisorption forces. A comparison of the affinity of vanadyl- and nickel-porphyrins towards the composite and the application of the Freundlich isotherm model suggests a multilayer adsorption mechanism on a heterogeneous surface. The study also characterizes the thermodynamic aspects of the adsorption processes, identifying them as exothermic and spontaneous, with a detailed comparison of metal-porphyrin affinities.

The next part of the work includes examining factors influencing desorption efficiency, such as solvent selection, temperature variations, mass loading, and the volume of eluent, to shed light on the optimization of desorption efficiency. Additionally, the study evaluates the composite's reusability and the effectiveness of metal-porphyrin recovery across multiple cycles.

Finally, this study embarks on investigating a groundbreaking demetallization process tailored for Basrah crude oils, leveraging a unique methodology that combines the dissociation of petroporphyrins from asphaltene with an adsorptive reaction to effectively remove metal porphyrins, specifically vanadyl, and nickel porphyrin. Central to this investigation is the comparative analysis of the demetallization efficacy on vanadyl and nickel tetraphenyl porphyrin dissolved in toluene versus actual Basrah crude oil samples, aiming to delineate the process's capability in targeting "free"-type metal porphyrins against the more asphaltenic molecule-associated "bound"-type metal porphyrins.

To address the challenge of bound-type metal porphyrins, the study innovates by introducing a hydrogen-donating polar solvent, 1-hexanol, into the crude oil to weaken the asphaltenic bonds, subsequently removing the solvent through evaporation to facilitate the crude oil's treatment with the CHS/ZX composite under varied operating conditions. This approach not only underscores the effectiveness of the CHS/ZX composite in removing vanadium and nickel from the pre-treated crude oil but also emphasizes optimizing these conditions to enhance metal recovery, showcasing significant removal efficiencies from both heavy and medium Basrah crude oils.

Moreover, this study extends beyond mere demetallization to conceptualize the process as an energy-saving, safe, and environmentally friendly solution, particularly highlighting the recovery and reuse of 1-hexanol to underscore the process's energy efficiency.

Figure 1.3 provides an overview of the research scope addressed in this study, which will be detailed in the upcoming chapters.

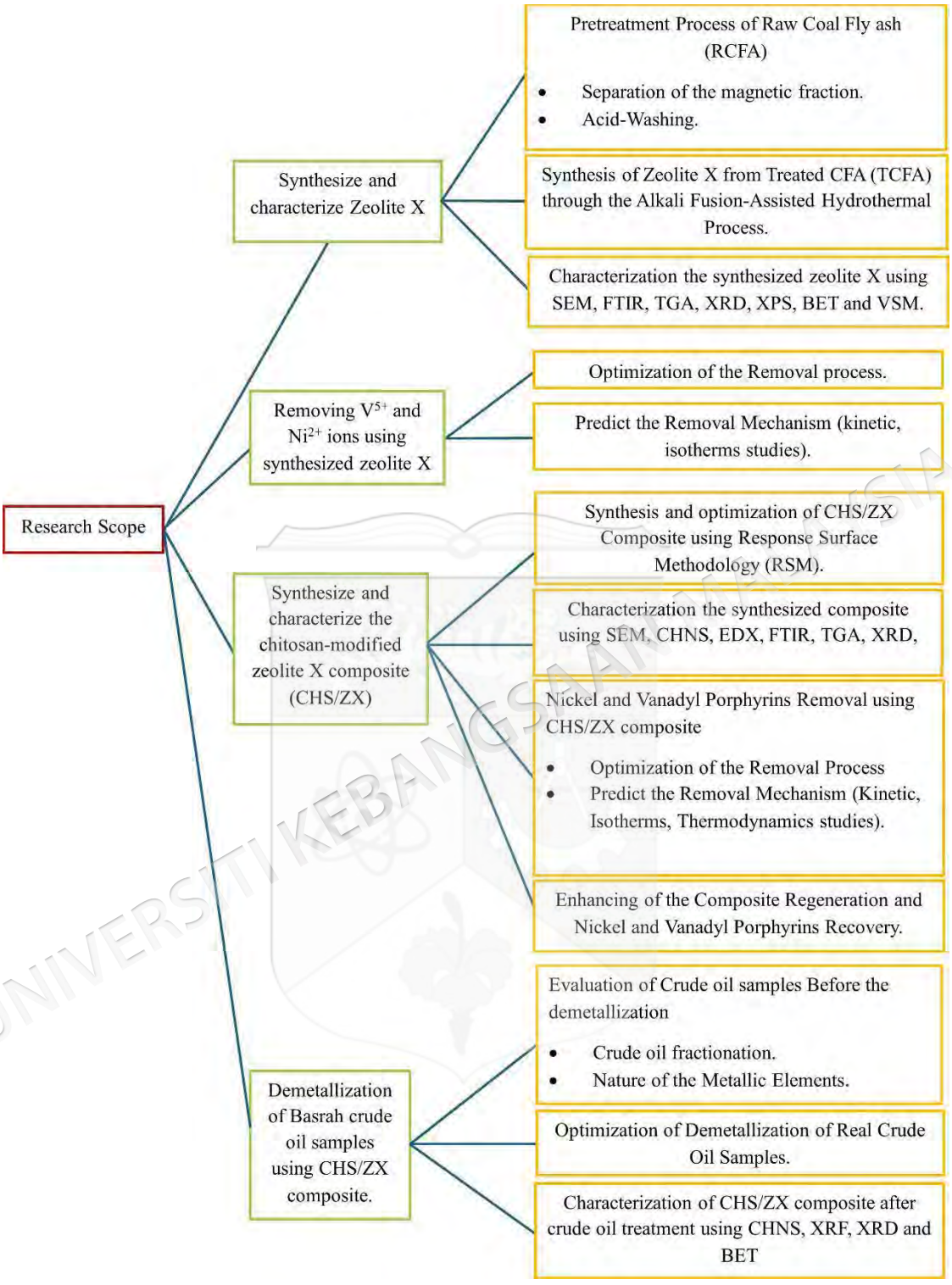

Figure 1.3 Flowchart of the comprehensive research scope

1.5 SIGNIFICANCE OF THE STUDY

The increasing demand for energy, coupled with the depletion of conventional light crude oil reserves, has necessitated a shift towards the use of heavier crude oil feedstocks. However, these feedstocks pose problems in terms of the presence of

impurities such as vanadium (V) and nickel (Ni), which give rise to significant problems during refining, such as catalyst deactivation, equipment corrosion, and environmental pollution. Traditional demetallization methods are limited by the following factors: high operating costs, high energy consumption, and negative environmental impacts. In the face of these challenges, the current study introduces a new adsorbent material, especially a chitosan-modified zeolite X composite (CHS/ZX), prepared from Malaysian fly ash. This is an innovative, eco-friendly solution that uses waste materials to come up with an environmentally friendly approach for crude oil purification.

The main reason this research is imperative because of its non-destructive method for demetallization; it preserves the precious porphyrins and effectively eliminates metal contaminants. Moreover, with the use of more advanced methodologies, the synthesis and efficacy of the CHS/ZX composite are improved, hence assuring it is scalable and cost-effective. By obviating the high temperatures and pressures usually required in conventional processes, this study presents a solution that is both energy-efficient and environmentally sustainable to a persistent industrial problem. More than that, the dual functionality of this composite in the removal of metal impurities and porphyrin recovery provides great transformative potential for sustainable refining methodologies and sophisticated industrial applications. As such, this study embodies a landmark in the field of heavy oil demetallization that echoes worldwide initiatives toward cleaner and more sustainable energy sources.

CHAPTER II

LITERATURE REVIEW

2.1 METALLIC CONSTITUENTS OF CRUDE OILS

Crude oil, a complex assemblage of hydrocarbons with varying molecular weights and other organic substances, originates from ancient plant and animal matter. This yellow-to-black liquid, located in geological formations below the earth's surface, is typically divided into its components through fractional distillation to produce various fuels. The term petroleum encompasses both naturally occurring unrefined crude oil and the refined products derived from it. As a fossil fuel, crude oil is produced when substantial amounts of deceased organisms, primarily zooplankton and algae, are buried under sedimentary rock and exposed to extreme heat and pressure (Fanchi & Fanchi 2016).

Crude oil components can be divided into multiple compounds and subdivisions based on the composition of the crude oil. Normally, crude oil will contain a percentage of dissolved gases, liquids, and solids. The liquids can be further divided into saturates, aromatics, and resins. Different types of solids may also exist in crude oil; however, the most prominent is solid asphaltene (Fakher et al. 2020).

Carbon and hydrogen are the primary constituents of crude oils, constituting approximately 82-87% and 12-15%, respectively. Sulfur is the next most prevalent element, with concentrations ranging from 0.05% to over 5%. Oxygen and nitrogen follow as the fourth and fifth most common elements in crude oil. Typically, oxygen content is below 2%, while nitrogen content is less than 0.1%. Other elements, including vanadium, nickel, calcium, potassium, iron, copper, zinc, boron, arsenic, selenium, silicon, and phosphorus, are present at trace levels (0.01-0.1%) or ultra-trace levels (less than 0.01%) (Tirado et al. 2023). The most common inorganic metals found in oil are in the form of water-dissolved salt ions such as Mg, Na, and Ca (Zhang et al. 2022b).

Normally, the desalter removes water-soluble inorganic salts, such as sodium or potassium chlorides (Mitra et al. 2022).

Nickel (II) and vanadyl (VO) (II) compounds, both porphyrins and non-porphyrins, are the most common metals found in crude oils. Chlorophylls, known for their widespread distribution and high concentration, are the primary precursors of porphyrins (Jumina et al. 2021). Porphyrins are categorized into two groups: those derived from the chlorophylls of marine algae and phytoplankton and those originating from terrestrial plant chlorophylls. The transformation of chlorophylls into porphyrins involves a series of reactions in the water column and during sediment burial. Filby determined that metalloporphyrins form during the early stages of diagenesis and catagenesis in source rocks (Tahoun et al. 2021).

Isolating metalloporphyrins is challenging due to their complex mixtures, but advanced spectroscopic and chromatographic techniques have facilitated their separation and identification (Aghahuseynova 2020). Vanadium and nickel porphyrins were discovered first, while organic forms of other metals were later identified using gas chromatography (GC) or high-performance liquid chromatography (HPLC) coupled with inductively coupled plasma-mass spectrometry (ICP-MS) or atomic absorption spectrometry (AAS) (McKenna et al. 2021).

Ultraviolet-visible (UV–vis) spectroscopy is frequently employed for identifying and quantifying porphyrins due to its high intensity and sensitivity towards both porphyrins and metal-free porphyrins. Some vanadium and nickel compounds exhibit strong optical absorption in the soret band around 400 nm. However, the intricate nature of hydrocarbon mixtures makes it challenging to characterize vanadium and nickel compounds present in low concentrations, likely due to complex formation or chemical modifications of the porphyrin ring. Consequently, non-porphyrins are characterized by the lack of distinct UV–vis spectroscopic bands. These might include atypical porphyrin or pseudo-aromatic tetradentate ligand systems, yet no non-porphyrins have been structurally identified in heavy petroleum. Isolating porphyrins from crude oils can minimize or eliminate interferences from other petroleum

compounds, thus enabling molecular characterization through ultrahigh mass resolution mass spectrometry (Banda-Cruz et al. 2021).

Mass spectrometry is an invaluable method for analyzing porphyrins, offering precise data on their molecular weights and elemental compositions. Through this technique, several porphyrin series have been identified in fossil fuels, all featuring the core structure N_4VO. In petroleum, the most frequently found porphyrins are etio (ETIO) and deoxophylloerythroetio (DPEP), which possess double bond equivalence (DBE) values of 17 and 18, respectively. Other petroporphyrins include dicyclic-deoxophylloerythroetio (Di-DPEP), rhodo-etio (rhodo-ETIO), rhodo-deoxophylloerythroetio (rhodo-DPEP), and rhodo-dicyclic-deoxophylloerythroetio (rhodo-Di-DPEP) (McKenna et al. 2021). The structures of these compounds are shown in Figure 2.1.

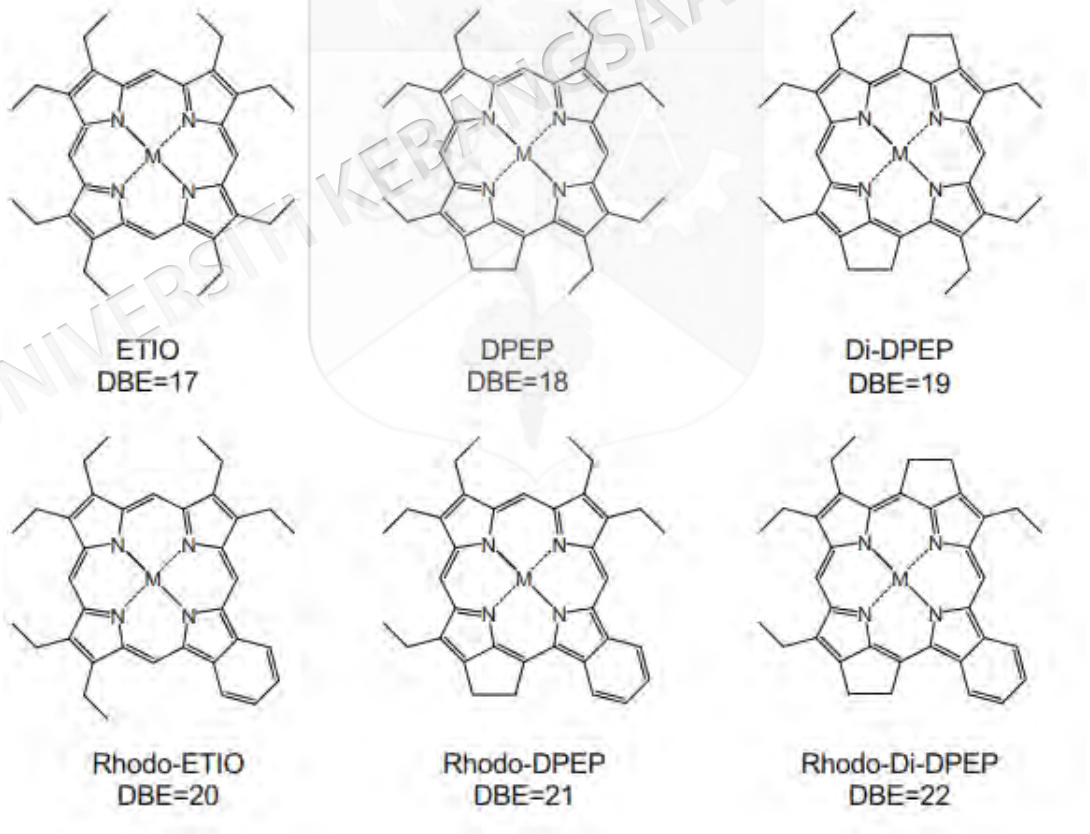

Figure 2.1 Common porphyrins in heavy petroleum

Source: McKenna et al. 2021

The concentrations of these geoporphyrins are highly variable, ranging from few ppm to 10^4 ppm (1%), which is sufficient to interfere with catalytic oil refining, because of the metals contained in the porphyrin complexes (Fan et al. 2020). These metal compounds can significantly hinder upgrading processes and frequently cause major issues in catalytic cracking and hydrodesulfurization units. Common problems include pore blocking, fouling of active sites, and alterations in catalyst selectivity (Ghassabzadeh et al. 2020). These issues can be mitigated by removing these troublesome compounds prior to further upgrading. Thus, gaining a thorouare understanding of their quantities, distributions, physicochemical properties, and chemical environments is crucial for developing effective catalytic processes and demetallization techniques.

Vanadium and nickel compounds are primarily located in the highly aromatic, polar resin and asphaltene fractions (Figure 1.1). These compounds tend to aggregate and associate significantly within these fractions, making the removal of metal compounds particularly challenging. As noted earlier, metals in petroleum can be found both as organometallic complexes (porphyrinic) and as high molecular weight complexes (non-porphyrinic) associated with asphaltenic components. Understanding the distribution of these metals is essential for their effective removal and demetallization (Fan et al. 2020).

2.2 THE SIGNIFICANCE OF THE FLUID CATALYTIC CRACKING (FCC) PROCESS IN PETROLEUM REFINERIES

The fluid catalytic cracking unit (FCCU) represents the heart of the refinery (Yadav et al. 2022); it serves as the central hub for converting low-quality, heavy hydrocarbon molecules into more valuable, lighter compounds. These refined products play a crucial role in the composition of transportation fuels, including gasoline, jet fuel, and diesel. Since its initial industrial implementation in 1942, fluid catalytic cracking (FCC) technology has propelled the FCCU to become a fundamental element in contemporary petroleum refining processes (Oloruntoba et al. 2022).

There are various FCC designs currently available in the market, but typically, an FCC unit comprises three main sections: the reactor, the distillation/separation

section, and the catalyst regenerator, as depicted in Figure 2.2. A crucial component of the FCC unit is the reactor-regenerator system, where heavy crude oil is converted into valuable products such as gasoline, diesel, and liquefied petroleum gas. The reactor itself is divided into two parts: the riser and the stripper. When the feedstock encounters the heated, regenerated catalyst at the base of the riser, it vaporizes. The vaporized hydrocarbons then break down into smaller molecules on the surface of the catalyst within the riser (Tasneem et al. 2024).

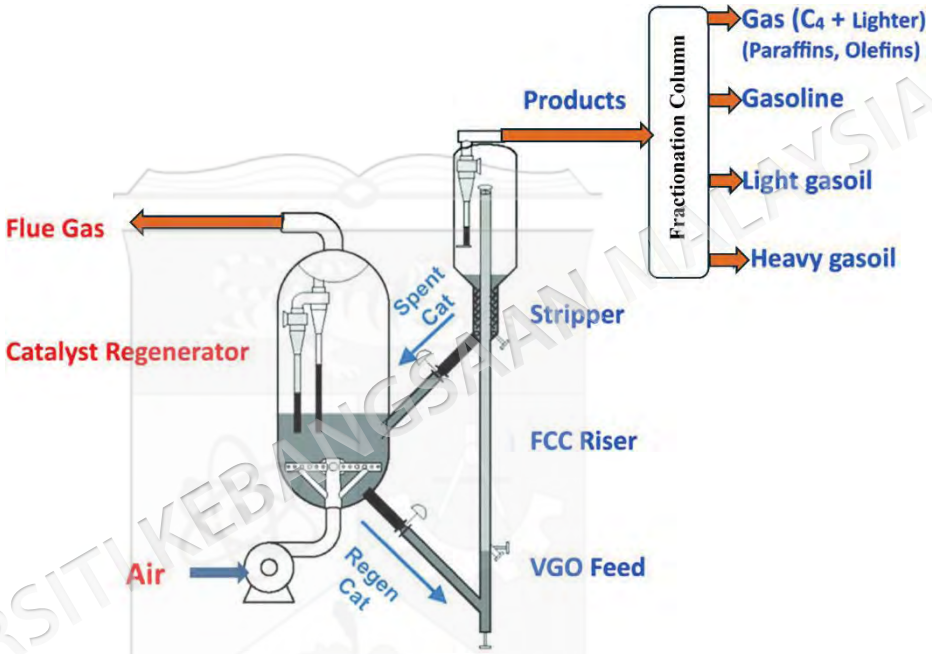

Figure 2.2 Schematic diagram of a Fluid Catalytic Cracking unit

Source: Tasneem et al. 2024

The FCC operation consists of five key processes: feed pretreatment, conversion, heat and pressure recovery, effluent separation, and product treatment (Sadeghbeigi 2020). The feedstocks, typically high-boiling-point petroleum fractions known as high-vacuum gas oil (HVGO) from the crude vacuum distillation unit, are first preheated to a temperature range of 149–400°C. These preheated feedstocks are then introduced into the riser inlet, where they come into contact with a stream of hot, regenerated catalyst from the regenerator. As the oil feed ascends the riser in a fluidized state, it cracks into smaller molecules before entering the reactor vessel. Here, the resulting effluent vapor is separated from the spent catalyst (Oloruntoba et al. 2022).

The cracked effluent vapor exits through the reactor's top outlet and is directed to the main fractionation unit for further processing and recovery of valuable products. Meanwhile, any remaining slurry is recycled back to the riser-reactor unit. During the cracking process in the reactor, a carbon-rich substance known as coke gradually deposits on the catalyst, which leads to a loss of catalytic activity. To restore the catalyst's effectiveness, the coked catalyst is removed from the bottom of the reactor and transferred by gravity to the regenerator. In the regenerator, the coke is burned off in a fluidized state through the injection of heat and air. Once cleaned, the regenerated catalyst is redirected back to the reactor section to continue the process loop (Oloruntoba et al. 2022).

Globally, more than 400 FCC/RFCC units are in operation, with a combined estimated capacity of 20 million barrels daily. These units are predominantly located in the United States, China, Japan, and Brazil, with new facilities under construction in some developing countries (Sadeghbeigi 2020). The FCC unit plays several significant roles that are crucial to the efficiency and profitability of oil refineries.

One of the primary roles of the FCC unit is processing extremely heavy crude oil fractions. As access to easily processed feeds diminishes, the FCCU has become vital for handling diverse feedstocks to maximize refinery profitability. These feedstocks include vacuum gas oil residues, vacuum distillates, vacuum distillation tower bottoms, atmospheric distillation tower residues, and more (OA et al. 2019). However, processing poor-quality feedstocks in the reactor unit can result in high coke formation rates and metal poisoning (Oloruntoba et al. 2022).

Another critical function of the FCCU is the production of high-quality gasoline. Currently, the FCCU serves as the major gasoline production hub, contributing to nearly 45% of global output. In addition to gasoline production, the FCCU is highly adaptable to the production of light olefins for the petrochemical industry. As the second-largest source of olefins, following the naphtha steam cracker, the FCCU accounts for 48% of the world's olefins production (Oloruntoba et al. 2022).

The FCCU also plays a significant role in supplying high-quality steam to various process units and for power generation. The combustion of coke in the regenerator generates substantial heat, producing a considerable amount of steam used in other refinery processes (Hsu & Robinson 2019a). Furthermore, the FCCU is known for its large throughput, short turnaround (TAR) times, and extended operational periods between shutdowns. In many refineries worldwide, the FCCU has the second-largest throughput, following the distillation unit.

Lastly, the FCCU has adapted to processing new feedstocks, including co-processing biomass-derived oils with conventional crude oil fractions. There is a strategic effort to utilize biomass-based feedstocks within existing FCC infrastructure under nominal operating conditions. This adaptation promotes biofuel production, fulfills renewable fuel obligations, and helps reduce emissions from the unit (Hsu & Robinson 2019b). The versatility and critical roles of the FCCU underscore its importance in modern petroleum refining.

2.3 IMPLICATIONS OF CRUDE OIL'S NICKEL AND VANADIUM CONTENT

The presence of Ni and V metals is undesirable, mainly because they cause poisoning and deactivation of the catalysts used in the refining process (Adanenche et al. 2023; Xie et al. 2023). Indeed, metal contaminants in fluid catalytic cracking (FCC) feeds are potentially more harmful than sulfur, which can be converted to gaseous forms and readily handled, whereas non-volatile metal contaminants tend to accumulate in the unit during cracking and eventually get deposited on the catalyst, together with coke (Jurado & Ancheyta 2022; Zhang et al. 2020a).

Metals are deposited on the catalyst, reducing its surface area by blocking pores and making it inactive (Bai et al. 2019b). These metals promote dehydrogenation reactions during cracking, increasing coke and dry gas production while decreasing gasoline output. For these reasons, heavy metals in crude oil shorten the catalyst lifespan in the hydrotreatment process. Additionally, high metal content in crude oil raises production costs by increasing the hydrogen needed and causing yield loss due to carbon rejection (Nazarova et al. 2020).

The catalyst used in the hydrotreatment process involves impregnating alumina with molybdenum and either cobalt or nickel precursors. The active phase of the catalyst was believed to be the Co/NiMoS phase, consisting of small, layered crystals. The edges and rim of these crystals are considered highly active for catalytic reactions because of the coordinative unsaturated sites (CUS) or sulfur anion vacancies. These sites, which are located at the edges of the slabs, can adsorb molecules with unpaired electrons and are crucial for catalytic reactions. The concentration of vacancies is influenced by the hydroprocessing conditions. However, strongly adsorbed species, such as metal deposits, nitrogen compounds, or coke molecules, can poison these active sites, leading to a loss of catalytic activity. This deactivation can occur even if only a fraction of the active sites is poisoned, emphasizing the sensitivity of the catalyst to contaminants and the potential impact on the overall catalytic process (Rana et al. 2021).

Additionally, there is a concern about the potential contamination of the environment because metals are released into the environment through combustion from fuels. Vanadium, in the form of vanadium oxide, is a severe irritant that reacts with mucous present in the human body. Nickel, in the form of nickel carbonyl, is carcinogenic (Valencia 2023). Furthermore, inorganic vanadium compounds produced during the processing facilitate intense ash fouling and high-temperature surface corrosion of equipment, reduction in the service life of turbo-jet and diesel engines and utility boilers, and gas corrosion of active elements of gas-turbine engines (Magomedov et al. 2017).

2.4 REMOVAL OF VANADIUM AND NICKEL VIA CONVENTIONAL DEMETALLIZATION TECHNOLOGIES

Vanadium and nickel compounds in heavy crude oil are found in organic forms, making them hard to remove during electric desalting. These compounds significantly impact upgrading processes like catalytic cracking and hydrogenation, primarily through catalyst poisoning. In catalytic cracking units, these metals affect the catalyst's activity and selectivity. Since the inception of the petroleum industry, various demetallization and upgrading technologies have been developed, including physical and chemical methods, coking, and catalytic hydroprocessing (Attia 2019).

Solvent de-asphalting (SOD) processes are commonly used in the refining industry to remove metals from heavy oil residues. These processes involve the extraction of paraffinic and naphthenic components using light alkanes, which causes the precipitation of high-molecular-mass asphaltenic and resinous compounds containing heavy metals and heteroatoms. The choice of solvent affects the yield and quality of the extract as well as the degree of demetallization (Sun & Meng 2020). Supercritical fluid extraction shows promise as a solvent extraction method, as it offers precise control over solubility and selectivity. The investigation conducted by Magomedov et al. (2020) scrutinized the solvent deasphalting of vacuum residue utilizing a carbon dioxide-toluene mixture. This study aimed to evaluate the influence of various process parameters and the composition of the mixture on both the yield and the composition of the deasphalted oil (DAO) produced. The findings indicated that the proposed mixture could achieve high-quality DAO when maintained in a single-phase liquid state. Specifically, the removal efficiencies for metals and Conradson carbon residue exceeded 90 wt.% and 80 wt.%, respectively.

Being an environmentally benign solvent with superb solubility and diffusivity for organics, supercritical water (SCW; Tc = 647 K and Pc = 22.1 MPa) has received widespread attention in the field of oil processing since the 1990s (Wang et al. 2017). Tang et al. (2020) investigated the demetallization of Tsingtao vacuum residuum (VR) and Tahe atmospheric residuum (AR), both containing over 300 ppm of vanadium and nickel, through pyrolysis in a supercritical water (SCW) environment. The results demonstrated that a metal removal rate exceeding 90% could be achieved within 2 h, which is significantly faster compared to pyrolysis conducted in a nitrogen environment.

Despite the high efficiency of solvent deasphalting (SDA) in reducing heavy metal content from various crude oil fractions, conventional SDA technologies incur significant operating costs primarily due to solvent regeneration from the deasphalting solution. Advanced SDA technologies employ supercritical conditions to heat the solvent, facilitating the release of deasphalted oil. This method allows for the direct recovery of most of the solvent, with only minor quantities associated with the product fractions requiring recovery through conventional stripping and condensation processes

(Magomedov et al. 2017). Furthermore, diluting with light solvents has been proven to be economically unreasonable. Although solvent deasphalting may yield deasphalted oil suitable for transportation, it produces a large amount of hard asphalt that is difficult to use (Wang et al. 2021b).

Distillation, a foundational method in crude oil refining, involves heating petroleum heavy oil to separate its components based on their boiling points. This process utilizes a fractional distillation column to recover various fractions. After distillation, a hydrotreatment process was employed to extract metalloporphyrins using a low-activity catalyst (Solouki et al. 2022). Although distillation offers advantages such as separation of adjacent boiling point compounds, it has limitations. This technique lacks selective removal of metals, resulting in decreased oil yield, and it transfers metals into heavy fractions, making it ineffective for metal removal as a standalone process (Sarkar et al. 2023).

Thermal cracking is a process that heats feedstock to high temperatures to produce lower molecular weight products. In addition to breaking down feedstock components, this process also involves polymerization and condensation, leading to the formation of polycyclic and polyaromatic compounds, and ultimately, coke. Thermal processes can be divided into release cracking and coking, depending on the conditions. Since the 1960s, visbreaking and coking have been widely adopted. Typically, thermal cracking operates at temperatures between 455 and 540°C and pressures ranging from 6.8 to 68.0 atm (Sviridenko et al. 2022).

Wang et al. (2021b) performed a thorough investigation into the cracking of Canadian oil sands bitumen (OSB) and Tahe atmospheric residue (AR). These substances are known for their high metal and asphaltene content. The aim of the study was to gain a better understanding of how to utilize ultra-inferior heavy oil. Canadian OSB contains a total nickel and vanadium content of 1300 ppm, which leads to significant aggregation of asphaltenes. With its significant asphaltene content of 19.3 wt.% and extensive asphaltene aggregation, Canadian OSB experiences rapid condensation during cracking, given its initial boiling point (IBP) of 500°C. Through adjustments to the cutting strategy, group composition, and metal distribution, it is

possible to modify the Canadian OSB. The cracking of Canadian OSB with an IBP of 350°C resulted in a significant reduction in viscosity, surpassing 99%. This reduction is similar to the cracking of Tahe AR, which contains 15.4 wt.% asphaltene and has a total metal content of 300 ppm.

Although the process contributes to the reduction of residual oil production from crude oil distillation, it is not without significant drawbacks. High energy losses, low conversion efficiency, and the formation of coke, olefins, and asphaltenes within the visbreaker are notable disadvantages. These issues result in the production of tar and other less recyclable residues, thereby diminishing the overall effectiveness and sustainability of the process (Magomedov et al. 2015).

Catalytic hydrotreating (HDT) is one of the most widely utilized processes for the elimination of impurities in heavy oil fractions. This process involves the hydrogenation and cleavage of C-C bonds in hydrocarbons using hydrogen gas and a catalyst, thereby converting them into compounds of lower molecular weight. Despite the characterization of HDT as a mature technology with limited areas for further investigation, the increasing availability of heavy oils and the imperative to upgrade these resources have driven ongoing research into the conversion of heavy hydrocarbons. Fixed-bed reactors are the most commonly used for HDT because of the advantages that they present over other types of reactors (Rodríguez et al. 2018).

Kohli et al. (2016) examined the extent of catalyst deactivation in hydrotreating by utilizing four different feedstocks. Their study demonstrated that deactivation by metals in the resin and asphaltene components of heavy crude oil and residues differs significantly. The results concluded that metals could deactivate catalysts used in hydroprocessing reactions, with the impact depending not only on their concentration but also on their nature. Metals in the resin component may have a negligible effect on deactivation, unlike those in the asphaltene component. Nickel compounds deactivated hydrodesulfurization (HDS) sites to a lesser extent than vanadium compounds. Additionally, heavy crude with high wax content suggests that long paraffinic or naphthene/aromatic chains contribute to coke formation, which covers HDS active sites

without solid coke precipitation. In contrast, solid coke forms in feedstocks with high asphaltene content.

Nevertheless, one major drawback of heavy oil hydroprocessing is the inevitable catalyst deactivation caused by the buildup of metals and coke. This issue becomes even more pronounced with extended operation and increased reaction intensity. Carbonation occurs quickly in the initial stages of the deactivation process, while metals accumulate as the treatment process continues. On the other hand, during hydrotreating reactions at elevated temperatures, asphaltene molecules transform into coke. Consequently, as observed in previous studies, both coke and metals gradually deposit on the catalyst over time (Rodríguez et al. 2018).

2.5 REMOVAL OF VANADIUM AND NICKEL VIA UNCONVENTIONAL DEMETALLIZATION TECHNOLOGIES

Given the drawbacks of the traditional methods mentioned above, it has become necessary to search for alternative approaches to overcome the difficulties associated with these methods. Numerous studies have been conducted in scientific publications regarding removing metals from heavy petroleum oil. Two prominent research groups in this field focus on different aspects. The first group is dedicated to creating a new and innovative technique for the extraction process, while the other group aims to enhance the comprehension of the removal mechanism. Many researchers in these groups have conducted studies using different model compounds rather than complex heavy oils. This approach allows for a clearer understanding of the mechanism in an ideal setting and avoids the complications of heavy crude oil composition (Attia 2019). Table 2.1 lists the most commonly used model compounds in previous studies.

Table 2.1 Different model compounds used in the demetallization process

Model compound
Nickel protoporphyrin disodium (Ni-PPDS)
Vanadyle tetraphenyl porphyrin (VO-TPP)
Vanadyl octaethyl porphyrin (VO-EP)
Nickel tetra-(3-methylphenyl) porphyrin (Ni-T3MP)

to be continued…

…continuation

Nickel tetraphenyl porphyrin (Ni-TPP)
Vanadyl oxide octaethyl porphyrin (VO-OEP)
Nickel etio porphyrin (Ni-EP)
Nickel octaethyl porphyrin (Ni-OEP)
Vanadyl etio porphyrin (V-EP)
Vanadyl mesotetraphenyl porphyrin (VO-MTPP)

Source: Jenifer et al. 2015

Scientists have used chemical methods with liquid reagents like acids or bases for many years to effectively remove metals from heavy crude oil. These methods have several advantages. They involve simple instrumentation and technological design, eliminating the need for catalysts, adsorbents, and hydrogen. Additionally, the processes can be carried out at low temperatures and pressures, preventing carbon deposits and major alterations in the hydrocarbon composition of the feedstock. Under mild conditions, the chemical composition of the oil components remains unaltered during the processes. (Kobotaeva & Skorohodova 2018).

Acids and bases play crucial roles in demetallizing various petroleum fractions by forming separable entities with metal compounds. The use of organic and inorganic acids for demetallizing fossil crude oil is well-documented and widely established. Hydrofluoric acid is particularly effective, achieving approximately 90% metal removal and 85-90% oil recovery (Attia 2019). Moreover, many research studies have explored the demetallization of crude oil using acids such as hydrochloric, nitric, phosphorous, and phosphoric acid, which can react with metal compounds in crude oil. These studies concluded that the reaction products were easily detachable and soluble in oil (Jenifer et al. 2015).

On the other hand, ammonium hydroxide and ammonium carbonate, which are bases dissolved in water, have been employed to react with metal complexes chemically, forming compounds that can be easily separated (Jenifer et al. 2015). The selection of an acid or base is contingent upon the oil fraction to be treated and the type of metals to be eliminated. Furthermore, the variables such as concentration and reaction conditions have a substantial impact on the results.

However, challenges arise when using sulfuric acid in the demetallization process, because sulfuric acid will convert to sulfur dioxide, leading to side reactions with unsaturated hydrocarbons and the formation of byproducts. This complexity hinders the elimination process and reduces efficiency (Magomedov et al. 2015). In addition, sulfuric acid reacts with hydrocarbons in the oil, which leads to an increase in the quantity of acid required for the process and a decline in the amount of oil produced.

Oxidation agents, known as oxidants, play a crucial role in demetallizing petroleum fractions by inducing electron loss through oxidation. This method is particularly effective for heavy feedstocks and demonstrates a high removal efficiency. Oxidants typically undergo chemical reactions with metal compounds, transforming them into more easily removable forms. Common oxidants include chlorine, sulfuryl chloride, dinitrogen tetroxide, benzoyl peroxide, and tert-butyl hydroperoxide. However, this method has limitations, including the potential loss of oxidant during the reactions. Additionally, certain oxidizing agents pose hazards and require special precautions during handling and disposal. Rigorous process control is essential to prevent undesirable reactions or degradation of petroleum fractions (Jenifer et al. 2015).

An electrochemical approach for metal removal from crude oil was also explored, using electrically charged surfaces to induce chemical changes. A study examined model metalloporphyrins and porphyrinic extracts from Venezuelan crude oil, achieving approximately 20% conversion for VO-TPP and 18% for Ni-TPP. Another study found that the choice of electrodes and protonating agents significantly influenced the results. It achieved 84% hydrodemetallization for VO-MTPP and 78% for VO-OEP using a glassy carbon electrode in a THF/methanol/perchloric acid medium. While effective, this method requires high voltage to achieve optimal metal removal efficiency (Jumina et al. 2021).

Microorganisms provide an environmentally friendly method for demetallizing crude oil by breaking down metalloporphyrins and using them as a carbon source. Salehizadeh et al. studied the action of *Aspergillus sp*. on VO-OEP, finding that 55% of it was degraded into free metal ions. This degradation was enhanced by Ag^{+} and reduced by Zn^{2+} and EDTA. In another study conducted by Dedeles et al. to investigate

the potential of P. *azelaica YA-1* to degrade Ni-PPDS, the results achieved a 77% degradation of Ni-PPDS and a 79% degradation of VOEP after 7 days. However, the degradation process using these microorganisms is slow and time-consuming (Arjoon1 & Speight 2022).

An alternative approach involves utilizing radiation, specifically ultrasonic and microwave irradiation, to enhance the demetallization efficacy of conventional treatment methods. Ultrasonic radiation activates chemical reactions via acoustic cavitation, concentrating energy in localized regions. In their investigation, Kobotaeva et al. (2018) explored the removal of nickel, vanadium, iron, and chromium from oil and fuel oil using chemical reagents containing acidic functional groups (1% o-phosphoric acid, concentrated o-phosphoric acid, sodium sulfate, and diethylenetriaminepentaacetic acid) combined with ultrasound exposure. The results revealed that iron and chromium removal efficiency from oil samples reached 98%, while nickel and vanadium removal efficiency reached up to 55%. The study posits that ultrasonic treatment's positive impact lies in the breakdown of organic metal compounds, including weak π-π and n-π complexes, as well as tetrapyrrole macrocycles present in oils and oil products. This breakdown facilitates the formation of new compounds that readily transition into the aqueous-acid phase.

Utilizing microwave-assisted techniques for metal and sulfur removal from crude oil has gained prominence as an efficient alternative to conventional methods. The distinctive features of microwave heating render it an appealing choice across various domains, including food, chemical, and environmental engineering. In contrast to traditional heating, microwave heating operates volumetrically, directly converting electromagnetic energy into heat by interacting with polar molecules or ions present in the material. This advantage mitigates limitations associated with traditional heating, such as undesirable temperature gradients inside the target substance (Solouki et al. 2022).

In their 2019 study, Attia et al. investigated the impact of traditional and microwave heating techniques on the concurrent removal of sulfur and heavy metals (including nickel and vanadium) from heavy crude oil. The results indicated that

traditional heating achieved maximum removal efficiencies of 90%, 79%, and 53% for vanadium, nickel, and sulfur, respectively. In contrast, microwave heating substantially improved the removal efficiency for these elements. Specifically, vanadium, nickel, and sulfur concentrations were reduced by up to 90%, 50%, and 99%, respectively (Attia 2019). While microwave-assisted demetallization has garnered attention in the literature, it is not without limitations. Firstly, achieving a high removal rate via hydrodemetallization under microwave heating necessitates elevated pressure. Furthermore, studies have highlighted lower heating efficiency in microwave-assisted demetallization processes (Li et al. 2019a).

Table 2.2 presents the unconventional methods with promising demetallization capabilities, along with their respective advantages and drawbacks.

Table 2.2 The significant features of the unconventional methods for demetallization.

Method	Advantages	Disadvantages
Ultrasonic radiations with chemical reactions	This improvisation gives higher efficiency of metal removal than the traditional method.	Applicable only to mild noncatalytic operations
Microwave radiations on desalting	This modified method gives a higher efficiency of metal removal than the traditional method.	Increase in microwave time caused difficulty in increasing the removal rate.
Micro-organisms	Good potential for metal removal.	Slow and time-consuming process.
Electrochemical methods	High metal removal efficiency.	High voltage is required for higher metal removal.
Ultrasonication	Removal efficiency improved by adding a suitable surfactant/solvent.	Reaction affected by power of ultrasonication and is hindered at high temperatures.
Photochemical method	Energy saving, solvent recovery, safe demetallization.	Difficulty in removing bound-type metalloporphyrins without solvent addition.
Oxidation	With a suitable oxidant, it can give high removal efficiency for heavy feedstock.	Loss of oxidant as it might be consumed for side reactions along with metal removal.

Source: Jenifer et al. 2015

In summary, elevated levels of metal ions in crude oils pose an additional financial burden on refineries processing heavy crude oil. This is manifested in the high

cost of hydrogen addition, yield loss due to carbon rejection, and catalyst deactivation. Consequently, a pre-treatment step is essential to mitigate these challenges by reducing the metal content in crude oil feeds before they enter the processing stream. Developing an effective pre-treatment step to remove or diminish metal ion concentrations could enhance the efficiency of conventional processing methods, resulting in substantial savings in time and cost. Currently, no known metal extraction step preceding hydroprocessing stages is simultaneously effective, economical, and capable of addressing catalyst deactivation and environmental concerns

As an alternative to conventional hydrodemetallization, the adsorptive demetallization (ADD) serves under ambient conditions. Adsorption is the backbone of ADD technology, metal compounds are selectively removed using specific adsorbents. The efficacy of ADD particularly its longevity, selectivity, and capacity largely hinges on the choice of adsorbent. Consequently, the adsorbent significantly influences the process's selectivity, capacity, and overall sustainability, including the regenerability of the adsorbents and the recoverability of adsorbate. The commonly investigated adsorbents include activated carbon, metal oxides, and zeolites.

Adsorbates can be removed through two distinct mechanisms based on the interaction between the adsorbent and the targeted adsorbates: physical adsorption (physisorption) and chemical adsorption (chemisorption). In physical adsorption, adsorbates and adsorbents primarily form weak van der Waals forces, allowing for relatively easy regeneration of the adsorbent. In contrast, chemical adsorption involves chemical bonding between adsorbates and adsorbents, altering the physical and chemical properties of the metal compounds and necessitating higher energy for regeneration (Ahmad 2015).

Adsorptive demetallization (ADD) holds promise due to its potential for regenerability, cost-effectiveness, and environmental friendliness when conducted under ambient conditions. However, challenges related to selectivity and diffusion remain significant in ADD. Consequently, substantial research efforts should prioritize the identification of adsorbents with high selectivity and capacity for metal complexes (Lee & Valla 2019).

Activated carbon (AC) refers to the highly carbonaceous materials having high porosity and sorption ability produced from wood, coconut shells, coal, cones, etc. AC is one of the frequently used adsorbents utilized in various industries for the removal of numerous pollutants from water and air bodies. Since AC is synthesized from agricultural and waste products, it has proved to be a great alternative to the traditionally used nonrenewable and expensive sources. For the preparation of AC, two basic processes, carbonization and activation, are used (Sharma et al. 2022). In 2021 Ali et al. investigated the potential for removing nickel from Iraqi crude oil using a simple pre-treatment method based on adsorption technology. The crude oil was treated with a high-surface-area adsorbent, specifically commercial granular activated carbon (GAC). The adsorption process was conducted in a batch mode unit under various operating parameters, including the adsorbent media amount, water/crude oil ratio, contact time, and agitation speed, to optimize the conditions for the best removal of nickel from the crude oil. The results indicated that GAC exhibited a high adsorption capacity, achieving an 87% removal of the total nickel content. The study also showed that the efficiency of the treatment increased with higher values of the operational parameters (Ali et al. 2021).

Despite the notable capacity of pure activated carbons for adsorbing metals from crude oil, several drawbacks remain. One major challenge is their lack of selectivity in removing the targeted contaminants. Furthermore, the efficacy of activated carbons in adsorptive demetallization is significantly limited by their low adsorption capability. This limitation is primarily due to the broad distribution of pore sizes and restrictions in mass transport (Silas et al. 2019).

Metal oxides have been employed in ADD and demonstrated efficacy in the demetallization of crude oil. Konne et al. (2017) investigated the use of aluminum oxide nanoparticles Al_2O_3+ sodium dodecyl sulfate (SDS), synthesized through a simple sol-gel method, for the demetallization of nickel from a crude oil-water mixture in a batch adsorption process. The study revealed that the removal rate increased steadily with the amount of adsorbent, from 0.02 to 0.1 g, achieving a maximum removal efficiency of 86.1% for Al_2O_3+SDS. In contrast, for Al_2O_3, the removal rate decreased as the adsorbent dosage increased, with the highest removal rate of 78% observed at the lowest

dosage of 0.02 g. Furthermore, at a constant adsorbent dosage, removal rates of 94% and 93% were achieved for a 1:3 crude oil-water mixture using Al_2O_3+SDS and Al_2O_3, respectively. These findings confirmed the superior capacity of Al_2O_3+SDS for removing Ni^{2+} ions from crude oil compared to Al_2O_3. However, these materials have limited capacity for the adsorption of metal compounds.

Zeolite-like sorbents, including materials such as primitive clay and granulated macroporous Al_2O_3-SiO_2, represent a category of structured porous silicas suitable for use as adsorbents in ADD. Iuzmukhametova et al. (2023) evaluated the use of a granulated macroporous Al_2O_3-SiO_2 adsorbent for adsorptive treatment. This method, proposed as an initial step for residue pretreatment in atmospheric and visbreaking residue refineries, operates at 485–510°C and a feed rate of 1 h^{-1}. The process achieved a total liquid product yield of approximately 73.0–75.0 wt%, coke deposition on the sorbent of 12.6–18.3 wt%, demetallization above 98%, and a reduction in carbon residue by 65–72%. However, the study encountered significant challenges. The high coke content on the adsorbent necessitates regeneration, which requires temperatures up to 750°C. This regeneration process reduces the macropore size and volume of the adsorbent, which significantly impacts its demetallization efficiency.

Zeolites, a versatile class of aluminosilicates, are recognized for both their natural occurrence and their industrial synthesis. They are extensively researched for a wide range of applications, including wastewater treatment (de Magalhães et al. 2022), catalysis (Morris & Nachtigall 2017), and adsorption (Ugwu et al. 2022). The unique properties of zeolites, driven by their structural characteristics and adjustable Si/Al ratios, make them highly adaptable for various uses. The X zeolite variant excels in heavy metal adsorption, thanks to its distinctive three-dimensional faujasite (FAU) framework, large surface area, and numerous acidic sites. Furthermore, extensive research has led to significant advancements in overcoming initial limitations, such as diffusion barriers and selectivity in competitive environments, through the incorporation of polymeric and inorganic components into zeolite composites (Rad & Anbia 2021). Therefore, the following discussions will delve into the exceptional benefits of zeolites and zeolite/polymer sorbents.

2.6 ZEOLITE

2.6.1 Background

Zeolites constitute a category of over 50 soft, white aluminosilicate minerals characterized by a tectosilicate structure, which is a three-dimensional framework of interconnected tetrahedra composed predominantly of aluminum, silicon, and oxygen atoms (see Figure 2.3a, b). These minerals exhibit a crystalline architecture formed from $[AlO_4]^{5-}$ and $[SiO_4]^{4-}$ units, with each tetrahedron sharing its four corner oxygen atoms with neighboring tetrahedra, as illustrated in Figure 2.3c–e (Khaleque et al. 2020). According to. Figure 2.3f, when each tetrahedron in the framework is centered by a silicon atom, the overall structure remains electrically neutral, similar to quartz (SiO_2). In zeolite frameworks, some silicon atoms, which are quadrivalent, are substituted by trivalent aluminum atoms, creating a net positive charge. This positive charge is counterbalanced by singly- and/or doubly charged cations such as sodium, potassium, calcium, and magnesium, which are distributed throughout the structure and contribute to the presence of large pores or rings(de Magalhães et al. 2022).

The general formula for zeolites can be expressed as

$$M_{a/b}\,[(AlO_2)_a(SiO_2)_y].cH_2O$$

where M represents an alkali or alkaline earth metal, b is the charge on that metal, a corresponds to the number of Al tetrahedra, y varies from 2 to 10 for Si tetrahedra, and c ranges from 2 to 7 for water molecules. The combined Si and Al tetrahedra create a structural framework within zeolites, featuring centrally located Si or Al atoms and oxygen atoms at the corners. These arrangements lead to pores and channels, as depicted in Figure 2.3a, b (IZA-SC 2024).

In Figure 2.3e, a sodium zeolite with low silica content (Si/Al = 1, Na/Al = 1, specifically zeolite 4A) exhibits an open cage structure within its lattice. It also features an extensive network of negatively charged channels that accommodate Na^+ cations. These channels result from the common oxygen atom shared between Si and Al tetrahedra (IZA-SC 2024). Additionally, the microscopically small pores or channels

(as shown in Figure 2.3a–c) are often referred to as 'molecular sieves' due to their ability to facilitate cation exchange during adsorption processes. Consequently, zeolites are widely used in separation and filtration applications.

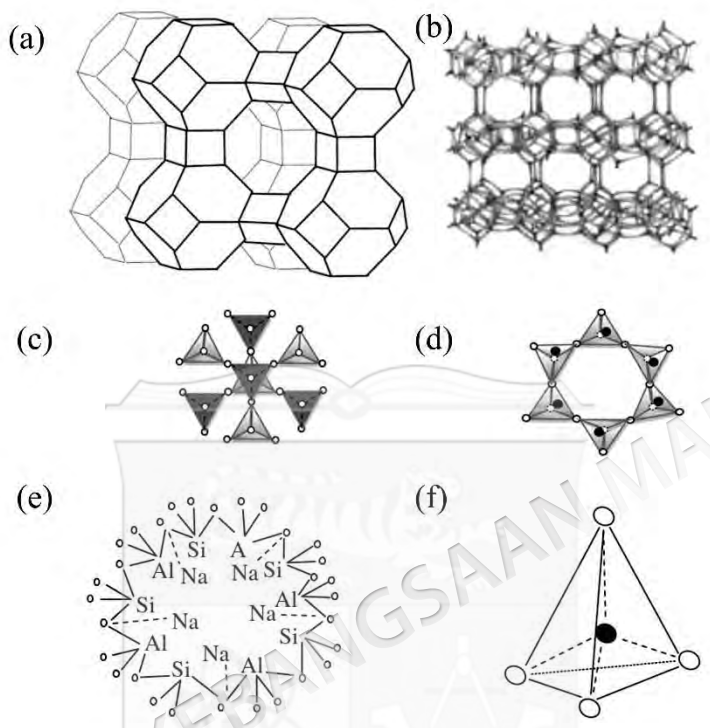

Figure 2.3 Zeolite Frameworks and Structural Units (a) the zeolite crystal structure. (b) showing cages and channels in 3D. (c) tectosilicate zeolite structure adds 3D. (d) Construction and framework of a zeolitic mineral's single-ring tetrahedron, (e) $[SiO_4]^-$ and $[AlO_4]^-$ in a ring of sodium zeolite. (f) graphic representation of a 3D viewpoint of a tetrahedral with centrally located Si or Al atoms.

Source: Khaleque et al. 2020

Zeolites possess a highly stable crystalline lattice structure, allowing for significant flexibility in ion exchange and reversible dehydration. Zeolites have the ability to incorporate additional cations, primarily sodium, potassium, magnesium, and calcium, as well as water molecules and tiny chemical molecules. Moreover, the ions and molecules within the cages are only weakly attached, allowing for their removal or replacement without causing damage to the zeolitic structure. This capacity, however, is influenced by the specific zeolites' chemical composition and crystalline structure (Andrunik & Bajda 2021).

Despite being discovered by Cronsted in 1756, the molecular sieve properties of zeolites were not explored until the mid-1920s. Unfortunately, there has been little

progress in utilizing natural zeolites for commercial purposes for quite some time. Researchers have been studying the synthesis of zeolites, specifically synthetic zeolites, by using pure chemicals or minerals found in natural resources or their by-products, such as coal fly ash (Längauer et al. 2021a).

2.6.2 Natural zeolites

Naturally occurring zeolites commonly crystallize within the tiny voids of basaltic rocks over time, or within volcanic tuffs or glass that have been modified via contact with salty water. Natural zeolites are created in several geological settings, including alkaline deserts, lake sediments, ash ponds, and marine sediments. These formations occur at relatively low temperatures under natural circumstances. Additionally, they undergo crystallization in relatively recent metamorphic rocks found in hilly areas. During the 1950s, geologists made a significant finding that revealed the widespread existence of large amounts of volcanic tuff. These deposits were composed mostly of zeolitic materials, which are substances with unique properties (Jha & Singh 2016a). Zeolitic crystals possess distinctive structures that are capable of retaining water, which may be removed with the use of heat. The dried crystals have a honeycomb-like structure with small gaps or pores that are around 2-10 Å wide (2–10 Å) (Li et al. 2019b). Natural zeolites have a commonly used formula is

$$(Li; Na; K)_p(Mg; Ca; Sr; Ba)_q[Al_{(p+2q)}Si_{n-(p+2q)}O_{2n}]\ m_oH_2O$$

where, p is the number of monovalent metal ion, q is the number of divalent metal ions, n is half the number of oxygen atoms and m_o is the number of water molecules.

Clinoptilolite and chabazite, which are types of natural zeolites, have diverse applications in fields such as water treatment, soil amendment for fertilizer application, and promoting plant development by improving nutrient retention. The use of clinoptilolite in agriculture, soil amendment, and feed additives has gained widespread acceptance due to its high silica concentration, which makes it resistant to acid. Wang et al. (2021b) investigated ways to improve soil's NH_4^+ holding capacity and reduce the energy consumption associated with industrial fertilizer production. They experimented

with various dosages of clinoptilolite mixed with soil to enhance NH_4^+ absorption, also simulating the process using the Freundlich and Langmuir equations under different conditions. The optimal ratio for high adsorption efficiency was found to be 0.01 g of clinoptilolite per 10 g of soil. The presence of both Na^+ and K^+ ions increased the NH_4^+ adsorption capacity of the clinoptilolite-amended soil more than Na^+ ions alone. The results concluded that clinoptilolite can significantly enhance soil nitrogen holding capacity, offering substantial potential to reduce the energy consumption in industrial urea production.

Zeidan et al. (2024) investigated the use of chabazite for adsorbing Congo red (CR), an anionic diazo dye, from aqueous solutions under different operational conditions. The study found that the natural zeolite had a maximum adsorption capacity of 26.525 mg/g. The adsorption efficiency increased with higher doses of chabazite but decreased with higher concentrations of CR and rising temperatures.

Natural zeolites, despite their benefits, have several significant disadvantages that limit their practical use in different applications. Senila et al. (2024) comprehensively discussed the disadvantages of natural zeolites, which can be briefly listed as follows:

I. Natural zeolitic tuffs contain a mixture of minerals.
II. Exchangeable cations in natural zeolites are highly variable.
III. The degree of crystallinity varies.
IV. Internal surface area, internal volume, and pore radius are variable.
V. Low adsorption capacity for some substances, requiring modification.
VI. Their affinity is mainly for cations, necessitating modification for other substances.
VII. Variable properties even within the same quarry.
VIII. May contain impurities, including traces of heavy metals, thus requiring purification or restricting uses for some purposes.

These disadvantages highlight the need for ongoing research to address the limitations of natural zeolites and enhance their application in environmental remediation. Further studies are essential to optimize their performance, understand long-term environmental impacts, and develop effective regeneration and disposal strategies. To solve these limitations, researchers started to investigate the synthesis of zeolites.

2.6.3 Synthetic zeolites

In 2019, the market for synthetic zeolite materials was valued at approximately US$5.2 billion annually, with projections indicating an increase to US$5.9 billion annually by 2023 (Collins et al. 2020). Synthetic zeolites offer several notable benefits due to their high purity and uniform crystal size, making them ideal for a wide range of industrial applications. Their production process, which takes only a few hours to a few days in a laboratory, allows for precise control over pore size, adsorbent surface characteristics, and thermal stability, resulting in a highly consistent and reliable product. These zeolites can be synthesized from various sources with diverse chemical compositions and physicochemical properties, providing versatility and adaptability to meet specific needs. The uniformity of synthetic zeolites enhances their performance in applications requiring precise specifications, making them a superior choice for industries that demand high-quality materials. Additionally, the ability to tailor the properties of synthetic zeolites, such as their pore size and surface characteristics, ensures they meet the stringent requirements of different industrial processes. Their excellent thermal stability further enhances their functionality, making them a valuable asset in high-temperature applications. Overall, synthetic zeolites' purity, consistency, and customizable properties underscore their significant advantages in industrial use (Khaleque et al. 2020).

Conventional synthesis of various types of zeolites typically occurs in closed reaction systems. In these systems, aluminum and silicon sources are combined to create a supersaturated solution, which is then heated at temperatures ranging from 30 to 180°C for durations spanning minutes to days. This process facilitates nucleation and

crystallization. The synthesis conditions for each type of zeolite are documented and published by the International Zeolite Association (Yoldi et al. 2019).

Research on synthetic zeolites has been conducted for many years, leading to continuous improvements in the synthesis process. However, issues such as low resource utilization and significant waste generation persist. Furthermore, the reliance on mineral resources and pure chemical reagents for raw materials significantly increases the cost of zeolite synthesis (Peng et al. 2021). As governments worldwide emphasize sustainable development and environmental protection, the principles of green chemistry are gaining increasing importance across various industries. Given the need for the industrialized production of zeolites in the future, there is growing interest among researchers in identifying an ideal green synthesis route for zeolites. Such a route would be simple, economical, and environmentally friendly, aligning with the goals of sustainability and cost-efficiency (Lin et al. 2022).

Synthesis procedures utilizing industrial wastes present two significant advantages over commercial zeolites synthesized from pure chemicals. Firstly, waste-derived zeolites are more cost-effective than their conventional counterparts. Secondly, using industrial wastes as sources of aluminum and silicon facilitates the valorization of by-products. The zeolitization mechanism from waste materials involves four stages: dissolution of aluminum and silicon, formation of a geopolymer, nucleation of the crystalline structure, and growth of the zeolite crystals. The primary parameters influencing this synthesis process include the available silicon and aluminum content, temperature, pressure, alkalinity, and the liquid-to-solid ratio (Yoldi et al. 2019).

Fly ash, an industrial by-product rich in silica and alumina, is abundant and cost-effective, making it a potential candidate for synthesizing synthetic zeolites (Makgabutlane et al. 2020a; Ochedi et al. 2020). The type of zeolite produced depends on factors such as temperature, pressure, reagent solution concentration, pH, activation process, aging period, and the Si, and Al oxides content of the starting materials (Makgabutlane et al. 2020b; Sivalingam & Sen 2018; Tauanov et al. 2018a). Zeolites can be categorized based on the Si/Al molar ratio in activated fly ash into low, intermediate, and high silica zeolites, as shown in Table 2.3. Generally, an increase in

the Si/Al ratio (from 0.5 to infinity) in zeolites enhances properties such as acid resistance, thermal stability, and hydrophobicity, while properties like hydrophilicity, acid site density, and cation.

Table 2.3 Classification of zeolites based on the grades

Zeolite grade	Si/Al molar ratio	Some of the common mineral names and their framework codes
Low silica	≤ 2	Analcime (ANA), cancrinite (CAN), Na-X (FAU), natrolite (NAT), phillipsite (PHI), sodalite (SOD)
Intermediate silica	2-5	Chabazite (CHA), faujasite (FAU), mordenite (MOR), Na-Y (FAU)
High silica	> 5	ZSM-5(MFI), zeolite-b (BEA)

Source: Jha et al. 2016

2.6.4 Faujasite type zeolites (FAU)

The first experimental investigations of FAU zeolites were conducted by Damour in 1848. In 1949, Barrer and Milton synthesized zeolite-type NaX, characterized by a Si/Al ratio ranging between 1.0 and 1.5, intended primarily for use in the adsorbent industry. Zeolite type Y, featuring a structure akin to that of X but with a higher Si/Al ratio (1.5 to 3.0), was synthesized by Breck in 1954. This development has contributed significantly to the adsorbent industry and facilitated advancements in processes involving hydrocarbon transformations through zeolite Y. The reduced aluminum content in these zeolites leads to a structure that exhibits enhanced thermal and acidic stability (Castro et al. 2020).

FAU is an aluminosilicate molecular sieve represented by the formula $|(Ca, Mg, Na_2)_{29}\ (H_2O)_{240}|\ [Al_{58}Si_{134}O_{384}]$-FAU. The synthetic FAU-type zeolites are categorized into two types: Linde X and Linde Y. These two types essentially differ in their Si/Al ratio. The SiO_2/Al_2O_3 ratio for X zeolite ranges from 1 to 1.5, while Y zeolite has a higher ratio. The FAU framework consists of 24-tetrahedra cuboctahedral units, also known as sodalite cages, which are connected by hexagonal prisms (double six-rings). This arrangement forms a three-dimensional porous channel structure along the [110] direction. The structure is characterized by 12-oxygen ring window openings with apertures of 8 Å and super-cages approximately 12 Å in size (IZA-SC 2024). Figure 2.4

displays a perspective of the FAU-type zeolite super-cage in the [111] direction. FAU is a thermally stable molecular sieve due to its spacious void volume and pore cavities in its 3-D channel structure. These features are well-suited for a range of applications, including ion exchange, catalysis, and adsorption (Julbe & Drobek 2015).

FAU-type zeolites are commonly synthesized through the hydrothermal method at low temperatures (ranging from 70 to 300°C, generally about 100°C). This process generally starts with sodium aluminate and sodium silicate, resulting in zeolite in its Na^+ form (Li et al. 2022). In acid catalysis applications, it is necessary to replace Na^+ ions with H^+ to form proton-zeolite. Additionally, for specific catalytic applications, various metal cations can be incorporated into the structure via impregnation or ion exchange. This modification changes the quantity and characteristics of acid sites, affecting the diffusion of starting materials and products. Zeolites X have numerous industrial applications, including gas or vapor adsorption, separation, and catalysis. They are used in processes such as the isomerization of 1-butene, alkylation of toluene with ethylene or methanol, and the cycloaddition of carbon dioxide to ethylene oxide (Julbe & Drobek 2015).

On the other hand, zeolite Y, with a silicon-to-aluminum ratio typically greater than 1.5, has been extensively utilized in various industrial fields because of its high thermal and chemical stability. For instance, the fluid cracking catalyst (FCC) process extensively employs ultra-stable Y zeolite (USY), typically obtained via the dealumination process from zeolite Y. USY serves as a catalyst during the refining of heavy petroleum distillates, leading to the production of various light products, including gasoline and diesel. Moreover, there has been a growing interest in the preparation of tubular membranes based on Faujasite zeolite, which is primarily utilized to purify alcohols through water separation via vapour permeation (Nazir et al. 2020).

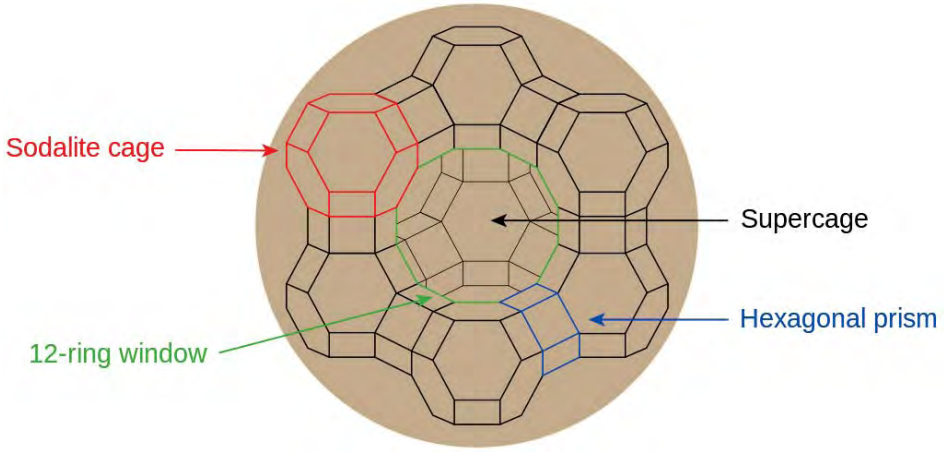

Figure 2.4 Structural features of the faujasite zeolite framework

Source: Zang et al. 2023

Despite the wide range of applications for zeolite X, its primary functions encompass catalysis, gas and organic component purification and separation, cation exchange, and adsorption. The extensive industrial uses of zeolite Na-X have driven its synthesis from various unconventional raw materials, including rice husk ash, metakaolin, oil shale ash, and coal fly ash. While the synthesis of hierarchical zeolite X using pure analytical chemicals has been documented recently, numerous studies have concentrated on producing zeolite X from fly ash.

NaX zeolite was synthesized from Huadian oil shale ash using the alkaline fusion-assisted hydrothermal method and applied to the removal of methyl blue. The synthetic zeolite exhibited a specific surface area of 366.87 m^2/g, a pore volume of 0.2085 cm^3/g, and an average pore diameter of 7.01 nm (BJH adsorption). The Optimal conditions yielded a methyl blue removal efficiency of 96.0%, and the zeolite showed excellent reusability. The efficiency of methyl blue removal was influenced by the presence of salts and salinity. The adsorption mechanism study revealed that electrostatic attraction, hydrogen bonding, and pore diffusion played significant roles in facilitating the adsorption of methyl blue onto the NaX zeolite (Shi et al. 2023).

Korpa et al. (2021) investigated the key parameters influencing the synthesis of type X and A zeolites from coal siliceous fly ash (FA). The synthesis process involved dissolving alkali-fused alumino-silicates followed by hydrothermal treatment. The findings highlighted that the SiO_2/Al_2O_3 ratio in FA, the NaOH/FA ratio, acid treatment

of pre-fused fly ash, and solution salinity significantly impact the type and properties of the resulting zeolites. For type X zeolite, it was found that FA with a SiO_2/Al_2O_3 ratio greater than 1.86 is ideal, specifically at a ratio of 3.15. Crystallization occurs more rapidly at higher temperatures; however, temperatures above 90°C cause X-type zeolite to transform into more stable phases. Extending the crystallization time from 1 to 72 hours increased the yield from 60% to 75%. The use of seawater during synthesis resulted in X-type zeolite with lower purity and specific surface area. Despite this, the synthetic zeolites exhibited high ion exchange capacity (> 320 meq/100 g), indicating their potential as effective adsorbents and catalysts for wastewater and industrial waste treatment.

Sivalingam et al. (2019) explored the synthesis of the nanocrystalline zeolite X (nZX) derived from coal fly ash sourced from eastern India, aimed at removing the textile dye crystal violet (CV) from aqueous solutions. The nZX was characterized through various methods including TEM, XRF, FESEM, XRD, FTIR, and BET. The nZX exhibited a surface area of 651.34 m^2/g, an average crystal size of 16.28 nm, particle size of 27.28 nm, 82% crystallinity, and a 91% yield. Under optimal conditions pH 9, a contact time of 60 min, temperature of 50°C, an initial dye concentration of 100 mg/L, and an adsorbent mass of 1.0 g/L nZX achieved a maximum CV removal efficiency of 99.52%. The Langmuir adsorption capacity peaked at 234.57 mg/g. Moreover, the nZX maintained high dye removal efficiency across five regeneration cycles, demonstrating its excellent reusability.

In research by Bai et al. (2022), zeolite was synthesized from a mixture of oil shale ash and coal fly ash to remove heavy metals from water. XRD and SEM analyses confirmed the conversion of the ashes into zeolite. The synthetic zeolite's adsorption capacity for heavy metals was tested using batch experiments. The findings revealed that the adsorption kinetics followed a pseudo-second-order model, while the Langmuir isotherm model provided a good fit for the isotherm data. The selectivity order for heavy metal adsorption was determined to be: $Pb^{2+} > Cr^{3+} > Cu^{2+} > Cd^{2+} > Zn^{2+}$.

2.6.5 Zeolite-based composites

While raw zeolite exhibits great adsorption capacity, challenges remain in its practical application. These challenges include the complex filtration of zeolite from aqueous solutions and the large pressure drop encountered by fixed-bed columns during adsorption (Zhang et al. 2017b). Furthermore, using zeolites to remove nickel and vanadium cations from crude oil faces significant challenges. According to Kukwa et al. (2019) study, X-ray diffraction (XRD) analysis of zeolite samples post-removal of these metal ions from the aqueous solution of crude oil in H_3PO_4 reveals that the zeolites disintegrate during the extraction and removal process.

Zeolites, due to their high concentration of silanol groups, favorable porosity, and extensive surface area, are well-suited as inorganic supports. In their protonic forms, these materials offer abundant surface hydroxyl groups that serve as effective adsorption sites. As inorganic supports, zeolites can facilitate the attachment of organic ligands, leading to the irreversible immobilization of metal cations through the coordination with donor atoms present on the ligands. Organic ligands containing nitrogen and sulfur, which are known for their strong selectivity for heavy metal ions, can be anchored to zeolite surfaces, allowing for the immobilization of metal cations from solutions without requiring additional waste processing or disposal. Consequently, surface-modified zeolites can immobilize cations not only through ion exchange and electrostatic interactions within their negatively charged framework but also by coordinating cations with donor groups on the ligands attached to their surfaces (Kukwa & Dann 2019).

In recent years, researchers have focused on zeolite-based composites as effective adsorbents for water treatment. These composites, which combine zeolites with inorganic materials or polymers, offer improved physicochemical stability, easier reusability, and higher adsorption capacity compared to raw zeolites (Abdelrahman et al. 2021).

a. Zeolite/inorganic composites

Researchers have blended zeolites with various materials to enhance their physicochemical properties for removing heavy metal ions, organic pollutants, and other contaminants from water. These materials include metal oxide nanoparticles (such as Fe_2O_3, Fe_3O_4, SiO_2, TiO_2, ZnO), carbonaceous materials (like activated carbon, carbon nanotubes, graphene oxide), hydroxyapatite, and silicate. Figure 2.5 illustrates the schematic of inorganic adsorbents combined with zeolites. Depending on the nature of zeolite, these blends fall into two categories: inorganic materials modified with natural zeolites and those modified with synthetic zeolites. Researchers have employed various methods (such as co-precipitation, hydrothermal, solvothermal, sol-gel, ultrasonic, and microwave techniques) to create zeolite/inorganic material composites (Rad & Anbia 2021).

b. Zeolite/polymer composites

Polymers can be categorized into two main types: natural and synthetic. Researchers have utilized various natural polymers such as cellulose (Ashraf et al. 2022) and chitosan (Mahmodi et al. 2020), along with synthetic polymers like poly vinyl chloride (PVC) (Jamshaid et al. 2020), polyvinyl alcohol (PVA) (Tabatabaeefar et al. 2020), polypropylene (Li et al. 2020a) and many others, to create zeolite/polymer-based composites for adsorbing toxic substances from water samples. These composites serve as an effective strategy for enhancing zeolite adsorption properties and ensuring their reusability. The resulting composites can take various forms, including beads, hydrogels, thin films, nanoparticles, and nanofibers. The synthesis involves dispersing zeolite particles within a polymer matrix to prevent the aggregation of zeolites in the medium (Rad & Anbia 2021).

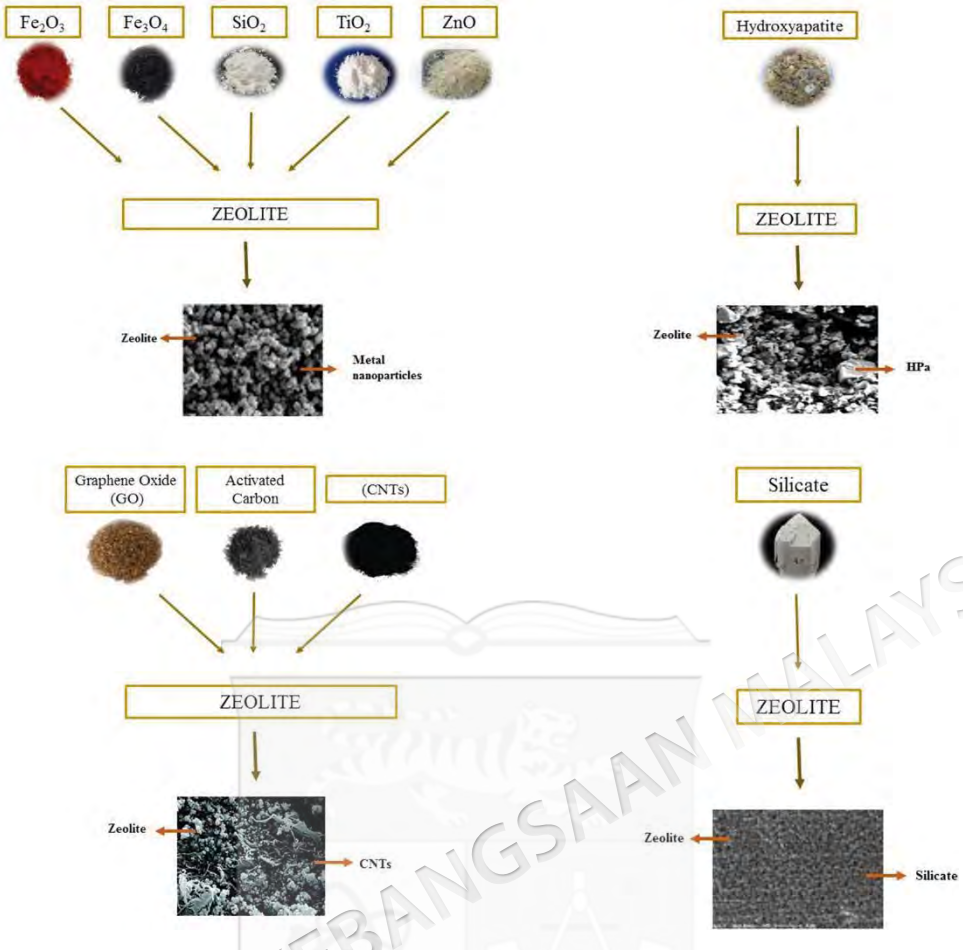

Figure 2.5 Schematic of inorganic adsorbents combined with zeolites.

Source: Rad et al. 2021

Biopolymers offer a more environmentally sustainable alternative to traditional polymers, primarily due to their renewable sources, biodegradability, and natural recycling through biological processes. One of the most familiar biopolymers is chitosan (CHS) for its potential in various adsorption applications, including gas capture and the removal of dyes and heavy metal ions. However, CHS is not without its limitations, which include inconsistent yields, non-uniform particle sizes, challenges in process reusability, and relatively low mechanical and chemical stability. To address these challenges, both physical and chemical modifications have been suggested to achieve more consistent particle sizes and to enhance the mechanical properties of CHS-synthesized forms (Liu et al. 2022).

2.7 COAL AND FLY ASH

One of the most prevalent and plentiful fossil fuels in the world, confirmed resources for coal are around 1000 billion tons globally (Tauanov et al. 2018). Coal continues to be widely utilized as a combustible substance in several developing and industrialized nations. Global coal consumption has seen significant changes in recent years, primarily driven by the energy needs of rapidly developing Asian economies. According to the International Energy Agency (IAE), In 2022, global coal demand reached a record high of 8.42 billion tonnes, marking a 4% increase from the previous year. This surge was fueled mainly by increased coal use in China and India, which saw growth rates of 4.6% and 9%, respectively. The demand in Indonesia also rose sharply due to industrial applications like nickel smelting (IEA), as shown in Figure 2.6.

A major drawback of relying on coal for energy is the accumulation of coal fly ash (CFA), which represents a significant environmental and health hazard (Tauanov et al. 2019). According to the literature, coal combustion results in the production of ash, which typically makes up 5-20% of the weight of the burnt coal. This ash consists of two components: coal bottom ash (CBA), which accounts for 5-15% of the ash's weight, and coal fly ash (CFA), which makes up 85-95% of the ash's weight (Zhou et al. 2022). After being used in combustion reactors, coal ash is typically disposed of as either wet or dry residues. The coarser component, coal bottom ash (CBA), settles at the bottom of these reactors and is mechanically collected following the combustion process. Conversely, coal fly ash (CFA), the finer portion, is collected either electrostatically or mechanically and stored in specific ash disposal sites following the combustion process (Meena et al. 2023).

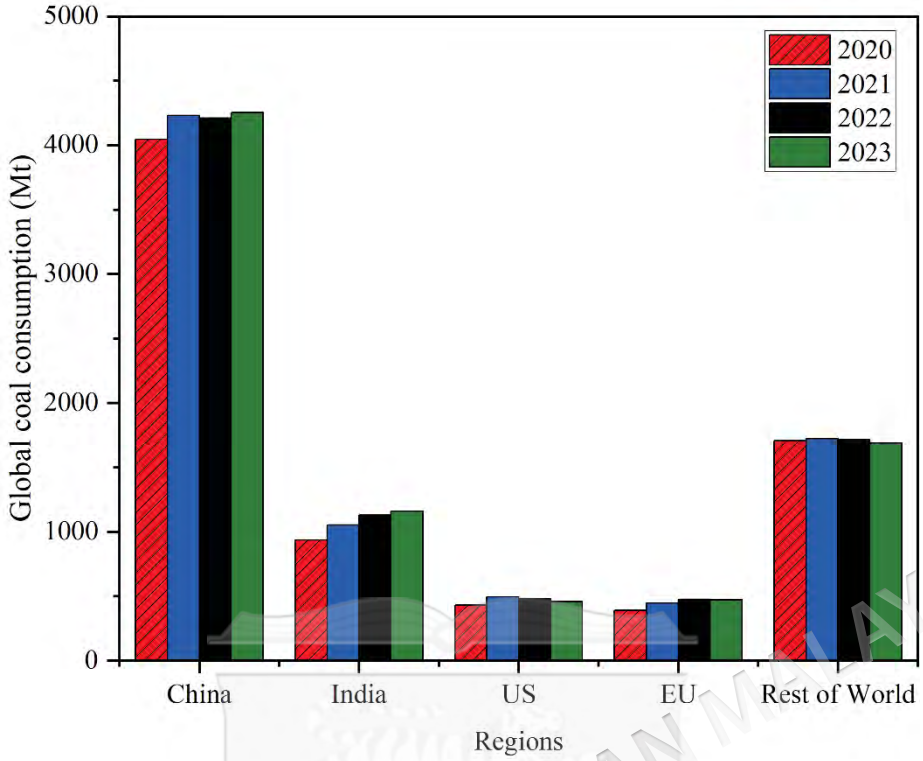

Figure 2.6 The global coal consumption from 2020 to 2023

Source: IEA 2024b

In 2022, Malaysia consumed approximately 32.6 million tonnes of coal, primarily for electricity generation. This marks a significant increase compared to previous years. In 2020, coal consumption was about 30.4 million tonnes, while in 2021, it rose to approximately 31.5 million tonnes. This upward trend in coal consumption reflects the growing energy demands in the country, despite efforts to diversify into renewable energy sources. Coal remains a dominant component of Malaysia's energy mix due to its availability and cost-effectiveness (Malaysia Energy Information Hub) (IEA 2024b). The increase in coal consumption also indicates a corresponding rise in CFA production.

According to statistics, approximately 600-800 million tonnes of coal fly ash (CFA) are produced globally each year. The USA and Europe contribute about 10% to this total, while India and China account for around 18% of global production. Currently, CFA is commonly stored in landfills, monofills (dedicated landfills for CFA), and ponds, or disposed of through simple stacking. However, these disposal methods pose significant environmental hazards due to the leachability, radioactivity,

and toxicity of CFA, leading to serious contamination of soil, natural water sources, and air. Additionally, these methods occupy vast areas of land, including fertile farmland, further exacerbating environmental and land use issues (Wang et al. 2020b).

2.7.1 Coal fly ash (CFA)

Coal-fired thermal power plants discharge a significant amount of CFA, which is a major component of solid waste. Electricity generation generates this by-product, resulting in an annual global production of 600 million tons of CFA. The temperature of the combustion process reaches a scorching 2000°C. At elevated temperatures, the majority of inorganic substances present in coal undergo melting and fusion. The chemical composition of CFA is dictated by the type of coal used and the specific temperature at which it undergoes combustion. The primary components of CFA include alumina, hematite, silica, calcium, magnesium, sodium, potassium, and titanium oxide. Mercury, cadmium, arsenic, cobalt, copper, lead, and chromium are substances that contribute to the poisonous nature of CFA (Aigbe et al. 2021).

The physicochemical properties of ash residues from coal and biomass combustion vary significantly. According to the American society for testing and materials (ASTM), CFA residues are categorized into two types based on their chemical composition: class F and class C. Class F ash residues contain over 70% combined SiO_2, Fe_2O_3, and Al_2O_3, and have a low lime content. In contrast, class C ash residues have a combined SiO_2, Fe_2O_3, and Al_2O_3 content ranging from 50% to 70% and are high in lime. Table 2.4 and Table 2.5 display the characteristics and typical chemical composition spectra of several kinds of CFA (Aigbe et al. 2021).

Table 2.4 Properties of CFA

CFA Feature	Characteristic Value
Colour	Greyish white
Average size of the particle (mm)	10-100
Specific gravity	2.1-3.0
Bulk density (g/cm3)	0.90-1.70
pH	6-8

Source: Aigbe et al. 2021

Table 2.5 Chemical properties of various CFA

Component (wt%)	Bituminous	Sub-bituminous	Lignite	Anthracite
SiO_2	20.00-60.00	40.00-60.00	15.00-45.00	43.50-47.30
Al_2O_3	5.00-35.00	20.00-30.00	10.00-25.00	25.10-29.20
Fe_2O_3	10.00-40.00	4.00-10.00	4.00-15.00	3.80-4.70
CaO	1.00-12.00	5.00-30.00	15.00-40.00	0.50-0.90
MgO	0-5.00	1.00-6.00	3.00-10.00	0.70-0.90
SO_3	0-4.00	0-2.00	0-10.00	-
Na_2O	0-4.00	0-2.00	0-6.00	0.20-0.30
K_2O	0-3.00	0-4.00	0-4.00	3.30-3.90
S	0.08-0.67	0.70-0.90	-	0.10-0.50
TiO_2	0.50-1.00	1.10-1.20	0.20-0.60	1.50-1.60
LOI	0-15.00	0-3.00	0-5.00	8.20

Source: Aigbe et al. 2021

Researchers began investigating suitable techniques for reusing coal fly ash (CFA) in the 1970s to mitigate environmental contamination. The pozzolanic reactivity of CFA was discovered in the 1980s, revealing its potential as a raw material for construction. Since then, CFA has been used in the construction of roads, roadbeds, pavements, landscaping, and embankments, among other applications, leading to substantial reuse (Wang et al. 2020b). However, the amount of CFA reused remains less than the amount generated, with only about 30% being reused (Figure 2.7) (Larsen et al. 2016). Consequently, while these methods can alleviate some of the environmental pressures caused by excessive CFA production, pollution remains an unavoidable issue.

Current research has increasingly focused on the synthesis of zeolites from silica-alumina-rich wastes such as fly ash, which can substitute for mineral resources and pure chemicals. Utilizing these resources, either directly or indirectly, not only decreases the expense of synthesizing zeolite but also minimizes environmental harm and improves the recovery of high-value CFA. Moreover, the presence of metal elements in fly ash facilitates the doping of certain metals, thereby enhancing the performance of the synthesized. Consequently, the use of silica- and aluminium-rich fly ash as a raw material for zeolite synthesis presents substantial potential for advancing the zeolite industry and effectively resolving the issue of fly ash reuse (Lin et al. 2022).

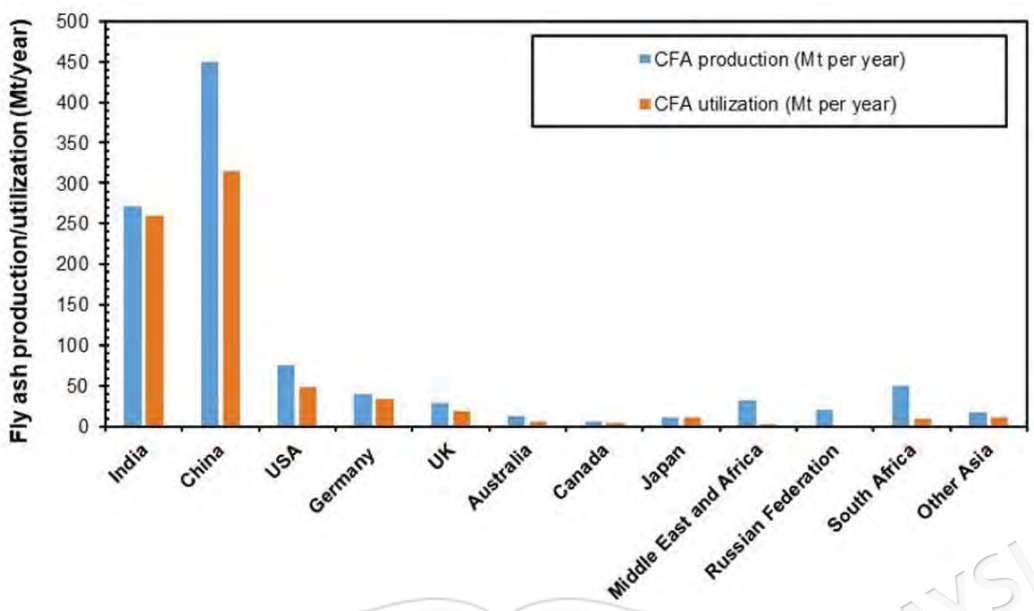

Figure 2.7 Production and utilization of CFA across the global

Source: Srivastava et al. 2022

2.7.2 Coal fly ash-zeolite synthesis

The synthesis process often employs methods such as hydrothermal, solvothermal, or ionothermal. These processes require three essential steps for zeolite formation: supersaturation, nucleation, and crystal growth as shown in Figure 2.8. One common method for synthesizing zeolites is hydrothermal synthesis, which entails heating SiO_2 and Al_2O_3 aqueous solutions in an alkaline environment, usually in sealed containers, to produce autogenous pressure as the temperature rises. Additionally, the zeolite shape that is formed may be controlled by using templates that direct structure, such as organic molecules and certain cations. The pH of the reaction mixture, process temperature and pressure, equilibration time and duration, reaction mixture composition (including structure-directing cations), and any pretreatment utilized all affect the zeolite crystal morphology that results from the hydrothermal method (Król 2019)

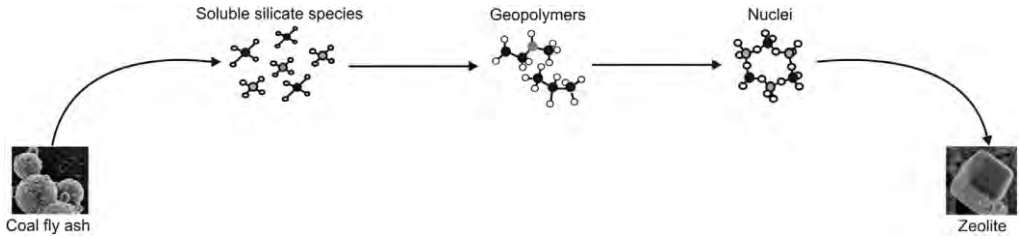

Figure 2.8 Diagram of the coal fly ash zeolitization process

Source: Belviso 2018

Cundy and Cox introduced a well-regarded framework for the production of zeolites. This model elucidates the state of balance between an unstructured gel phase and a basic solution, resulting in the creation of the organized zeolite phase. The authors present a comprehensive examination of the thermodynamic and kinetic aspects of the processes that occur during zeolite synthesis. Based on their concept, the amorphous material achieves equilibrium with anions and cations in the solution, leading to the creation of a tiny region of localized order known as nucleation. The nucleated region expands by assimilating anions and cations from the solution, while the disordered phase dissolves further to maintain a state of balance with the solution. The key variables governing this synthesis process are temperature, alkalinity, Si/Al ratio, cation concentration, and time. The model provides a quantitative description of the impact of temperature on the rates of dissolution and reaction of Al and Si. It highlights a significant correlation between solution alkalinity and nucleation rate. Ostwald's rule of consecutive transformations elucidates the gradual replacement of early-forming, possibly meta-stable phases (such as zeolites A, X, or P) by more stable structures (such as sodalite) as time progresses. The breakdown of meta-stable zeolites is accelerated in alkaline solutions with higher hydroxide content, making this change particularly noteworthy(Buzukashvili et al. 2024).

Fly ash-zeolite synthesis process predominantly employs hydrothermal and fusion methods, which are recognized for their effectiveness in this application. Hydrothermal synthesis involves treating fly ash with an alkaline solution at elevated temperatures, promoting the formation of zeolite structures. Fusion methods, on the other hand, entail the high-temperature melting of fly ash with a solid alkali, followed by dissolution in water, resulting in zeolite crystallization upon cooling. These methods are further optimized through the integration of microwave-assisted reactions, which

provide enhanced control over the reaction rate and zeolite morphology. Microwave-assisted heating notably decreases the times of synthesis in comparison to traditional heating techniques, therefore enhancing the efficiency of zeolite production. This technological progress has facilitated the creation of several types of zeolites that are particularly engineered for extracting heavy metals from water (Buzukashvili et al. 2024).

A study by Makgabutlane et al. (2020b) investigated the synthesis of zeolite A from Class F South African coal fly ash using complete microwave irradiation. By varying the microwave synthesis time, irradiation power, and Si/Al ratio, the researchers aimed to optimize conditions for minimal impurities. The main finding was that increased microwave irradiation power and time significantly improved the crystallization of zeolite A by providing sufficient energy to dissolve Al and Si from the coal fly ash. The synthesized zeolite A demonstrated a BET surface area of 29.54 m^2/g and a cation exchange capacity of 3.10 mequiv/g, underscoring its potential for environmental remediation. Similarly, Murakami et al. (2023) synthesized mesoporous zeolites (20–100 nm) from coal fly ash using microwave heating. This method led to faster crystallization and the formation of larger pores compared to oil bath heating. Despite both methods achieving similar saturated ion adsorption performance, zeolites synthesized via microwave heating exhibited a higher ion adsorption rate. These studies highlight the critical role of hydrothermal and fusion methods in advancing zeolite synthesis from fly ash, emphasizing their potential to enhance the efficiency of heavy metal extraction.

Research has extensively explored the potential applications of zeolites synthesized from fly ash, focusing on materials such as NaP1, 4A, X, KM, F, chabazite, herschellite, and faujasite, which possess high cation exchange capacity (CEC) due to their Al/Si ratio (Buzukashvili et al. 2024). Notably, Ściubidło and Majchrzak-Kucęba (2019) developed fly ash-based sorbents for capturing NO_2 from exhaust gases at room temperature. They synthesized and modified Na-X, SBA-15, and MCM-41 with polyethylene glycol (PEG). Testing showed that zeolite Na-X-(FA) had the highest sorption capacity at 44.7 mg NO_2/g. PEG impregnation improved SBA-15(FA)'s

capacity from 1.6 to 3.2 mg NO_2/g but reduced capacities for Na-X(FA) and MCM-41(FA). The sorbents could be fully regenerated by heating to 100°C.

In addition to traditional hydrothermal methods, developed an alternative technique involving the thermal treatment of CFA with a base and a salt. This process includes crushing and washing the cooled products to remove unreacted bases and salts, with the choice of salts significantly influencing the resulting zeolite structures, such as cancrinite formed with NaOH-KNO_3 and sodalite with NaOH-$NaNO_3$ (Jha & Singh 2016a). Despite its potential, the molten salt method, characterized by high-temperature requirements, long activation periods, and low selectivity for high CEC zeolites, has not seen widespread adoption among researchers (Buzukashvili et al. 2024). A summary of the methods used for synthesizing fly ash zeolites is provided in in Table 2.6. Future sections will delve into recent studies that have employed popular synthesis methods for producing zeolites from CFA.

2.7.3 Conventional hydrothermal method

Several hydrothermal activation techniques were established in the 20th century to synthesize various coal fly ash-based zeolites (Längauer et al. 2021a; Liu et al. 2019; Wang et al. 2020c). Fly ash is combined with the NaOH or KOH solution in the one-step hydrothermal process. The combination is then put into a sealed container. Zeolite is formed when crystallization takes place in water, which is the reaction medium under carefully regulated pressure and temperature conditions. Figure 2.9 illustrates a typical flow chart that outlines the many procedural stages needed to implement this process (Wang et al. 2024b).

Liu et al. (2019) conducted a comprehensive study on the process of zeolite synthesis using the one-step hydrothermal approach. The study findings clarify that zeolite synthesis using this approach consists of three stages:

1. Dissolution Stage: In an alkaline solution, the silicon and aluminum components of fly ash dissolve to generate silicate and aluminate ions.

2. Condensation Stage: An aluminosilicate gel is formed by the concentration of silicate and aluminate ions.

3. Crystallization Stage: Zeolite is formed when the aluminosilicate gel crystallizes into crystal grains that progressively increase.

Several parameters, such as reaction duration, Si/Al ratio, reaction temperature, and alkaline solution concentration, impact the efficiency and kind of zeolite generated during synthesis. Liu et al. (2019) conducted a follow-up study to investigate the impact of three important factors NaOH content, reaction duration, and reaction temperature on the production of type A zeolite. Their investigation produced a number of crucial observations:

1. The Concentration of NaOH: Type A zeolite forms when the optimal sodium hydroxide concentration is used.

2. The Temperature of reaction: The type and purity of zeolite depend on the reaction temperature. For instance, at 120°C, type A zeolite tends to produce sodalite.

3. The Time of Reaction: Excessively extended reaction times lead to impurities in type A zeolite.

The ideal parameters to produce type A zeolite with a 97.9% crystallinity were determined to be a NaOH concentration of 2.6 mol/L, a crystallization temperature of 90°C, and a crystallization period of 6 h. Moreover, the ratio of Si/Al ratio has a substantial impact on the process of zeolite formation. Specifically, a Si/Al ratio of about 1 typically results in type A zeolite, a Si/Al ratio of 11.5 generally leads to type X zeolite, and a Si/Al ratio of 1.53 usually yields type Y zeolite (Lin et al. 2022).

Although the one-step hydrothermal technique is the most straightforward and commonly employed, it has certain drawbacks. The minimal reactivity of mullite and quartz in fly ash hinders their involvement in the process, resulting in reduced purity and yield of the zeolite (Wang et al. 2024b).

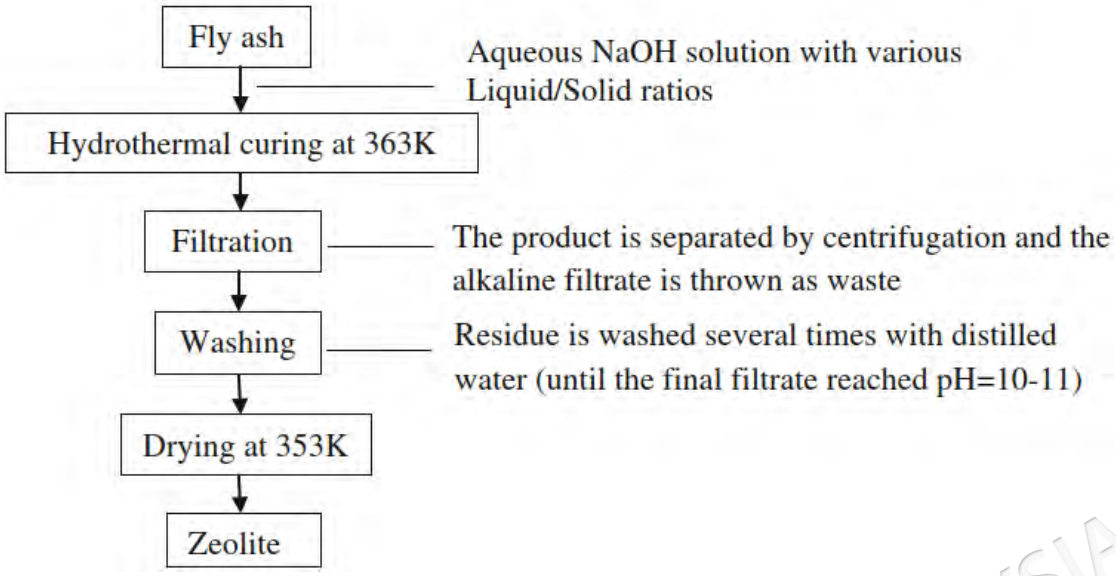

Figure 2.9 Diagram of the traditional hydrothermal synthesis process

Source: Jha et al. 2016

Table 2.6 A summary of the methods employed for synthesis of fly ash

Method	Liquid/Solid	Reagent	Temp. (°C)	T (h)	Zeolite	Remarks
Conventional hydrothermal	8	NaOH, KOH, Na_2CO_3	90–150	24–96	Chabazite, Na-P1, Phillipsite, Sodalite, zeolite KH, 4A, A, P, Zeolite X, Y	Low yield, low purity, structural heterogeneity
Microwave Assisted hydrothermal	8	NaOH	100	0.25-2	Na-P1	Synthesis time very less
Fusion and Hydrothermal	10	NaOH/or Sodium aluminate	500-600	1-2	Faujasite Na-A, Na-X, or zeolite X	More yield
		Water	90–100	6		
Molten salt	-	KOH, KNO_3, NaOH, $NaNO_3$, NH_4F, NH_4NO_3	350	3-6	Sodalite	No addition of water, irregular morphology
				24	Cancrinite	-

Source: Jha et al. 2016

To overcome the challenges of producing low-purity zeolite using the one-step hydrothermal method, researchers have devised the two-step hydrothermal technique for synthesizing fly ash-based zeolite (Guo et al. 2020). This approach first extracts silicon and aluminum from fly ash through an initial hydrothermal reaction. Afterward, additional chemicals are used to modify the Si/Al ratio in the solution, and then a further hydrothermal reaction is conducted to synthesize the zeolite (Li et al. 2017). The procedure for synthesizing zeolite by the two-step hydrothermal approach is illustrated in Figure 2.10 (Lin et al. 2022).

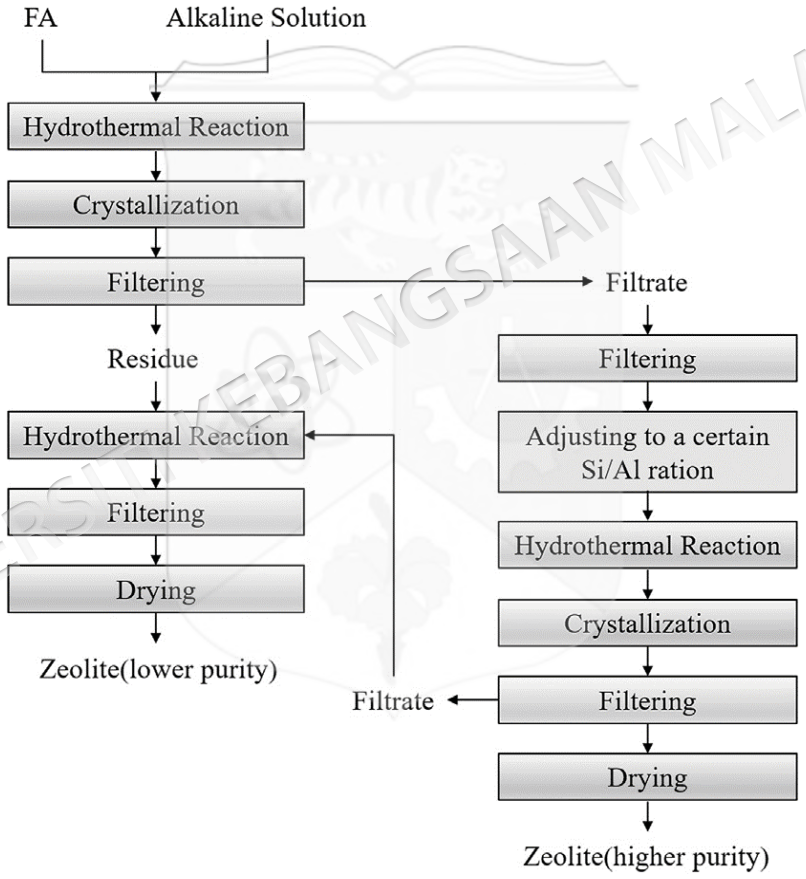

Figure 2.10 Hydrothermal Two-Step Zeolite Synthesis Process

Source: Lin et al. 2022

Iqbal et al. (2019) employed the two-step hydrothermal technique to produce fly ash-based 4A zeolite. The synthesized zeolite exhibited a markedly greater for both the specific surface area and thermal stability, in contrast, reduced crystal size in comparison to the commercial 4A zeolite. Likewise, Guo et al. (2020) utilized this

approach to produce nano-scale kaolinite zeolite, resulting in superior levels of purity compared to the one-step hydrothermal process.

The two-step process for zeolite synthesis results in greater purity and yield compared to the one-step hydrothermal method (Sun et al. 2018). However, although the two-step hydrothermal process has some benefits, it encounters difficulties in effectively using the silicon and aluminium present in fly ash, resulting in the generation of significant quantities of waste liquid (Wang et al. 2024b).

2.7.4 Fusion-assisted hydrothermal treatment

To overcome the disadvantages of traditional hydrothermal activation, the fusion-assisted hydrothermal method emerged as a suitable alternative. The modified method involves two distinct stages: first, a high-temperature fusion of a mixture of fly ash and alkali, followed by the subsequent hydrothermal activation of the fused product. The key factors in the studied process that can impact the quality and yield of the final product are the fusion temperature and duration, alkali type and concentration, and crystallization time. Research has shown that this method can achieve a zeolitic yield of up to 62% (Jha & Singh 2016b). Figure 2.11 displays a flow chart illustrating the synthetic process.

In the fusion method, the initial stage often involves pretreatment, which is essential for extracting the primary precursors required for zeolite synthesis, particularly silica and alumina. This pretreatment aims to enhance the efficiency of the reaction and increase the yield of zeolite. During this stage, the inactive components in fly ash (quartz and mullite) undergo a reaction with an alkali reagent, often NaOH in powdered form, at a high temperature ranging from 550 to 600 ◦C (Szerement et al. 2021). This reaction is described by the following equations:

$$SiO_2(s) + 2NaOH \rightarrow Na_2SiO_3(s) + H_2O \quad (2.1)$$

$$Al_2O_3(s) + 2NaOH \rightarrow 2NaAlO_2 + H_2O \quad (2.2)$$

The following equation represents the subsequent stage, a conventional hydrothermal process:

$$NaOH_{(aq)} + Na_2Al(OH)_{4(aq)} + Na_2SiO_{3(aq)} \quad (2.3)$$
$$\xrightarrow{Mix} [Na_x(AlO_2)_y(SiO_2)_z]NaOH.H_2O_{(gel)}$$
$$\xrightarrow{Temperature} Na_p[(AlO_2)_n(SiO_2)_q].H_2O_{(zeol)}$$

Berkgaut et al. (1996) investigated the use of two methods conventional hydrothermal treatment and fusion with NaOH for synthesizing zeolites from coal fly ash, comparing their effectiveness in terms of product types, cation exchange capacities (CEC), and the factors influencing the outcomes. The results indicated that the conventional hydrothermal treatment transforms coal fly ash into zeolite P and hydroxysodalite in a NaOH medium. This process sees quartz dissolve slowly while mullite remains stable, with the formation of zeolite P being favored by the presence of residual coal. The treated fly ash achieves a CEC that stabilizes around 250-300 meq/100g. In contrast, the fusion method proves significantly more effective. An endothermic reaction at 170-180°C produces a new Na aluminosilicate, which then transforms into either zeolite P or zeolite X upon subsequent hydrothermal treatment at 100°C. Zeolite X forms after aging the aluminosilicate gel, whereas zeolite P forms without aging. This method results in zeolites with higher CEC values of approximately 400-420 meq/100g, indicating superior efficiency. The fusion process allows for precise control over the type of zeolite produced by manipulating the treatment conditions, leading to purer and more effective cation exchangers.

In a study by Ren et al. (2020), a single-phase submicron zeolite Y (FAZ-Y3) was effectively synthesized from coal fly ash (CFA) using an alkali fusion hydrothermal method without the need for organic structure-guiding agents. The findings showed that the type and purity of the zeolite were heavily influenced by the preparation parameters, with zeolite P being the major competing phase. Optimized conditions resulted in FAZ-Y3 with an average size of 250 nm, a specific surface area of 386.9 m^2/g, and a crystallinity of 92.73% when prepared at 80°C for 12 h using an inorganic liquid-phase directing agent, showcasing excellent thermal stability. In acetone adsorption tests, the Langmuir and Bangham models aptly described the data, indicating internal diffusion as the primary resistance to mass transfer. FAZ-Y3 demonstrated an adsorption capacity

reaching approximately 82% of that of commercial zeolite Y (CZ-Y) and exhibited significant regenerability.

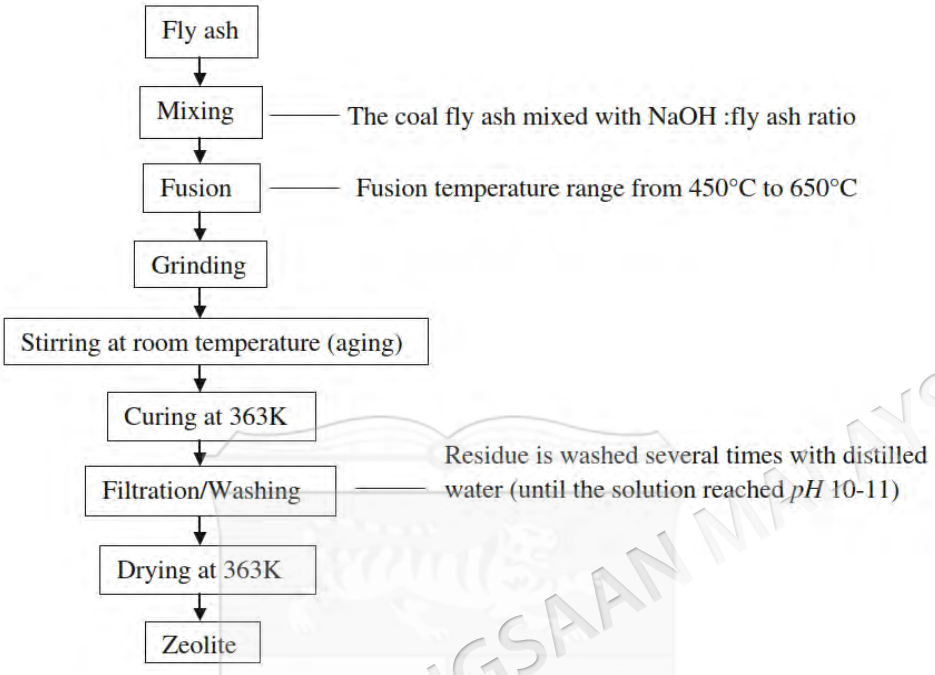

Figure 2.11 Flowchart of fusion-assisted hydrothermal synthesis process

Source: Jha et al. 2016

In the study conducted by Küçük et al. (2023), NaP and LTA zeolites were synthesized from fly ash using an alkali fusion-assisted hydrothermal method, with variations in the NaOH/ash ratio, crystallization time, and temperature. To reduce costs, NaP zeolite was produced without additional aluminum and silicon sources. These zeolites were tested for the adsorption of Cu(II), Cd(II), Pb(II), and Zn(II) ions. Adsorption capacities followed the order Pb(II) > Cu(II) > Cd(II) > Zn(II) for both zeolite types. NaP zeolite achieved maximum adsorption capacities of 42.9 mg/g for Cu(II) and 117.3 mg/g for Cd(II), while LTA zeolite showed higher capacities of 140.1 mg/g for Cu(II) and 223.5 mg/g for Cd(II)..

SSZ-13 zeolite was synthesized from fly ash using a combined alkali fusion hydrothermal method. The optimal synthesis parameters were determined to be NaOH/FA=1.4, SiO_2/Al_2O_3=50, H_2O/SiO_2=1800, TMAda-OH/Al_2O_3=7, 10% SSZ-13 seed, with a crystallization temperature of 160°C and a duration of 40 h. Utilizing these conditions, a series of Fe-SSZ-13 catalysts were prepared through three distinct

methods and subsequently tested for their efficacy in catalytic oxidation with H_2O_2 for NO removal. The results indicated NO removal efficiencies of 78% for Fe-SSZ-13-SSIE, 87% for Fe-SSZ-13-LIE, and 84% for Fe-SSZ-13-IM. The study concluded that the high catalytic performance was attributed to the dual functionality of strong Brønsted acidity on the catalyst surface and the presence of highly dispersed isolated Fe^{3+} ions, which facilitate the rapid decomposition of H_2O_2 into OH radicals, thereby enhancing NO oxidation. This study underscores the potential of utilizing fly ash-based catalysts for dual purposes of waste utilization and pollutant removal (Li et al. 2023).

Petrovic et al. (2021) successfully synthesized nanoporous zeolite for CO_2 adsorption from industrial-grade biomass combustion fly ash, produced by one of the largest power plants in the UK. The synthesis followed a fusion-assisted hydrothermal method, and the resulting zeolite was characterized by X-ray diffraction. Thermogravimetric analysis (TGA) was used to evaluate CO_2 adsorption capacity, showing that the nanoporous adsorbent, under 100 mol% CO_2 at atmospheric pressure, achieved an equilibrium capacity of over 0.8 mmol CO_2/g at 50°C. The characterization results aligned with the CO_2 adsorption data, confirming the nanoporous structure of the synthesized zeolite. This study demonstrates the potential of converting industrial fly ash into effective CO_2 adsorbents.

Li et al. (2018) proposed a novel method to synthesize faujasite zeolite from coal fly ash (CFA) using microwave digestion and alkali fusion-assisted hydrothermal treatment. The optimal synthesis conditions included microwave alkali fusion for 15 minutes at 450°C, stirring the suspension for 4 h at room temperature, followed by crystallization for 12 h at 90°C. The synthesized zeolite was then tested for Cd(II) removal from aqueous solutions. Optimal parameters for this process were an adsorbent dose of 0.5 g/L, pH 6, a contact time of 90 minutes, and an initial Cd(II) concentration of 20 mg/L, resulting in a removal rate of 98.55%. The maximum adsorption capacity for Cd(II) was determined to be 86.96 mg/g. Comparative studies indicated that the synthetic zeolite was a more efficient adsorbent for Cd(II) removal from wastewater. This microwave digestion and alkali fusion-assisted hydrothermal method proved to be an effective and energy-efficient technique for synthesizing zeolite from CFA.

Shabani et al. (2022) investigated the process of producing biodiesel, utilizing coal fly ash-based hydroxy sodalite (HS), as a catalyst in the conversion process. The HS zeolite was synthesized using a fusion-assisted hydrothermal method. The mesoporous zeolite synthesized has high crystallinity with a surface area of 45 m^2/g. The efficacy of the F-HS catalyst in biodiesel synthesis was evaluated before and subsequent to ion exchange modification using KOH. The unaltered catalyst demonstrated an impressive biodiesel output of 84.10% with a fatty acid methyl ester (FAME) content of 65%, which satisfies the established biodiesel requirements. Nevertheless, the zeolite treated with KOH exhibited diminished crystallinity, mesoporosity, and surface area, resulting in a decreased grade of biodiesel with a mere 51.50% percentage of fatty acid methyl esters (FAME). Remarkably, the coal fly ash-based zeolite exhibited a higher level of effectiveness as a heterogeneous catalyst when compared to the traditional NaOH homogeneous catalyst.

Yang et al. (2019) examined the effects of NaOH and Na_2CO_3 on the activation of fly ash prior to synthesizing high-purity A4 zeolite. Additionally, the removal efficiency of Cu^{2+} from aqueous solutions using the synthesized zeolite was assessed. The study identified several critical factors influencing the green synthesis of zeolite, including the alkali mixture ratio, alkali melting temperatures, solid-to-liquid ratios, and crystallization times and temperatures. Orthogonal test results underscored the importance of the alkali mixture ratio. By combining NaOH and Na2CO3 in a mass ratio of 1:2.8, the optimal conditions—temperature (760°C), solid/liquid ratio (1:5), and crystallization time (4 h) resulted in a maximum relative crystallinity of 75.8%. The superior results were attributed to the synergistic effect of Na_2CO_3 and NaOH, which provided an optimal concentration of OH^- and Na^+ ions and maintained a stable OH^- concentration throughout the reaction process. This combination facilitated the highest activation of silicon and aluminum in fly ash, culminating in the highest degree of crystallization with minimal energy and water consumption.

Murukutti et al. (2022) investigated the synthesis of pure nano zeolite-A and zeolite-X from coal fly ash (CFA) sourced from Indian thermal power plants. The synthesis process involved an alkali fusion method followed by a hydrothermal technique. Initially, the fly ash was fused with Na_2CO_3 at 800°C for 2 h. The resulting

fused mass was then treated with 3 M NaOH solutions and subjected to a hydrothermal reaction, producing zeolite-A and zeolite-X. The specific surface areas of zeolite-A and zeolite-X were determined to be 58.29 m^2/g and 164.34 m^2/g, respectively. TG-DTA studies revealed the transformation of nano-crystalline to micro-crystalline zeolites accompanied by the loss of adsorbed water. The synthesized nano-crystalline zeolites demonstrated high ion exchange capacities for Cs^+ and Sr^{2+} ions in simulated nuclear waste solutions.

The significant benefits and drawbacks of hydrothermal and fusion procedures are outlined in Table 2.7.

Table 2.7 Advantages and disadvantages of a classic hydrothermal, fusion methods

Method	Advantages	Disadvantages
Hydrothermal method	lower temperature of reaction, lower energy consumption	more waste, relatively time-consuming, low conversion
Fusion method	faster speed of reaction and purity of the final product, less waste	high temperature, relatively expensive

Source: Szerement et al. 2021

Researchers have demonstrated an increasing interest in developing efficient and economical techniques for manufacturing Faujasite-type zeolite, given its extensive industrial applications, particularly in the chemical and petrochemical sectors.

2.8 STRUCTURE OF CHITOSAN

Chitosan is derived from the N-deacetylation of chitin, as depicted in Figure 2.12a. The ideal structure of chitosan, illustrated in Figure 2.12c, consists of glucosamine units linked through condensation. This structure forms a complex double helix with a pitch of 0.5 nm and six sugar residues per helix turn. The presence of abundant hydroxyl (-OH), ether (-O-), and amino ($-NH_2$) groups in chitosan's structure results in multiple intramolecular and intermolecular hydrogen bonds. Figure 2.12d illustrates the molecular model of chitosan, highlighting two types of intramolecular hydrogen bonds. These hydrogen bonds significantly affect chitosan’s solubility, viscosity, and

crystallinity. Additionally, chitosan is unique among polysaccharides due to its high content of primary amines, making it a rare polycationic polymer with a pKa of approximately 6.5 (Freitas et al. 2020).

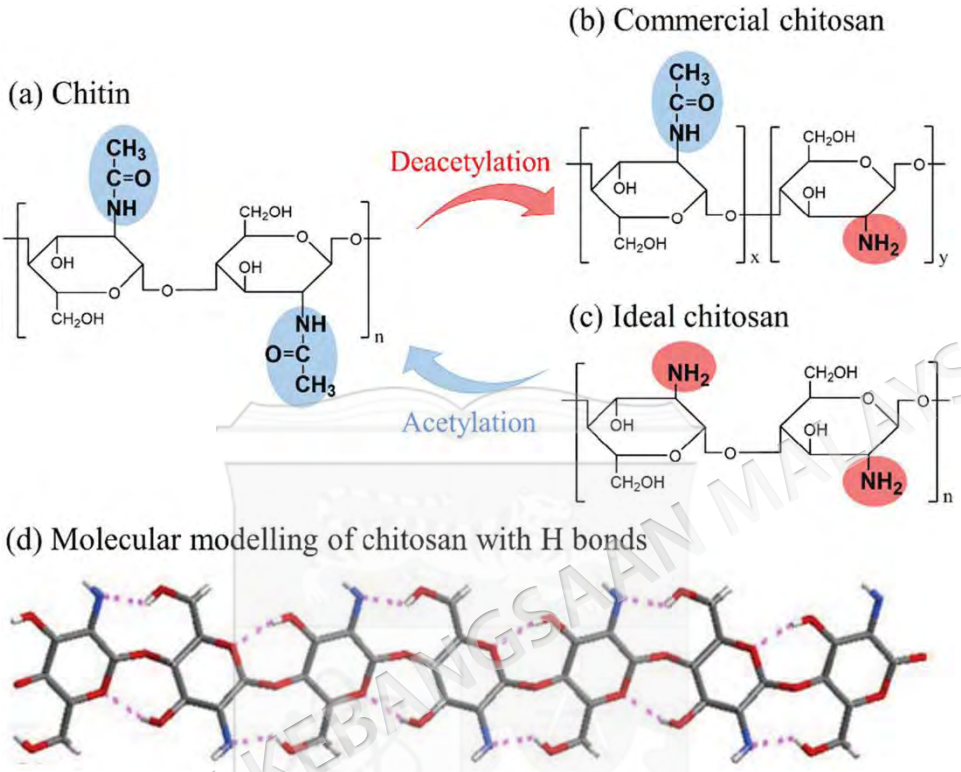

Figure 2.12 (a–c) Chemical structure of chitin and chitosan; and (d) intramolecular H bonds between chitosan (C: gray bar; O: red bar, N: blue bar; H: white bar, H bonding: purple dotted line)

Source: Wang et al. 2022

2.9 PREPARATION OF CHITOSAN

Chitosan (CHS), unique among natural polysaccharides for containing an amino group, is derived from the deacetylation of chitin, a substance abundantly found in nature (Gu et al. 2019). Chitin is produced in quantities of approximately 10 billion tons annually, making it the second most abundant biopolymer after cellulose. It is primarily found in sources such as crab and shrimp shells, fungi, and insects (Ahmed et al. 2020). Preparing chitosan from crustacean shells involves four key steps: demineralization, deproteinization, decolorization, and deacetylation, as depicted in Figure 2.13a. The degree of deacetylation determines the nitrogen content in chitin, which ranges from 5% to 8% (w/v), predominantly in the form of primary aliphatic amino groups similar

to those in CHS. Additionally, the presence of the primary and secondary hydroxyl group and amino/acetamido reactive functional groups as shown in Figure 2.13b imparts CHS with a superior ability to coordinate metals compared to other natural polymers used in adsorption (Liu et al. 2022).

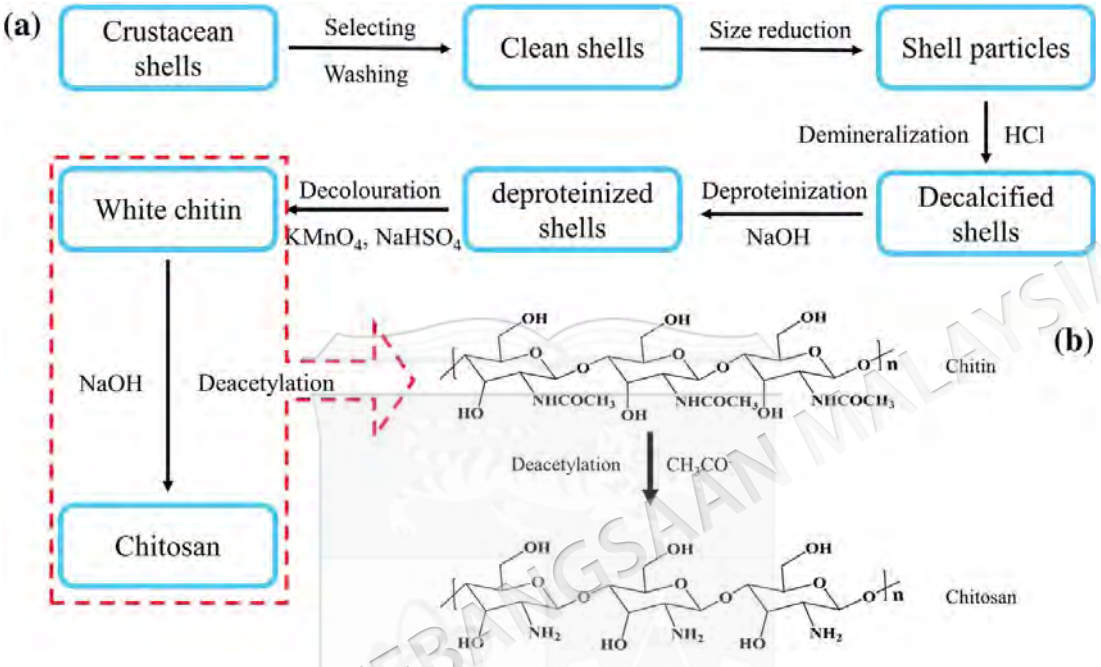

Figure 2.13 Schematic for the preparation of chitosan

Source: Liu et al. 2022

2.10 CHITOSAN-BASED MATERIALS PREPARATION

Chitosan is commercially available in the form of either flake or powder. The material may be utilized in its original state or transformed into diverse structures, including nanofibers, micro/nano-spheres, membranes, and scaffolds, to suit various purposes. The process of modifying the structure of chitosan and its derivatives offers a wide range of possibilities for various applications, as outlined by Kassem et al. (2019).

2.10.1 Microspheres

Chitosan microspheres are relatively simple to produce and are utilized in a variety of applications, including adsorption, separation, and biosensing. A commonly used method for creating chitosan gel microspheres involves introducing droplets of dissolved chitosan into acetic acid into a precipitation solution, usually an alkaline solution. By controlling the size of the droplets, microspheres of different diameters can

be produced. For instance, dried microbeads formed using a medical syringe with a needle have an approximate diameter of 2 mm (Zhuang & Wang 2019). This technique requires minimal equipment, making it feasible in almost any laboratory setting. To improve the efficiency of chitosan microsphere production, spray-drying has been developed as an alternative method. This technique involves feeding a chitosan solution into a spray dryer, where the solution is atomized into fine droplets. As the solvent quickly evaporates, the chitosan solidifies into free-flowing particles (Zhang et al. 2020b).

2.11 MODIFICATION OF CHITOSAN

Although chitosan (CHS) possesses strong adsorption capabilities, its applications are limited by its solubility in acidic environments, low mechanical stability, and low repeatability. Furthermore, structural challenges, such as low solubility in neutral media and the reduced positive charge of amino groups, hinder its broader use (Iqbal et al. 2023). Recent improvements in chitosan derivatives and polymer complexes have led to improved properties. The synthesis of chemically modified chitosan involves using various active groups, such as amino, primary, and secondary hydroxyl groups, which provide significant benefits. Importantly, these derivatives maintain the inherent properties of chitosan while offering enhanced characteristics by integrating diverse modified active groups (Mutreja et al. 2020).

Chemical modifications of CHS undergo to improve its solubility in water, enhance its rheological properties, and increase its stability against heat and oxidation. The reactive chemical groups in CHS include NH_2 groups and OH groups located at positions C3 and C6. Generally, the primary OH group located in C6 is more reactive than the secondary OH group located in C3. Among the NH_2 and OH groups, the NH_2 is more reactive due to its free rotational capability. To develop N-, O-, and N, O-modified derivatives, chemical reactions can be performed on amino, hydroxyl, or both groups (Iqbal et al. 2023). Depending on the conditions, OH groups may undergo etherification, esterification, crosslinking, graft copolymerization, and O-acetylation. In contrast, NH_2 groups may be modified through acetylation, quaternization, Schiff's base

reactions, and grafting (Wang & Zhuang 2022). Different methods for modifying CHS are illustrated in Figure 2.14.

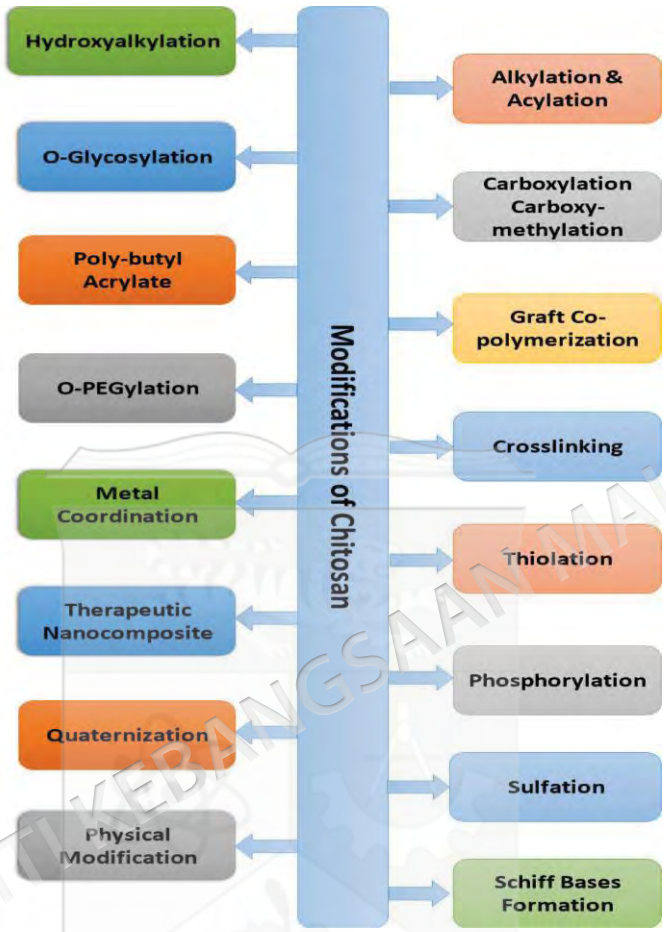

Figure 2.14 The chemical modifications of chitosan for various applications.

Source: Iqbal et al. 2023

The most straightforward way to modify polymers is through physical modification. This process usually involves blending or amalgamating two modifying agents to generate a new material with distinct physical properties. This mixing process aims to develop materials that exhibit optimal chemical, mechanical, structural, biological, and morphological characteristics. Compared to other available methods, this approach is considered practical and cost-effective, and it requires less time to implement (Iqbal et al. 2023). Physical modification generally involves combining chitosan (CHS) or its derivatives with organic or inorganic materials or transforming these components into different forms, such as porous particles, microspheres, gel

particles, fibers, and membranes, without altering the intrinsic features of CHS (Liu et al. 2022b), as illustrated in Figure 2.15. Modifying the physical properties of CHS can improve its ability to adsorb substances and address the challenges of separating solids from liquids after adsorption, as stated by Song et al. (2017). Physical methods, such as physical crosslinking and blending, are both convenient and effective for modifying polymers.

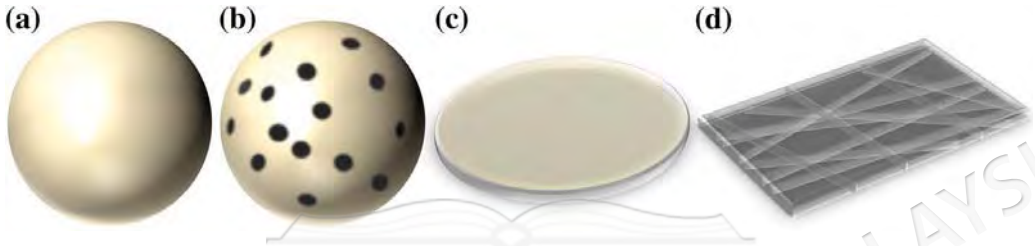

Figure 2.15 The morphology of physically modified CHS composites(a) microspheres, (b) porous microsphere, (c) membrane, and (d) fiber/hollow fiber

Source: Liu et al. 2022

2.11.1 Physical crosslinking of chitosan

Physical crosslinking provides a simple and effective technique for developing chitosan derivative hydrogels. This technique forms a three-dimensional network structure through physical interactions, including electrostatic interactions, hydrogen bonding, and hydrophobic forces, rather than relying on chemical bonds (Hu et al. 2019). These physical interactions exhibited reversibility features, and the sol-gel transformation in chitosan derivative hydrogels is generally affected by environmental factors such as pH, ionic strength, and temperature. Due to the absence of auxiliary crosslinkers, these hydrogels exhibit low toxicity. However, they often suffer from low mechanical strength and inconsistent properties, such as variable pore size.

2.11.2 Blending

The physical integration of chitosan with different substances results in the formation of chitosan-based composites that exhibit a variety of properties. Chitosan can be blended with various materials, including biomaterials, nanomaterials, carbonous materials, and zeolites. The key characteristic of chitosan composites is their ability to overcome the limitations of chitosan by incorporating the advantages of blended materials. The blending procedure typically involves the use of a chitosan hydrogel for

encapsulation. Specifically, chitosan solutions are mixed uniformly with various blending materials, followed by the sol-gel transition. Chitosan blending can involve additional techniques such as adsorption, crosslinking, and covalent grafting, depending on the properties of the co-blending ingredients (Wang & Zhuang 2022).

A recent method for polymer modification, which involves the mechanical mixing of two distinct polymers, has resulted in the development of a new category referred to as polymer blends. These blends consist of physical mixtures of structurally distinct polymers or copolymers that interact through secondary forces, without forming covalent bonds, and are miscible at the molecular level. The miscibility of these polymer-polymer mixtures is often due to specific interactions such as hydrogen bonding, dipole-dipole interactions, and charge transfer complexes. Various techniques have been utilized to investigate the miscibility of polymer blends; however, many of these methods are complex, costly, and time intensive. Consequently, there is a growing demand for the development of simpler, more cost-effective, and faster approaches to evaluate polymer blend miscibility. The modification of polymers has attracted considerable attention due to their wide range of potential applications (Rajeswari et al. 2020).

Blends composed of synthetic and natural polymers can possess a diverse array of physicochemical properties, combining the processing capabilities of synthetic polymers with the biocompatibility and biological interactions of natural polymers. Natural polymers have been extensively studied as biotechnological and biomedical resources due to their distinctive attributes, such as nontoxicity, biodegradability, and biological compatibility. Blending natural polymers with chitosan presents a promising approach for modifying the properties of natural polymers and creating innovative composite materials derived from them (Wang & Zhuang 2022).

Research has extensively focused on creating natural polymer-chitosan composites using various natural polymers, including starch (Karua & Sahoo 2020), collagen (Andonegi et al. 2020), proteins (Wang et al. 2020a), and natural rubber (Sukthawon et al. 2020). On the other hand, the modification of chitosan by synthetic polymers is of great interest due to their notable characteristics. It can improve

properties such as flexibility, conductivity, water retention, and mechanical strength while preserving biodegradability and sorption performance.

2.12 CHITOSAN-ZEOLITE MATERIALS

Advanced technological cycles rely on microporous and mesoporous minerals. Naturally occurring microporous materials are valued for their biocompatibility and renewability. Zeolite, a prominent microporous hydrated aluminosilicate mineral containing alkali metals, is commercially available for adsorption and catalyzation applications. However, its efficiency can be reduced due to the large volume of water that occupies the active sites of the zeolite. Chitosan, a widely utilized polysaccharide, has found applications in various fields, particularly in medicine, though its limited mechanical properties have restricted its use. Chitosan/zeolite composites offer enhanced properties compared to the individual parent materials, making them suitable for a wide range of applications. The combination of microporous and biocompatible materials, featuring both positive and negative charges, micro/nanopores, and improved mechanical properties, provides a promising platform for diverse applications (Mahmodi et al. 2020).

The distinctive characteristics of chitosan-modified zeolite composites add to their versatility and potential significance. Significantly, these composites have an increased surface area, which allows for a higher concentration of active sites that enhance adsorption and catalytic efficiency. Furthermore, the mechanical characteristics of chitosan, such as its pliability and robustness, collectively augment the overall mechanical durability of the composites. Moreover, the natural compatibility of chitosan makes it possible to use these composites in various biomedical applications without causing any negative consequences, thereby broadening their potential spectrum of use.

Selecting suitable synthesis methods is crucial for customizing the structures and characteristics of chitosan-modified zeolite composites. Several techniques, such as in situ synthesis, impregnation, template-assisted synthesis, and surface modification, have been employed to fabricate these composites. The choice of the synthesis method significantly influences critical parameters, including the composite

morphology, pore size distribution, and interfacial interactions between chitosan and zeolite. By meticulously optimizing the synthesis parameters, researchers can attain precise control over composite properties, thereby enhancing the desired characteristics for specific applications (Mahmodi et al. 2020).

2.13 APPLICATIONS OF CHITOSAN-ZEOLITE COMPOSITE

The diverse uses of chitosan-modified zeolite composites highlight their adaptability and their potential influence on society. Within the realm of environmental engineering, these composites have demonstrated remarkable efficacy in several applications, including air purification, wastewater treatment, and soil remediation. Their remarkable adsorption capacity and ion-exchange capability allow for efficient elimination of pollutants from air and water sources. Furthermore, chitosan-zeolite composites demonstrate significant catalytic activity, making them valuable in a range of industries, such as petrochemicals and fine chemicals. Moreover, their ability to interact well with living organisms and their ability to release substances in a controlled manner makes them highly favorable options for drug delivery systems. They also show great potential in other biomedical fields, including tissue engineering and wound healing. Applications of chitosan/zeolite composites are summarized in Table 2.8

Table 2.8 Zeolite/chitosan frameworks and their applications.

Material	Applications	Comments	Reference
Clinoptilolite zeolites-chitosan-magnetic Fe_3O_4	Mercury from liquid condensate hydrocarbon	The removal of mercury from liquid condensate hydrocarbon exhibited a notable enhancement of up to 30% when utilizing zeolite modified with chitosan, compared to pristine clinoptilolite zeolite.	(Kusrini et al. 2017)
Zeolite/chitosan	Removal of arsenic	Enhanced hydrophobicity thanks to the enlargement of the pore size of the membrane upon the addition of zeolite content.	(Mukhopadhyay et al. 2019)
Zeolite/chitosan/bentonite/active carbon	Removal of cadmium	Enhanced soil pH and decreased biological effectiveness of heavy metals.	(Yi et al. 2019)
Chitosan-coated Na–X zeolite from fly ash	Removal of arsenic	The removal of arsenic was significantly performed by the formation of bonds of As–N and As–O. Moreover, the surface hydroxyl group of Al–OH and –NH_2 facilitated arsenic removal from wastewater.	(Han et al. 2019)
Zeolite/Chitosan/polyvinyl alcohol	Adsorption of methyl orange	Nanofiber mechanical properties can be tuned by zeolite. adsorption mechanism obeys the Freundlich model. pH reduction enhanced adsorption.	(Habiba et al. 2018)
Zeolite/chitosan/PVA	Adsorption	Nanofiber removed Cr (VI), Fe (III), and Ni (II) ions from wastewater.	(Habiba et al. 2017)
Fly ash-zeolite-chitosan	Adsorption of heavy metal ions	Removal of chromium (VI) from the acidic mine drainage	(Thacker et al. 2023)
Magnetic ZSM-5 zeolite/chitosan/polyacrylonitrile	Absorption	Nanofiber-coated sponges facilitated water-oil separation for many cycles.	(Samadi et al. 2017)
Zeolite Y-chitosan	Catalyst	Mesoporous substrate enabled for CO_2 fixation.	(Kumar et al. 2018)
Zeolite X loaded in PLA/chitosan nanofiber	Drug release	Doxorubicin was loaded in zeolite and following the Fickian diffusion release mechanism.	(Abasian et al. 2019)
Zeolite-loaded alginate/chitosan	Wound dressing	Hydrogel beads used as a topical hemostat. Promote blood coagulation via multiple mechanisms: erythrocyte adhesion, factor concentration, and the ability to serve as a mechanical barrier to blood loss.	(Fathi et al. 2018)

Source: Mahmodi et al. 2020

2.14 REGENERATION OF EXHAUSTED ADSORBENTS

During the adsorption process, the adsorbent eventually becomes fully saturated as all adsorption sites are occupied, leading to equilibrium. At this point, the adsorbent is considered exhausted or spent (Patel 2021). This spent adsorbent presents a significant drawback, as it becomes a solid hazardous waste that is often disposed of in landfills, contaminating underground and surface water sources (secondary pollution problems). In some regions, spent adsorbents are incinerated, causing additional environmental and societal issues. Although spent adsorbents can be repurposed for uses such as fertilizers, catalysis, feed additives, biologically active compounds, and nanoparticle synthesis, these applications are not environmentally sustainable (Baskar et al. 2022).

This solid waste problem can be addressed through various regeneration processes. The regeneration of adsorbents is influenced by multiple factors, including the type of adsorbent used, the characteristics of the adsorbate, the interactions between the adsorbate and adsorbent, the specific treatment process employed, and the overall cost of regeneration. Common techniques for sorbent regeneration include the use of thermal energy (Márquez et al. 2022), microwave irradiation (Gagliano et al. 2021), ultra-sonication (Daghooghi-Mobarakeh et al. 2020), dielectric barrier discharge plasma (Kandel et al. 2022), and other methods. However, some of these techniques have notable drawbacks. For instance, some methods require long durations and high energy consumption, while others cause irreversible changes to the structural, chemical, and physical properties of the sorbents. The conditions of regeneration, such as temperature, pressure, and humidity, play a crucial role, especially for adsorbates with a high affinity for the adsorbent.

For example, compounds with high molecular weights, like n-dodecane a nonpolar volatile organic compound (VOC) with a high boiling point (216°C) and a small kinetic diameter (4.3 Å) can easily penetrate the micro-pores of adsorbents. In such cases, regeneration becomes particularly challenging because these bulky compounds cannot easily desorb from narrow micro-pores. This process necessitates harsh treatments, such as high temperatures and pressures, to remove the sorbed

adsorbate from the adsorbent (Dutta et al. 2019). Table 2.9 outlines these processes, highlighting their advantages and disadvantages.

Table 2.9 Advantages and disadvantages of various adsorbent regeneration processes

Regeneration Method	Advantages	Disadvantages
Thermal regeneration	Efficient	Highly expensive, Degrade the pores of adsorbent, Time consuming, Create air pollution
Supercritical fluid extraction	Efficient, Less time consuming	Highly expensive, Degrade the pores of adsorbent
Biological method	Efficient, Less time consuming, Eco-friendly	Very slow, Block the pores of adsorbent, Only applicable for biodegradable pollutants
Advance oxidative method	Efficient	Highly expensive, Degrade the pores of adsorbent, Time consuming
Micro-wave regeneration	Efficient, Less time consuming, Eco-friendly	Highly expensive, Degrade the pores of adsorbent, Required further treatment
Ultrasound regeneration	Efficient, Less time consuming, Eco-friendly	Highly expensive, Degrade the pores of adsorbent
Ozonation	Efficient	Highly expensive, Degrade the pores of adsorbent, Formation of acidic surface, Required before treatment

Source: Patel 2021

One cost-effective and efficient method for regenerating adsorbents is desorption, which reverses the adsorption process. Desorption studies provide valuable insights into the nature of adsorption, whether physical or chemical. These studies also assess the adsorbent's performance for future use, helping to reduce the overall cost of the adsorption process. There are two main types of desorption:

1. Thermal Desorption: This method uses heat to perform desorption. While it is fast and efficient, it is also very expensive. Additionally, it requires pre-treatment, can release hazardous contaminants, involves unsafe process parameters, and faces regulatory and public perception challenges.

2. Chemical Desorption: This approach is environmentally sustainable, inexpensive, very fast, and highly promising with great potential.

This section highlights that solid waste disposal, including waste adsorbents, remains a global issue. Regenerating spent adsorbents is essential for eliminating hazardous solid waste and promoting sustainable development. Solvent desorption is considered the most favorable option due to its cost-effective and efficient regeneration process (Patel 2021).

2.15 DESORPTION

The process of desorption involves the treatment of used adsorbent materials with either a solution, a solvent, or a combination of both. This treatment disrupts the bond between the adsorbent and the adsorbate, allowing the adsorbate to be released from the solution. After this treatment, the adsorbent is ready to undergo another cycle of adsorption. The eluting agent, which can be a specific solution or solvent, plays a crucial role in this desorption process. The process can be executed using either batch or column methodologies.

1. Preliminary Rinsing: Initially, the spent adsorbent is rinsed with water to remove impurities.

2. Application of Eluting Agent:

The application of an eluting agent can be carried out using either the batch or column method. In the batch method, the spent adsorbent is mixed with the eluting agent, agitated at a specific speed, and maintained at a set temperature for a predetermined period. In the column method, the eluting agent is passed through the spent adsorbent at a controlled flow rate, which is slower than that used in previous adsorption trials. This slower flow rate ensures effective desorption by minimizing the volume required for regeneration.

3. Final Washing: The treated adsorbent is thoroughly rinsed with water to eliminate any residual eluting agent.

4. Preparation for Reuse: The adsorbent is then conditioned for subsequent adsorption cycles.

The complete sequence of adsorption, leading to the creation of spent adsorbent, followed by desorption to regenerate fresh adsorbent, is defined as one cycle. Multiple cycles are performed during experimental procedures to facilitate the reuse of the spent adsorbent and to assess the efficiency of the desorption process as described by Machado et al. (2024).

In the context of adsorption-desorption processes, the evaluation of adsorbate (pollutant) behavior involves measuring both the quantities of adsorbed and desorbed substances. After each cycle, two key parameters are assessed:

Firstly, desorption efficiency (percentage of desorption) is determined, which indicates the proportion of the adsorbed pollutant successfully desorbed during the desorption phase. This is calculated by taking the ratio of the desorbed adsorbate quantity to the initial amount adsorbed and expressing it as a percentage. Secondly, the quantity of desorbed adsorbate is quantified, which represents the absolute amount of pollutant released from the adsorbent material, measured in milligrams per gram (mg/g). This value provides insights into the desorption process's effectiveness and the adsorbent's capacity to release the pollutant. Mathematically, these parameters are expressed as follows:

$$Desorption\ efficency\ (\%) = \frac{C_{des}}{C_{ads}} \times 100 \quad (2.4)$$

$$Amount\ of\ desorbed\ \left({}^{mg}/_{g}\right) = \frac{C_{des}}{m} \times V \quad (2.5)$$

where, C_{des} represents the concentration of the desorbed adsorbate in milligrams per gram (mg/g), C_{ads} denotes the concentration of the adsorbed adsorbate in milligrams per gram (mg/g), m is the amount of adsorbent in grams (g), and V is the volume of the desorbing solution in liters (Machado & Mulky 2024).

Desorption efficiency serves as a crucial metric for assessing the potential reuse of adsorbents. Over multiple cycles, there is a general trend of diminishing desorption efficiency and a reduction in the adsorbent's mass. This observation leads to the conclusion that desorption, which inverses the adsorption process, can be readily

executed in both laboratory and industrial environments. Additionally, the reusability of the regenerated adsorbent is evaluated through simple equations and by examining the number of desorption cycles implemented.

2.15.1 Eluent

The eluent is crucial in the desorption process, as the efficiency of separating the adsorbate from the spent adsorbent is contingent upon the type of eluent used. Eluents facilitate the detachment of bound adsorbates from the exhaust adsorbent. In essence, the term "eluent" refers to the carrier component of the mobile phase, either in liquid or gas form, utilized in chromatography. The eluent propelled the analyte through a chromatographic system. Additionally, eluents have applications in organic chemistry for extraction purposes. During desorption, the eluent was instrumental in dislodging the adsorbate from the exhausted adsorbent.

Critical criteria for selecting an appropriate eluent include its compatibility with both the adsorbate and adsorbent, its efficacy in breaking the adsorbate-adsorbent bond, the pH of the eluent, its complexing capabilities, and its organic modifier content. Several parameters, including the type and concentration of the eluent, the desorption method (batch or column), the volume, and the pH, are critical in selecting the appropriate eluent. Eluent choice, whether anionic, cationic, or organic solvent, depends on the specific adsorbate-adsorbent system being analyzed (Patel 2022). The eluent concentration was optimized to avoid structural damage to the exhausted adsorbent that could result from excessive concentrations, whereas lower concentrations may decelerate the desorption rate and necessitate a higher volume of eluent. The volume of elution correlates well with the breakthrough volume, facilitating the accurate determination of excess adsorption isotherms for organic eluent components on different materials without requiring specialized equipment. Additionally, the pH of the eluent is a crucial factor affecting desorption efficiency, as it influences the charges on both the eluent and solute ions. The ion exchange process is particularly significant in this context (Baskar et al. 2022).

In conclusion, solvent desorption involves the use of an eluent or solvent to break the bonds between the adsorbate and adsorbent, and a range of parameters influence the effectiveness of this desorption process.

2.16 REGENERATION OF CHITOSAN-BASED ADSORBENTS

Chitosan-based composites have been extensively and successfully utilized as adsorbents; however, there is a risk that the adsorbed pollutants may leach into the environment after the adsorption process. Once saturated, these adsorbents become toxic and are not easily biodegradable. Therefore, it is crucial to fully recover spent chitosan adsorbents before disposal to prevent environmental contamination. The strong affinity of chitosan-based composites for a range of inorganic and organic contaminants suggests that the regeneration process may be slow. Therefore, regenerating exhausted chitosan adsorbents is crucial for the efficient and environmentally friendly removal of contaminants from water and their cost-effective application on a large scale (Vakili et al. 2019a).

The selection of an appropriate method for regenerating adsorbents depends on the characteristics of both the adsorbent and the adsorbate, factors such as costs and processing requirements. Thus, the chosen regeneration strategy should be environmentally sustainable, straightforward to implement, profitable, efficient, and capable of facilitating the reuse of the spent adsorbent (Vakili et al. 2019a).

The regenerability of chitosan-based adsorbents is influenced by several factors, including low mechanical stability, chemical instability, and biodegradability associated with chitosan. Despite the drawbacks of thermal and biological regeneration methods, specific limitations of chitosan further impact its suitability for adsorbent regeneration. Notably, chitosan exhibits high sensitivity to elevated temperatures, rendering it unsuitable for prolonged exposure to heat (Rodrigues et al. 2020). Additionally, the presence of oxidizable or hydrolyzable bonds within the chitosan backbone makes it susceptible to biodegradation by microorganisms (Stoleru et al. 2017).

From practical and economic perspectives, chemical treatment emerges as a preferred approach for regenerating saturated chitosan-based adsorbents. This method involves washing the adsorbents with a suitable desorption agent or eluent. Chemical regeneration offers simplicity, convenience, effectiveness, and cost-effectiveness. Various chemicals can serve as desorption agents, facilitating the release of specific species from spent adsorbents (Shahadat & Isamil 2018).

An appropriate eluent for regenerating chitosan-based adsorbents should efficiently recover the adsorbent, enabling its reuse in adsorption. In addition, this agent should not be expensive, harmful to the environment, or destructive to chitosan-based adsorbents, and can restore the physical and adsorption properties of chitosan close to the original state. Thus, selecting an appropriate eluent with effective desorption features is crucial for successfully desorb and regenerating exhausted adsorbents. Researchers have explored various eluants, including acids, alkalis, salts, and organic solvents, which have been utilized in different investigations for efficient desorption and regeneration of chitosan-based adsorbents, thereby recovering adsorbate molecules (Abdulrasool et al. 2021).

Solubility, a fundamental chemical property, characterizes the capacity of a solute to dissolve within a solvent. Notably, dyes exhibit solubility in organic solvents, rendering solvent-based desorption agent's viable choices for liberating dyes from adsorbents. Among these agents, organic compounds such as acetone and alcohols (specifically ethanol and methanol) have demonstrated successful desorption of various dye types from chitosan-based adsorbents (Vakili et al. 2019b).

Methylene Blue (MB) loaded on magnetic chitosan nanoparticles modified with N,N-bis(carboxymethyl) glutamic acid (G-MCTS) was regenerated using ethanol, double-distilled water, and acetone solutions (Zhu et al. 2016). Among these desorption agents, ethanol demonstrated the highest efficiency, exceeding 90%. Consequently, regeneration experiments were conducted using ethanol for five cycles, during which the adsorption capacity showed minimal decline in the first four cycles.

In further investigations, an ethanol/ammonia solution (volume/volume ratio of 3:2) was utilized for the regeneration of magnetized chitosan-coated lignocellulose fiber (CHS/LCF) following the adsorption of Acid Red 18 (AR 18). Remarkably, the adsorption rate during the initial cycle reached 99.5%, and this high efficiency was sustained at 99.9% even after ten consecutive cycles (Zhou et al. 2016). In a separate investigation conducted by Gul et al. (2016) acetone was employed to regenerate magnetic chitosan crosslinked with graphene oxide (Fe_3O_4-GO), which had been saturated with Methyl Violet (MV) and Alizarin Yellow R (AY). Following four cycles of regeneration, the adsorption rate exhibited a decrease of 4.2% for MV and 10.5% for AY. In particular, the dye removal efficiency for MV diminished from 89.1% in the initial cycle to 84.9% by the fourth cycle, while for AY, it declined from 65.6% to 55.1% during the same period.

The efficiencies of adsorption and desorption generally decline as the number of regeneration cycles increases. This reduction may be attributed to the occupied adsorption sites with strongly bound molecules. Further, the effect of pH on the degradation and dissolution of chitosan can alter its structure, thereby affecting the performance of chitosan-based adsorbents during regeneration. Enhanced adsorption effectiveness typically correlates with higher desorption efficiency due to the larger quantity of adsorbed molecules. However, it is essential to recognize that a single desorption agent typically targets a specific type of adsorbate to recover it rather than multiple species. The use of such agents can mitigate secondary pollution and reduce waste by facilitating the recovery, reuse, or recycling of materials, which can then be utilized as raw inputs in other industrial applications (Vakili et al. 2019b).

CHAPTER III

ALKALINE FUSION-ASSISTED HYDROTHERMAL SYNTHESIS OF ZEOLITE X FROM MALAYSIAN FLY ASH FOR EFFICIENT NICKEL AND VANADIUM IONS REMOVAL

3.1 INTRODUCTION

Zeolites are a promising alternative to activated carbon as an adsorbent for heavy metals. Zeolites are cost-effective and selective and have been used to purify water since the 19th century (Yuna 2016). Zeolites are aluminosilicates with a hydrated crystalline structure and a 3D atomic arrangement (Jin et al. 2021). They have high porosity, surface area, and are easily functionalized, making them attractive for use in various fields, including wastewater treatment, the petroleum industry, environmental applications, research catalysis, and ion exchange (Yadav et al. 2021). There are 234 different types of zeolites that have been found so far. The International Zeolite Association gave each of these crystalline microporous materials a unique three-letter code, such as BEA (Zeolite Beta), FAU (Faujasite), MOR (Mordenite), and so on. These types are different in structure and how they behave. About 20 of these zeolites are used in industry, but only five are known as the "Big Five." The term "Big Five" refers to the five most commercially significant zeolites in the industry. These five zeolites BEA (Beta), FAU (Faujasite), FER (Ferrierite), MOR (Mordenite), and MFI (ZSM-5) are called the "Big Five" because they are the most widely used and studied due to their unique structural and chemical properties. These properties make them particularly effective in various industrial applications such as catalysis, adsorption, and ion exchange. Their widespread use and versatility in industrial processes have earned them this designation (Narayanan et al. 2020). Due to the limited applications of natural zeolite, many attempts have been made to obtain zeolite in the laboratory. Environmental considerations influence the current trend regarding zeolite synthesis, necessitating the use of natural or waste-derived raw materials in the process (Król 2020).

In recent years, extensive research has been conducted on faujasite zeolites (X and Y) due to their application in separation and catalysis engineering within the petrochemical sectors. Differentiating between zeolites X and Y, which share a similar XRD pattern, relies on their varying compositional ratios (SiO_2/Al_2O_3). Specifically, zeolite X maintains a Si/Al ratio of 1 to 1.5 (Koop-Santa et al. 2024), while zeolite Y possesses a Si/Al ratio exceeding 1.5 (Reiprich et al. 2022).

Zeolite Na-X is characterized by a standard unit cell composition Na_{86} $[(AlO_2)_{86}$ $(SiO_2)_{106}]$ mH_2O, accompanied by a pore measurement of 0.74 nm. The building units of zeolite X are formed when Si and Al tetrahedra are coupled to form a sodalite unit, which has the shape of a truncated octahedron having square and hexagonal faces (refer to Figure 2.3). Despite having a wide array of applications, the principal utilizations of zeolite X pertain to catalysis, gas and organic component purification and separation, cation exchange, and adsorption. Because zeolite Na-X is used in extensive industries, researchers are interested in synthesis from a diverse range of unconventional source materials (El Bojaddayni et al. 2023).

Coal is a significant energy source, contributing 22% to global energy consumption (Ren et al. 2020b). The burning of coal in power plants creates by-products including, coal fly ash (CFA) and coal bottom ash (CBA) (Fukasawa et al. 2017). CFA represents over 70% of these by-products, with an estimated production of 700 million metric tons annually, which may increase with the growing electricity demand. In 2016, Malaysia produced approximately 6.8 million tons of CFA from six coal-fired power stations (Ghazali et al. 2019). However, the storage of CFA can lead to dust emissions and groundwater contamination, which pose health risks. Apart from the health and environmental concerns, the disposal process incurs high costs (Curpen et al. 2023). The composition of CFA varies based on the coal used in the process. siliceous CFA, known as class F, consists of over 70% SiO_2, Al_2O_3, and Fe_2O_3/Fe_3O_4 oxides (present as quartz, mullite, and hematite/magnetite), with less than 10% CaO. In contrast, class C, or calcareous CFA, contains 50% SiO_2, Al_2O_3, and Fe_2O_3/Fe_3O_4 oxides, with CaO content exceeding 10% (Wang et al. 2021a). The use of CFA in zeolite synthesis has garnered attention due to Several considerations, including waste recycling,

valorization, versatile applications, and enhanced properties (Dere Ozdemir & Piskin 2019; Um & Jeon 2021).

So far, various methods, including hydrothermal treatment (one-step), fusion followed by hydrothermal treatment (two-step), molten salt treatment, microwave irradiation, and ultrasound technique, have been utilized for synthesizing zeolites, depending on the required zeolite type, with the first two methods being the most common (Tauanov et al. 2020). The primary limitation of the hydrothermal method is that it achieves a zeolite phase yield of just 20–60 wt.% because only a small portion of the coal fly ash undergoes reaction (Längauer et al. 2021a; Yang & Park 2019). In contrast, alkaline fusion is crucial for producing high-purity silicate and aluminosilicate by dissolving the crystalline phases in the ash used for synthesis. Compared to hydrothermal synthesis, the zeolite produced through the indirect method is highly pure (Belviso 2018). The zeolite production process includes alkaline calcination, ageing, and crystallization. The product type depends on the parameters at each stage, like time, temperature, and ratio of reaction components (Aldahri et al. 2017; Sivalingam & Sen 2019).

Many studies have been conducted to prepare high-purity zeolite, with researchers focusing on enhancing various parameters such as crystallization time, temperature, NaOH concentration, etc. The concentration of NaOH has a significant effect on the purity of synthesised zeolite. The base concentration determines the composition of the molar ratio of the prepared primary gel and subsequently influences the structural composition, morphology, and particle size distribution of the zeolite samples. This finding is consistent with the study by Najafi et al. (2022), which concluded that pH adjustment leads to the controlled binding of precursor components and the controlled synthesis of nanoparticles. Therefore, optimizing this parameter is of paramount importance. Furthermore, the particle size in the low alkaline range is smaller than in the high alkaline pH range. Therefore, particles within the low alkaline range are extremely fine, and their modifications from the initial stages of the synthesis process until just before gel formation are negligible due to the low concentration of $^{-}$OH ions within this pH range. The size of precursor particles expands as the pH

increases due to the heightened concentration of ^{-}OH ions at a basic (alkaline) pH, leading to an accelerated rate of hydrolysis (Rahmani-Azad et al. 2022).

The main objectives of this chapter are:

1. To synthesize high-purity zeolite type X utilizing the fusion-assisted hydrothermal method from Malaysian treated coal fly ash, employing a two-step pretreatment process.
2. To assess the efficiency of synthesized zeolite X in removing Ni^{2+} and V^{5+} ions under various parameters, including initial ion concentrations, zeolite dosage, contact time, pH, and the presence of co-existing ions.

In subsequent sections, the chapter will elaborate on the methods used to characterize the structure of both raw and treated fly ash-derived zeolites, employing various analytical techniques such as N_2 adsorption/desorption, Fourier transform infrared spectroscopy (FT-IR), scanning electron microscopy (SEM), X-ray fluorescence spectroscopy (XRF), and X-ray diffraction (XRD). Furthermore, the chapter will analyze isotherm and kinetic data to provide a comprehensive understanding of the adsorption mechanism.

3.2 EXPERIMENTAL

3.2.1 Chemicals

The Tenaga Nasional Berhad (TNB) Thermal Power Co., Ltd. supported the research by providing raw coal fly ash (RCFA). Sodium hydroxide (NaOH) and nickel (II) nitrate hexahydrate ($Ni(NO_3)_2.6H_2O$, purity >99 %) were purchased from R&M, Malaysia. Cobalt (II) nitrate hexahydrate ($Co(NO_3)_2.6H_2O$, purity >99 %), Lead(II) nitrate ($Pb(NO_3)_2$, purity >99 %) and, ammonium metavanadate (NH_4VO_3, purity ≥99.0%) were purchased from Merck, Malaysia. Concentrated hydrochloric acid (HCI, 85–87 % purity) was purchased from Merck & Co., USA. All reagents were analytically pure without further purification. Deionized water used in this study was supplied by Millipore water purification system.

3.2.2 Pretreatment process of RCFA

a. Separation of the magnetic fraction of RCFA

The treatment involves sequential steps, beginning with drying RCFA at 100°C for 24 h, followed by manual crushing to prepare the material for further processing. A sieve with a mesh diameter of 250 μm was employed to achieve consistent particle size, ensuring uniformity. Afterward, the RCFA was calcinated at 800°C for 90 min to eliminate residual unburned carbon. Subsequently, a mixture of fly ash and water was prepared, with a ratio of 1: 2 fly ash-to-water, and mechanically stirred for 3 h to achieve thorough homogenization. To magnetic fraction separation, using a magnet with a removable plastic cover to isolate the magnetic fraction from the raw ash. The plastic cover was subsequently separated from the magnet, washed to eliminate magnetic remnants, and the magnetic separation was iteratively performed until all magnetic particles are effectively extracted from the raw ash material. The non-magnetic fraction (NCFA) was dried at 100°C and stored at room temperature until use.

b. Acid-washing treatment of non-magnetic fraction of coal fly ash (NCFA)

Firstly, 20 g of NCFA was added to HCl with a 20% w/w acid concentration, maintaining an acid/CFA ratio of 20 mL acid per g of NCFA. The mixture was stirred continuously at a rate of 300 rpm at a temperature of 90°C for 2 h. The solid sample was then filtered from the acid solution and washed iteratively with deionized water until the solution reached a neutral pH. The sample was dried overnight at 110°C and labelled as (TCFA) for further use.

3.2.3 Synthesis of zeolite X from row coal fly ash (RCFA) and treated coal fly ash (TCFA)

Zeolite is produced without adding templates or seeds, using RCFA, sodium hydroxide, and water. Initially, a uniform mixture of RCFA samples and sodium hydroxide was prepared in a mass ratio of 1:1.2. Subsequently, this mixture was subjected to calcination at 550°C for 1.5 h to activate the silicon and aluminum elements. Next, deionized water and the alkali-melted solid were mixed in a liquid-solid mass ratio of 5:1. The suspension was stirred at room temperature for 16 h before being transferred

to a Teflon-lined high-pressure reactor and sealed. The homogeneous solution was maintained in a hot air oven, without stirring, for 6 to 24 h at temperatures ranging from 80 to 100°C. Finally, the solution was thoroughly washed with DI water (Deionized water) to eliminate excess sodium hydroxide. Afterwards, it was filtered and dried overnight at 110°C. Figure 3.1 represents the flow chart for the synthesis process.

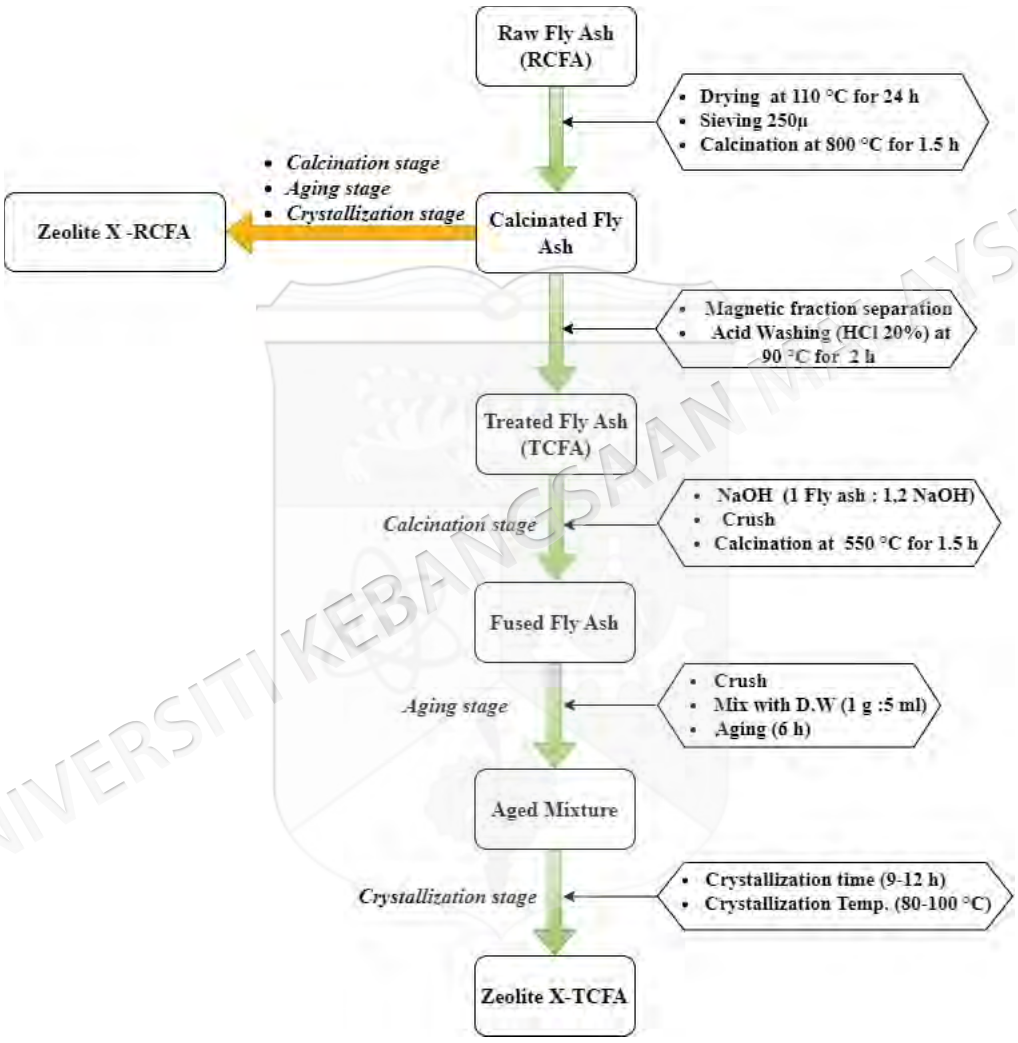

Figure 3.1 Flowchart of synthesis procedure

3.2.4 Instruments and material characterization

X-ray fluorescence spectroscopy (XRF) was used to determine elemental analysis, employing a Philips PW2404 spectrometer with a rhodium tube, scintillation counter, and LiF 200 crystal, operating at 50 kV and 70 mA. The analysis was conducted on RCFA, treated CFA samples, and synthesized zeolites. Powder X-ray diffraction (XRD) was utilized to analyze the crystallography and structural properties of RCFA, fused

CFA, and synthesized zeolites using a model XRD-6000 Shimadzu diffractometer. The diffractometer had a scan speed of 4°C/min and a 2 range of 5° to 40°. Field emission scanning electron microscopy (FESEM) was performed with a LEO-1455 VP electron microscope to estimate the surface morphology of RCFA, fused CFA, and synthesized zeolites.

Fourier-transform infrared spectroscopy (FT-IR) was conducted using a Perkin Elmer (PC) Spectrum 100 FT-IR with a resolution of 4 cm^{-1} and a range of 300–4000 cm^{-1} to characterize the chemical functional groups of the synthesized zeolites. The Brunauer–Emmett–Teller (BET) and Barrett–Joyner–Halenda (BJH) methods were applied using a Thermo–Finnigan Shopmatic 1990 series N_2 sorption analyzer to measure the specific surface area and pore distribution of RCFA and synthesized zeolites. Samples were degassed for 12 h at 150°C to remove dirt or moisture, and N_2 adsorption and desorption were analyzed in a vacuum chamber at -196°C. Thermogravimetric analysis (TGA) was carried out using a TGA 1000i (Instrument Specialists Inc, USA) to determine the thermal stability of synthesized zeolites. The samples were heated from 25°C to 600°C in an alumina crucible to remove contaminants and moisture.

The magnetic properties of RCFA and treated CFA samples were studied using a vibrating sample magnetometer (VSM) from Quantum Design, USA. The pH and conductivity of solutions containing raw CFA and synthesized zeolites were measured by mixing 0.3 g of sample with 25 mL of deionized water, shaking for 24 h, filtering, and then using a pH meter (LAQUA Model PH1100) and conductivity meter (BEL Engineering Model W12D). Loss on Ignition (LOI) was measured for synthesized zeolites by heating samples in an oven at 110°C for 24 h and in a muffle furnace at 900°C for 4 h, with results expressed as a percentage of weight loss based on a 0.5 g sample weight.

Finally, Microwave Plasma Atomic Emission Spectroscopy (MP-AES) was used to determine the concentration of metals in solutions using a TAS-990 (Beijing).

3.3 BATCH ADSORPTION EXPERIMENTS

Simulated petroleum wastewater containing either Ni^{2+} or V^{5+} ions was prepared by dissolving the appropriate metal salts in deionized water. The adsorption behavior of these metals using zeolite X-TCFA was studied through batch experiments conducted at room temperature. Several parameters were systematically examined, including the initial concentration of metal ions, contact time, adsorbent dose, solution pH, and the effect of competing ions.

To explore the impact of metal ion concentration, the nickel ion levels in the test solution ranged from 50 mg/L to 300 mg/L, and vanadium ion levels ranged from 10 mg/L to 100 mg/L, simulating the concentrations found in real wastewater. The synthetic zeolite X-TCFA dose and contact time were kept constant at 0.1 g and 180 min, respectively. To determine the optimal contact time, samples were taken at intervals between 15 and 240 min, with metal concentration fixed at 100 mg/L and adsorbent dose at 0.1 g.

The adsorbent dose of zeolite X-TCFA varied from 1 to 10 g/L to assess the effect of adsorbent loading, while the metal concentration and contact time remained constant at 100 mg/L and 180 min. The influence of pH on adsorption was evaluated across a pH range of 2 to 12, using 0.1 M HCl and NaOH for adjustments. The selectivity of zeolite X-TCFA for Ni^{2+} and V^{5+} was tested in the presence of competing ions ($Co^{2+}$and Pb^{2+}) at concentrations of 10 mg/L, 50 mg/L, and 100 mg/L.

After the adsorption experiments, the samples were centrifuged at 4000 rpm for 5 min, and the concentrations of metal ions in the supernatant were measured using microwave plasma atomic emission spectroscopy (MP-AES).

The following information about Ni^{2+} or V^{5+} removal rate (%) and adsorption capacity (mg/g) is based on equations (3.1) and (3.2):

$$R\% = \frac{C_0 - C_t}{C_0} \times 100\% \quad (3.1)$$

$$q_e = \frac{C_0 - C_e}{m} \times V \quad (3.2)$$

where C_0 and C_e represent the concentrations of heavy metal ions in the solution before and after adsorption (mg/L), respectively. V represents the volume of heavy metal solution that is used (L), and m represents the amount of adsorbent that is utilized (g).

3.4 RESULTS AND DISCUSSIONS

3.4.1 Elemental analysis and crystallographic structure of RCFA, TCFA, and synthetic zeolites X

Research into the zeolitization of fly ash has revealed that the composition of fly ash is a crucial factor in the production of zeolite X (Zhang et al. 2022a). Table 3.1 presents the XRF results for RCFA, indicating that it primarily consists of SiO_2 (54%), followed by Al_2O_3 (24%), Fe_2O_3 (10%), and trace amounts of Na_2O, CaO, and MgO. These findings aligned closely with a study conducted by (Gong et al. 2021), which also reported a high concentration of amorphous aluminosilicate in RCFA. RCFA contained a significant amount of silicon (Si) and aluminum (Al), making it an excellent starting material for producing zeolite X. Notably, the weight percentages (wt.%) of SiO_2, Al_2O_3, and Fe_2O_4 were all greater than 70%, which classified this RCFA as a Class F type, as per the specifications outlined in ASTM C618-84 (Yang et al. 2019b). Joseph et al. (2020) suggested that Type-F RCFA was likely produced by the combustion of a mixture containing anthracite and bituminous coal. It is worth noting that the findings presented in Table 3.1 closely aligned with the optimal Si/Al ratio of 1 to 2, as specified by the international zeolite association for producing zeolite X from fly ash (Längauer et al. 2021). Furthermore, it was observed that the Si/Al ratio decreased to less than 2 for the TCFA due to the pretreatment processes. The findings suggested that pretreatment processes can adjust the Si/Al ratio in a manner conducive to targeted zeolite synthesis. The silicon-to-aluminum ratio significantly influenced the ion exchange capacity of a given zeolite because it dictated the number of exchangeable cations within the framework's pores. A lower Si-to-Al ratio resulted in a greater charge imbalance within the framework, but it also led to more M^+ counter ions, which balanced this charge imbalance (Zambare et al. 2019).

Table 3.1 Chemical composition of RCFA, NCFA, TCFA and zeolite X synthesized

Material/ elemental (%)	SiO_2	Al_2O_3	Fe_2O_3	Na_2O	CaO	MgO	SiO_2/Al_2O_3
RCFA	54.42	24.14	10.11	0.45	4.21	1.18	2.25
NCFA	59.21	29.92	1.12	0.38	3.31	0.71	1.97
TCFA	63.33	35.41	0.22	0.21	0.5	0.43	1.78
Zeolite X-RCFA	44.71	29.82	8.58	13.62	4.30	1.26	1.50
Zeolite X-TCFA	43.51	30.19	0.18	22.71	0.21	0.12	1.44

The VSM analysis in Figure 3.2 indicated the presence of magnetic species in RCFA. RCFA exhibited the highest saturation magnetization value in the magnetic hysteresis loop compared to NCFA and TCFA. The results suggest a significant presence of ferromagnetic iron oxides in RCFA. The significance of the magnetic separation process becomes evident when comparing the magnetization (Ms) values of the RCFA and the NCFA. Notably, the M_S value decreased from 2.19 to 1.51, and this reduction persisted even after acid treatment, with the Ms value reaching 1.43 for TCFA. The effect of acid washing can be seen through the dissolution of the salt oxides present in the composition of the CFA, where the concentration of most of the metal oxides decreased and reached less than 2%, as indicated by the results of the XRF analysis, and this indicates the effectiveness of the acid used in the treatment process. Another benefit of the treatment process was adjusting the silicon-to-aluminum ratio in the prepared zeolite composition. The ratio was ideal (1.44) for TCFA-derived zeolite X and slightly higher (1.50) for RCFA-derived zeolite X. An increase in the concentration of sodium oxide (Na_2O) indicated the success of the zeolite preparation process. The rise in sodium ions within the synthesized zeolite's composition was attributed to the alkali fusion of fly ash with sodium hydroxide during preparation (Koshlak 2023).

(a)

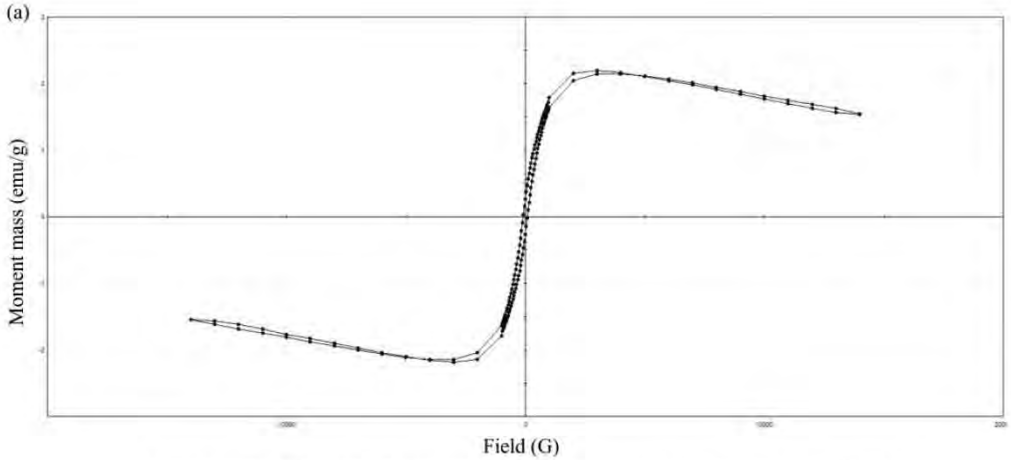

Coercivity (Hci): 88.318 G	Experiment Time: 1530 sec	Hci, Negative: -88.832 G
Hci, Positive: 87.805 G	Magnetization (Ms): 2.1916 emu/g	Mass: 1.9000E-3 g
Mr, Negative: -0.26413 emu/g	Mr, Positive: 0.26548 emu/g	Ms, Negative: -2.1894 emu/g
Ms, Positive: 2.1938 emu/g	Retentivity (Mr): 0.26481 emu/g	Sensitivity: 15 emu

(b)

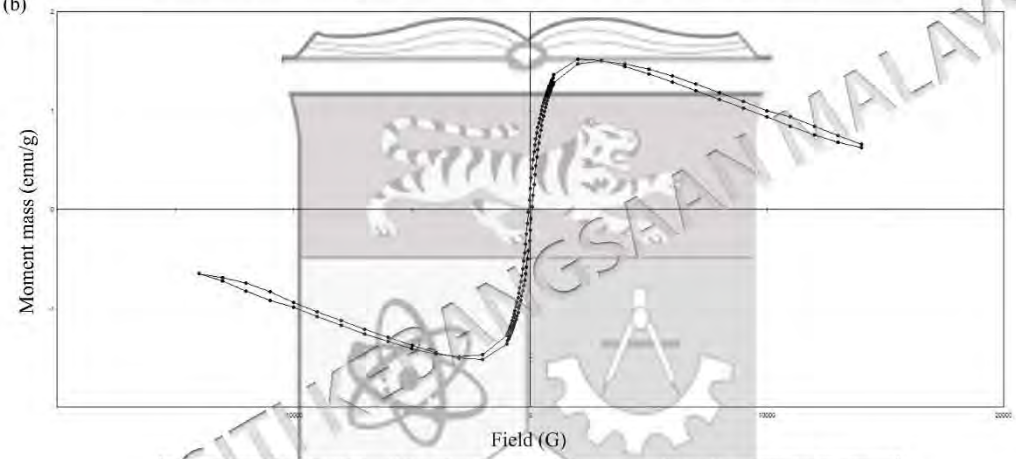

Coercivity (Hci): 70.655 G	Experiment Time: 1530 sec	Hci, Negative: -70.681 G
Hci, Positive: 70.628 G	Magnetization (Ms): 1.5197 emu/g	Mass: 1.1000E-3 g
Mr, Negative: -0.21082 emu/g	Mr, Positive: 0.21214 emu/g	Ms, Negative: -1.5185 emu/g
Ms, Positive: 1.5211 emu/g	Retentivity (Mr): 0.21148 emu/g	Sensitivity: 15 emu

(c)

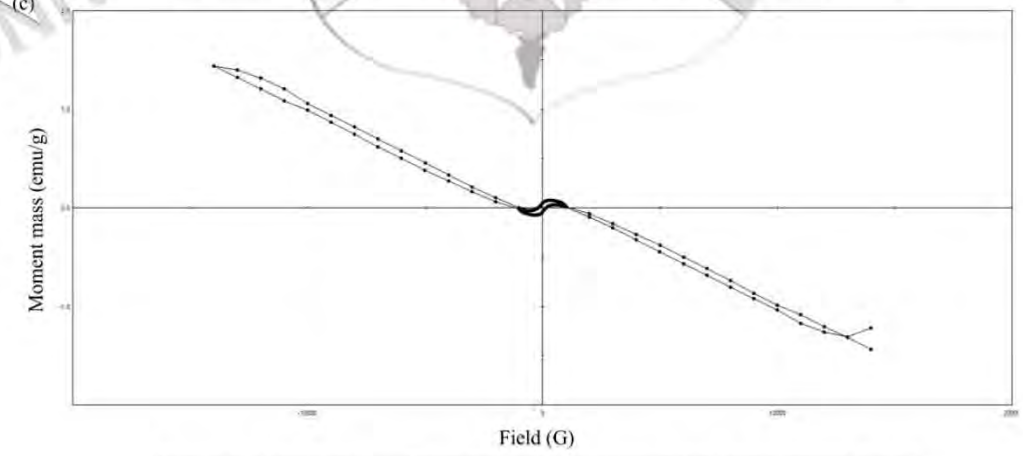

Coercivity (Hci): 610.68 G	Experiment Time: 1530 sec	Hci, Negative: 1046.3 G
Hci, Positive: -175.05 G	Magnetization (Ms): 1.4362 emu/g	Mass: 1.2000E-3 g
Mr, Negative: -43.504E-3 emu/g	Mr, Positive: 46.261E-3 emu/g	Ms, Negative: -1.4359 emu/g
Ms, Positive: 1.4364 emu/g	Retentivity (Mr): 44.883E-3 emu/g	Sensitivity: 15 emu

Figure 3.2 Magnetization curves of (a) RCFA, (b) NCFA, and (c) TCFA.

Figure 3.3a displays the X-ray diffraction pattern of RCFA. The figure revealed that RCFA predominantly consists of quartz (SiO_2), mullite ($3Al_2O_3.2SiO_2$), magnetite, and hematite, which aligned with the chemical composition of RCFA. Additionally, the XRD spectrum exhibited a broad hump between 20° and 40°, indicating the presence of amorphous glassy material. The inclusion of NaOH in the fly ash fusion process introduced additional Na^+ cations, which are recognized for their role in stabilizing the sub-building units within the zeolite framework during fly ash zeolitization. Furthermore, the OH^- ions from NaOH served as mineralizing agents, facilitating the depolymerization of the silicon content in fly ash minerals into monomeric species. The increase in sodium oxide content resulted from the solid-state reaction between RCFA and NaOH, resulting in the dissolution of the most common mineral phases in RCFA: quartz and mullite, and produces new mineral phases, including sodium aluminate and sodium silicate, as illustrated in Figure 3.3b and Equation (3.3). The new phase, known as fused RCFA, was easily grindable and exhibited a bright green colour, with previous studies confirming its ready solubility in both water and alkaline solutions (He et al. 2020).

$$NaOH + xAl_2O_3.ySiO_2 \xrightarrow{fusion} Na_2SiO_3 + Na_2AlO_2 + H_2O \qquad (3.3)$$

Based on the findings of prior studies on synthesizing zeolite X from fly ash using the alkaline fusion method followed by hydrothermal crystallization, it becomes evident that this approach is the most selective for the desired zeolite. Furthermore, crystallization temperature and time were the synthesis process's most influential factors (Korpa et al. 2021). Figure 3.3c, and d presented the effect of synthesis temperature and time on the production of zeolite X from fused RCFA. XRD diffractograms (Figure 3.3c) illustrate that when hydrothermal synthesis was conducted at 90 °C (fixed crystallization time 12 h), a pure phase of zeolite X-RCFA was successfully synthesized. However, at temperatures exceeding 90°C, the crystalline of zeolite X diminished, leading to its transformation into a more stable phase known as sodalite, at temperatures below 90°C, no change was observed in the fused ash phases. This lack of change indicated that the temperature was not high enough to facilitate the transformation of the existing phases in the fused ash into zeolite crystals. Concerning the duration of crystallization, it was noticeable that zeolite X formed with a limited

degree of crystallinity under 12 h. However, when the synthesis time was extended to 24 h, an unidentified contaminant phase co-crystallized alongside zeolite X. To compare and demonstrate the effectiveness of the treatment processes on the type of zeolite produced, the optimal conditions employed for preparing zeolite X from RCFA were used to synthesize zeolite from TCFA. Figure 3.3e displays the X-ray diffraction patterns of the TCFA-derived zeolite X, revealing a significant increase in crystallinity and the absence of peaks of contaminated phases.

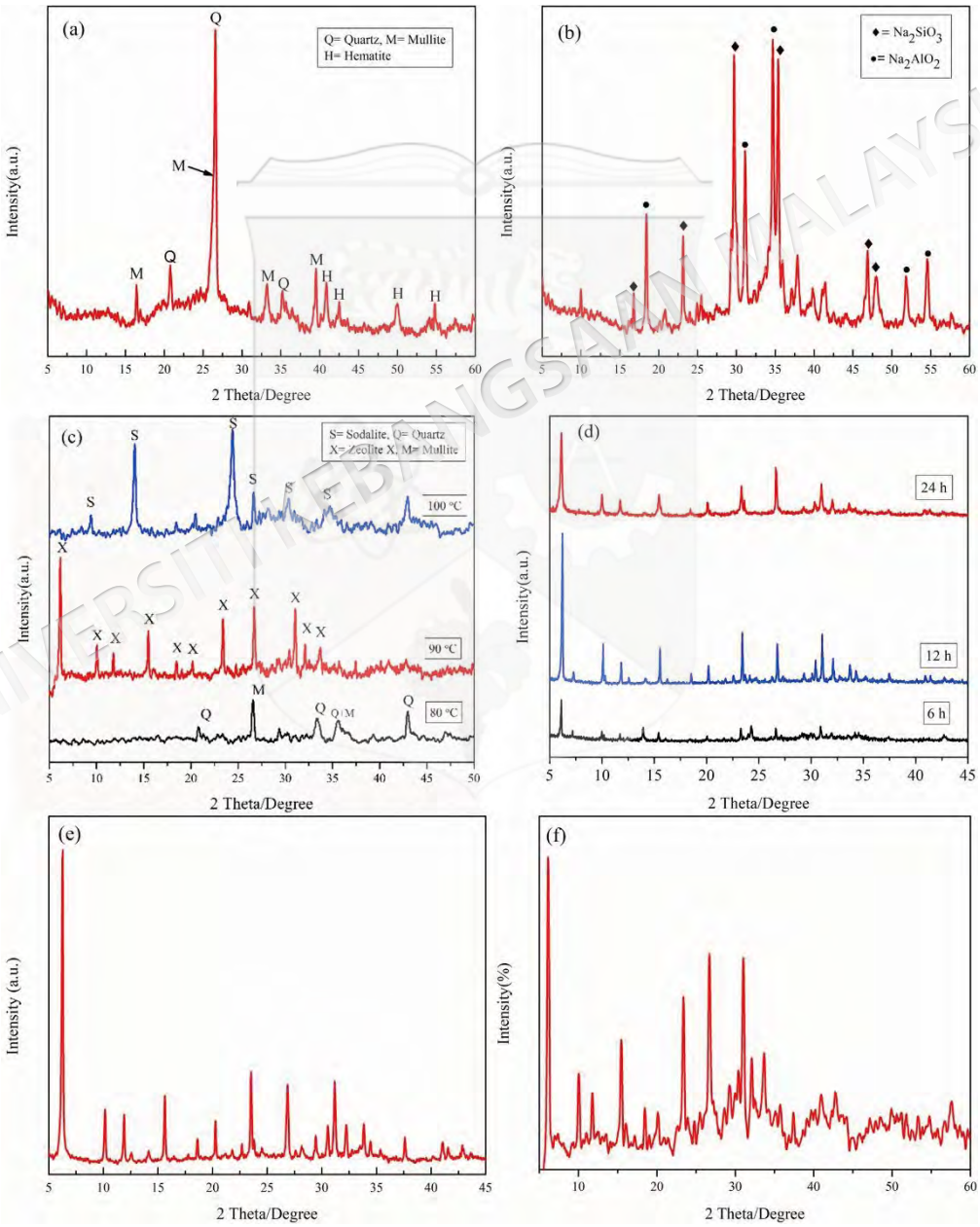

Figure 3.3 XRD patterns showing (a) RCFA, (b) fused RCFA, effect of (c) crystallization temperature, (d) crystallization time on synthesis zeolite X using RCFA, (e) zeolite X-TCFA, and (f) zeolite X-RCFA.

The NaOH present in the reaction mixture acts as an activator during the fusion process to form soluble silicate and aluminate, further took part in zeolite formation during hydrothermal treatment, and adjusted the sodium content of raw material. The amorphous phase characterizing the chemical/mineralogical CFA composition easily dissolved into an alkaline solution, and sodium ions stabilized the sub-building units (especially the six-member ring) of zeolite frameworks, mainly during hydrothermal processes. Insufficient content of alkali might lead to minimal extraction of alumino-silicates from fly ash which adversely affected the crystallization process(Korpa et al. 2021).

The effect of the TCFA to NaOH ratio on the crystallinity of the resultant zeolites was studied by varying the ratio from 1:0.8 to 1:1.6 g/g and shown in Figure 3.4. It can be seen from Figure 3.4 that the crystallinity of X zeolite changed from 58.13%-85.29% and reached a maximum at 1:1.2 g/g. The more NaOH added to the mixture during fusion, the higher the production of Na-salt soluble in water, which led to enhanced crystallinity of zeolite produced in subsequent stages (Bai et al. 2018). However, when the alkalinity in the system was too high (1:1.6), it was not favorable for the stable existence of crystal nucleus during the crystallization process because the alkalinity could activate the decomposition of Si and Al to sodium silicate and aluminate in the framework or could form sodalite instead of zeolite. Therefore, the TCFA to NaOH ratio was optimized at 1:1.2 g/g.

The solid-liquid ratio is a crucial factor for the synthesis of zeolites, which affects the zeolite formation rate, silica-alumina ratio, and product particle size. Figure 3.5 shows the effect of the solid-liquid ratio (1:3 to 1:9 g/mL) on the crystallinity of the synthetic zeolites. It can be found that the crystallinity of the X-type zeolite increased first and then decreased with the increasing amount of deionized water. At low alkalinity (solid-liquid ratio, 1:9 g/mL), a poor crystallized X phase was observed since the low concentration of hydroxyl ions could not depolymerize the silica source to provide sufficient solubilized aluminosilicate species to form nuclei. On the contrary, high alkalinity (solid-liquid ratio, 1:3 g/mL) reduced the crystallinity remarkably, probably due to the dissolution of the already-formed crystals in excess hydroxyl ions (Bai et al. 2018).

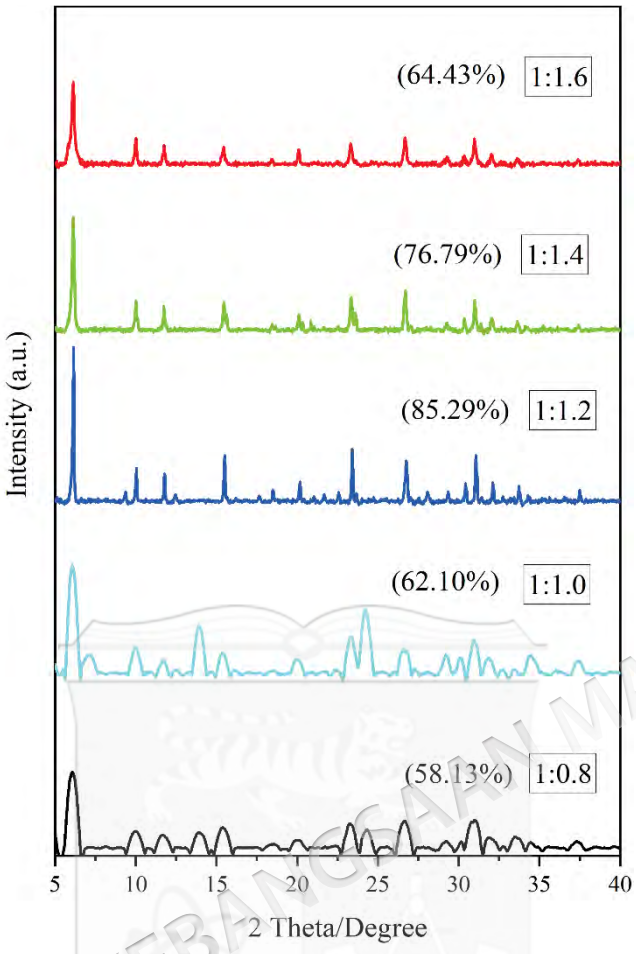

Figure 3.4 XRD patterns of the products obtained with different TCFA to NaOH ratios (fusion temperature, 550°C; solid-liquid ratio, 1:5 g/mL; crystallization temperature, 90°C; crystallization time, 12 h)

Furthermore, less solvent may have led to changes in the amount of extracted Si and Al species, impacting the Si/Al ratio of the fused fly ash synthesis slurry and resulting in a mixed phase zeolitic product. Therefore, it was crucial to control the amount of deionized water in the system to ensure the reactants formed Na-X zeolite. The Na-X zeolite with high crystallinity (89.75%) can be obtained when the solid-liquid ratio was 1:5 g/mL.

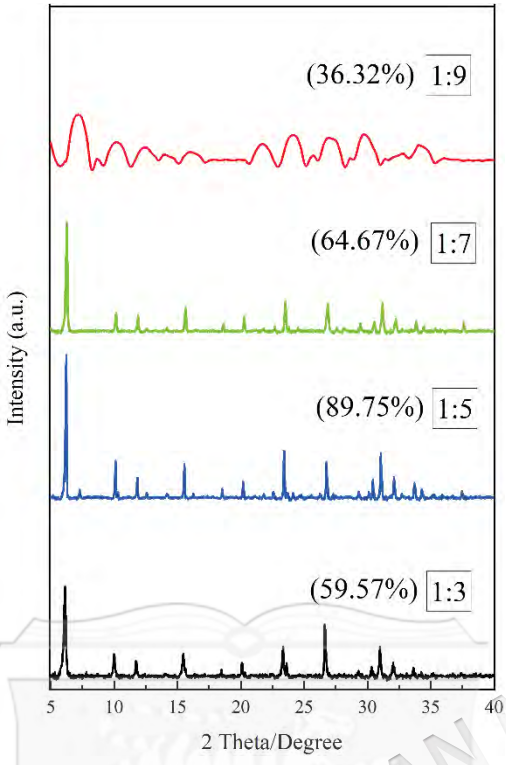

Figure 3.5 XRD patterns of the products obtained at different solid-liquid ratios (fusion temperature, 550°C; ash to NaOH ratio, 1:1.2 g/g; crystallization temperature, 90°C; crystallization time, 12 h)

3.4.2 Validation of zeolite X structure

The results from SEM analysis of RCFA and zeolite X-RCFA offer valuable insights into the morphological changes during the synthesis process. The images in Figure 3.6a show the spherical shape of the RCFA particles, which aligned with previous studies (Yadav et al. 2022). This phenomenon was explained by the cooling effect during solidification. Additionally, the smooth surface of CFA particles can be attributed to the presence of an amorphous glass phase (Alterary & Marei 2021). The primary goal of the fusion process, aimed at dissolving crystalline phases resistant to dissolution under ambient conditions, was successfully achieved. SEM images, in agreement with the XRD results, substantiated these findings. Figure 3.6b illustrated the transformation of the spherical RCFA particles into a porous, agglomerated mass following fusion. The SEM image in Figure 3.6c revealed that zeolite X-RCFA exhibited well-formed pyramidal octahedral-shaped crystals accompanied by some intergrowth crystals. In comparison, zeolite X-TCFA (Figure 3.6d) showcased well-defined individual crystals of zeolite X particles without intergrowth, highlighting the impact of pretreatment processes that enhance the degree of crystallinity and purity in zeolite X-TCFA.

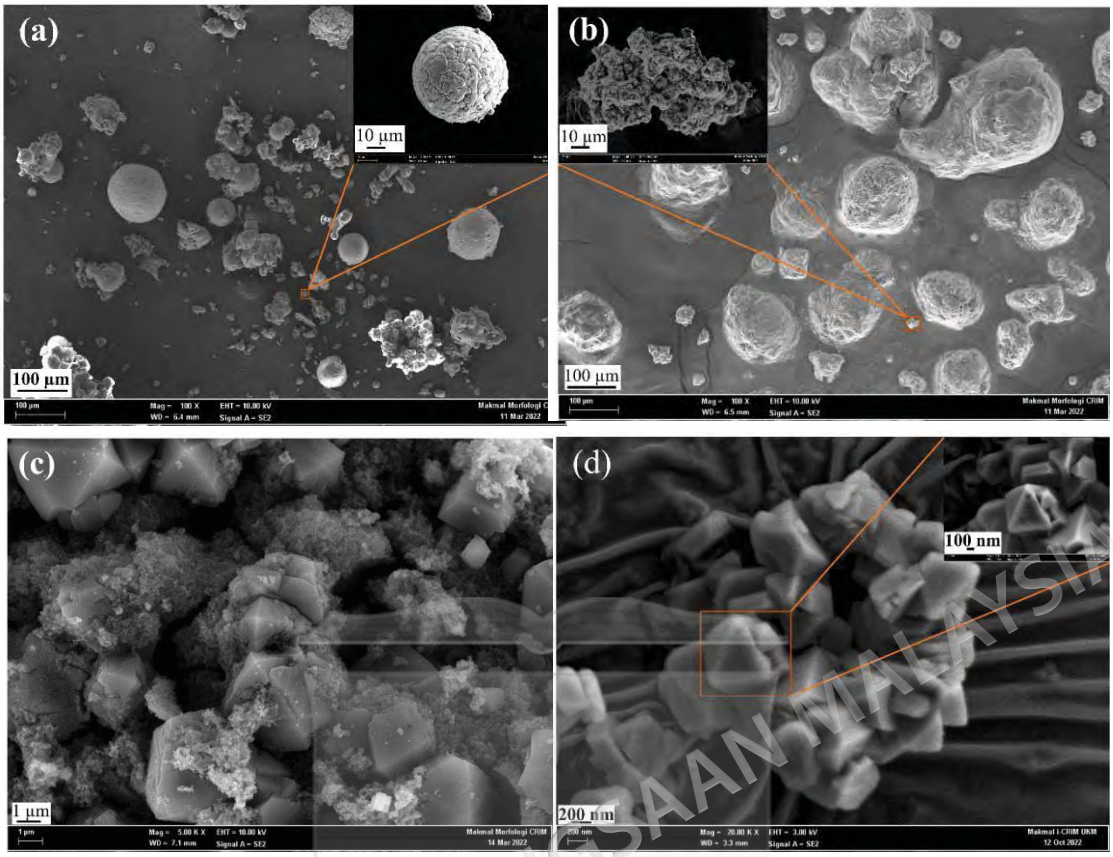

Figure 3.6 SEM micrographs of (a) RCFA (b) fused RCFA with NaOH (c) synthetic zeolite X RCFA (d) synthetic zeolite X -TCFA at 90˚C for 12 h.

Figure 3.7 illustrates the N_2 adsorption-desorption isotherms and pore size distribution of RCFA, zeolite X-RCFA, and zeolite X-TCFA. According to the IUPAC classification, the isotherms of all three materials were categorized as type IV with type H4 hysteresis loops, indicative of mesoporous structures (Pei et al. 2019). The pore-size distribution analysis revealed that RCFA and zeolite X-RCFA predominantly consisted of mesopores (20–50 nm) with minor microporosity (60–150 nm). On the other hand, the hysteresis loop in the isotherm indicates the pore structure and shape of the synthesized zeolite. The loop's shape (H4 type) of zeolite X-TCFA was associated with narrow slit-like pores. The pore size distribution curve in Figure 3.7 f indicated that the synthesized zeolite X from TCFA has a narrow range of pore diameters, predominantly in the 2-20 nm range. The presence of pores in this size range further supported the mesoporous character suggested by the isotherm. The high purity of zeolite X influenced the formation of these mesoporous structures (Panitchakarn et al. 2014) where zeolite derived from TCFA exhibited an optimal mesopore distribution and a large surface area. The specific surface area of RCFA was 4 m^2/g, whereas zeolite X-

RCFA and zeolite X-TCFA exhibited values of 115 m^2/g and 452 m^2/g, respectively. This substantial increase in specific surface area in the synthesized zeolite X was attributed to the texture of the zeolite micropores. Additionally, the surface area of zeolite X-TCFA was fourfold larger than that of zeolite X-RCFA, owing to the higher crystallinity of zeolite X-TCFA (Sakthivel et al. 2013).

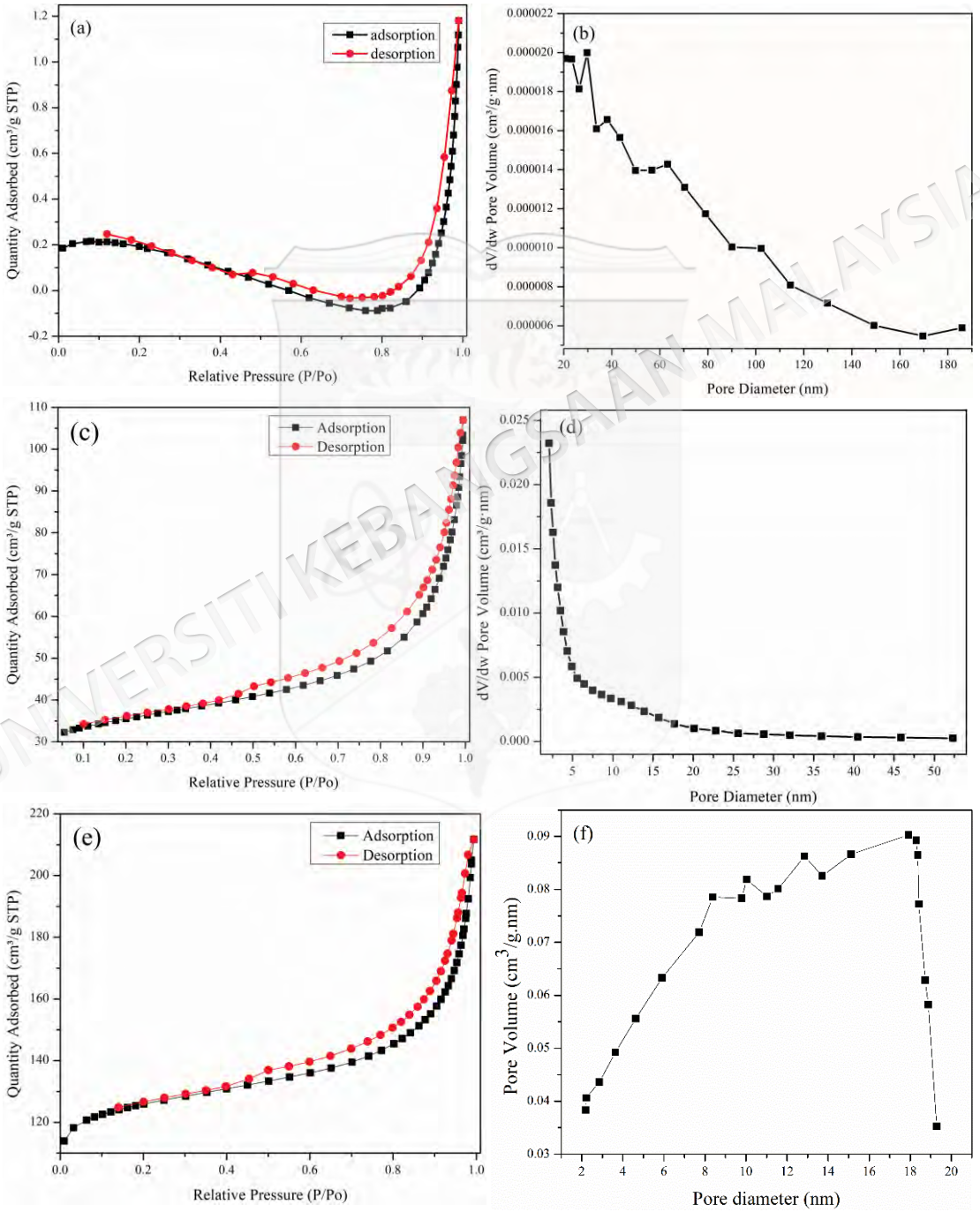

Figure 3.7 N_2 adsorption-desorption isotherms and pore size distributions for (a, b) RCFA, (c, d) zeolite X-RCFA, and (e), (f) zeolite X-TCFA.

Figure 3.8 shows the FT-IR spectra of zeolites X-RCFA and TCFA. The bands at 450 and 668 cm^{-1} were attributed to the bending vibration and symmetric stretching vibration modes of Si-O or Al-O bonds, respectively. The band at 561 cm^{-1} was assigned to the stretching vibration of Al-OH. The band around 750 cm^{-1} was considered the stretching mode of tetrahedral atoms. The intense vibration bands at 980 and 1650 cm^{-1} belonged to Si-OH and H-OH bonds (Murukutti & Jena 2022). Comparative FT-IR analysis revealed that the FT-IR bands observed in zeolite X-RCFA and X-TCFA were similar, suggesting identical building blocks. These results confirmed the successful synthesis of zeolite from both types of fly ash used. Furthermore, FT-IR spectral data can identify any contaminant phases that might have crystallized alongside the desired zeolite phase. Since the purity of the product is our primary concern, particular attention was focused on the double ring vibration bands (500–650 cm^{-1}), which indicated potential contaminant phases that may have co-crystallized with zeolite X. Furthermore, the comparison between the spectra of both products revealed an additional peak in the spectrum of zeolite prepared from raw fly ash (Zeolite X-RCFA) at a wavelength of 660 cm^{-1}. This additional peak was attributed to one of the pollutant phases (such as Zeolite A and P) co-crystallizing with the desired phase during growth. Conversely, the absence of contaminant phase bands in the zeolite X-TCFA spectra confirmed the successful synthesis of high-purity, single-phase Zeolite X using TCFA. The disappearance of the peak around 1500 cm^{-1} for ZX-TCFA was likely attributed to the removal of impurities during the pretreatment process. Previous studies have indicated that the formation of bands near 1500 cm^{-1} in zeolitization products was due to the presence of -C=O and/or C-H bonds in carbonates. These bonds are associated with impurities within the synthesized zeolites (Yadav et al. 2021). Therefore, the absence of this peak in ZX-TCFA suggested that the pretreatment effectively removed these carbonate-related impurities, leading to a purer zeolite product.

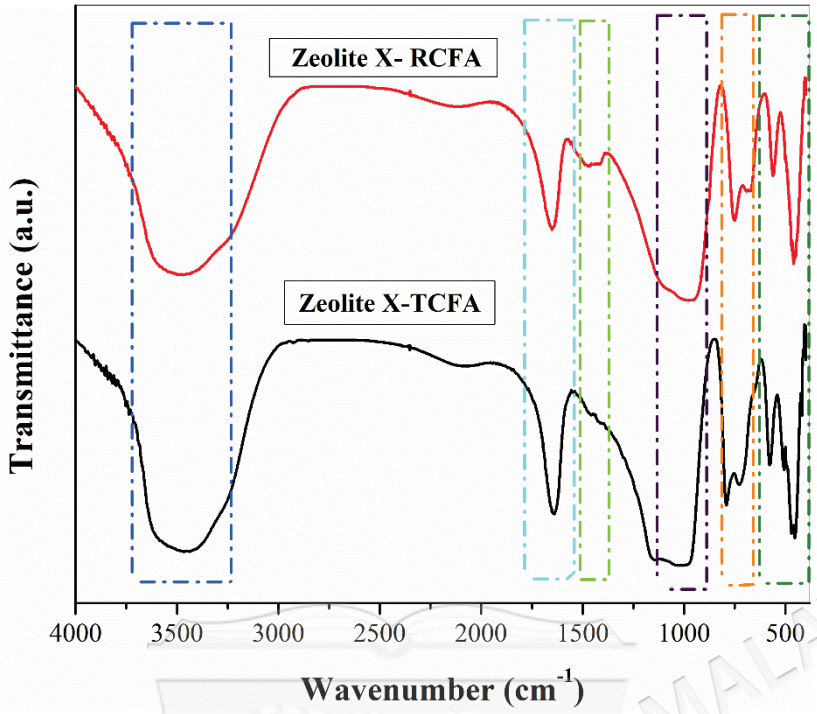

Figure 3.8 FT-IR spectra of synthetic zeolite X-RCFA and zeolite X-TCFA

3.4.3 Physical properties (pH, conductivity, humidity, loss of ignition (LOI) and thermal stability) of RCFA, zeolite X-RCFA and zeolite X-TCFA

The pH of the three samples falls within the alkaline range (as shown in Table 3.2). The alkalinity of fly ash can be attributed to the interaction of mineral cations, such as calcium, potassium, and others, with anions like hydroxide and carbonates. In contrast, the prepared zeolite exhibited a higher alkaline pH than the fly ash, primarily because of the presence of hydroxyl groups substituted onto the active sites within the zeolite structure due to the hydrothermal treatment with NaOH during the synthesis process (Seki et al. 2019). Regarding conductivity, it was worth noting that fly ash exhibited low conductivity despite its high content of positive ions, attributed to unburned carbon particles, considered non-conductive material. Conversely, the conductivity of zeolite derived from treated ash was lower than that of its counterpart derived from raw ash. This phenomenon was primarily attributed to the high purity and crystallinity of the former zeolite, in consistency with the results of the XRF analysis (Shi et al. 2021a). The loss of ignition in CFA was typically caused by unburned carbon and unstable mineral phases at high temperatures (Liu et al. 2021a). According to the humidity analysis, the RCFA contained 2.8% moisture, which can be attributed to the presence of unburned carbon (as indicated by the LOI analysis, which showed a 1% unburned carbon content) that readily absorbed water from the atmosphere. On the other hand,

the synthesized zeolites, with their large surface area and porous structure, exhibited weight loss due to the loss of water molecules adsorbed on the surface in the cavities of their crystals (Wang et al. 2022).

Table 3.2 Physical properties of RCFA, zeolite X- RCFA and zeolite X-TCFA

Material	Physical properties			
	pH	Conductivity (µS)	Loss of ignition (%)	Humidity
RCFA	7.8	548.0	1.00	2.88
Zeolite X-RCFA	9.3	974	25	-
Zeolite X-TCFA	9.0	712	20	-

The CFA-derived zeolite may find applications involving high temperatures or heat treatment during regeneration. Therefore, it was essential to determine the thermal stability of the products. Furthermore, the main objective of this study is to determine the quality of zeolite derived from CFA. Previous studies indicated that the critical factor in the process of preparing was the degree of crystallinity and the percentage of conversion of CFA into zeolite (ratio of reactants to products) (Tauanov et al. 2020).

Figure 3.9 displays the TGA analysis of the synthesized zeolites. The results indicated that zeolite X-RCFA and X-TCFA lost approximately 25% and 20% of their weight as the temperature increased from 40°C to 200°C. This weight loss was attributed to releasing free and physically bound water from the zeolite pores (He et al. 2020). Notably, zeolite X-TCFA exhibited a 5% lower weight loss than zeolite X-RCFA, likely because zeolite X-TCFA possessed a larger external surface area and a more favorable mesoporosity distribution. (Musyoka et al. 2015). Additionally, the significant weight loss observed in zeolite X-RCFA could be attributed to a high concentration of cationic species, such as Ca^{2+} and Mg^{2+}, instead of Na^{+} within the zeolite framework, potentially leading to a pore-filling effect (Majchrzak-Kucęba 2013).

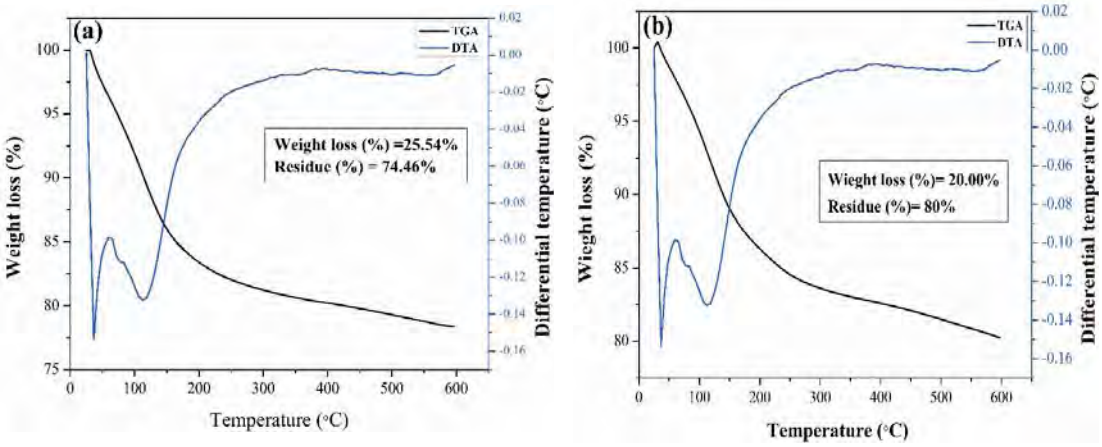

Figure 3.9 TGA and DTG curves of (a) zeolite X-RCFA and (b) zeolite X-TCFA at heating rate of 10°C/min in oxygen

3.5 ADSORPTION STUDIES

As-synthesized X zeolites, as well as fly ash samples were utilized for the adsorption of Ni and V ions to determine the adsorption capacity of those materials. Figure 3.10 shows the superior adsorption capacities of zeolites X towards heavy metals compared to fly ash samples and, simultaneously, the treated samples compared to untreated ones. The adsorption capacities and removal rates of targeted metals varied due to differences in the SiO_2/Al_2O_3 ratio in the synthesized zeolites, as well as differences in the purity (Sivalingam & Sen 2018b). Conversely, the data depicted a notable enhancement in the efficacy of ion removal facilitated by the synthesized zeolite compared to the precursor material, fly ash. This improvement was ascribed to disparities in the structural composition and surface area between the two materials.

Since zeolite X-TCFA showed better purity with pyramidal octahedral structure, high surface area, and lower Si/Al ratio hence, the removal of metal ions Ni^{2+} and V^{5+} was carried out using zeolite X-TCFA.

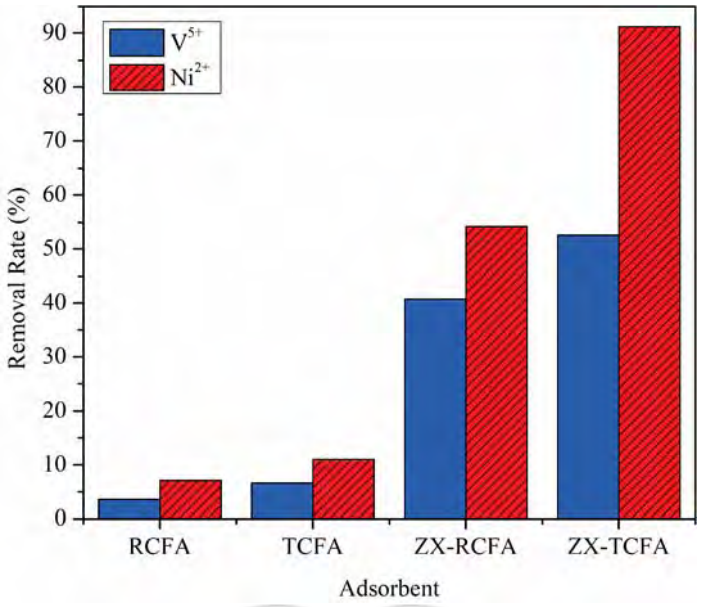

Figure 3.10 The impact of treatment processes on the removal efficiency of nickel and vanadium ions utilizing fly ash samples and synthesized zeolites

3.5.1 Impact of initial concentration

An essential factor in removing heavy metals using zeolite is the initial concentration of ions in their aqueous solutions. The initial concentration significantly influenced the removal rate and adsorption capability of Ni^{2+} and V^{5+}, as illustrated in Figure 3.11a, b, respectively. It was observed that the rate of Ni^{2+} ion removal steadily decreased as the initial concentration of Ni^{2+} ions increased. When the initial concentration ranged from 50 to 100 mg/L, the removal rate exceeded 95%. However, when the concentration was increased to 200 mg/L, the removal rate dropped to 83%. This decrease in removal rate indicated that as the concentration of Ni^{2+} ions increased, the rate at which the adsorption sites on the zeolite surface are utilized also increased, thereby reducing its capacity for adsorbing Ni^{2+} ions (Han et al. 2019). Similarly, as the concentration increased, the rate of V^{5+} ion removal decreased. At lower concentrations (10–50 ppm), zeolite X-TCFA removed approximately 50% of the vanadium ions, but this figure dropped to 15% at higher concentrations. The decline in the removal rate can be attributed to the increased presence of V^{5+} ions in the solution, limiting ion transfer on the zeolite surface due to a lack of accessible adsorption sites (Gan et al. 2020).

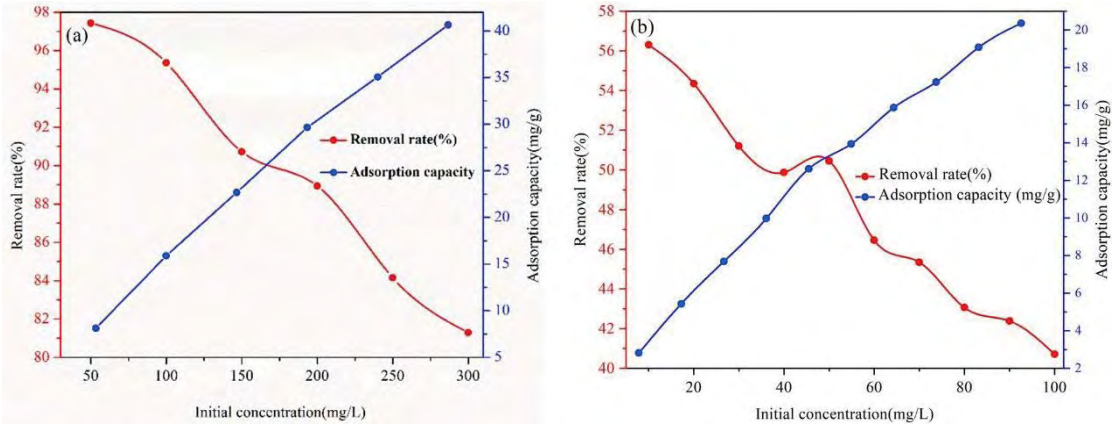

Figure 3.11 Effect of initial concentration of metal ions (a) nickel and (b)vanadium

3.5.2 Impact of contact time

The removal rate of Ni^{2+} and V^{5+}, as well as the adsorption capacity, are shown to change over time in Figure 3.12a and b, respectively. The findings are depicted in Figure 3.12a, indicated that the adsorption of Ni^{2+} by zeolite X-TCFA is a dynamic process that progressed through several stages before arriving at an equilibrium state. In the first hour, there was a rapid increase in the rate of removal of Ni^{2+} as well as in the capacity of adsorption. However, the growth rate slowed down from 60 to 180 min, eventually reaching equilibrium at 180 min. The adsorption of V^{5+} on zeolite X-TCFA also showed a similar trend to the adsorption of Ni^{2+}. The concentration of V^{5+} decreased rapidly within the first 60 min and reached a maximum at 210 min. Afterward, the adsorption stabilized at 240 min (Figure 3.12b). Based on the results, the attachment of Ni^{2+} and V^{5+} ions to zeolite X-TCFA occurred in two stages: a fast stage and a slow stage. During the fast stage (the first 60 min), the rate of removal and the capacity to absorb Ni^{2+} and V^{5+} ions increased rapidly. This rapid increase was attributed primarily to the abundance of vacant active sites on the surface of zeolite and the high concentration of Ni^{2+} and V^{5+} ions in the solution (He et al. 2020). As the adsorption process progressed, the concentration of Ni^{2+} and V^{5+} ions in the solution decreased, and the active sites on the surface of zeolite X-TCFA became occupied. Consequently, it became more challenging for ions to migrate from the solution to the surface of the zeolite X-TCFA. With increasing contact time, the adsorption rate gradually diminished until it reached equilibrium (Murukutti & Jena 2022). In subsequent experiments, the optimal adsorption times for Ni^{2+} and V^{5+} were determined to be 180 min and 240 min, respectively.

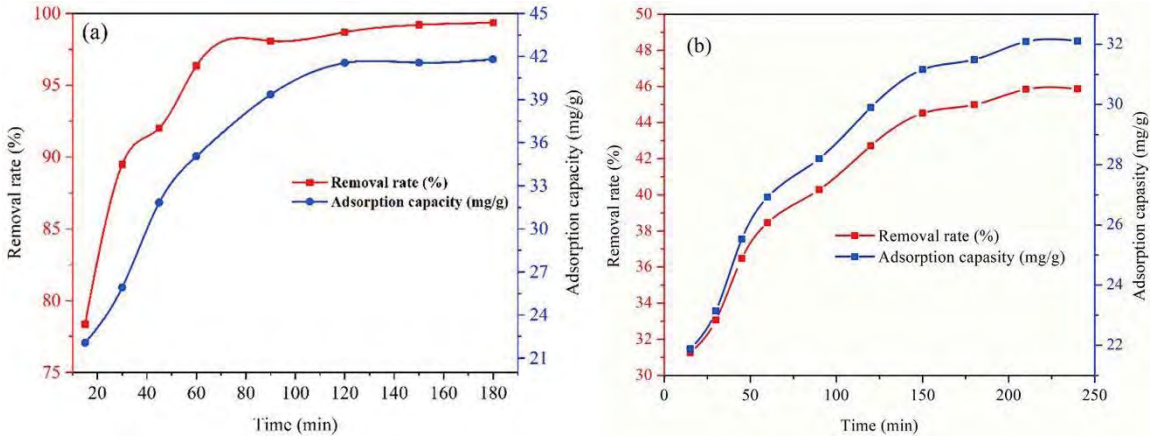

Figure 3.12 Effect of contact time (a) nickel and (b) vanadium

3.5.3 Impact the zeolite X-TCFA dosage

The rate of removal and adsorption capacity of Ni^{2+} and V^{5+} varied with the amount of zeolite added, as depicted in Figure 3.13a and b. According to the adsorption curve, as the zeolite dose increased from 1 g/L to 6 g/L, there was an increase in the rate of Ni^{2+} removal while the adsorption capacity declined. This trend can be attributed to the growing number of active sites resulting from the increased amount of zeolite, leading to a rapid increase in Ni^{2+} removal (Aljerf 2018), albeit at the expense of the overall adsorption capacity. At a dose of 10 g/L, the removal rate stabilized at 99.3%. Simultaneously, the adsorption capacity was limited to 9.93 mg/g due to the overcrowding of zeolite particles and the overlapping of adsorption sites. The impact of zeolite X-TCFA dosage on the removal of V^{5+} ions were also assessed using a solution concentration of 50 mg/L, with varying zeolite amounts ranging from 1 to 10 g/L. The results indicated that the removal efficiency of V^{5+} ions by zeolite X-TCFA increased with an increasing zeolite dose, reaching up to 60% at 6 g/L. Beyond this point, the adsorption efficiency slightly decreased but remained stable with further increases in zeolite X-TCFA dosage, as depicted in Figure 3.13b. To optimize the utilization of zeolite while ensuring the effective removal of Ni^{2+} and V^{5+}, the amount used in the following experiments is 6 g/L.

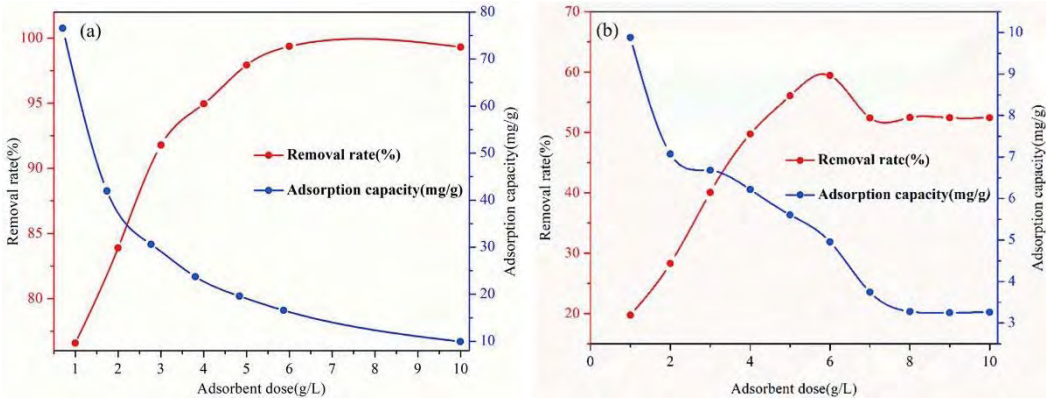

Figure 3.13 Effect of adsorbent dose (a) Nickel and (b) Vanadium

3.5.4 Impact of pH solution

The pH level of the solution can have a significant impact on the adsorption experiments, highlighting its importance as an essential factor to consider (Zhu et al. 2018). The pH influenced the valence and concentration of heavy metal ions in aqueous solutions, as well as the surface chemistry of adsorbents (Wang et al. 2018). Figure 3.14a and b depict the impact of solution pH on the adsorption capacity and removal rate of Ni^{2+} and V^{5+} ions. Increasing the pH of the Ni ions solution from 2 to 7 resulted in a significant increase in both adsorption capacity (from 3.22 to 31.8 mg/g) and removal rate (from 9.67% to 95.39%). A high concentration of H^{+} ions (low pH) competed with Ni ions for adsorption on the active sites of the adsorbent surface, making it more challenging for Ni^{2+} to adsorb (He et al. 2020). Conversely, OH^{-} ions can react with Ni^{2+} at higher pH levels to form $Ni(OH)_2$ precipitates. From the above information, it was evident that the removal rate of Ni ions exceeded 98% at pH 12, primarily due to the deposition of nickel hydroxide. To get an accurate description of how well synthetic zeolite can remove Ni^{2+}, the effects of competitive adsorption and precipitation must be kept to a minimum (Iqbal et al. 2019). The pH of the solution significantly influenced the adsorption process of V^{5+} by zeolite X-TCFA. It was observed that V^{5+} ions had a higher adsorption rate at low pH levels, specifically between 2 and 4. As the pH increased to 5.0, both the capacity and removal rate of V^{5+} decreased sharply. There was only a slight fluctuation in the adsorption process at alkaline pH levels. It is well-known that pH influences the protonation or deprotonation of surface functional groups, consequently affecting the surface charge of hydrated heavy metals (Cao et al. 2017). In a solution with a pH range of 4.0–10.0, the dominant

form of V ions is VO^{3-}. VO^{3-} form is an electroneutral complex within the solution, facilitating the migration of anions to the surface of zeolite X and their exchange with surface hydroxyl groups (Tseng et al. 2023).

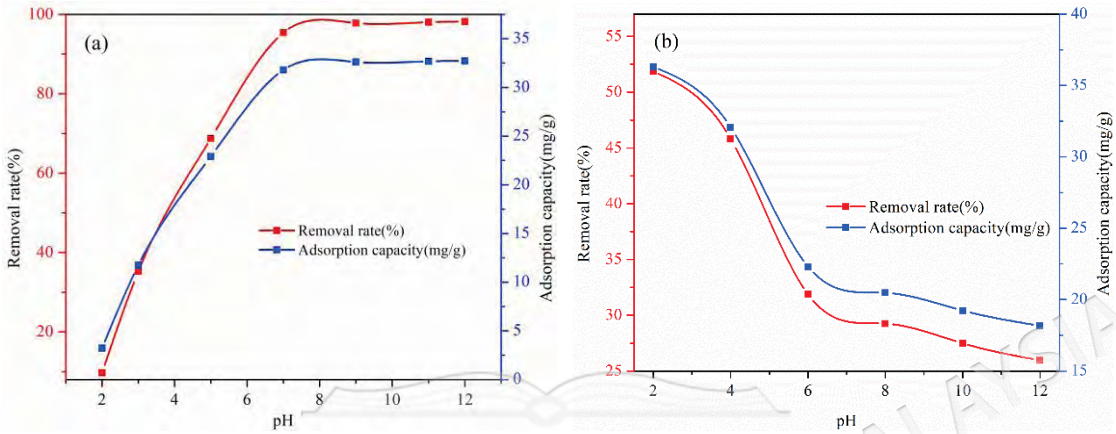

Figure 3.14 Effect of pH solution (a) nickel and (b) vanadium

3.5.5 Impact of competitive ions

From a mixture of metals containing four different cations (Ni^{2+}, V^{5+}, Co^{2+}, and Pb^{2+}), the efficiency of zeolites in selectively removing the targeted metals was investigated. The results demonstrated that zeolite X effectively absorbs all metal cations, as depicted in Figure 3.15. Furthermore, the capacity of the synthesized zeolite to remove nickel and vanadium from the mixture decreased compared to the individual solution. This decline was attributed to the competition for binding to the active sites on the surface of the zeolite by cations present in the solution. The initial concentration of ions in the solution noticeably impacted the efficacy of ion removal using zeolite X. The initial concentration of ions was inversely proportional to the removal rate. This effect can be attributed to the reduced availability of active sites on the surface of zeolite X relative to the growing number of free cations in the solution.

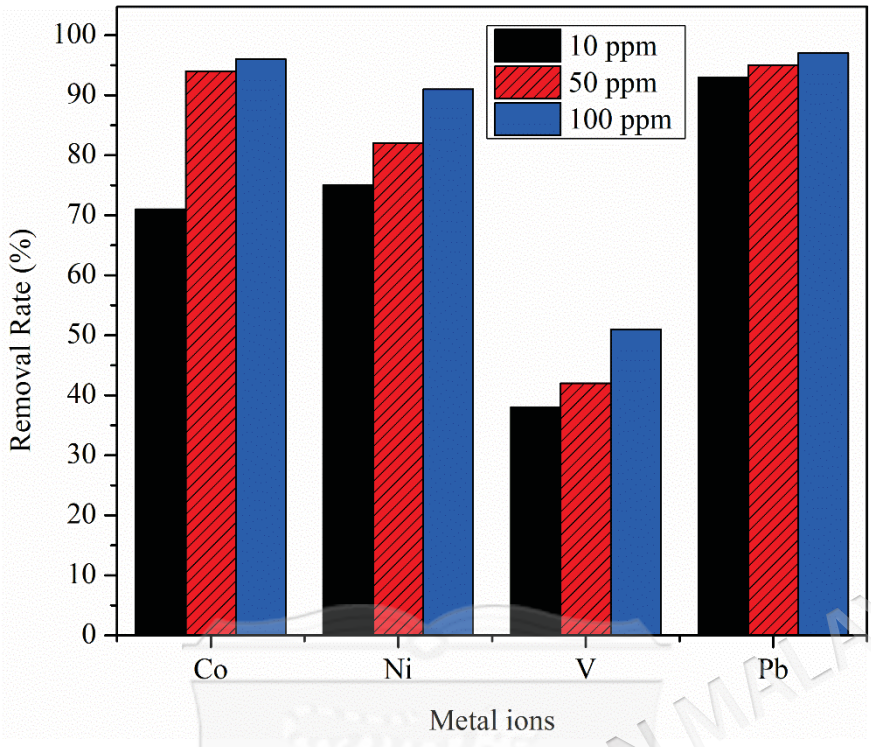

Figure 3.15 Selectivity of synthetic zeolite X for removal of Ni^{2+} and V^{5+} ions from the mixture at different concentrations

3.6 ADSORPTION KINETICS

Based on the results of the existing adsorption experiments, the kinetics of ion adsorption by zeolite were studied using the pseudo-first-order kinetic model and the pseudo-second-order kinetic model, respectively. The pseudo-first order, Lagergren equation (He et al. 2020):

$$\ln(q_e - q_t) = \ln q_e - k_1 t \tag{3.4}$$

Where K_1 is the Lagergren constant (min^{-1}), q_t and q_e are the amount of adsorbed cations (mg/g) by the adsorbent at equilibrium and at time t (min). The pseudo-second order kinetic equation, developed by Ho and McKay (Wang et al. 2024a), as shown in the equation (3.5):

$$\frac{t}{q_t} = \frac{1}{k_2 q_e^2} + \frac{t}{q_e} \tag{3.5}$$

where k_2 is the equilibrium rate constant for the pseudo-second order adsorption (g/mg min) and can be evaluated from the slope of the plot. This model assumes that the rate-limiting step may involve chemical adsorption, where valence forces play a role through the sharing or exchange of electrons between the adsorbent and the adsorbate (Visa 2016). The fitting curves and equation parameters of the pseudo-first and pseudo-second order dynamics equations are shown in Figure 3.16 and Table 3.3

Based on the R^2 value, the pseudo-second-order kinetic model described the data slightly better than the first-order model, implying that chemical adsorption involving valence forces was the rate-controlling step of adsorbate-adsorbent interactions. This phenomenon occurred through the transfer, exchange, or sharing of electrons between the targeted V and Ni ions and the binding sites of the zeolite. Table 3.3 reveals that the correlation coefficient for the pseudo-first-order dynamics model was lower compared to the pseudo-second-order dynamics model.

Table 3.3 Pseudo-first and pseudo-second order kinetic model parameters

Metals	**Pseudo first order kinetic model**			**Pseudo second-order kinetic model**			$q_{e\ exp.}$
	q_e(mg/g)	K_1/(min^{-1})	R^2	q_e(mg/g)	K_2 (g/mg.min)	R^2	
Ni^{2+}	23.768	0.672	0.929	41.320	0.821	0.999	41.55
V^{5+}	24.241	0.724	0.834	32.148	0.865	0.998	32.38

Moreover, the pseudo-second-order dynamics model yielded a correlation coefficient close to 1 for both Ni and V ions. Notably, the q_e values predicted by the pseudo-first-order kinetic model significantly deviate from the experimental q_e values. Conversely, the q_e values predicted by the pseudo-second-order adsorption model exhibited greater consistency with the experimental q_e values (Hu et al. 2022). Therefore, the pseudo-second-order adsorption model was better suited for describing the adsorption processes of Ni^{2+} and V^{5+} onto synthesized zeolite in this study.

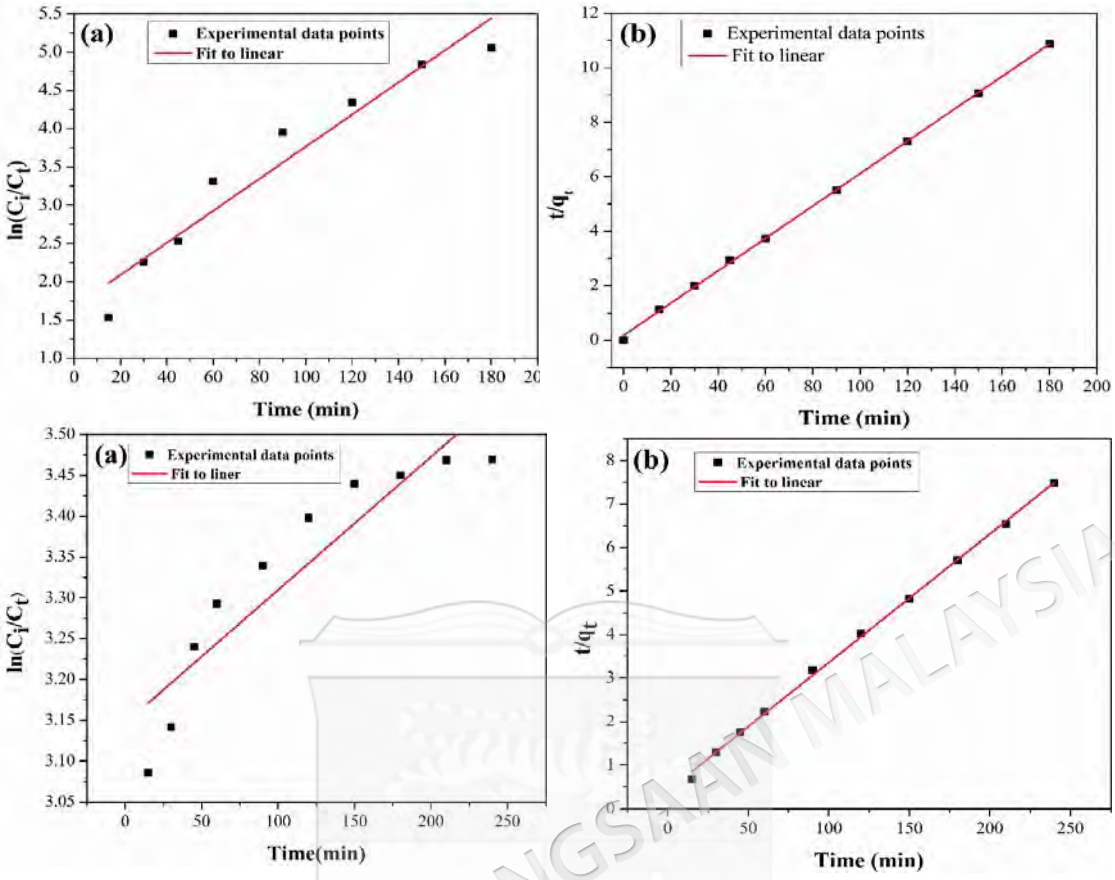

Figure 3.16 (a) pseudo-first-order and (b) pseudo-second-order curves of adsorption kinetics with Ni^{2+} (upper) and V^{+5}(Lower) uptake over synthetic zeolite X-TCFA with different initial concentration.

3.7 ADSORPTION ISOTHERM

Adsorption isotherms were often used to study the interaction between molecules of the adsorbate and active sites on the surface of the adsorbent. The Langmuir and Freundlich (Bai et al. 2022) adsorption isotherm models were employed to analyze the experimental results in this study. The Langmuir equation was written in a form that was easy to understand:

$$\frac{C_e}{q_e} = \frac{1}{q_{max}K_L} + \frac{C_e}{q_{max}} \tag{3.6}$$

K_L(L/mg) represents the Langmuir adsorption constant, q_{max} (mg/g) signifies the theoretical monolayer adsorption capacity of the adsorbent, C_e (mg/L) represents the equilibrium concentration of heavy metal ions in the solutions, and q_e (mg/g) indicates

the number of heavy metal ions assimilated by the adsorbent's surface. The linear form of the Freundlich equation was represented by:

$$\ln q_e = \ln K_F + \frac{1}{n_F} \ln C_e \quad (3.7)$$

K_F (mg/g) represents the Freundlich isotherm constant, while n denotes the Freundlich exponent, which characterizes the strength of the molecules adhering to each other (adsorbent and adsorbate). Figure 3.17 displays the fitted isotherms, and Table 3.4 presents the associated parameters and correlation coefficients. The equilibrium data for both metals demonstrated a better fit with the Langmuir model compared to the Freundlich model.

The Langmuir isotherm assumed a monolayer adsorption mechanism where all sites have uniform adsorption capacities, and no interactions occur between adsorbed molecules (Butyrskaya 2024). On the other hand, the Freundlich model is an empirical model used to describe non-uniform energy adsorption on non-uniform surfaces (Qiu et al. 2018). These experiments investigated the adsorption isotherms of Ni and V at room temperature on synthetic zeolite X-TCFA, with the results presented in Table 3.4.

Table 3.4 The parameters that fit the isothermal curve for Ni^{2+} and V^{5+} adsorption by zeolite X-TCFA.

Metals	**Langmuir**			**Freundlich**		
	K_L	q_{max}(mg/g)	R^2	K_F	n	R^2
Ni^{2+}	0.171	57.91	0.978	0.374	1.610	0.928
V^{5+}	0.216	42.22	0.997	0.016	0.988	0.937

A comparison of the correlation coefficients of both employed models revealed that the Langmuir model shows a higher correlation coefficient. These results indicated that it was better fitted for describing the adsorption isotherms of nickel and vanadium ions on the surface of the synthesized zeolite. Therefore, monolayer adsorption was the primary mechanism governing the adsorption of metal ions on the surface of synthetic zeolite X. This also implied that synthetic zeolite X possessed a uniform surface and constant particle mass. The Langmuir coefficient K_L value was within the range of 0 and 1, indicating that the adsorption of Ni^{2+} and V^{5+} on zeolite X was favorable. Zeolites

comprise silicon and aluminum oxides, and their hydroxylated surfaces acquire negative charges in an aqueous solution. The electrostatic attraction between these negatively charged adsorbent sites and the positively charged ions and cation exchange caused the metal ions to bind to the coal ash-derived zeolite X.

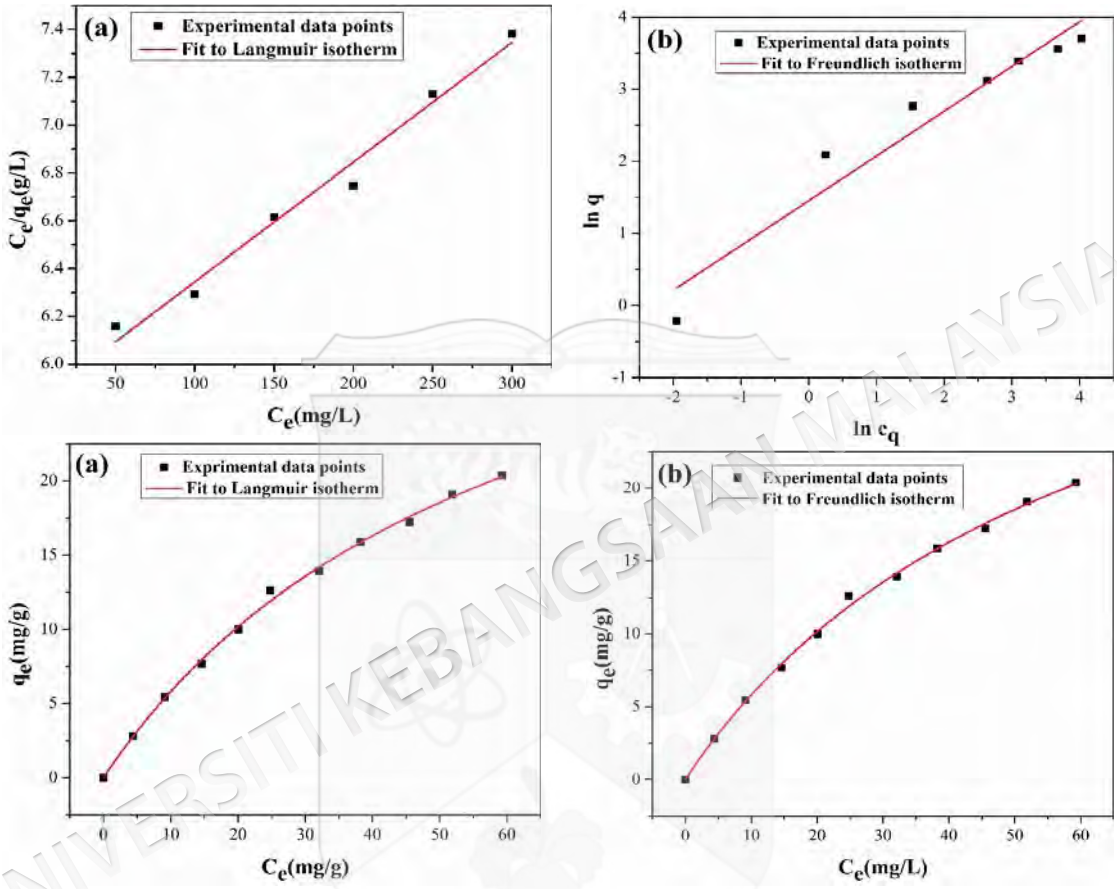

Figure 3.17 (a)Langmuir and (b)Freundlich isotherm model for Ni^{2+} (upper) V^{5+} (lower) adsorption on synthetic zeolite X-TCFA.

The parameter "n" value signifies the degree of heterogeneity in the Freundlich model equation, determining the extent of preference and intensity in the adsorption process. Adsorption was deemed favourable when the parameter value lay within the range of $0 < 1/n < 1$, indicating the heterogeneity of the adsorbent surface (Caetano et al. 2023b). Since $n_{Ni} = 1.610$ was greater than $n_V = 0.988$, it can be concluded that Ni molecules exhibited a higher adsorption intensity on the surface of zeolite X-TCFA compared to V molecules. Whereas the value of parameter K_F was related to the ability to form interactions between the adsorbent and the adsorbate as a result of the closeness of the adsorbent to the surface of the adsorbent and the particles of the adsorbate. As

K_F, Ni = 0.374 was greater than K_F, V = 0.016, it is possible to state that the affinity of Ni molecules is greater for the surface of zeolite X-TCFA in relation to V and, consequently, the adsorption capacity for the use of zeolite X-TCFA was greater for Ni than for V.

Table 3.5 summarizes the Ni^{2+} and V^{5+} uptake abilities of various adsorbents and previously reported zeolites. The adsorption capacity exhibited by the zeolite X synthesized in this experiment surpassed that of numerous natural and synthetic adsorbents. Compared with fly ash-derived zeolite mentioned in the previous literature, zeolite X prepared in this study showed a higher ability to remove nickel ions. Therefore, zeolite prepared from treated fly ash exhibited a commendable adsorption performance for heavy metals. Simultaneously, this synthesis process was environmentally friendly, as the precursors involved in the synthesis are harmful solid wastes that have been recycled to support and preserve the environment.

Table 3.5 Comparison of Ni^{2+} and V^{5+} uptake capacities of various adsorbents

Ni			V		
Adsorbent	**q_e (mg/g)**	**References**	**Adsorbent**	**q_e (mg/g)**	**References**
Iranian natural zeolite	3.4	(Merrikhpour & Jalali 2013)	Ferric groundwater treatment residual	15.62	(Zhang et al. 2019)
Synthesized β-Zeolite	7.92	(Liu et al. 2017)	Red mud modified saw dust biochar	16.60	(Ghanim et al. 2020)
Ukraine clinoptilolite	13.03	(Sprynskyy et al. 2006)	Humic acid	19.2	(Yu et al. 2018)
Zeolite X synthesized from coal fly	15.94	(Zhang et al. 2018)	D2EHPA impregnated resins (DIRs)	24.80	(Zheng et al. 2018)
Zeolite synthesized from red mud	41.15	(Xie et al. 2018)	D2EHPA and TBP impregnated resins (D-TIRs)	29.95	(Zheng et al. 2018)
Zeolite A synthesized from fly ash	47.0	(He et al. 2020)	Coated solvent impregnated resin (CSIR)	34.25	(Bao et al. 2018)
This study	41.55		This study	32.38	

3.8 THE PROPOSED MECHANISM OF NICKEL (II) AND VANADIUM (V) REMOVAL BY SYNTHETIC ZEOLITE X

Based on the X-ray photoelectron spectroscopy (XPS) analysis of zeolite X (ZX-TCFA) before and after the adsorption of nickel (Figure 3.18a) and vanadium (in an acidic medium (pH = 3)) (Figure 3.18b) and the deconvolution of the vanadium peak (Figure 3.18c), we can conclude the adsorption mechanism of ions on the zeolite surface. XPS provides crucial information about the surface composition, chemical states, and bonding environments, making it ideal for elucidating adsorption mechanisms (Medykowska et al. 2022).

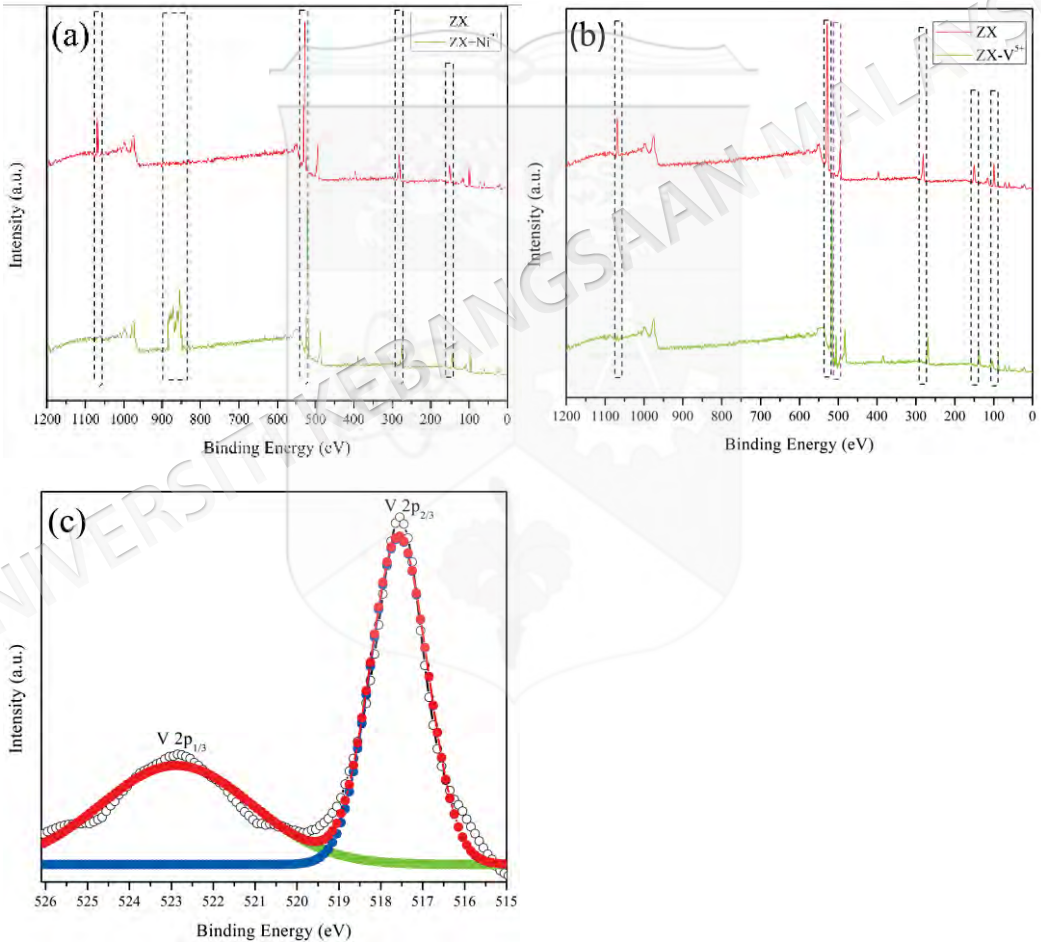

Figure 3.18 XPS survey scan of ZX-TCFA before and after adsorption of metal ions: (a) Ni^{2+}, (b) V^{5+}, and (c) high-resolution XPS spectra of the V 2p peaks after vanadium adsorption.

The XPS spectra for the Ni 2p and V 2p regions provided direct evidence for the adsorption of nickel (Ni^{2+}) and vanadium (V^{5+}) ions on the zeolite X surface. The

Ni 2p region (around 850–880 eV) showed no peaks before adsorption, confirming the absence of nickel on the zeolite surface. However, after adsorption, distinct peaks were observed at approximately 855–857 eV (Ni $2p_{3/2}$) and 872–875 eV (Ni $2p_{1/2}$), which were characteristic of (Ni^{2+}) species. Satellite peaks around 861–863 eV further confirmed the (2+) oxidation state, indicating successful adsorption of nickel onto the zeolite surface through possible electrostatic interactions and coordination with surface sites (Angaru et al. 2022).

Similarly, the V 2p region (around 515–525 eV) provided evidence for vanadium adsorption. The deconvolution of V 2p peaks revealed peaks at approximately 517.2 eV (V $2p_{3/2}$) and 524.5 eV (V $2p_{1/2}$), corresponding to (V^{5+}) species. These binding energies were characteristic of vanadium in the (V^{5+}) oxidation state, confirming that vanadium remained in its original oxidation state after adsorption. The appearance of these peaks indicated that vanadium was adsorbed on the zeolite surface, possibly through electrostatic attraction and coordination with surface oxygen sites, similar to the behavior observed for nickel (Medykowska et al. 2022).

The O 1s peak (530–533 eV) provided insights into the interactions between oxygen atoms on the zeolite surface and the adsorbed metal ions. Before adsorption, the O 1s peak for pure zeolite X was centered around 531 eV, representing oxygen in the framework (Si-O-Si, Al-O-Si) and surface hydroxyl groups (Si-OH, Al-OH). After the adsorption of (Ni^{2+}), a shift to a higher binding energy (around 532–533 eV) was observed. This shift suggested a change in the electronic environment of oxygen atoms, likely due to the formation of Ni-O bonds, indicative of surface complexation or chemisorption (Sellaoui et al. 2021).

Similarly, after (V^{5+}) adsorption, the O 1s peak also shifted to a slightly higher binding energy, indicating the formation of V-O bonds. This shift was consistent with the formation of inner-sphere complexes, where (V^{5+}) ions formed coordination bonds with surface oxygen atoms. The changes in the O 1s peak for both Ni and V adsorptions suggested that chemisorption played a significant role in the adsorption process, involving strong interactions between the metal ions and oxygen groups on the zeolite surface (Lv et al. 2022).

The Na 1s peak (around 1071 eV) provided evidence for the ion exchange mechanism during the adsorption of both (Ni^{2+}) and (V^{5+}). Before adsorption, the Na 1s peak was prominent, indicating the presence of exchangeable sodium ions (Na^{+}) in the zeolite framework. After adsorption of either (Ni^{2+}) or (V^{5+}), the intensity of the Na 1s peak significantly decreased. This reduction in intensity suggested that a substantial number of (Na^{+}) ions were replaced by (Ni^{2+}) or (VO^{2+}) species, confirming that ion exchange was a key mechanism for both metal adsorptions (Chen et al. 2020).

The similar behavior of Na 1s peak reduction for both metal ions indicated that the zeolite X matrix effectively facilitated ion exchange, replacing its exchangeable cations with the metal ions from solution. This was consistent with the high cation exchange capacity of zeolite X, which was crucial for the adsorption of divalent and multivalent metal ions (Sellaoui et al. 2021).

The Si 2p (100–105 eV) and Al 2p (74–76 eV) peaks provided information on the stability of the zeolite framework during the adsorption process. For both (Ni^{2+}) and (V^{5+}) adsorption, there were no significant changes in the binding energies or intensities of the Si 2p and Al 2p peaks. This stability suggested that the aluminosilicate framework of zeolite X remained intact, indicating that the adsorption of both metals occurred primarily on the surface or through exchangeable ions rather than by altering the framework itself (Liu et al. 2021b). This reinforced the conclusion that the adsorption processes involved surface interactions such as ion exchange and chemisorption without modifying the zeolite structure. Figure 3.19 illustrates the proposed removal mechanism.

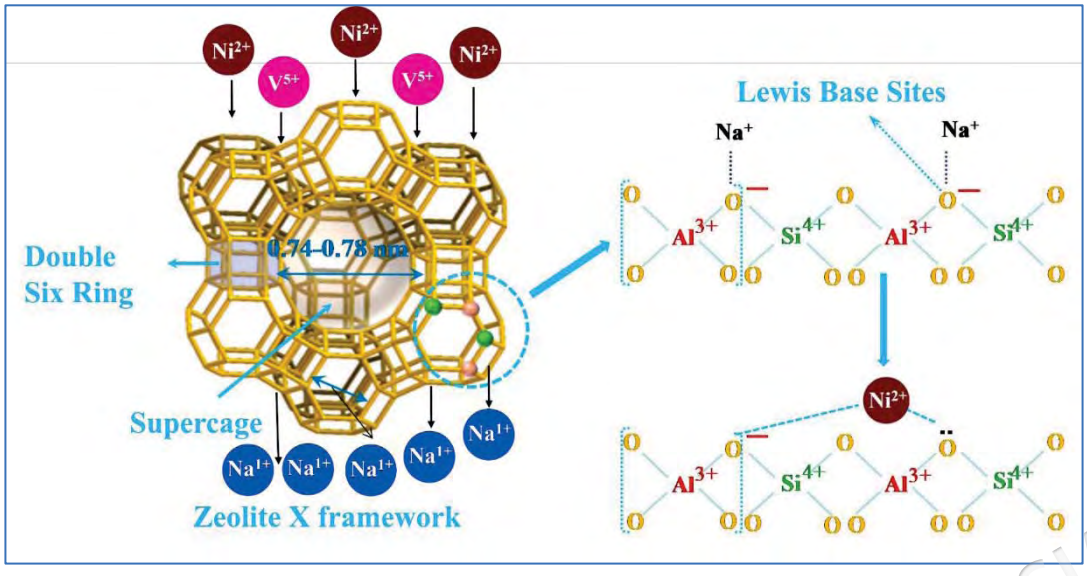

Figure 3.19 Mechanism of nickel and vanadium ion removal by zeolite X.

3.9 SUMMARY

In the present chapter, the synthesis of Zeolite X was studied by alkali-fusing the fly ash, followed by a hydrothermal treatment method using Malaysian coal fly ash as the precursor. The main objectives were to assess the impact of fly ash pretreatment process, study synthesis parameters, the properties of the resulting zeolite X, and the efficiency of TCFA-derived zeolite X for removing Ni^{2+} and V^{5+} under various parameters. Magnetic separation was employed to control the removal of magnetic components from RCFA. VSM results indicated that TCFA had a lower saturation magnetization value (approximately 1.51 emu/g) than RCFA. The acid-washing of RCFA significantly reduced undesirable metal oxides, as evidenced by XRF results indicating the content of polluted oxides below 12% in TCFA composition. XRD analysis revealed that under optimal preparation conditions (time = 12 h, temperature = 90°C, CFA/NaOH = 1:1.2 g/g, Solid: liquid = 1:5 g/mL), the utilization of TCFA led to the synthesis of high-purity, single-phase zeolite X, contrasting with the zeolite derived from RCFA. BET analysis showed that TCFA-derived zeolite X had a higher specific surface area (452 m^2/g) than RCFA-derived zeolite X (115 m^2/g). SEM images indicated that zeolite X-TCFA exhibited enhanced crystallinity and purity, with well-defined individual crystals and no intergrowth, unlike zeolite X-RCFA. In comparing FTIR spectra, it was evident that zeolite X-RCFA displayed an additional peak at 660 cm^{-1}, implying co-crystallization with a contaminant phase, whereas zeolite X-TCFA

exhibited successful synthesis devoid of contaminant phase bands. For Ni^{2+} and V^{5+} ion adsorption using TCFA-zeolite X, four key parameters (initial concentration, contact time, zeolite dosage, and pH) were examined for their impact on the removal process. Kinetics studies favored the pseudo-second-order kinetic model, implying that chemical adsorption governed the adsorbate-adsorbent interactions. Additionally, the Langmuir and Freundlich adsorption isotherm models were employed to analyze the experimental results, with the Langmuir model providing a superior fit due to its higher correlation coefficient. The integrated analysis of XPS data for Ni and V adsorption on ZX highlighted that both metals were adsorbed through a combination of ion exchange and surface complexation (chemisorption) mechanisms. Overall, this study highlights the potential of X-type zeolite synthesized from TCFA as an environmentally friendly, cost-effective solution for heavy metal removal.

CHAPTER IV

CHITOSAN/COAL FLY ASH- BASED ZEOLITE X COMPOSITES: A NOVEL APPROACH FOR ADSORPTIVE SEPARATION AND RECOVERY OF NICKEL AND VANADYL PORPHYRINS

4.1 INTRODUCTION

Petroleum-derived chemicals supply a significant portion of the world's energy demand. As conventional oil sources decline, the oil industry has turned to exploring heavy oils as a more cost-effective alternative, given their abundance and lower barrel prices (Elahi et al. 2019). However, converting unconventional crude oils (heavy and extra-heavy hydrocarbon) poses challenges due to their high content of resin, asphaltenes, halogenated hydrocarbon, and high concentrations of heavy metals (Adolfo et al. 2022). Crude oil contains various metal contaminants, with concentrations ranging from a few ppm to over a thousand ppm. The predominant metals in the studied crude oils are nickel (Ni) and vanadium (V). These metals primarily exist as porphyrin-like compounds, while the remaining are non-porphyrin compounds (Attia et al. 2020). Electric desalting is effective in removing most non-porphyrin metals from crude oil. However, nickel and vanadium are found in crude oils as oil-soluble organic metal compounds (Solouki et al. 2023), making them resistant to removal through this method. (Chacon-Patino et al. 2021). In spite of being present in trace amounts in oil, these compounds have the potential to significantly alter the physical-chemical properties of the oil (Silva et al. 2017). Additionally, they are known to accelerate the corrosion of pipes and equipment (Nguyen et al. 2022), deactivate catalysts (Attia et al. 2020), and compromise the quality and yield of refining products, ultimately contributing to environmental pollution (Sama et al. 2018). In light of the aforementioned drawbacks, it is indeed crucial to ensure the efficient removal of porphyrins. Conversely, porphyrin compounds find extensive applications in organic solar cells, molecular devices, and photodynamic therapy (Shi et al. 2021b).

Various methods are available for treating crude oil to effectively eliminate impurities, especially nickel (Ni) and vanadium (V) impurities. These methods involve a combination of traditional physical, chemical, and biological approaches such as hydrodemetallization and solvent extraction (Ali & Abbas 2006). However, these techniques often require significant investments in equipment, especially for hydrogenation-based removal of nickel and vanadium. Additionally, the catalysts used in these processes are challenging to regenerate, leading to difficulties in waste catalyst disposal. Solvent extraction is viable primarily for residues with a high bitumen content, but it comes with high investment costs and operational expenses (Sadeghi et al. 2021). Therefore, the utilization of non-destructive isolation methods is more advantageous compared to chemical treatment approaches (Silva et al. 2019).

Adsorptive demetallization (ADM) is considered one of the most promising methods for demetallization due to several reasons, such as its requirement for mild operating conditions, its ability to achieve a significant demetallization effect, and its high selectivity towards organometallic compounds. In the ADM process, specialized adsorbents efficiently remove metal compounds through selective adsorption. As a result, adsorbents are vital in determining the selectivity, capacity, and sustainability of the process. Examples of studied adsorbents include chitosan and its derivatives (Wang et al. 2011a), activated carbon (Caetano et al. 2023b), graphene (Chen et al. 2018) and zeolite (Rocha Aguilera et al. 2016).

Zeolites are a type of crystalline and microporous aluminosilicates that contain tetrahedral units of SiO^{4-} and AlO^{4-}. The Si or Al atoms are located centrally, while the O atoms are situated in the corners, forming pores and channels. These structures have a net negative charge, which is balanced by additional cations, such as Na^{+}, K^{+}, Ca^{2+}, and Mg^{2+} that are located in the voids (Król 2020). Zeolites possess a stable framework structure, and their weak intermolecular bonds allow for the removal of ions and molecules from their pores without damaging the structure. There are three types of zeolites based on their Si/Al molar ratio: low silica zeolites (Si/Al < 2), intermediate silica zeolites (2 < Si/Al < 5), and high silica zeolites (Si/Al > 5) (Hu et al. 2021). The zeolite X (ZX) is one of the well-established zeolites with a large surface area (200-900 $m^2.g^{-1}$), spacious channels and cages, and large openings. As a result, this type of zeolite

possesses a high adsorption capacity and efficient cationic exchange properties. In real life, instead of excellent mechanical and chemical features adsorbent, the adsorbent should be cheap and sustainable. Indeed, cheap ZX (rich Si and Al species) can be synthesized from waste like coal fly ash (Kunecki et al. 2023). Incorporating zeolite and biopolymers in hybrid or composite materials is a potential approach to enhance zeolite properties. This method aims to optimize the zeolite's capacity to retain organic molecules while maintaining environmental friendliness, high adsorption capacity, chemical stability, and biodegradability (Jawad et al. 2020; Mostafa et al. 2021).

Chitosan (CHS) is a type of biopolymer that is positively charged and made up of D-glucosamine units. It is formed by removing acetyl groups from chitin, a substance found in the shells of crustaceans and insects. CHS has many useful chemical and biological properties, including biocompatibility, high reactivity, safety, biodegradability, hydrophilicity, adsorption capacity, chelation, chirality, and antimicrobial activity (Pal et al. 2021). Due to the presence of hydroxyl (-OH) and amino (-NH_2) groups on its chain, CHS can be used to remove various water pollutants, such as pharmaceuticals, dyes, and metal ions (Karimi-Maleh et al. 2021). Moreover, there is a growing interest in CHS research within the petroleum industry. The applications showcase the versatility of the utilization of CHS across various stages of the petroleum industry, ranging from exploration, extraction, refining, transportation, and environmental remediation. This underscores its potential as a sustainable alternative, underscoring the importance of ongoing research in this field (Negi et al. 2021). However, CHS-based adsorbents are often sensitive to pH, mechanically unstable, and prone to swelling (Begum et al. 2021).

This biocompatible mesoporous material, CHS/ZX, possesses narrow pore size distributions and high surface areas, making it well-suited for various applications due to its low toxicity and biocompatibility. In response to increasing environmental concerns, industries are turning to bio-based and bio-compatible materials, with the CHS/ZX composite emerging as an attractive option, offering natural, cost-effective material with controlled properties. The CHS/ZX structure can be changed, which includes the zeolite pore diameter and the presence of nearby ions. This makes it more useful for biomedical uses, adsorption, and catalysis. The effectiveness of these

composites is closely linked to both surface chemistry and porosity (Mahmodi et al. 2020).

The potential of the CHS/ZX composite derived from coal fly ash as a demetallization agent for removing metal porphyrins has not yet been investigated. It is anticipated that this composite will demonstrate improved removal capacity, regulated recovery behavior, and efficient regeneration. Therefore, the objectives of this chapter are:

1. To identify the optimal synthesis parameters for a chitosan-modified zeolite X composite using Response Surface Methodology (RSM) to achieve maximum adsorption efficiency.

2. To evaluate the CHS/ZX composite's effectiveness in extracting vanadyl and nickel porphyrins from model solutions in toluene and to explore the removal mechanism.

3. To optimize the recovery process of metal porphyrins from the saturated composite under various operational conditions.

This chapter provides an in-depth analysis of the removal and recovery properties of the CHS/ZX composite. A comparative study was performed with its individual components, considering different parameters and examining the related mechanisms, including kinetic, equilibrium, and thermodynamic behaviors.

4.2 EXPERIMENTAL

4.2.1 Chemicals

Medium molecular weight CHS with the degree of deacetylation of 75–85% is purchased from R&M in Malaysia. Tetraphenyl-21H,23H-porphyrin vanadium (IV) oxide (VO-TPP) and nickel-5,10,15,20-tetraphenyl porphyrin (Ni-TPP) were supplied by Sigma Aldrich. The molecular structure of vanadyl and nickel porphyrins is depicted Figure 4.1 (VO-TPP:$C_{44}H_{28}N_4VO$, 679.66, purity > 99%, Figure 4.1(a); Ni-TPP:$C_{44}H_{28}N_4Ni$, 671.41, purity > 99%, Figure 4.1(b)). The solvents used were of analytical grade: toluene (99.9%) and chloroform (99.9%) from Sigma Aldrich, ethanol

(95%) from Acros organics, methanol (99.9%) from HmbG, acetic acid from (R&M) and N,N-Dimethylformamide (DMF) (99.8%) from Sigma Aldrich.

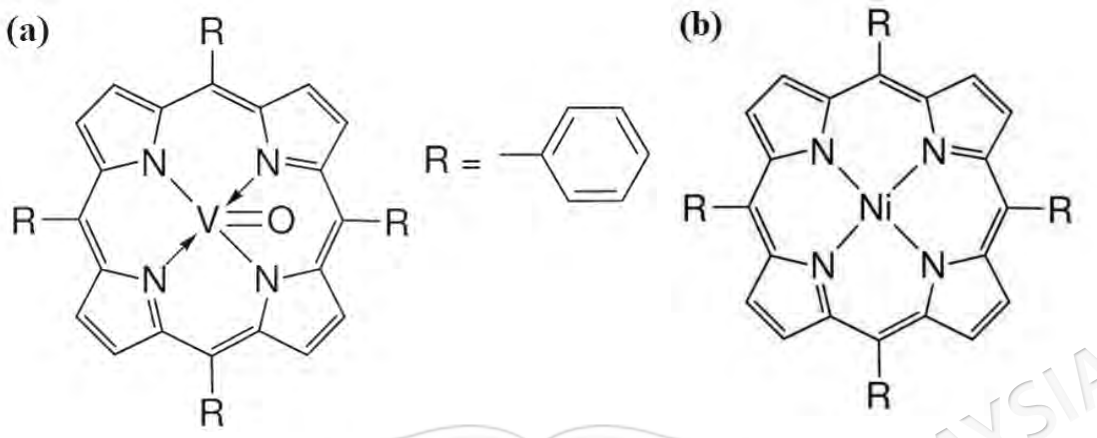

Figure 4.1 Molecular structure of: (a) Vanadyl-TPP; (b) Nickel-TPP.

4.2.2 Preparation of the CHS/ZX composites

Initially, chitosan (CHS) was dissolved in 200 mL (2% v/v) acetic acid in a 500 mL beaker at room temperature with stirring for 3 h. The pH of the CHS solution was gradually raised from around 3.4 to 5.0 by carefully adding 1 M NaOH aqueous solution drop by drop. Then, a water dispersion of ZX (produced in Section 3.2.3) was introduced into the CHS solution, creating a well-mixed CHS/ZX combination. The amounts of CHS and ZX utilized were determined based on the CCD experiment design. The suspension was stirred vigorously for 2 h until a uniform mixture was achieved. Subsequently, the suspension was slowly added to a precipitation bath containing 500 mL (0.50 M) NaOH. Agitation at 100 rpm was maintained for 3 h. Following this, the resulting beads were filtered and rinsed with deionized water to eliminate any remaining NaOH. Finally, the beads were air-dried at 90°C and then ground to the desired size.

4.2.3 Point of zero charge of CHS/ZX composite

The salt addition method was employed to ascertain the point of zero charge (PZC) of the CHS/ZX composite, as outlined by (Ayub et al. 2020). In this method, 25 mL of 0.1 M NaCl solution was distributed into ten different Erlenmeyer flasks. The pH of the CHS/ZX suspensions was adjusted to values ranging from 3 to 12 using either 0.1 M

hydrochloric acid or 0.1 M sodium hydroxide, with measurements taken using a pH meter. 0.1 g of the composite was added to each flask, and the mixture was agitated at 200 rpm on a magnetic stirrer at room temperature for 24 h. Following equilibrium, we filtered the contents and recorded the pH of the filtrates. The PZC, the pH at which the total surface charge of the biosorbent is neutralized, was determined by plotting the initial pH against the change in pH.

4.2.4 Instruments and material characterization

The SHIMADZU 1800-PC ultraviolet-visible (UV-Vis) spectrophotometer was used to determine the concentration of the metal porphyrin solution in the toluene. Field emission scanning electron microscopy (FESEM), using LEO-1455 VP electron microscope, was used to estimate the surface morphology of CHS and CHS/ZX. The elemental composition of (C/H/N) was determined by Flash EA1112 (organic trace element analyzer). A Perkin Elmer (PC) spectrum 100 Fourier transform infrared spectroscopy (FT-IR) with a resolution of 4 cm^{-1} and a range of 300–4000 cm^{-1} was used to figure out the chemical functional group of CHS, ZX, and CHS/ZX composite. On the Thermo–Finnigan Shopmatic 1990 series N_2 sorption analyzer, the Brunauer–Emmett–Teller (BET) and Barrett–Joyner–Halenda (BJH) methods were used to measure the specific surface area and pore distribution. All the samples were degassed for 12 h at 150°C to get rid of any dirt or moisture that was on the surface. In a vacuum chamber at -196°C, the surface assimilation and desorption of N_2 were looked at. Thermogravimetric analysis (TGA) was used to determine the stability of CHS, ZX and CHS/ZX using TGA 1000i, Instrument Specialists Inc, USA. Powder X-ray diffraction (XRD) was used to investigate the crystallography and structural properties of CHS, ZX, and CHS/ZX composite. For the XRD analysis, model XRD-6000 Shimadzu diffractometer was engaged. The diffractometer had a scan speed of 4°C min^{-1} A^2 range of 5° to 40° was used. The X-ray photoelectron spectroscopy (XPS) test was conducted using an Axis Ultra DLD instrument equipped with an Al KαX-ray source.

4.2.5 Experiments design

The primary objective of experimental design is to optimize the impact of the factors and their interactions in a process. This approach aims to enhance parameter

performance and reduce experimental inaccuracies (Bezerra et al. 2008). By identifying the most critical variables through a limited number of experiments, it facilitates a more efficient selection process. To investigate the effects of variables, we employed a well-established response surface methodology known as central composite design (CCD). Furthermore, a regression analysis was conducted to fit the equations, and the significance of the effects of parameters, including chitosan dose (A) and zeolite dose (B), was examined for each metal porphyrin compound. Design Expert 7.0 software (Stat Soft Inc., Tulsa, USA) was utilized for this analysis. The levels of independent variables are provided in Table 4.1. Central composite design (CCD) was employed to evaluate the removal percentage. This approach led to 13 trials utilized for optimizing the removal of vanadyl and nickel porphyrins. To mitigate the influence of uncontrolled factors, the experimental sequence was executed randomly. Table 4.2 presents the experimental design points, encompassing 2n factorial points, 2n axial points, nc central points (with five replicates), along with the outcomes for the response variables. Here, n represents the count of numeric factors. The determination of experimental error and data reproducibility was conducted using the central points (Elouahed et al. 2024).

Table 4.1 Independence variables and their coded levels for the optimization of metal porphyrins removal.

Coded Variables	Factors	Coded level				
		-2	-1	0	+1	+2
X_1	A: Chitosan (g)	0.6	1	2.00	3	3.40
X_2	B: Zeolite (g)	4	5.00	7.5	10	11.00

To establish a mathematical relationship between the response and independent variables, the following quadratic equation model was employed:

$$y = b_0 + \sum_{i=1}^{2} b_i x_i + \sum_{i=1}^{2} \sum_{j=1}^{2} b_{ij}\, x_i\, x_j + \sum_{i=1}^{2} b_{ii}\, x_i^2 \qquad (4.1)$$

In equation (4.1), y represents the response variable of metal porphyrin removal percentage, and x_i and x_j denote the independent variables (CHS and ZX dose) for each trial. The equation includes parameters such as b_0 as the model constant, b_i as the linear coefficient, b_{ii} as the quadratic coefficient, and b_{ij} as the cross-product coefficient.

Table 4.2 The experimental design of the CHS/ZX matrix using CCD.

Run	A: Chitosan (g)	B: Zeolite (g)
1	0.58	7.5
2	2	11
3	2	7.5
4	3.41	7.5
5	3	10
6	1	10
7	3	5
8	2	7.5
9	1	5
10	2	7.5
11	2	7.5
12	2	7.5
13	2	4

Analysis of variance (ANOVA) was employed to assess the significance of the model terms through the examination of p-values and F-values. A p-value less than 0.05 indicated the significance of the test variables, and the magnitude of the F-value was adequate for the model terms. Importantly, the non-significance of lack of fit was deemed reasonable and affirmed the validity of the quadratic model (Elouahed et al. 2024).

4.2.6 Construction of calibration curves and estimation of detection and quantification limits

The preparation of metal porphyrin solutions, specifically 200 ppm of VO-TPP and 100 ppm of Ni-TPP, was achieved by dissolving the respective compounds in 50 mL of toluene under controlled conditions (50°C, stirring at 200 rpm). The solution volume was increased to 200 mL by adding toluene in three 50 mL increments. Once fully dissolved, the solutions were transferred to a 250 mL volumetric flask. To construct the calibration curve, twenty standard solutions were derived from these metal porphyrin solutions by diluting specified volumes into 25 mL volumetric flasks and adjusting the volume with toluene to the mark.

The concentration of metal porphyrinic samples was determined through UV-visible spectrophotometry, utilizing a Shimadzu UV-1200 model operating between 300 – 700 nm wavelengths. Measurements were conducted in a 12.5 × 12.5 × 45 mm cuvette, with toluene as the reference. The Lambert-Beer Law facilitated the calculation of metal porphyrins concentration.

For the calculation of the limit of detection (LOD) and limit of quantitation (LOQ), we employed the standard deviation of the response and the calibration curve's slope, as delineated by the following formulas, referencing the methodology outlined in literature (Mashhadizadeh et al. 2013):

$$LOD = 3.3 \times \frac{S_b}{m} \quad (4.2)$$

$$LOQ = 10 \times \frac{S_b}{m} \quad (4.3)$$

where S_b represents the standard deviation of the regression line's y-intercept, and m denotes the calibration curve's slope.

4.2.7 Adsorption experiments

The experimental procedure involved the adsorption of metal porphyrins from toluene using the CHS/ZX composite. The interaction between metal porphyrin and the CHS/ZX composite was analyzed through liquid-solid adsorption experiments conducted in batches. Furthermore, to investigate the kinetic and thermodynamic mechanisms underlying the adsorption of metal porphyrin onto the CHS/ZX composite, the adsorption capacities of the composite for VO-TPP and Ni-TPP were measured, and the corresponding adsorption isotherms were obtained. The metal porphyrins concentration was determined on the basis of the measured absorbance. The adsorption capacity of metal porphyrins at different time points could be calculated using equation (4.4).

$$q_t = (C_0 - C_t)V/M \quad (4.4)$$

C_0 represents the starting concentration of metal porphyrin (mg/L), C_t signifies the concentration of metal porphyrin at a specific time point 't' (mg/L), V represents the volume of the metal porphyrin solution (L), and M stands for the amount of composite added (g).

$$q_e = \frac{(C_0 - C_e)V}{M} \tag{4.5}$$

where Ce denotes the concentration of metal porphyrin in equilibrium (mg/L),

4.2.8 Equilibrium models

The experimental results were applied to evaluate four kinetic models to explore the adsorption mechanism. Equations (4.6) through (4.9) were utilized to analyze the pseudo first order (PFO) (El Kaim Billah et al. 2023), pseudo second order (PSO) (Khnifira et al. 2021), Elovich (Musah et al. 2022), and intraparticle diffusion (El Kaim Billah et al. 2023) models, respectively.

$$q_t = q_e(1 - e^{-k_1 t}) \tag{4.6}$$
$$q_t = k_2 q_e^2/(1 + k_2 q_e t) \tag{4.7}$$
$$q_t = \ln(AB)/B + \ln(t)/B \tag{4.8}$$
$$q_t = k_p t^{0.5} + C \tag{4.9}$$

where q_t is the capacity of adsorption at equilibrium (mg/g), q_e is the capacity of adsorption at time (mg/g) k_1 is the adsorption rate constant of PFO (min^{-1}), k_2 is the adsorption rate constant of PSO (min^{-1}), A, B are constants of Elovich model, k_p is the intraparticle diffusion rate constant (g/mg.min) of intraparticle diffusion model, C is the intercept plot.

The equilibrium data were then evaluated to assess their suitability for three isothermal models, the first being the Langmuir model (Şimşek et al. 2023), the second being the Freundlich model (Majdoubi et al. 2024) and the third being the Dubinin-Radushkevich (Musah et al. 2022). The associated model parameters were estimated

and examined to gain insights into the potential adsorption mechanisms. The integral format of the model equations is presented in equations (4.10) to (4.12).

$$q_e = \frac{K_L q_{max} C_e}{1+K_L C_e} \quad (4.10)$$

$$q_e = K_F C_e^{1/n} \quad (4.11)$$

$$q_e = q_{max}\, e^{-K_{D-R}\left(RT \ln\left(1+\left(\frac{1}{C_e}\right)\right)\right)^2} \quad (4.12)$$

Where C_e is the equilibrium concentration (mg/L), K_L is the Langmuir constant (L/mg), K_F and 1/n Freundlich constants, K_{D-R} is the Dubinin-Radushkevich constant (mol^2/kJ^2), R is the gas constant (8.314 J/mol.K), and T is the absolute temperature (K).

The parameters of thermodynamics were employed to analyze the change in energy throughout the process of adsorption and to ascertain its spontaneity (Bonetto et al. 2021; Mohamed et al. 2022). Parameters of thermodynamics, including ΔG° (free energy), ΔH° (enthalpy), and ΔS°(entropy), were determined using the subsequent equations:

$$\Delta G° = \Delta H° - T\Delta S° \quad (4.13)$$

$$\Delta G° = -RT \ln K \quad (4.14)$$

$$\ln K = \frac{\Delta S°}{R} - \frac{\Delta H°}{RT} \quad (4.15)$$

It is important to recognize that the determination of thermodynamic parameters such as ΔG°, ΔH°, and ΔS° relies heavily on the accurate estimation of the thermodynamic constant (K). The Langmuir isotherm is commonly employed to describe adsorption data at equilibrium (Musah et al. 2022).

The appropriate method to calculate the equilibrium constant for an adsorption system involves obtaining adsorption isotherms at various temperatures and performing nonlinear fitting on these isotherms. From the best-fitted model at each temperature, an equilibrium constant is determined for each respective isotherm. These equilibrium constants, typically expressed in L/mg, must be converted to a dimensionless form to

be used in the Van 't Hoff equation. This conversion involves several steps. Initially, the Langmuir equilibrium constant (K_L), given in L/mg, is converted to L mol^{-1} by multiplying the K_L value by 1000, thus changing L/mg to L/g. This result is then multiplied by the molecular weight of the adsorbate (in g/mol) and the standard concentration of the adsorbate (1 mol/L). The final step involves dividing by the activity coefficient, which was considered dimensionless. It was assumed here that the adsorbate solution is sufficiently diluted, allowing the activity coefficient to be considered as unitary. After these calculations, the parameter K_L becomes dimensionless (Lima et al. 2019).

4.2.9 Desorption experiments

Desorption experiments were conducted in 50 mL capped Erlenmeyer flasks, each containing a specified volume of the selected eluent. A calculated mass of CHS/ZX composite, saturated with metal porphyrins, was then suspended in this eluent. The mixture was stirred at 200 rpm across various temperatures for predetermined time intervals. At equilibrium, the CHS/ZX composite was separated from the mixture by centrifuging at 4000 rpm for 5 min. The concentration of porphyrins was determined based on the measured absorbance. The desorption capacity of the CHS/ZX metal porphyrins could be calculated using the equation (4.16) as follows:

$$q_{des} = \frac{C_{des} \times V}{M} \tag{4.16}$$

where, q_{des}, desorption is the amount of metal porphyrin desorbed from per gram of porphyrin saturated sorbent at equilibrium (mg/g), C_{des} is the metal porphyrin concentration in the desorbing solution (mg/L), V is the eluent solution volume (L), and M is the metal porphyrin saturated CHS/ZX weight (g).

Desorption efficiency (%) of metal porphyrins was calculated using the following Equation:

$$\%\ des = \frac{q_{e\ des}}{q_{e\ ads}} \times 100 \tag{4.17}$$

where des % is VO-TPP/Ni-TPP desorption efficiency (%) and $q_{e\ des}$, desorption and $q_{e,\ ads}$ are VO-TPP/Ni-TPP desorption and adsorption capacity (mg/g), respectively.

4.2.10 Preparation of saturated CHS/ZX composite

Before starting the desorption test, the CHS/ZX composite was saturated by adding 2 g of adsorbent in an Erlenmeyer containing 200 mL of 20 mg/L vanadium and nickel porphyrins in toluene solution individually. The flask was shaken with controlled temperature (30°C) at 200 rpm until adsorption equilibrium (24 h). After that, the saturated CHS/ZX composite was separated from the solution by vacuum filtration and dried at 80°C until constant weight. The UV-vis spectrophotometer was then employed to determine the absorbance of the VO-TPP and Ni-TPP solutions at their respective strong absorption peak wavelengths of 548 nm and 528 nm, respectively. The experiment was performed in duplicate and taking the average of the results. Then, the concentration of both metal porphyrins solution was calculated using the Lambert-Beer law (Mäntele & Deniz 2017). The amount of metal porphyrins removed by adsorption from the stock solution was calculated using Equation (4.18).

$$q_{ads} = \frac{C_0 - C_{e\ ads}}{V \times M} \tag{4.18}$$

where, q_{ads}, is the amount of metal porphyrins at equilibrium (mg/g), C_0 is the initial concentration of metal porphyrins in toluene (mg/L), $C_{e\ ads}$ is the concentration of metal porphyrin in the toluene phase at equilibrium conditions (mg/L), V is the volume of metal porphyrin solution (L), and M is the CHS/ZX weight (g).

4.2.11 Effect of different operating variables on metal porphyrins desorption efficiency

a. Effect of saturated CHS/ZX weight

Different weights of metal porphyrins saturated CHS/ZX composite mass varying from 10 to 50 mg were used to determine the effect of composite weight on porphyrins desorption efficiency. Except the composite mass, the other variables were kept constant, and desorption study was conducted as explained in Section 4.2.9.

b. Effect of eluent volumes

Desorption experiments were performed using different volumes of eluent varying from 10 to 40 mL. Except the volume of eluent, the other variables were kept constant, and desorption study was conducted as explained in Section 4.2.9.

c. Effect of contact time

The desorption study was conducted on a hotplate stirrer at 200 rpm for various time intervals ranging from 45 to 450 min. Samples were taken at different time intervals, filtered, and analyzed the desorbed metal porphyrin content, as outlined in Section 4.2.9.

d. Effect of temperature

Chloroform was used as an eluent to study the effect of varying temperatures (30 to 100°C) on the desorption efficiency of metal porphyrins from a saturated CHS/ZX composite, following the procedures outlined in Section 4.2.9.

e. Effect of different initial porphyrin concentrations

Batch experiments were conducted to assess the effects of varying initial metal porphyrin concentrations (10-80 mg/L) on the desorption of porphyrins from a saturated CHS/ZX composite. The adsorption experiments were carried out as detailed in Section 4.2.7. Subsequently, the composite saturated with metal porphyrins was subjected to the desorption process using chloroform as an eluent, as described in Section 4.2.9.

4.2.12 Regeneration and reusability of CHS/ZX composite

Regeneration of the sorbent is an important step to check economically the feasibility of adsorption process. Successive batches of vanadyl and nickel porphyrins adsorption and desorption were conducted to assess the porphyrin recovery capability and regeneration of the CHS/ZX adsorbent through successive processes. The desorption experiments were conducted as described in Section 4.2.9. The desorption experimental conditions, including temperature, agitation time, and solid/liquid ratio, were consistent

with those obtained through the optimization process. Solution samples were taken at a specific interval. The adsorption and desorption efficiencies were calculated using equations. (4.16) and (4.18).

4.3 RESULTS AND DISCUSSION

4.3.1 Adsorbent characterization

Table 4.3 summarized the CHN analysis result and the result showed that the chitosan displays high percentages for each of the C, H and N components. This can be attributed to the fact that CHS is a linear polysaccharide composed of D-linked D-glucosamine and N-acetyl-D-glucosamine (refer to Figure 2.12), which were randomly distributed. On the contrary, in the case of ZX, which was a crystalline aluminosilicate, the results indicated the presence of only oxygen and the absence of coal residues. Notably, the percentages of C, H, and N in CHS/ZX were lower than those in CHS, which can be attributed to the introduction of silicon and aluminum elements. It is worth mentioning that this signifies a successful intercalation process of CHS in ZX.

Table 4.3 Results of CHN analysis

Sample	CHN analysis (%)		
	C	H	N
CHS	38.063	6.218	7.074
ZX	-	5.113	-
CHS/ZX	13.299	3.598	1.867

Figure 4.2 shows the XRD patterns of the CHS, ZX and CHS/ZX bio-composite. The pure CHS exhibited a broad peak at 2θ: 20.88°, indicates the presence of amorphous carbon structure (Han et al. 2019), whereas pure ZX typically displayed diffraction peaks belong to octahedral structure of zeolite at 2θ: 6.15°, 10.04°, 11.76°, 15.48°, 18.46°, 20.12°, 23.37°, 26.70°, 29.12°, 30.37°, 30.99°, 32.06°, and 33.61° (Kumar et al. 2018). Similarly, the same zeolite phase was detected on CHS/ZX but displayed a much higher intense peak than ZX. Using peak at 2θ: 6.25, the crystal size of the zeolite phase on ZX, calculated according to Debye Scherrer's equation, is 21.81 nm, while CHS/ZX showed a large increment of crystallite size with values of 54.90 nm (Table 4.4). This finding can be attributed to the fact that the bio-composite surface particles exhibited a

greater tendency towards agglomeration, which was consistent with SEM images. A previous study that examined the nano-bio composite of CHS with different zeolites also revealed similar findings (Moghaddam et al. 2022), along with an increase in pore size in the composite relative to the parent materials, as shown by the BET analysis.

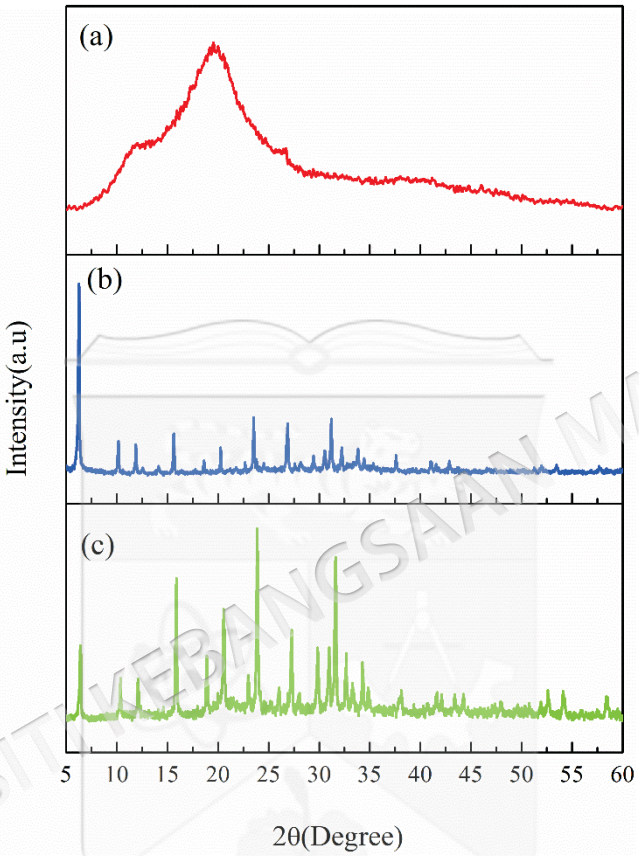

Figure 4.2 XRD patterns of (a) CHS, (b) ZX, and (c) CHS/ZX.

The enhancement of peak intensity observed in the XRD pattern of the CHS/ZX composite can be attributed to several factors related to the interaction between chitosan and zeolite.

Firstly, chitosan has been shown to promote increased crystallinity when incorporated into composites. The study by Marroquin et al. (2013) demonstrated that the addition of materials like Fe_3O_4 and carbon nanotubes to chitosan resulted in sharper and more pronounced peaks in the XRD pattern, indicative of enhanced crystallinity. Similarly, in the CHS/ZX composite, chitosan likely facilitates a more ordered arrangement of the zeolite particles, thereby increasing the overall crystallinity of the composite. This is reflected in the XRD pattern as more intense peaks.

Secondly, the combination of chitosan and ZX likely results in a synergistic effect, where the interaction between these two materials enhances the structural properties of the composite. The study on PE/TPS blends found that chitosan improves the homogeneity and interfacial adhesion in composites, contributing to enhanced structural properties (Afkhami et al. 2021). This suggests that in the CHS/ZX composite, similar synergistic effects are contributing to the observed increase in peak intensity. Chitosan may interact with the zeolite framework through its functional groups, leading to the stabilization and reinforcement of the crystalline structure. This interaction could be responsible for the observed increase in peak intensity, as chitosan helps maintain a stable and ordered crystalline framework within the composite.

Lastly, the presence of chitosan may have contributed to the stabilization of the zeolite's crystalline structure. Chitosan's ability to interact with and stabilize other materials, as evidenced in the study on chitosan nanocomposites (Marroquin et al. 2013), suggested that it played a similar role in the CHS/ZX composite, preventing structural degradation and maintaining the integrity of the crystalline structure. This stabilization is crucial in producing the well-defined and intense peaks seen in the XRD analysis.

The nitrogen gas adsorption method provided a clearer view of the BET surface area. The values presented in Table 4.4 indicated that CHS had the lowest BET surface area of 4 m^2/g, these results aligned with the findings from previous studies (Teimouri et al. 2016). In contrast, ZX and CHS/ZX exhibited BET surface areas of 452 m^2/g and 251 m^2/g, respectively. According to Pei et al. (2019), CHS is typically characterized by a non-porous structure, while ZX demonstrated the presence of mesopores structure. Indeed, ZX synthesis from treated CFA via alkaline fusion-hydrothermal had resulted formation of zeolite with high porous structure which in thus positively impact the surface area of adsorbent mesoporous texture. These findings in agreement with Figure 4.3b which showed that the CHS/ZX isotherm type IV for having formation of micropores ($d < 2$ nm) and mesopores ($2 \text{ nm} < d < 50$ nm) structures (Wang et al. 2020d). The specific surface area (S_{BET}) of the synthesized composites was found to be larger than that of CHS. This was likely attributed to the presence of zeolites with high

S_{BET}, which were dispersed across the CHS bed, thereby enhancing its overall surface area.

Table 4.4 BET surface area, pore volume and pore size of ZX, CHS and CHS/ZX composite.

Sample	Crystallite size (nm)	Surface area (m^2/g)	Average pore size (nm)	Pore volume (cm^3/g)
CHS	-	4	-	-
ZX	21.81	452.565	6.120	0.111
CHS/ZX	54.90	251.872	12.811	0.573

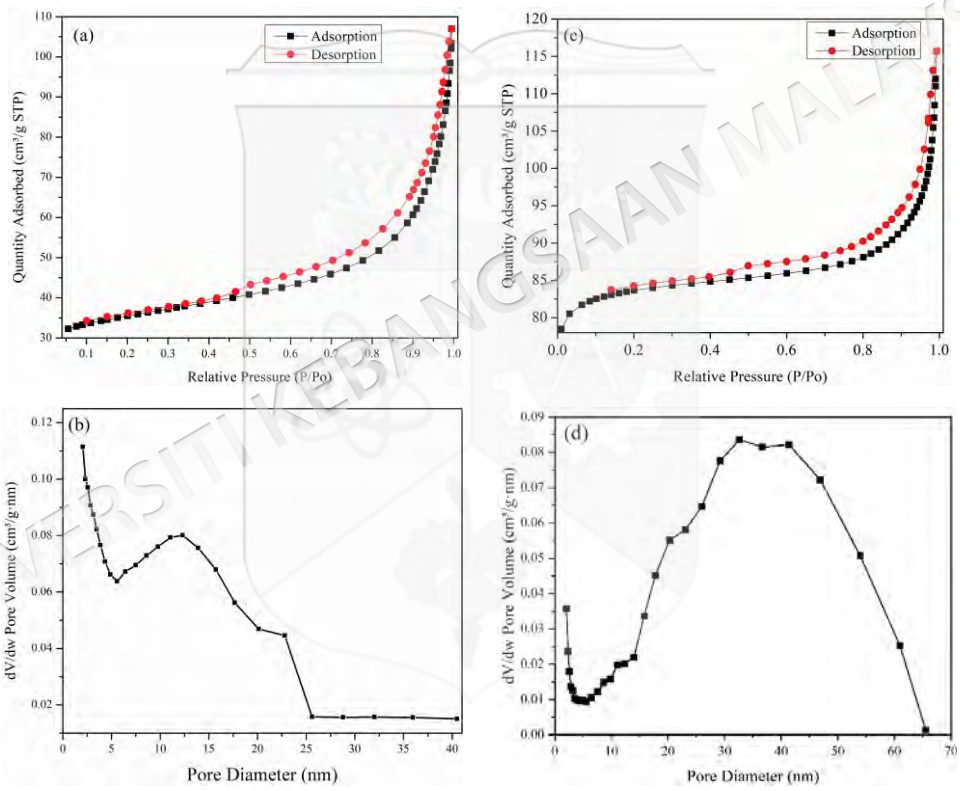

Figure 4.3 N_2 adsorption-desorption isotherm and pore size distribution of (a), (b) CHS, and (c), (d) CHS/ZX

Figure 4.4 depicts the SEM images of three materials: CHS, ZX, and the CHS/ZX composite. Starting with pure CHS (Figure 4.4a), its surface morphology appeared smooth and nonporous, which aligned with the literature (Kumar et al. 2018). In contrast, the SEM images from the previous study revealed bipyramidal particles with a smooth surface morphology for ZX (Figure 4.4b), where particle sizes around 21 nm. Now, due to a grafting reaction, the SEM images of the CHS/ZX composite

depicted in (Figure 4.4c, d) show a uniform distribution of ZX bipyramidal particles within the CHS biopolymer matrix. This results in a granular texture on the otherwise smooth chitosan surface, a layered structure, and the formation of large cavities. The presence of ZX particles between the layers of chitosan contributed, to some extent, to an increase in the pore size and particle size of the composite, which was consistent with the BET results (Figure 4.3). Overall, it was clearly shown that the particle structure plays an important role in controlling the BET surface area of the material, while the dispersion of ZX particles has a positive effect on the pore properties of CHS/ZX.

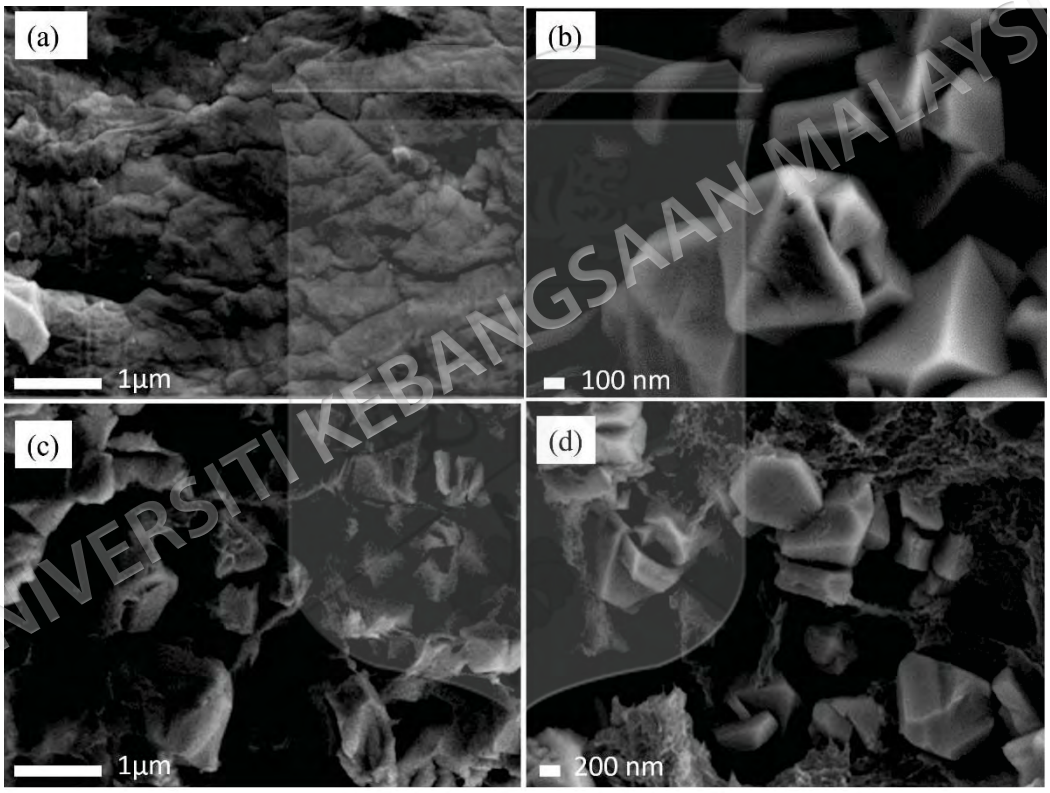

Figure 4.4 Scanning electron micrographs (a) CHS, (b) ZX, (c), and (d) CHS/ZX

Qualitative elemental composition determinations were obtained through EDX microanalysis, as shown in Figure 4.5. The graphical representation illustrates the peaks and corresponding weight percentages of the elements, specifically C, N, O, Si, and Al. These elements are essential constituents of both chitosan (CHS) and zeolite X (ZX), which are the primary components of the synthesized composites.

The presence of carbon (C) and nitrogen (N) is primarily attributed to the chitosan structure, which contains amine (NH_2) and hydroxyl (OH) functional groups. Oxygen (O) is detected as a common element in both chitosan and zeolite, indicating the presence of hydroxyl and silanol (Si-OH) groups. Silicon (Si) and aluminum (Al) are key components of the zeolite framework, contributing to its crystalline structure and adsorption properties. Detecting these elements within the synthesized composites validates the successful formation of CHS/ZX composites and provides insights into the material's structural integrity. As indicated by the EDX mapping, the uniform distribution of these elements suggests that chitosan was effectively integrated into the zeolite matrix. This integration is crucial for enhancing the composite's mechanical strength, thermal stability, and adsorption capacity, which are essential for its intended applications. These results were aligned with the XRD results showed an increase in the crystallinity of the composite.

Moreover, the relative weight percentages of these elements can give further insights into the compositional balance and the efficiency of the synthesis process. For instance, a higher concentration of Si and Al would reinforce the zeolite's structural framework, while the presence of C and N would confirm the incorporation of chitosan, potentially leading to improved adsorption characteristics.

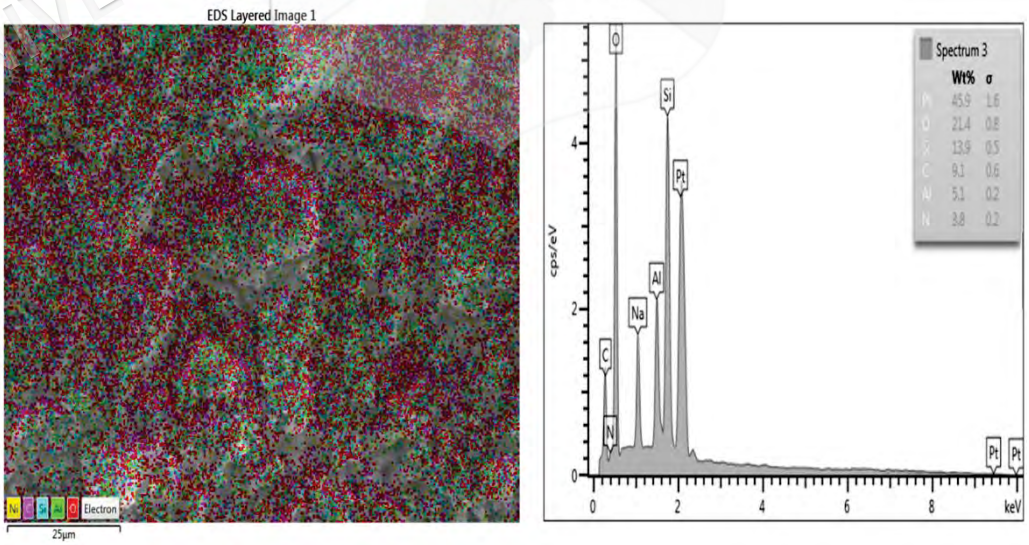

Figure 4.5 EDX and mapping of CHS/ZX

Figure 4.6 shows the FT-IR spectrum of CHS, ZX, and CHS/ZX composite. The CHS revealed absorption band as follows: 3413 cm^{-1} (–OH stretching) , 2923 and 2875 cm^{-1} (–CH stretching vibration) (Fang et al. 2014), 1655 cm^{-1} (C=O stretching vibration of the secondary amide) and 1593 cm^{-1} (N–H bending vibration of amide band) (Kanimozhi et al. 2016), 1325 cm^{-1} (C–N stretching vibration), 1157 cm^{-1} (C–O–C stretching vibration of CH–O–CH), 1088 and 1027 cm^{-1} (C–O stretching vibration) in the polysaccharide structure (Sivakami et al. 2013). In the case of ZX, the result showed absorption band at 3469 cm^{-1}, 970 cm^{-1}, 750 cm^{-1}, 670 cm^{-1}, 560 cm^{-1}, and 460 cm^{-1}, which corresponded to the vibration of T–OH, Si–OH bond stretching, symmetric Si–O–T (T = Si or Al) bond stretching, Si–O stretching in the tetrahedral structure of SiO_4, Si–O stretching, and Al–OH (Luo et al. 2018; Yang et al. 2019a). The FTIR spectrum of CHS/ZX demonstrated the amalgamation of absorbance bands arising from the CHS and ZX functional groups. The band at 560 cm^{-1}, elucidated the vibration of the external linkage between tetrahedral units, and the band at 460 cm^{-1} was also observed in the synthesized composites. The bands at 2920 and 2875 cm^{-1}, related to the stretching vibration of the -CH bonds in the CHS ring, were reduced in the synthesized composite, in contrast, certain bands were notably absent, including the bands of Si-OH, stretching modes of tetrahedral atoms, symmetric stretching vibration mode of Al-O, and vibration of Al-OH bands evidencing the chemical interaction between CHS and ZX (Han et al. 2019; Jawad et al. 2020). This was believed to indicate the successful formation of the CHS/ZX composite. It was also noticed that the ZX peaks were more prominent compared to CHS in the CHS/ZX composite, possibly due to an electrostatic interaction between the negatively charged sites of ZX (Si−O−) and the positively charged sites of CHS (NH_3^+) (Kumar et al. 2018).

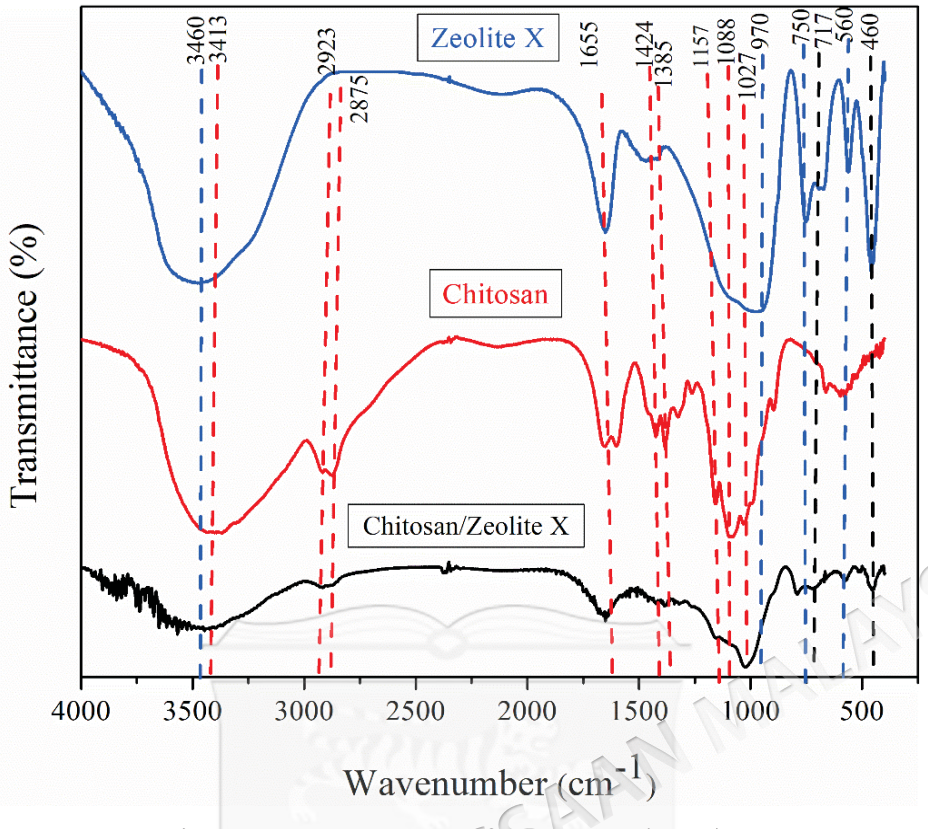

Figure 4.6 FT-IR spectra of ZX, CHS, and CHS/ZX

A detail analysis of TGA curves for CHS, ZX, and CHS/ZX composite was showed in Figure 4.7. The TGA for CHS in Figure 4.7a reveals two distinct decomposition temperatures. The initial temperature range of 47-125°C with a total weight loss of 15% corresponds to the loss of adsorbed water (Kumar et al. 2018). What's noteworthy is that the temperature required for this water release (125°C) was higher than that for free water, which is typically around 110 °C. This behavior can be attributed to the strong hydrogen bonding between the water molecules and the active groups (-NH_2, -OH) of CHS, as suggested by Patel et al.(2023). The most significant weight loss occurs in the range of 150°C to 350°C, where the material's weight dropped sharply by 44%. This stage likely represented the thermal degradation of the chitosan polymer backbone. The degradation could involve the breakdown of glycosidic linkages in chitosan, releasing smaller molecules such as oligomers and monomers (Nagireddi et al. 2019). The curve flattened gradually after 350°C, suggesting a slower rate of weight loss by 26%, which finally stabilized at around 14% of the original mass by 600°C. In the case of ZX (Figure 4.7b), the TGA curve exhibited rapid decline in mass by 20% up to ~150 °C. This stage corresponded to the loss of physically adsorbed water on the zeolite's surface (He et al. 2020). At higher temperatures (450°C to 600°C),

the mass remained relatively stable at about 80%. Furthermore, the thermogram of CHS/ZX is shown in (Figure 4.7c). In the initial degradation stage (up to ~150°C), the weight of the material declines slightly by 13%. This modest decrease suggested releasing a small number of volatile substances, likely including water and other low molecular weight volatiles. As the temperature increased to the second stage (150°C to 400 °C), a significant weight loss was observed, with the material's mass reducing by 32%. This substantial reduction likely indicated the thermal degradation of the chitosan polymer backbone (Díaz-Flores et al. 2021). In the third stage, extending from 300°C to 600°C, the rate of weight loss slowed considerably around (15%). The TGA curve gradually flattened, suggesting that the remaining material degraded more slowly. This stage culminated in the material's weight stabilizing at about 40% of it is original mass by 600°C. This reduction was primarily attributed to the release of hydroxyl groups present in the composition of zeolites while the metal oxides remained intact. The CHS/ZS composites exhibited a higher percentage of residue in comparison to CHS alone. The reason behind that was during pyrolysis (burning), the composite formed a char layer with a complex structure on its surface. This char layer acted as an insulating layer, slowing down the release of volatile substances from the composite (Mahdavi et al. 2021). Therefore, the formation of the CHS/ZX composite will affect the second degradation step within the char layer and improve the thermal stability of the composites in comparison to chitosan.

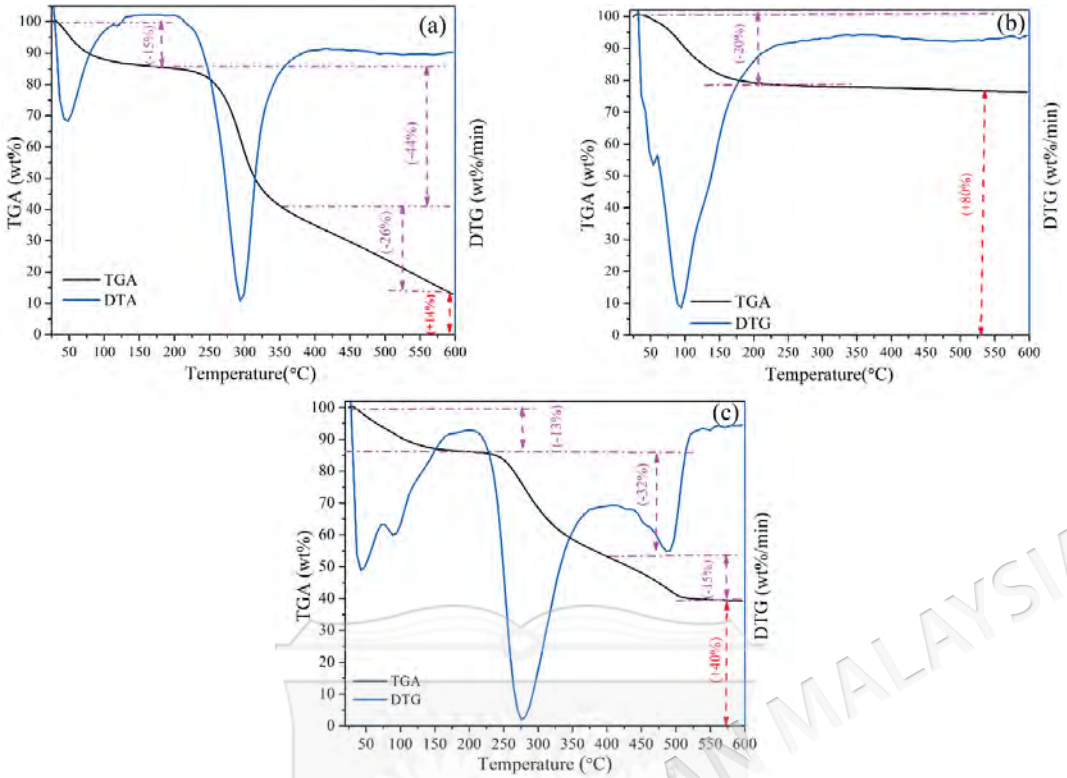

Figure 4.7 TGA patterns of (a) CHS (b) ZX, and (c) CHS/ZX composite, (-) indicates weight loss and (+) indicates the remaining mass.

Assessing the pH_{PZC} value, also referred to as the point of zero charge, is essential for understanding interactions at the solid-liquid interface during adsorption processes. Variations in surface charge across different pH levels critically influence how the surface interacts with adsorbed species. For example, when adsorbing cationic species onto a surface with a predominantly positive charge, repulsive forces are likely to reduce the adsorption capacity. While several techniques can determine the surface charge, adding salt remains the simplest and most effective method. This approach involves analyzing the charge transfer between the surface and the solution by monitoring the final pH once equilibrium is achieved (Majdoubi et al. 2024).

Figure 4.8 illustrates the point of zero charge (pH_{PZC}) for the CHS/ZX composite stands at 7.5. In scenarios where the solution's pH exceeds this value, the composite's surface charge becomes negative, thereby enhancing its affinity for cations. Conversely, when the solution's pH falls below the pH_{PZC}, the surface becomes positively charged, favoring the adsorption of anions. Nonetheless, if adsorption still occurs despite the pH

not aligning with the charge requirements of the adsorbent, this indicates the involvement of additional mechanisms beyond mere electrostatic attraction.

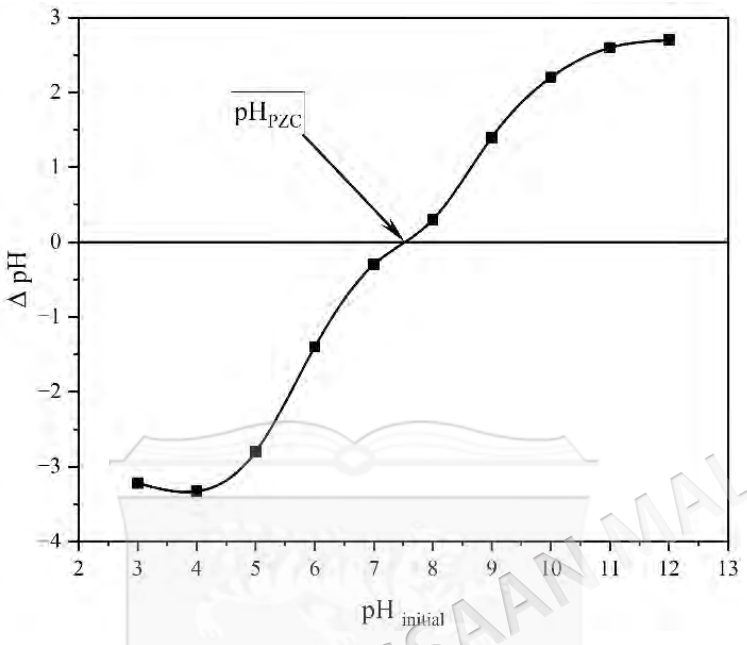

Figure 4.8 PCZ plot of the CHS/ZX composite

The X-ray photoelectron spectroscopy (XPS) analysis, presented in Figure 4.9 and Table 4.5, provided a comprehensive understanding of the surface chemistry and elemental composition of the CHS/ZX composite before and after the adsorption of VO-TPP and Ni-TPP, respectively. Figure 4.9a shows the initial broad survey scan spectrum, featuring distinct peaks such as oxygen (O1s) at about 532 eV indicative of hydroxyl groups in chitosan and oxygen in the zeolite framework. Sodium (Na1s) peaks at around 1070 eV, and silicon (Si2p) peaks near 102 eV, highlighting the zeolite's structural components. Additionally, nitrogen (N1s) at approximately 400 eV and carbon (C1s) at about 285 eV peaks confirmed the integration of chitosan into the composite. After the adsorption of Ni-TPP, Figure 4.9b demonstrates significant spectral changes, most notably the appearance of Ni2p peak at approximately 855 eV, affirming the successful nickel adsorption on the composite's surface. Similarly, after VO-TPP adsorption, Figure 4.9c shows a new V2p peak at 517 eV, indicating vanadyl porphyrin attachment and further altering the electronic environment of the composite.

Figure 4.9d depicts the deconvolution of the Ni 2p spectra. The enlarged view of the peak at 855.0 eV can be ascribed to the binding energy of Ni 2p3/2, as shown in

(Keyhaniyan et al. 2018). According to the literature, the typical peak of metallic Ni at 852.9 eV, which can be assigned to the binding energy of Ni 2p3/2 (Muthurasu et al. 2024) and is attributed to impurities in the synthesized zeolite X. Furthermore, as shown in the spectra of Ni 2p3/2, the peak appearing at 855.4 eV is attributed to the coordinated Ni atoms in Ni-TPP (Keyhaniyan et al. 2018). The XPS spectrum shown in Figure 4.9e displays the characteristic peak of vanadyl porphyrin adsorbed on the surface of the CHS/ZX composite. The peak centred at approximately 517 eV indicates the presence of V2p, which is associated with the vanadyl group in vanadyl porphyrin, according to references (Chen et al. 2018). The significance of this peak stems from its direct correlation to the oxidation state of vanadium. In this context, the vanadium in the vanadyl group typically exhibits an oxidation state of +4, coordinated within the organic porphyrin ring (Jia et al. 2020).

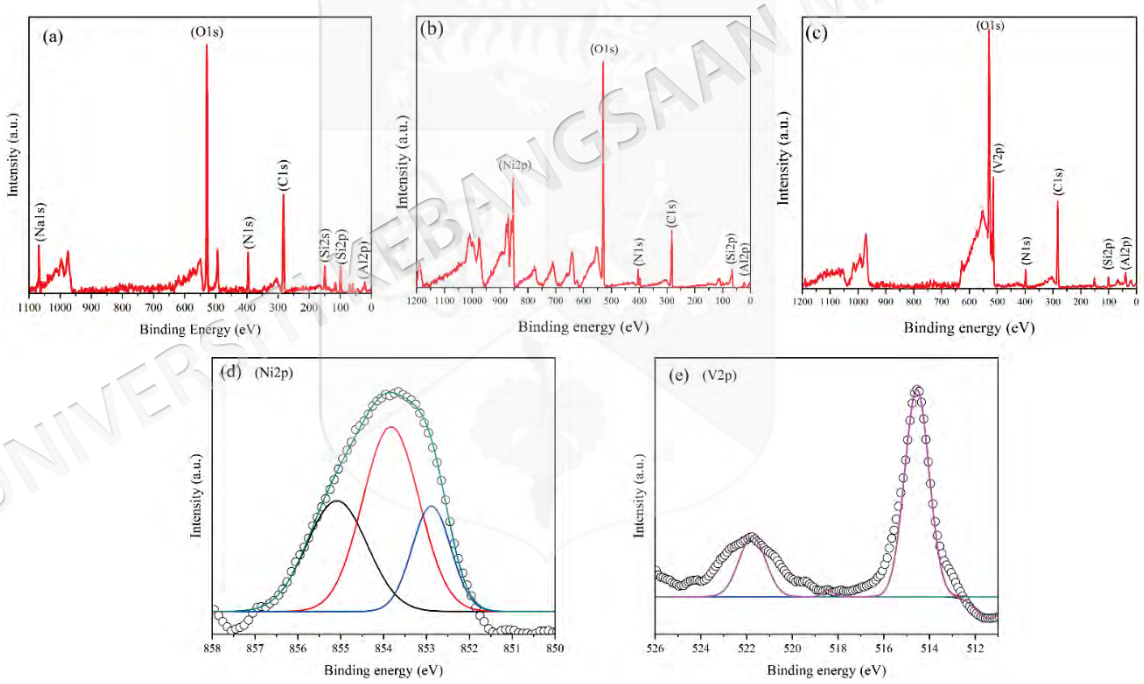

Figure 4.9 XPS survey scan of (a) CHS/ZX, (b) CHS/ZX+Ni-TPP, and (c) CHS/ZX+VO-TPP; high resolution of (d) Ni2p and (e) V2p spectra of CHS/ZX+Ni-TPP and CHS/ZX+VO-TPP, respectively.

Table 4.5 Elemental analysis results of the CHS/ZX surface using XPS technology.

Sample	C1s,	O1s,	N1s,	Si2p,	Al2p,	V2p,	Ni2p,
				wt%			
CHS/ZX	38.65	39.84	7.59	9.8	3.97		
CHS/ZX+V	40.2	42.2	4.64	6.94	2.18	3.89	-
CHS/ZX+Ni	39.13	41.08	4.25	6.83	2.51	-	6.2

4.3.2 Determination of best matrix formulation on adsorption capacity using design expert software

Regression analysis was used to study the relationship of empirical or predicted models generated from experiment data. Among the models (linear, two-factor interaction (2FI), quadratic, and cubic polynomial) that can fit the response, the quadratic model was suggested as the best for the response generated from experimental design. Table 4.6 depicts the sequential model sum of the square for the generated data. The fitting summary for the model was selected based on the sequential model sum of the square, the lack of fit test, and the model summary statistics. Besides, the quadratic model was the best due to its highest-order polynomial with significant reaction terms. The reaction model revealed an insignificant lack of fits, which ensured the model was good with low error (Elouahed et al. 2024).

The experimental design of CCD matrixes and the percentage removal of metal porphyrins are presented in Table 4.7. A total of 13 adsorption experimental runs were generated employing detailed conditions designed by RSM. The design was meant to enhance the best matrix formulation composite for the adsorption of metal porphyrins, which was determined from the optimum synergy of the two materials via percentage removal values recorded.

Table 4.6 Sequential model sum of squares

	VO-TPP removal					Ni-TPP removal					
Source	**Sum of Squares**	**Degree of freedom**	**Mean Square**	**F-value**	**p-value**	**Sum of Squares**	**Degree of freedom**	**Mean Square**	**F-value**	**p-value**	
Mean	47462.33	1	47462.33			33781.39	1	33781.39			
Linear	42.30	2	21.15	114.10	< 0.0001	5.55	2	2.77	23.89	0.0007	
2FI	41.15	1	41.15	8.50	0.0172	24.85	1	24.85	35.17	0.0002	
Quadratic	282.87	2	141.43	16.69	0.0007	245.75	2	122.87	39.37	< 0.0001	Suggested
Cubic	0.8260	2	0.4130	4.38	0.0796	0.3355	2	0.1678	1.76	0.2642	Aliased
Residual	0.4715	5	0.0943			0.4772	5	0.0954			
Total	47829.94	13	3679.23			34058.35	13	2619.87			

Table 4.7 Actual and predicted response for the adsorption of metal porphyrins onto CHS/ZX using central composite design (CCD)

Run	A: Chitosan (g)	B: Zeolite (g)	Ni-porphyrin removal rate (%)		V-porphyrin removal rate (%)	
			Predicted	Actual	Predicted	Actual
1	0.58	7.5	57.05	56.85	66.07	65.74
2	2	11	55.19	55.27	63.90	63.64
3	2	7.5	51.62	51.22	62.62	63.10
4	3.41	7.5	45.60	45.98	53.73	54.11
5	3	10	47.82	47.53	55.51	55.45
6	1	10	60.90	61.02	70.65	71.09
7	3	5	45.23	44.93	53.85	53.38
8	2	7.5	51.62	51.57	62.62	62.77
9	1	5	53.19	53.45	63.44	63.19
10	2	7.5	51.62	51.43	62.62	62.65
11	2	7.5	51.62	51.84	62.62	62.23
12	2	7.5	51.62	52.02	62.62	62.37
13	2	4	44.48	44.58	52.48	52.78

The quadratic model for vanadyl and nickel porphyrins removal in terms of coded variables were suggested by the program as follows:

$$Ni - TPP\ removal\ (\%) = 51616 - 4.04781A + 3.78599B - 2.4925AB - 0.147375A^2 - 0.892375B^2 \quad (4.19)$$

$$VO - TPP\ removal\ (\%) = 62.624 - 4.36216A + 4.04104B - 3.2075AB - 1.3595A^2 - 2.217B^2 \quad (4.20)$$

The outcomes of the analysis of variance (ANOVA) presented in Table 4.8 highlight the significance of the linear effects of variables for both porphyrins. Additionally, both the interactive effect of CHS dose with ZX dose and the quadratic effect of CHS dose and ZX dose were found to be significant in relation to the removal of metal porphyrins. The significance of each term was determined by assessing the values of F and p; a higher F-value and a lower p-value indicated the increased significance of the terms (Chen et al. 2021).

At a 95% confidence level, the reaction model demonstrated significance, as evidenced by the computed F values of 395.25 and 475.67 for the removal of vanadyl and nickel porphyrins, respectively, reflecting very low probability values ($p < 0.001$). This high significance of the fitted model underscores the reliability of the regression model in predicting the removal of metal porphyrins. Furthermore, the p-values, serving as indicators of the significance of each regression coefficient and the interaction effect of cross products, affirmed the reliability of this regression model in predicting metal porphyrins removal, with smaller p-values indicating greater significance of the corresponding coefficient. Additionally, model terms with p-values less than 0.05 were considered statistically significant (Chen et al. 2021).

The coefficient of determination (R^2) values for both suggested models were notably high, measuring 0.9965 for vanadyl and 0.9971 for nickel. This high R^2 signified the suitability of these models in describing the experimental data. The R^2 values indicated that the models account for less than 1% of total variations for both metal porphyrins. A higher R^2 was desirable as it enhanced the model's ability to predict the response more accurately (Khan et al. 2021).

Determining the coefficient of variance (CV) value is crucial as it represents the ratio between the standard error of the estimate and the mean value of the observed response, expressed as a percentage. These metric gauges the reproducibility of the model. The model can be considered reproducible if the CV value is less than 10%. In the case of the removal percentages of vanadyl and nickel porphyrins on CHS/ZX, the obtained CV values were 0.71 and 0.66 (as shown in Table 4.9), respectively, indicating the reproducibility of the models (Bouazizi et al. 2016).

Table 4.8 Results of RSM and analysis of variance applied to metal porphyrins removal using CHS/ZX composite

	VO-TPP removal					Ni-TPP removal					
Source	**Sum of Squares**	**Degree of Freedom**	**Mean Square**	**F-value**	**p-value**	**Sum of Squares**	**Degree of Freedom**	**Mean Square**	**F-value**	**p-value**	
Model	366.32	5	73.26	395.25	< 0.0001	276.14	5	55.23	475.67	< 0.0001	significant
A	152.23	1	152.23	821.24	< 0.0001	131.08	1	131.08	1128.95	< 0.0001	
B	130.64	1	130.64	704.78	< 0.0001	114.67	1	114.67	987.63	< 0.0001	
AB	41.15	1	41.15	222.01	< 0.0001	24.85	1	24.85	214.03	< 0.0001	
A^2	12.86	1	12.86	69.36	< 0.0001	15.11	1	15.11	130.12	< 0.0001	
B^2	34.19	1	34.19	184.46	< 0.0001	9.54	1	9.54	82.15	< 0.0001	
Residual	1.30	7	0.1854			0.8127	7	0.1161			
Lack of Fit	0.8292	3	0.2764	2.36	0.2125	0.4058	3	0.1353	1.33	0.3822	Not significant
Pure Error	0.4683	4	0.1171			0.4069	4	0.1017			
Cor Total	367.62	12				276.96	12				

Table 4.9 Statistical parameters of variance applied to vanadyl and porphyrins removal by CHS/ZX composite

Parameters	VO-TPP Removal	Ni-TPP Removal
Standard Deviation	0.4305	0.3407
Mean	60.42	50.98
Correlation of Variance %	0.7125	0.6684
R^2	0.9965	0.9971
Adjusted R^2	0.9939	0.9950
Predicted R^2	0.9820	0.9873
Adequate precision	62.1659	70.9555

Based on the ANOVA results, the reaction variables with significant influenced on metal porphyrins removal were the CHS dose (A) and ZX dose (B). Furthermore, the interaction term AB also exhibited a significant impact on the response of metal porphyrins removal. The ANOVA analysis indicated that the CHS dose (A) was the most influential parameter, as evidenced by the $F_{VO\text{-}TPP}$ value of 821.24 and the $F_{Ni\text{-}TPP}$ value of 1128.95. The lack of fit, indicated by F-values of 2.36 and 1.33 for vanadyl and nickel removal, respectively, suggests a 2.36% and 1.33% probability that the "Lack of fit for F-value" could be attributed to noise (Asikin-Mijan et al. 2017). Nevertheless, the ANOVA analysis revealed an insignificant lack of fit in the model, affirming that the model adequately fits the experimental data (Bouazizi et al. 2016). Moreover, the comparison between predicted and actual values for porphyrins removal, with adjusted R^2 values of 0.9965 and 0.9971 (Table 4.9) for vanadyl and nickel removal, respectively, demonstrated that the model accounted for 99.65% and 99.71% of variability (Figure 4.10). Hence, the polynomial model proved to be accurate and generally suitable for practical use.

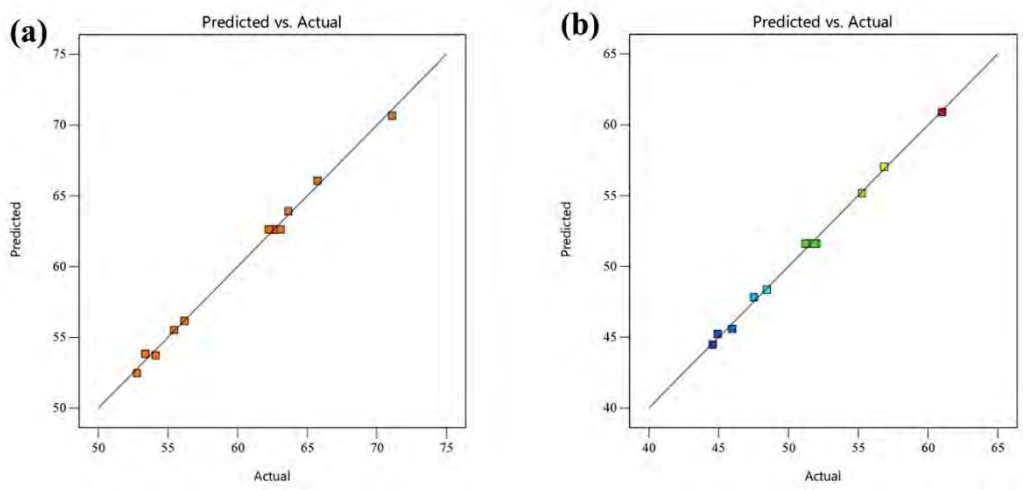

Figure 4.10 Predicted value vs. actual of (a) vanadyl porphyrin removal ;(b) nickel porphyrin removal

Furthermore, an examination of residuals was conducted to assess the adequacy of the reaction model. Residuals, representing the difference between the observed and predicted responses, were analyzed using the normal probability plot (Figure 4.11a, b) and the residuals versus predicted response plot (Figure 4.11 c, d). The normal probability plot of the residuals indicated that the errors followed a normal distribution, forming a straight line and appearing statistically insignificant. Simultaneously, the plot of residuals versus predicted response exhibited a random scattering within the limits. As a result, it is anticipated that the model provides a reliable estimation and demonstrates the capacity to assess the correlation of the variables (Asikin-Mijan et al. 2017).

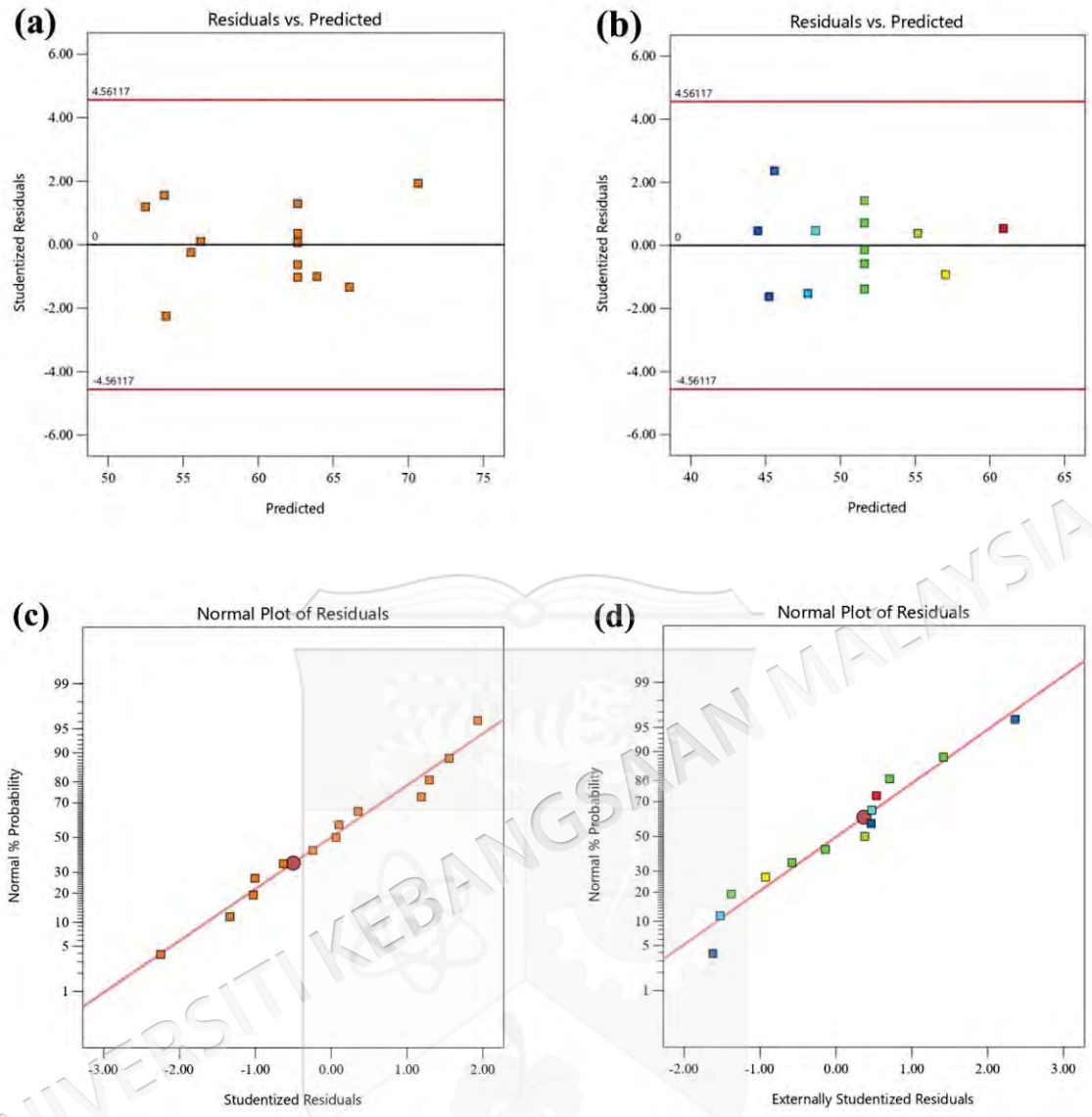

Figure 4.11 Normal probability plot of the residuals for (a) vanadyl porphyrin removal; (b) nickel porphyrin removal; and plot of the residuals vs. predicted response for (c) vanadyl porphyrin removal; (d) nickel porphyrin removal

The regression equation is visually presented through three-dimensional (3D) response surface plots and two-dimensional (2D) contour plots in the general graphical representation. The 3D response surface plots and 2D contour plots (Figure 4.12) provide insights into the impact of the two variables on metal porphyrins removal. Notably, the graphical representation indicates that reducing the CHS dose and increasing the ZX dose positively influences metal porphyrins removal until reaching an optimal value.

In Figure 4.12, the 3D and 2D plots depict the interaction effect between the CHS dose (A) and ZX dose (B) on removing nickel and vanadium porphyrins. The observation suggests that a reduction in the CHS dose, transitioning from a low level (1 g) to a high level (3 g), results in a decline in metal porphyrins removal concurrently with a continuous increase in ZX dose.

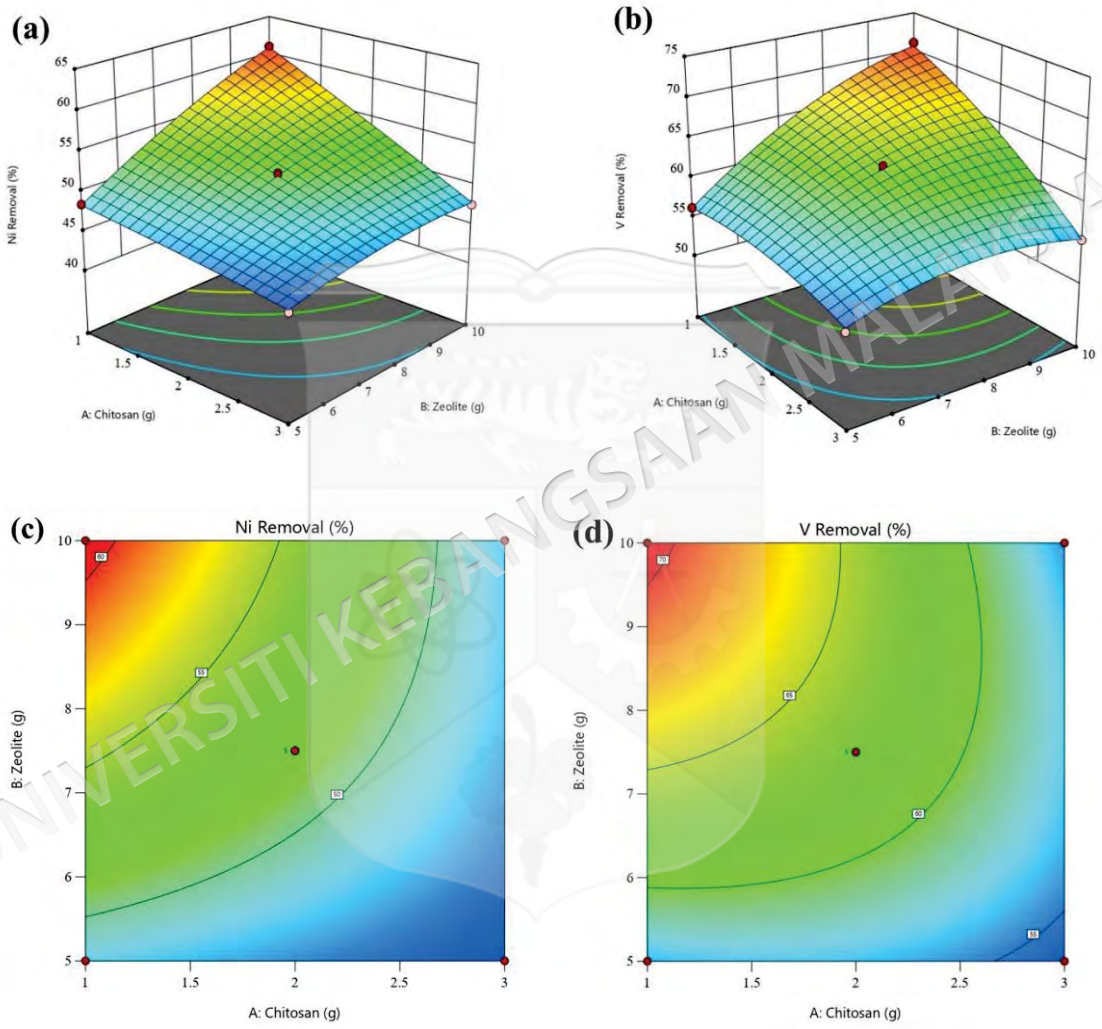

Figure 4.12 3D-response surface plot (a, b) and, 2D-contour plot (c, d) for the interaction of the two variables

4.4 MODEL VALIDATION STUDY

To assess the predictive accuracy of the model, optimal reaction parameters, as suggested by the model in Table 4.10, were implemented across three separate trials of the VO-TPP/Ni-TPP adsorptive removal using the CHS/ZX composite. The

experimental outcomes demonstrated that the removal efficiencies for metal porphyrins closely aligned with the model's predictions, registering an average deviation of 2.64% for VO-TPP and 2.59% for Ni-TPP. Although the actual adsorption performance slightly underperformed relative to the expectations set by the response surface methodology (RSM), the results affirm the model's substantial accuracy and reliability in predicting the adsorption behaviors of VO-TPP and Ni-TPP with the CHS/ZX composite.

Table 4.10 Comparative results of confirmatory experiments for model validation.

Number	Parameters		Ni-TPP Removal			VO-TPP		
	Chitosan (g)	Zeolite (g)	Predicted Removal Rate (%)	Experimental Removal Rate (%)	Error (%)	Predicted Removal Rate (%)	Experimental Removal Rate (%)	Error (%)
1	1.024	10	60.754	59.522	2.027	70.542	67.872	3.784
2	1	9.829	60.592	58.207	3.936	70.456	69.593	1.224
3	1.1	10	60.275	59.175	1.824	70.158	68.105	2.926

4.5 VALIDATION OF THE SPECTROPHOTOMETRY ANALYSIS METHOD

Figure 4.13 displays the calibration curve for the standard solutions of metal porphyrins. The method's calibration sensitivity was assessed based on the slope of the calibration curves (Figure 4.13). The method's linear range was determined to be from 0.1 to 20 mg/L for metal porphyrin samples. Under these conditions, acceptable homogeneity of variances and the validity of the reported limits of quantitation and linearity (LOQ and LOL) were confirmed by statistical methods, including regression coefficient (R^2) estimation, the "Lack-of-fit" method, and one-way analysis of variance (ANOVA, confidence level: 95%, degrees of freedom: 2) (Khorshid et al. 2021). This broad linear range demonstrates advantageous attributes of this analytical method, such as optimization accuracy for maximum precision and satisfactory accuracy.

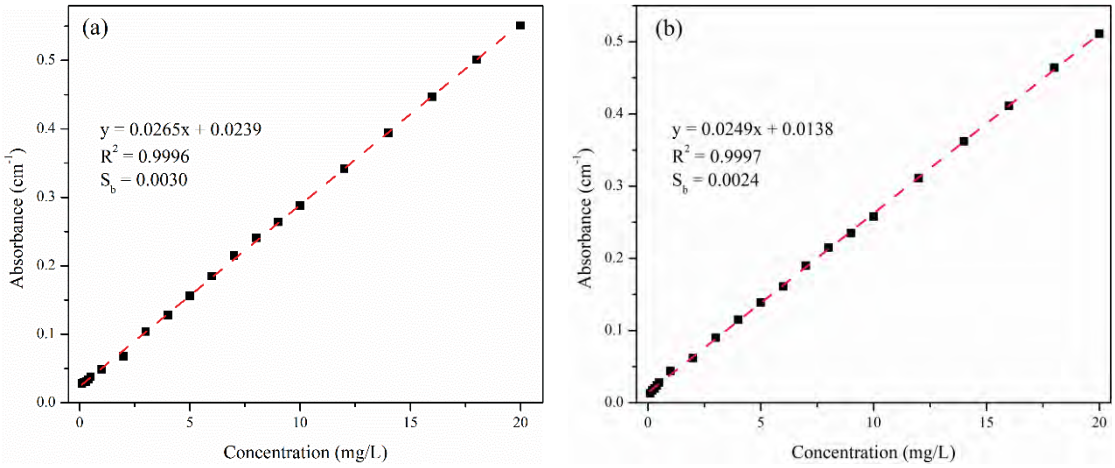

Figure 4.13 Calibration curve of (a) VO-TPP and (b) Ni-TPP in toluene

The limit of detection (LOD) was defined based on, and in accordance with, the slope of the calibration curves (calibration sensitivity), which were 0.0265 and 0.0249 (a.u.) mg/L, resulting in LOD values of 0.376 and 0.291 mg/L for VO-TPP and Ni-TPP analysis, respectively. The limit of quantitation (LOQ) was determined to be 1.142 and 0.970 mg/L for total VO-TPP and Ni-TPP, respectively.

4.6 ENHANCED ADSORPTION OF METAL PORPHYRINS VIA CHS/ZX COMPOSITES

As a preliminary study to demonstrate the impact of grafting chitosan (CHS) with zeolite (ZX) on the removal of metal porphyrins from a model solution, we evaluated the porphyrin removal capabilities by ZX, CHS, and their composite (CHS/ZX), as depicted in Figure 4.14. We used standard solutions of metal porphyrins in toluene at concentrations ranging from 10 to 50 mg/L to simulate a broad spectrum of conditions reflective of those found in various crude oils, such as Arabian crude oils (Ali & Abbas 2006).

Our results demonstrate that the CHS/ZX composite exhibits superior adsorption performance compared to CHS and ZX when used individually for the adsorption of metal porphyrins. This enhancement is primarily attributed to the composite's increased specific surface area and pore size, as confirmed by BET characterization, which provides more active sites for adsorption and reduces internal diffusion resistance, thereby enhancing the efficiency of mass transfer. Furthermore, FTIR analysis confirms the presence of multiple functional groups within the CHS/ZX

structure, which facilitates stronger interactions between the composite and the metal porphyrins (VO-TPP and Ni-TPP). The experimental data clearly show that the adsorption capacities for VO-TPP and Ni-TPP on the modified CHS/ZX composite are significantly higher than those observed with the unmodified CHS, thereby validating the effectiveness of the composite structure.

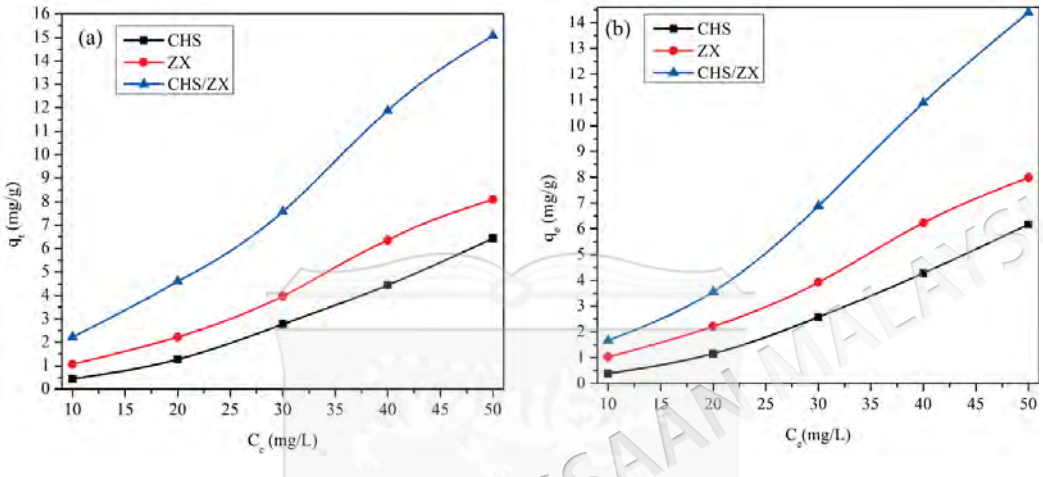

Figure 4.14 Comparison of adsorption of (a) VO-TPP, (b) Ni-TPP by ZX, CHS, and CHS/ZX composite: contact time = 600 min, temperature = 25°C, dose = 3 g/.L.

4.7 INFLUENCE OF CHS/ZX DOSAGE

This study aimed to clarify the influence of the dose of CHS/ZX on the behavior of adsorption of porphyrin complexes. Experiments were conducted using dosages ranging from 0.006 to 0.012 g, while maintaining constant reaction conditions (T = 25°C, C_0 = 10 mg/L, and V = 5 mL). The resultant data, depicted in Figure 4.15a and b, were subjected to analysis using the pseudo-second-order kinetic model, and the outcomes are presented in Table 4.13 for comprehensive evaluation and comparison. The data result indicates that an increase in the dosage of CHS/ZX or the ratio of adsorbent and metal porphyrins leads to a decrease in q_e. For example, when the CHS/ZX dosage was increased from 0.006 to 0.012 g, the amount of VO-TPP adsorbed (q_e) decreased from 8.016 to 2.725 mg/g, while the amount of Ni-TPP adsorbed (q_e) decreased from 7.762 to 2.188 mg/g. The direction of the curves of qt-t at various dosages closely resembles that shown in Figure 4.16.

The adsorption process at various CHS/ZX dosages exhibited similar behaviour concerning the initial concentration of porphyrin and reaction temperature, as demonstrated by the successful fit of the pseudo-second-order equation. Moreover, a higher CHS/ZX dosage facilitated greater availability of binding sites for the adsorption of metal porphyrins, resulting in a larger value of $k_{2(VO\text{-}TPP/Ni\text{-}TPP)}$ (Wang & Guo 2020). As reported in previous literature (Sahmoune 2019), $k_{2(VO\text{-}TPP)}$ was slightly higher than $k_{2(Ni\text{-}TPP)}$, and $q_{e\ (Ni\text{-}TPP)}$ was greater than $q_{e\ (VO\text{-}TPP)}$ under the same conditions.

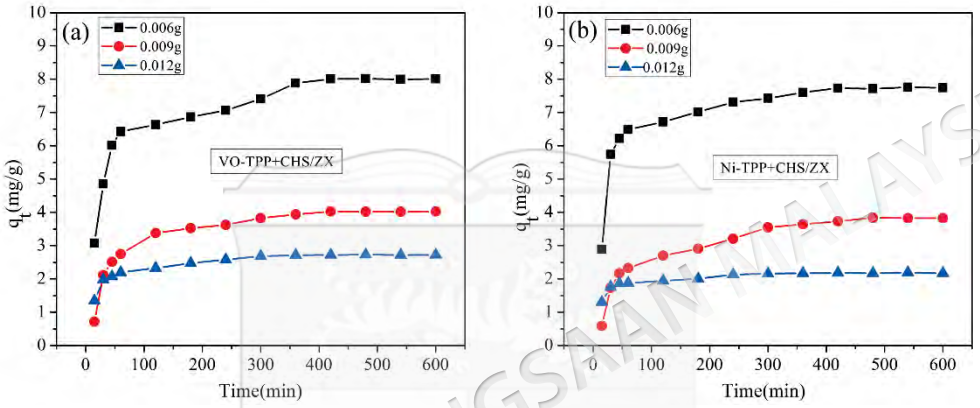

Figure 4.15 Effect of adsorbent dosage on the adsorption of (a) VO-TPP and (b) Ni-TPP by CHS/ZX: C_0 = 10 mg/L, contact time = 600 min, temperature = 25°C.

4.8 INFLUENCE OF TIME AND ADSORPTION KINETIC

Predicting changes in adsorption over time is crucial when planning adsorption processes. To understand this process, various mechanisms, such as mass transfer across external boundary layer films, surface adsorption, and molecular diffusion within pores, are considered. The adsorption kinetics were studied using PFO and PSO models, the Elovich model, and intraparticle diffusion outlined in equations (4.6-(4.9) and illustrated in Figure 4.16 and Table 4.11.

Moreover, the (qt-t) curves exhibit three distinct stages: a rapid stage ($t < 90$ min), a slow stage (90 min $< t <$ 420 min), and a stability stage ($t >$ 420 min). During the rapid stage, there was a significant increase in adsorption capacity, which suggesting that the initial interaction between porphyrins and the CHS/ZX composite is characterized by a rapid adsorption rate due to a surface effect, one can deduce that adsorption of porphyrin onto CHS/ZX composite is likely characterized as physical

Table 4.11 Kinetic models parameters

		Elovich equation			Diffusion equation			The pseudo-first-order equation			The pseudo-second-order equation			
Sample	T (°C)	A (g/mg)	B (mg/(g.min))	R^2	C (mg/g)	Kd (mg/(g. $min^{0.5}$))	R^2	$q_{e\ cal}$ (mg/g)	K_1 (1/min)	R^2	$q_{e\ cal}$ (mg/g)	K_2 (g/(mg.min))	R^2	$q_{e\ exp}$ (mg/g)
VO-TPP	25	3.554	0.745	0.896	5.027	0.211	0.756	9.027	0.034	0.918	9.692	0.005	0.962	9.571
	40	1.200	0.695	0.908	3.703	0.228	0.796	8.063	0.027	0.879	8.831	0.008	0.936	8.672
	55	0.445	0.598	0.900	2.513	0.261	0.781	7.611	0.019	0.916	8.588	0.013	0.938	8.133
Ni-TPP	25	3.488	0.775	0.873	4.841	0.204	0.748	8.679	0.035	0.861	9.333	0.004	0.921	9.211
	40	0.490	0.581	0.875	2.742	0.265	0.727	7.991	0.019	0.938	8.960	0.005	0.939	8.212
	55	0.313	0.586	0.909	2.020	0.260	0.778	7.251	0.016	0.953	8.260	0.011	0.957	7.433

adsorption (Chen et al. 2017). However, as the active sites of the composite are partially occupied, the rate of adsorption decreases considerably (Aljerf 2018). Ultimately, the adsorption process reaches equilibrium at 420 min.

Figure 4.16a to f and Table 4.11 indicate that PSO model possesses the highest correlation coefficients among the other kinetic models at different temperatures. Additionally, the values of $q_{e\ cal\ (VO\text{-}TPP)}$ obtained from PSO equation are in excellent agreement with the experimental values of $q_{e\ exp}$, with only a relative error of approximately 3% (see Table 4.13). These findings apply to the adsorption process of Ni-TPP as well. Thus, the metal porphyrin adsorption processes are accurately fitted and described by PSO model (Munagapati et al. 2018). Furthermore, the value of $k_{2\ (VO\text{-}TPP)}$ (g/mg·min) at 25, 40, and 55°C is 0.005, 0.008, and 0.013, respectively, while the value of $k_{2\ (Ni\text{-}TPP)}$ is 0.004, 0.005, and 0.011, respectively. These values increase with rising temperature, indicating that higher temperatures enhance the driving force and adsorption rate, leading to faster adsorption (Akazdam et al. 2017). Under identical circumstances, $k_{2(Ni\text{-}TPP)}$ is slightly lower than $k_{2\ (VO\text{-}TPP)}$, while $q_{e\ (Ni\text{-}TPP)}$ is greater than $q_{e\ (VO\text{-}TPP)}$. The difference in structure between Ni-TPP and VO-TPP could explain this phenomenon. The non-planar configuration of VO-TPP facilitates bonding with CHS/ZX, resulting in a faster adsorption rate compared to Ni-TPP. On the other hand, while the planar structure of Ni-TPP reduces its steric hindrance, it also limits its accessibility to the CHS/ZX composite surface, leading to a lower equilibrium adsorption capacity compared to VO-TPP (Chen et al. 2018).

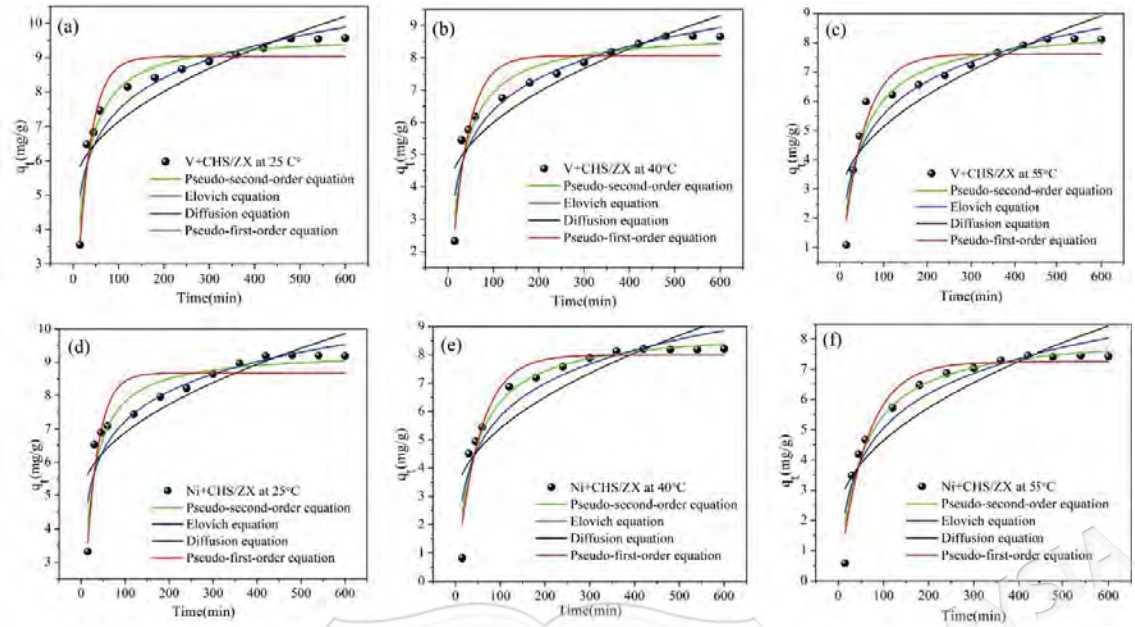

Figure 4.16 Time effect and fitting kinetic models for VO-TPP (a, b, c) and Ni-TPP (d, e, f) adsorption on CHS/ZX composite: C_0 = 10 mg/L, dose = 3 g/L.

Table 4.12 displays diverse adjustment results from comparable studies, which can be attributed to the utilization of adsorbents possessing distinct surface characteristics.

According to Chen et al. (2017), PFO model best suits the data of kinetic of the adsorption process of Ni-OEP by asphaltene. In contrast, another study by Chen and his colleagues (2018) determined that PSO is most suitable for the data of kinetic of the nickel-porphyrin adsorbed by graphene. This implies that the more intricate surface chemistry of asphaltene enables interactions that cannot occur on the surface of graphene. Moreover, Caetano et al. (2023) summarized that the Elovich equation is the most appropriate model for the kinetic data for porphyrin adsorbed by coconut shell activated carbon (CSAC). By examining the capacity of adsorption values shown in Table 4.12, it becomes apparent that the conditions selected in this study (including the type of solvent, the adsorbent utilized, solid-to-liquid ratio, and porphyrins concentration) exhibit superior performance in the adsorption processes when compared to those employed by (Caetano et al. 2023b; Chen et al. 2017, 2018).

Table 4.12 Comparison of findings from various studies investigating metal porphyrins adsorption by different adsorbent materials at a temperature of 25°C.

Metal Porphyrin	Parameters	Asphaltene	Graphene	Coconut Shell Activated Carbon	This study
VO-TPP	q_e (mg/g)	4.562	4.587	-	9.571
	t_e (min)	750	250	-	480
Ni-TPP	q_e (mg/g)	4.450	5.136	6.833	9.211
	t_e (min)	750	250	600	420

Table 4.13 Kinetic parameters of pseudo-second-order model

Sample	C_0 (mg/L)	$q_{e\ cal}$ (mg/g)	K_2 (g/mg.min)	R^2	$q_{e\ exp}$ (mg/g)	Dose of CHS/ZX (g)	$q_{e\ cal}$ (mg/g)	K_2 (g/mg.min)	R^2	$q_{e\ exp}$ (mg/g)
VO-TPP	5	1.283	0.002	0.967	1.270	0.006	8.156	0.005	0.951	8.016
	12	2.975	0.006	0.973	2.770	0.009	4.327	0.006	0.966	4.022
	20	6.615	0.048	0.969	5.87	0.012	2.778	0.023	0.971	2.725
Ni-TPP	5	1.130	0.002	0.963	1.12	0.006	7.948	0.004	0.920	7.762
	12	2.719	0.005	0.968	2.45	0.009	4.119	0.005	0.962	3.84
	20	5.868	0.046	0.931	4.74	0.012	2.203	0.017	0.956	2.188

4.9 INFLUENCE OF INITIAL CONCENTRATION AND ADSORPTION ISOTHERMS

The study aimed to determine the impact of the initial concentration of the solution on the adsorption capacity of VO-TPP/Ni-TPP in CHS/ZX at equilibrium. To achieve this, we investigated adsorption isotherms and evaluated the relationship between equilibrium concentration and adsorption capacity. The investigation covered a concentration range of 5-20 mg/L, while keeping other reaction conditions constant (temperature = 25°C, dose = 1 g/L, and time = 600 min). The concentrations were chosen based on prior studies in this field (Caetano et al. 2023; Chen et al. 2017, 2018), ensuring that our methods align with established practices and enhance the comparability of our results. The resulting data was analyzed using Equation (4.5), and the data set (Ce, qe) was plotted to create a visual representation of the findings. Furthermore, fit curves were generated using the Langmuir, Freundlich and Dubinin-Radushkevich isothermal models to help interpret the data.

The results of the study, including the plots and fit curves, are presented in Figure 4.17 and were analyzed using the pseudo-second order kinetic model, as illustrated in Table 4.13. According to the results, an increase in the initial concentration of porphyrin or a decrease in the ratio of adsorbent and metal porphyrins results in an increase in q_e. For instance, $q_{e\ (VO\text{-}TPP)}$ rises from 1.270 to 5.870 mg/g as the concentration varies from 5 to 20 mg/L, while $q_{e\ (Ni\text{-}TPP)}$ increases from 1.120 to 4.740 mg/g. These findings suggest that higher concentrations facilitate the dispersion of porphyrins in the solution, thereby increasing the likelihood of these molecules adhering to the active sites of the adsorbent. Furthermore, curves of qt-t follow a similar trend for the different initial porphyrin concentrations, as seen in Figure 4.18. The correlation coefficients are high, and the relative error of q_e is approximately 3%, indicating that the PSO equation fits the adsorption process well. The results are reported in Table 4.13, where $q_{e\ cal}$ is in good agreement with the $q_{e\ exp}$ at various initial concentrations. On the contrary, when the initial concentration increases, the $k_{2(VO\text{-}TPP/Ni\text{-}TPP)}$ increases. This change in k_2 with initial concentration is consistent with other reported adsorption systems, such as the study by Wanyonyi et al. (2014), who examined the adsorption of Congo red from aqueous solutions using roots of *Eichhornia crassipes*. They observed

that the value of k_2 increased with rising concentration. This phenomenon can be attributed to the fact that, at higher concentrations, the rate of interaction between porphyrin molecules and CHS/ZX is influenced by the collision of porphyrin molecules with one another (Chen et al. 2018).

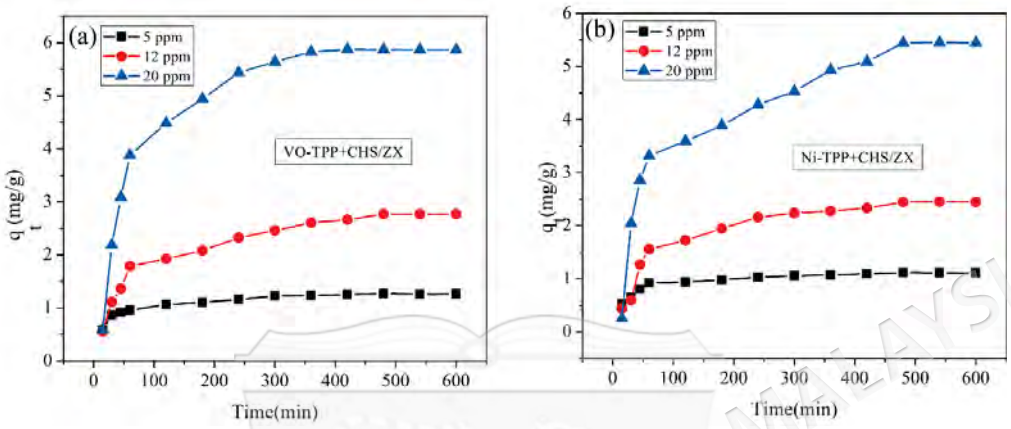

Figure 4.17 The effect of initial porphyrin concentration (a) VO-TPP and (b) Ni-TPP.

To achieve this, we investigated adsorption isotherms and evaluated the relationship between the equilibrium concentration and adsorption capacity. The resulting data was analyzed using equation (4.5), and the data set (C_e, q_e) was plotted to create a visual representation of the findings. Furthermore, fit curves were generated using the Langmuir and Freundlich isothermal models to help interpret the data. The results of the study, including the plots and fit curves, are presented in Figure 4.18. It became evident that the capacity of adsorption at equilibrium of metal-porphyrins by CHS/ZX is notably higher as solutions with higher concentrations were used. This can be attributed to the fact that a higher dosage of metal porphyrins in the solution enhances the likelihood of contact between the adsorbate and adsorbent, thereby promoting their interaction. These interactions may lead to the formation of multiple layers of adsorbate on the adsorbent surface, resulting in a higher adsorption capacity at equilibrium.

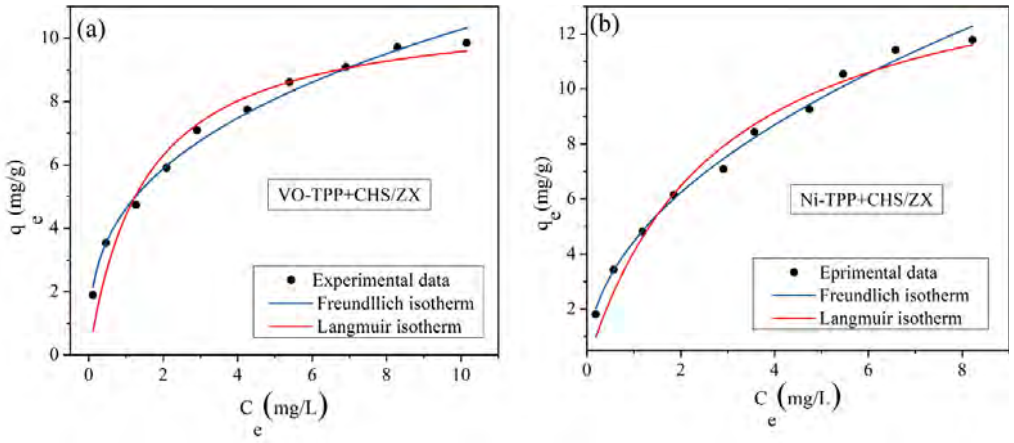

Figure 4.18 Isothermal fitting models of (a) VO-TPP (b) Ni-TPP at 25°C.

The equilibrium data were examined to assess their conformity with the Langmuir, Freundlich and Dubinin-Radushkevich (D-R) isotherm models. Table 4.14 displays the calculated fitting parameters. Freundlich model is a theoretical framework for explaining adsorption processes that take place on surfaces with varying characteristics and adsorption energies (Wang & Guo 2020). Unlike other models, the Freundlich model allows for the possibility of multilayer adsorption, as there is no predicted maximum saturation capacity (Al-Ghouti & Da'ana 2020). To determine the most accurate fit, it is necessary to consider properties of the structure of adsorbent and adsorbate.

Table 4.14 The parameters of the isothermal models for adsorption VO-TPP and Ni-TPP by CHS/ZX.

Isotherm model	**Parameters**	**VO-TPP**				**Ni-TPP**			
		25°C	30°C	35°C	40°C	25°C	30°C	35°C	40°C
Langmuir	q_{max} (mg/g)	11.005	11.986	13.069	15.113	15.580	14.947	16.232	17.101
	K_L (L/mg)	0.670	0.375	0.246	0.152	0.354	0.301	0.206	0.151
	R^2	0.950	0.985	0.994	0.986	0.970	0.981	0.980	0.994
Freundlich	K_F (mg/g (mg/L)$^{-1/nF}$)	4.620	3.630	3.011	2.389	4.464	3.838	3.161	2.636
	n	2.880	2.271	1.971	1.684	2.080	1.986	1.761	1.633
	R^2	0.988	0.965	0.962	0.954	0.990	0.975	0.976	0.979
Dubinin-Radushkevich	q_{max} (mol/kg)	0.01289	0.01284	0.01289	0.01321	0.01578	0.01450	0.01425	0.01419
	K_{D-R} (mol^2.J^2)	1.1784	2.309	3.756	6.466	2.108	2.132	3.125	5.144
	E (kJ/mol)	0.651	0.465	0.364	0.278	0.486	0.484	0.399	0.311
	R^2	0.771	0.856	0.910	0.951	0.814	0.814	0.849	0.896

For instance, the surface of CHS/ZX has diverse polar functional groups such as hydroxyl, primary amin, ether, amide, and exchangeable cations, which may interact with the acid and base active groups of metal porphyrins in distinct ways. Furthermore, the presence of a variety of acidic and basic groups within the composition of the metal complex raises the possibility of speculating about the potential occurrence of multilayer interaction (inter-interaction) between the porphyrin molecules themselves. This suggested that the Freundlich model can accommodate complex adsorption phenomena that are not accounted for by simpler models. 'n' is a constant in the Freundlich equation and represented an important indicator of the degree of heterogeneity of the adsorbent material and provides information about the adsorption process's favourability and intensity (Al-Ghouti & Da'ana 2020). When the value of 1/n falls between 0 and 1, it suggested the favourability of adsorption and heterogeneity of the adsorbent material. For CHS/ZX, the 'n' value of VO-TPP is greater than that of Ni-TPP, indicating that VO-TPP demonstrates a higher adsorption intensity on CHS/ZX compared to Ni-TPP. The K_F parameter is another important parameter that is related to the adsorption process and indicates the ability of the adsorbent and adsorbate to form interactions. With K_F values of 4.620 and 4.464 for the adsorption of VO-TPP and Ni-TPP onto CHS/ZX, respectively, which exceed those of asphaltene adsorption (0.650 for vanadyl and 0.316 for nickel porphyrins) (Chen et al. 2017), as well as activated carbon adsorption (3.142 for nickel porphyrin) (Caetano et al. 2023b), it can be concluded that CHS/ZX exhibits a greater affinity for both of vanadyl and nickel porphyrins than both asphaltene and activated carbon, resulting in a higher adsorption capacity. According to (Caetano et al. 2023b; Chen et al. 2017), Ni-porphyrin molecules exhibited stronger adsorption on the surface of CHS/ZX than asphaltene and activated carbon, as evidenced by a higher value of n (CHS/ZX) (2.080) compared to n (asphaltene) (1.300) and n (CSAC) (1.969). The q_{max} values for Ni and V porphyrin were compared for various adsorbent materials. CHS/ZX exhibited higher q_{max} values (15.580, and 11.005 mg/g for Ni and V porphyrin, respectively) compared to graphene (9.376, 8.304 mg/g for Ni V porphyrin, respectively) (Chen et al. 2018) and asphaltene (5.882, 3.571 mg/g for Ni and V porphyrin, respectively) (Chen et al. 2017) (refer to Table 4.12). These results suggest that CHS/ZX has a higher selectivity as well as a greater adsorption capacity for Ni and V porphyrin in comparison to other adsorbents.

Furthermore, the Dubinin-Radushkevich (D-R) isotherm is useful for providing key insights into energy parameters associated with adsorption, specifically through the calculation of the mean free energy of adsorption (E). The (D-R) model uses terms with S.I. units such as mol^2/kJ^2 and kJ/mol. Therefore, for this isotherm model to be applicable, the concentration and adsorption capacity must be expressed in S.I. units, specifically mol/L and mol/kg, respectively.

According to the D-R equation, the K_{D-R} value is utilized to compute the mean energy of adsorption, given by $E = 1/(2K_{D-R})^{0.5}$ (Salehi et al. 2020). This parameter, E, is crucial for identifying the type of adsorption mechanism involved. When the value of E ranges between 8 and 16 kJ/mol, the adsorption mechanism is indicative of chemical adsorption. Conversely, values of E less than 8 kJ/mol suggest that the adsorption mechanism is primarily physical adsorption. For the VO-TPP and Ni-TPP molecules in our study, E values were found to be below 8 kJ/mol, indicating that the adsorption of metal porphyrins onto the synthesized composites predominantly occurs via physisorption.

4.10 INFUENCE OF TEMPERATURE AND ADSORPTION THERMODYNAMICS

To investigate the effect of temperature on the removal of vanadyl and nickel porphyrins from a toluene solution using CHS/ZX, the study was conducted at 25, 40, and 55°C while keeping the other reaction conditions constant (C0 = 10 ppm, m = 0.005 g, V = 5 mL). Based on data in Figure 4.19, it is evident that, at 25°C, 40°C, and 55°C, $q_{e\ (VO-TPP)}$ and $q_{e\ (Ni-TPP)}$ decreases as the temperature increases. Specifically, the values of $q_{e\ (VO-TPP)}$ decreased from 9.571 mg/g to 8.672 mg/g and 8.133 mg/g, while those of $q_{e\ (Ni-TPP)}$ decreased from 9.333 mg/g to 8.960 mg/g and 8.260 mg/g, respectively.

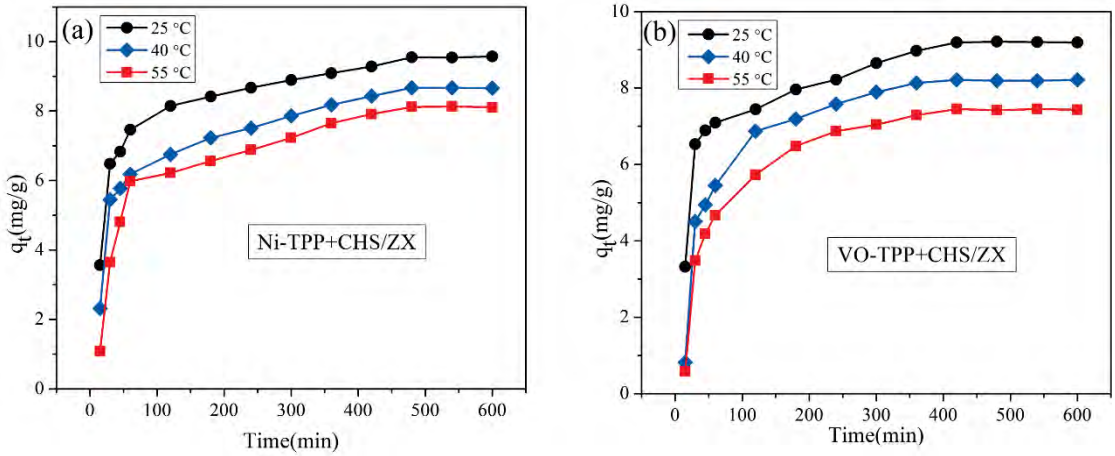

Figure 4.19 The effect of temperature on the adsorption of VO-TPP (a) and (b) Ni-TPP on CHS/ZX

To evaluate the adsorption processes, the thermodynamic parameters such as ΔG°, ΔH°, and ΔS° are taken into account. Equation (4.14) is used to obtain ΔG°, and the Langmuir model is utilized to calculate K_L as shown in Table 4.14. Van't Hoff equation used to determine the free energy (with slope = -ΔH°/R) and enthalpy (with intercept = ΔS°/R) as shown Figure 4.20. The parameters of thermodynamics are presented in Table 4.15. The value of free energy (ΔG°) was employed to evaluate the spontaneity of the process (Sahmoune 2019). The negative values of free energy revealed that the processes of adsorption occur spontaneously for vanadyl and nickel porphyrins. In all experiments, the free energy value showed an inverse relationship with reaction temperature, suggesting that higher temperatures inhibit the driving forces for metal porphyrin adsorption and vice versa. These findings aligned with the results of the kinetics study (see Section 4.8).

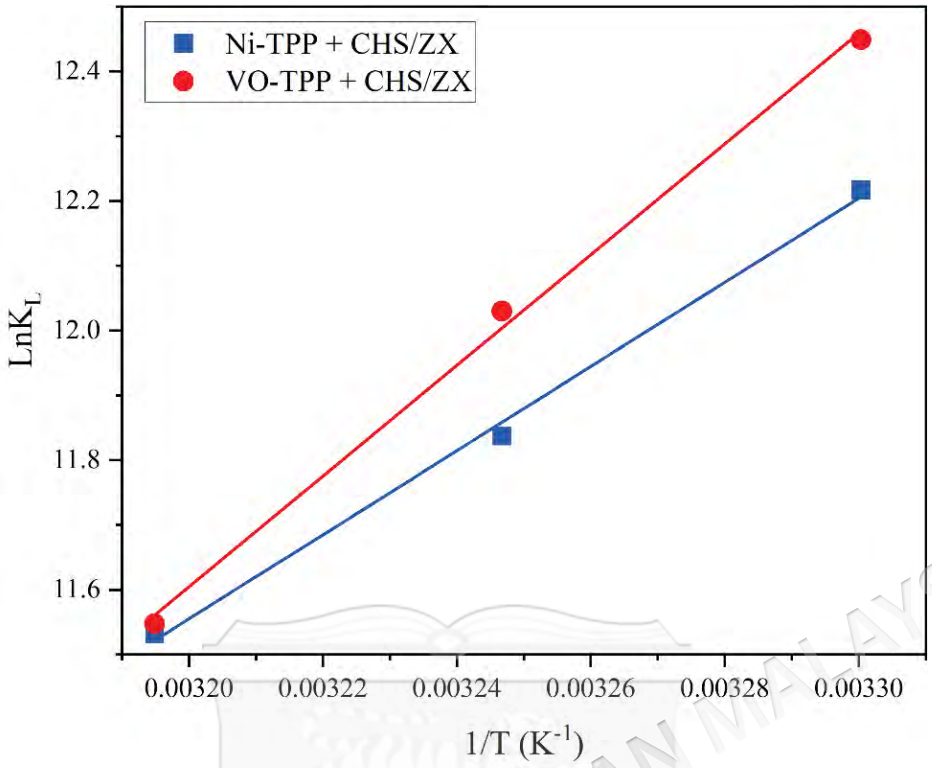

Figure 4.20 Plots of Van't Hoff equation

As shown in Table 4.15, the free energy values were between -30.011 to -31.360 kJ·mol^{-1}. As stated by Tarekegn et al. (Tarekegn et al. 2021), when the free energy values fall within the range of 0 to 20 kJ·mol^{-1}, it indicated that the prevailing process was physisorption. Conversely, when the values range from -400 to -80 kJ·mol^{-1}, it suggested that the prevailing process was chemisorption.

Table 4.15 Thermodynamic parameters of VO-TPP/Ni-TPP

Sample	ΔH° (kJ/mol)	ΔS° (J/mol·K)	T (K)	K_L	ΔG° (kJ/mol)
CHS/ZX+VO-TPP	-71.023	-130.795	303	2.55. 10^5	-31.360
			308	1.676. 10^5	-30.804
			313	1.035. 10^5	-30.050
CHS/ZX+Ni-TPP	-53.987	-76.692	303	2.0218. 10^5	-30.776
			308	1.383. 10^5	-30.312
			313	1.019. 10^5	-30.011

Based on our results, the adsorption of metal porphyrins by CHS/ZX was characterized as physisorption. These findings were in line with the results of adsorption

kinetics (refer to Section 4.8). The initial stage of adsorption, observed as the rapid stage within the first hour, suggested that the initial adsorption process was primarily physical in nature. Similarly, the enthalpy values categorized the adsorption process as either exothermic or endothermic. Table 4.15 displays negative enthalpy values at the tested temperatures, indicative of an exothermic nature in the metal-porphyrin adsorption process (Sarada et al. 2017). These findings were consistent with the kinetic results of adsorption presented in Section 4.8. The study indicated that lower temperatures positively influence the adsorption process of porphyrin complexes by the CHS/ZX composite. According to the thermodynamic results, the enthalpy values range from -53.987 to -71.023 $kJ \cdot mol^{-1}$, which is significantly higher than that of hydrogen bonds in the adsorption process (ranging from -5 to -30 $kJ \cdot mol^{-1}$) (Mechnou et al. 2022). Hence, it can be deduced that the interactions between metal porphyrins and CHS/ZX exhibit a chemical nature. In essence, the adsorption process encompassed a chemical reaction in one of its stages. Analysis of the thermodynamic parameters, encompassing free energy and enthalpy, supported the inference that both types of adsorption-monolayer and multilayer-govern the interaction process between metal porphyrins and CHS/ZX. This conclusion implied that metal porphyrin molecules undergo adsorption in diverse forms.

Valuable insights into the disorder of the process at the interface between the solid surface of the adsorbent and the solution can be gained by examining the alterations in the system's entropy (Silva-Medeiros et al. 2016). Table 4.15 indicated that the transfer of VO-TPP and Ni-TPP molecules from the solution with toluene to the adsorbed state on the CHS/ZX surface occurs in an orderly manner, as evidenced by the negative values of $\Delta S°$ within the temperature range of 303 to 313 K (Sahmoune 2019). Comparing the thermodynamic study parameters for both complexes, it is evident that the vanadium complex exhibited higher values than the nickel complex (see Table 4.15). This indicated that the adsorption process of the vanadium complex is more favorable and is associated with a greater release of heat. The polar characteristics of both the adsorbate and adsorbent play a significant role in influencing the behavior of the adsorption process. In the present study, both the vanadium complex and the CHS/ZX composite exhibit higher polarity compared to the nickel complex, which accounts for the ease of adsorption observed in the case of the vanadium complex.

4.11 XPS ANALYSIS AND PROPOSED ADSORPTION MECHANISM OF METAL PORPHYRINS ONTO CHS/ZX COMPOSITE

The XPS analysis provided valuable insights into the adsorption mechanism of Ni-TPP and VO-TPP onto the CHS/ZX composite, revealing several types of interactions: coordination bonds, hydrogen bonding, and π interactions. Each interaction type was identified based on the specific changes in binding energy, intensity, and peak shapes in the high-resolution XPS spectra of key elements (Ni 2p, V 2p, O 1s, N 1s, and C 1s).

Coordination interactions were evident from the deconvoluted peaks in the Ni 2p and V 2p spectra (refer to Figure 4.9 d and e). The Ni 2p spectrum displayed a prominent peak at around 853-854 eV, with satellite features at approximately 856-858 eV, confirming the presence of Ni in the +2-oxidation state. The binding energy and satellite features indicated that Ni was in a chemically complex environment, likely forming coordination bonds with oxygen-containing groups, such as hydroxyls (-OH) or silanol groups (Si-OH) on the composite surface (Kloprogge & Wood 2020). Similarly, the V 2p spectrum exhibited a peak at around 514-516 eV, characteristic of V in the +5-oxidation state (V(V)), which is typical for vanadyl (VO^{2+}) species. This peak position suggested that V was interacting with surface groups of the composite, possibly through coordination bonds with oxygen donors (Alharthi et al. 2024). The O 1s spectrum (Figure 4.21a) further supported the presence of coordination interactions, with a peak at ~530.5 eV corresponding to lattice oxygen (M-O-M) in metal oxides or silanol groups coordinated with metal centers like Ni and V. This indicated that oxygen atoms on the composite surface were involved in forming Si-O-M or Al-O-M bonds, confirming the formation of coordination bonds. Additionally, the N 1s spectrum (Figure 4.21b) showed peaks around ~398 eV and ~405-406 eV, corresponding to pyridinic or pyrrolic nitrogen and quaternary nitrogen, respectively. These peaks suggested that nitrogen atoms in the porphyrin rings were involved in coordination with metal centers, providing further evidence for chemisorption (Ma et al. 2022).

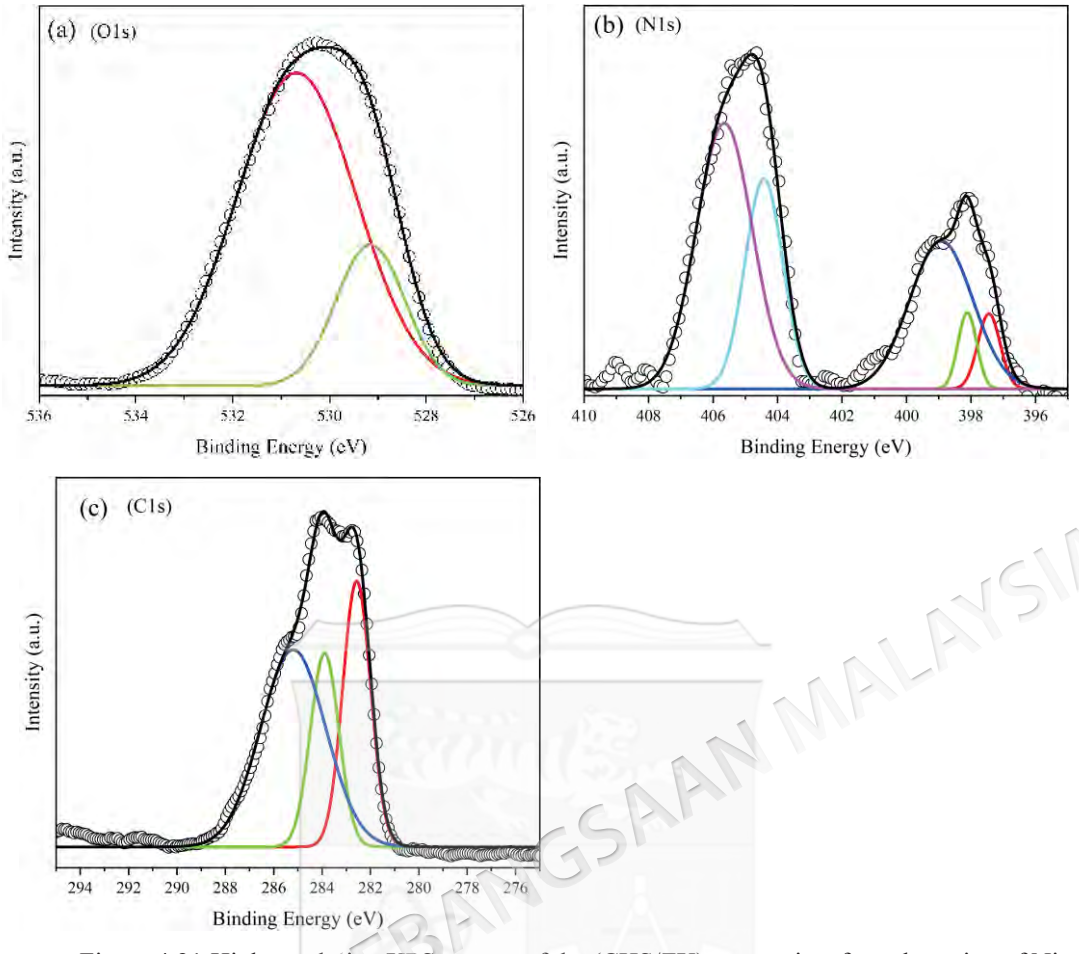

Figure 4.21 High-resolution XPS spectra of the (CHS/ZX) composite after adsorption of Ni-TPP and VO-TPP: (a) O 1s spectrum, (b) N 1s spectrum, and (c) C 1s spectrum.

Hydrogen bonding interactions were suggested by the shifts in the O 1s and N 1s spectrum. The O 1s spectrum showed a peak at ~532 eV, which was associated with hydroxyl groups (-OH) and silanol groups (Si-OH) on the zeolite surface and in the chitosan matrix. These groups are known to form hydrogen bonds with nitrogen-containing groups, such as those found in the porphyrin ring structures of Ni-TPP and VO-TPP (Zhao et al. 2021). The peak at this binding energy indicated that the hydroxyl groups were likely involved in hydrogen bonding with the adsorbed metalloporphyrins. Similarly, the N 1s spectrum displayed a peak around ~400 eV, which corresponded to amino groups ($-NH_2$) in the chitosan backbone. These amino groups are capable of forming hydrogen bonds with hydroxyl or other oxygen-containing groups on the composite, further stabilizing the adsorption process (Ma et al. 2022).

π interactions, such as π-π stacking or cation-π interactions, were indicated by the deconvoluted peaks in the C 1s and N 1s spectra. The C 1s spectrum showed (Figure

4.21c) a peak at ~284.8 eV, corresponding to aromatic carbon (C=C) from the porphyrin rings of Ni-TPP and VO-TPP. The presence of this peak suggested that π-π aggregation interactions could occur between the π-electron-rich porphyrin rings and any π-systems (Ding et al. 2021) or aromatic groups that might be present on the composite surface or that π interactions could involve cations (e.g., protonated amino groups or Na^+ ions) interacting with the π-electron clouds of the porphyrins (Kloprogge & Wood 2020). The N 1s spectrum also supported the possibility of π interactions with its peak at ~398 eV, corresponding to pyridinic or pyrrolic nitrogen in the porphyrin rings. These nitrogen environments are part of the conjugated aromatic system in the porphyrin structure and are likely involved in π interactions due to the electron-rich π system, potentially engaging in cation-π interactions with positively charged groups on the composite (Castillo & Vargas 2016). The proposed mechanism, based on the XPS results, is depicted in Figure 4.22.

The XPS analysis provided strong evidence for a multi-interaction adsorption mechanism involving coordination bonds, hydrogen bonding, and π interactions. The deconvoluted peaks and shifts in binding energy across the Ni 2p, V 2p, O 1s, N 1s, and C 1s spectra consistently supported these interactions, confirming the complex nature of the adsorption process of metalloporphyrins onto the CHS/ZX composite.

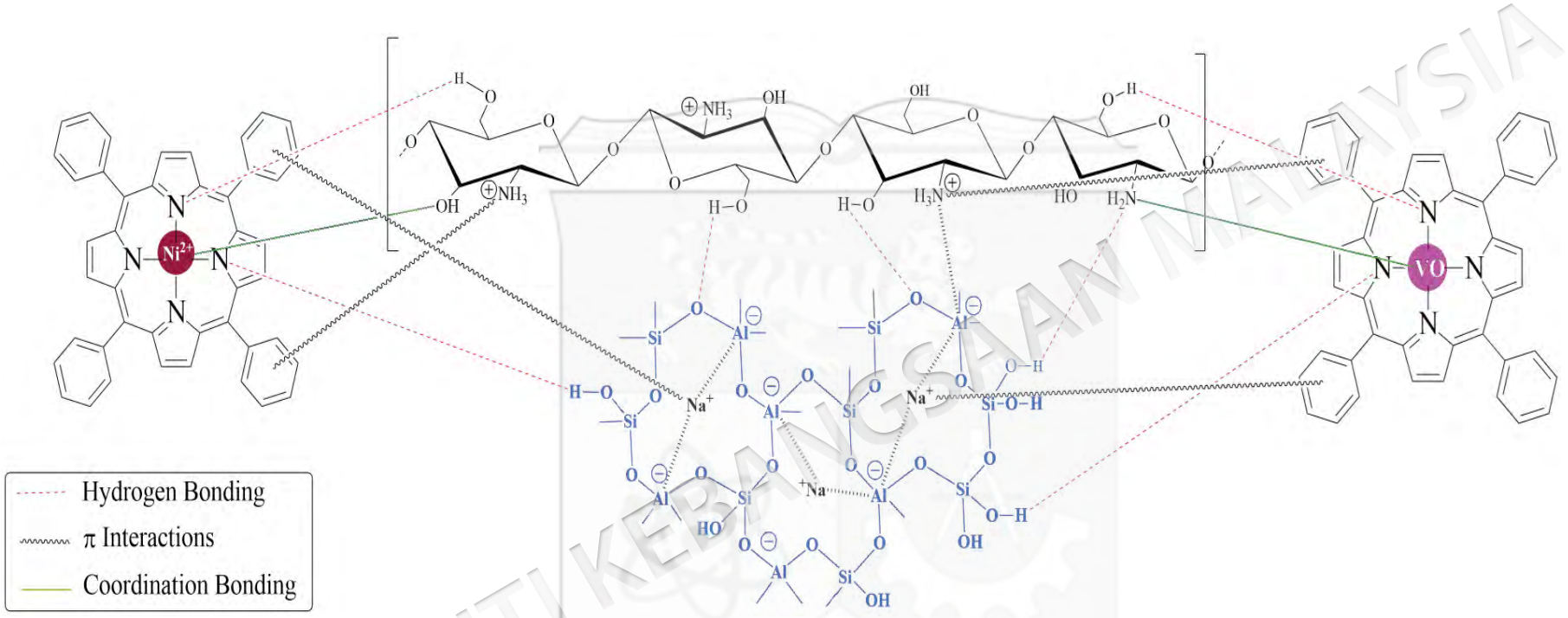

Figure 4.22 The mechanism of removing nickel and vanadyl porphyrins using the CHS/ZX composite.

4.12 Desorption study (recovery study)

4.12.1 Effect of eluents type

The adsorbents can be used in the multiple sorption/desorption cycles by applying desorption process, and it notably reduces the cost of treatment procedure, adsorbents supply and the disposal problems of exhausted adsorbents (Bayuo et al. 2024). In the present study, five different eluents have been used to investigate metal porphyrins desorption from CHS/ZX composite. As can be seen from Figure 4.23, It was observed that the most efficient desorption of metal-porphyrins was achieved using chloroform. While hydrophobicity typically enhances the efficiency of organic regenerating agents (Genç et al. 2022), our findings reveal that chloroform, despite having lower hydrophobicity than toluene, showed higher efficiency in removing the adsorbed metal-porphyrin complexes from the adsorbent. This unexpected result can be explained by the competitive interactions between toluene and the porphyrin molecules for adsorption sites (Coltre et al. 2020). Toluene, structurally more similar to porphyrins, likely engages with the adsorption sites more readily, thereby reducing its desorption efficacy compared to chloroform.

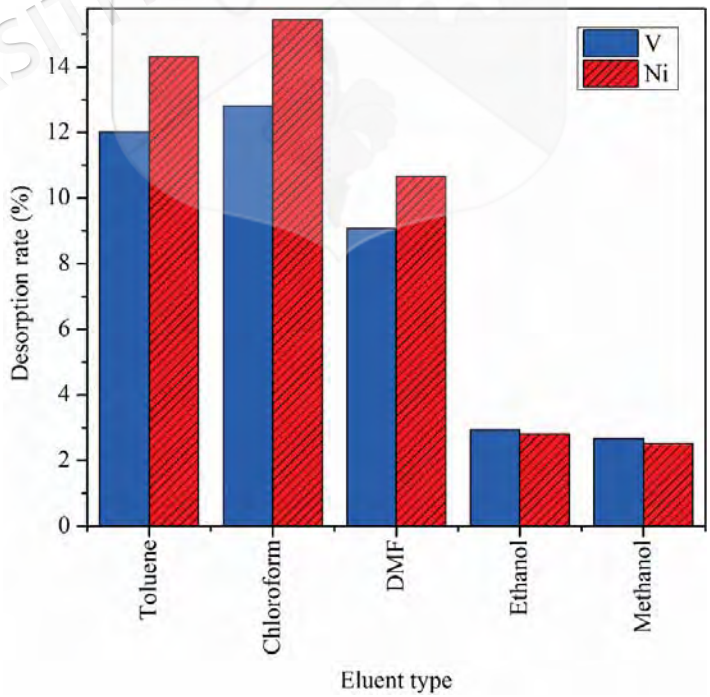

Figure 4.23 Effect of eluent type on the desorption of metal porphyrins

4.12.2 Effect of temperature

Temperature is one of the important parameters which plays significant towards adsorbate desorption. Based on obtained data, desorption efficiency was found to be increased with increase in temperature from 30−90°C (as shown in Figure 4.24). The use of higher temperatures during the desorption process might have influenced the increase in the agitation degree of the solvent molecules, promoting a reduction in their viscosity and an increase in the diffusion rate on the surface of the adsorbent (Caetano et al. 2023a). This increases its energy level in relation to the adsorbed and solvated states, a necessary condition for the desorption of organic molecules. Temperature can also be a key factor in increasing the solubility of porphyrinic molecules in the eluent, thereby enhancing the desorption rate. However, further temperature increases reduced the desorption efficiency of metal porphyrins. According to Mohammad et al. (2020), an increase in temperature leads to enhanced desorption efficiency up to a certain limit. Beyond this point, further temperature increases result in the extraction of more inactive compounds, which may be due to greater diffusion of metal porphyrins into the solid phase.

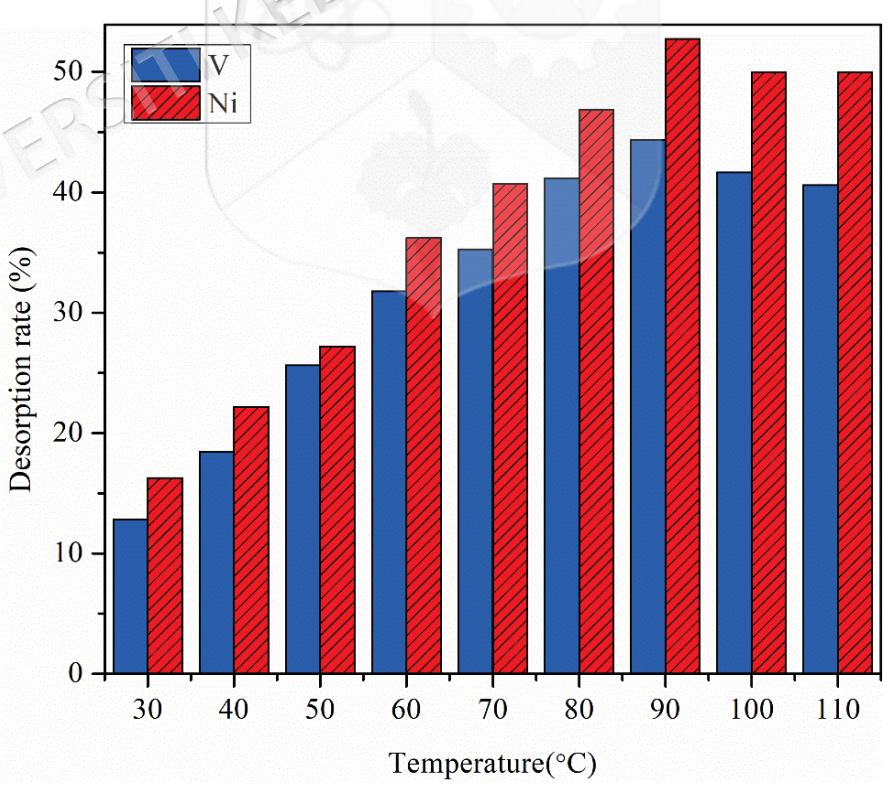

Figure 4.24 The effect of temperature on desorption of metal porphyrin using thermo-chemical method

4.12.3 Effect of saturated composite weight

The effect of CHS/ZX composite loading on desorption efficiency of metal porphyrins was also investigated by varying the mass loading ranging from 10 to 50 mg, while temperature and contact time were kept constant at 90°C, and 5 h, respectively. Figure 4.25 shows that the metal porphyrins desorption percentage significantly reduced by increasing the dose of CHS/ZX composite loading from 10 to 50 mg. The decrease in metal porphyrin desorption efficiency with increasing adsorbent amount was suggested to be the result of increasing particle interaction and aggregation, leading to a reduction of total adsorbent surface and decrease in diffusional path length under constant elution concentration and volume (Daneshvar et al. 2017). As the composite loading increases, the eluent volume to composite ratio decreases, thereby diminishing the eluent's impact on porphyrin desorption.

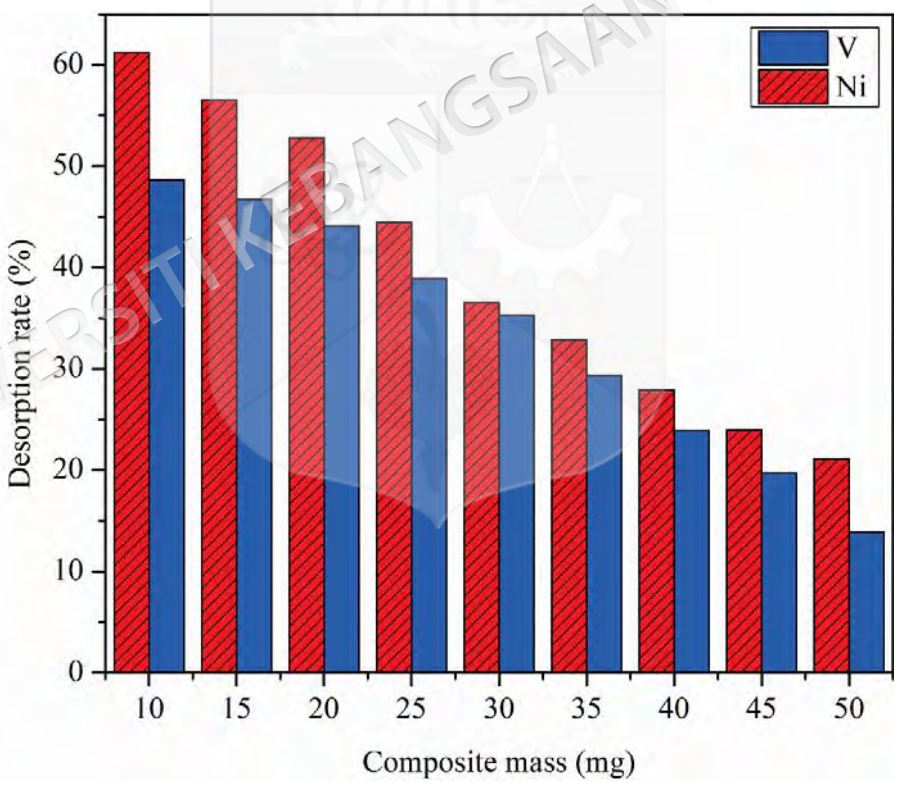

Figure 4.25 Effect of different metal porphyrins saturated CHS/ZX composite loading

4.12.4 Effect of eluent volumes

The effect of different volumes (10 to 40 mL) of chloroform on desorption efficiency of metal porphyrin from CHS/ZX composite was studied, while composite loading,

temperature and contact time were kept constant at 10 mg, 90°C and 5h, respectively. As can be seen from Figure 4.26, metal porphyrins desorption efficiency increased with an increase in the eluent volume between 10 and 30 mL, then it reached a plateau up to 40 mL. The reasons for this observation can be attributed to the fact that the increasing eluent volume provided a more effective interaction between the eluent and solid phases. By increasing the eluent volume, the ratio of eluent volume in relation to the composite mass is increased. It means that there is a higher eluent volume for a known porphyrin loaded CHS/ZX composite and the impact of eluent on the porphyrin desorption efficiency is increased. The plateau pattern at higher volumes shows that increasing the eluent volume more than the optimum value had no significant effect on the metal porphyrins desorption efficiency (Daneshvar et al. 2017).

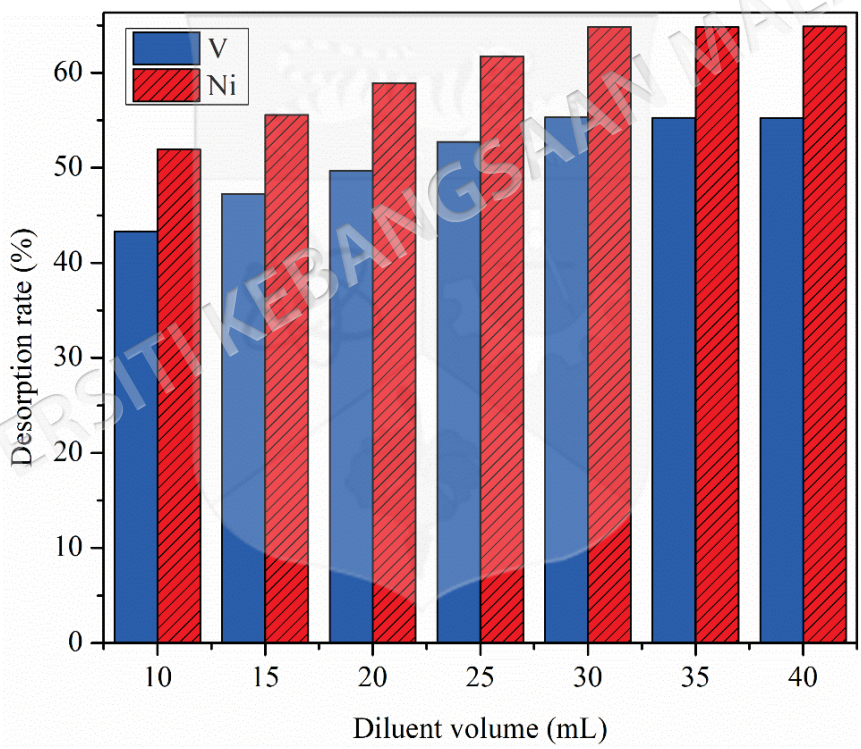

Figure 4.26 Effect of different eluent volume

4.12.5 Effect of contact time and kinetic models

Figure 4.27 shows the effect of contact time at initial porphyrin concentration of 20 mg/L. The porphyrin desorption was rapid in the first 3 h, then continued with a slower rate during 3-6 h and finally remained constant up to 7 h. These findings are attributed to the fact that at the initiation of the experiment, the solid phase exhibited a high

concentration of porphyrins. Furthermore, the initial phase is characterized by the purity of eluents, likely contributing to an intensified driving force for the concentration gradient. As time progresses, a reverse scenario unfolds wherein the concentration of porphyrins diminishes in the solid phase while concurrently increasing in the liquid phase. Consequently, the rate of porphyrin desorption decreases until equilibrium is achieved (Daneshvar et al. 2017).

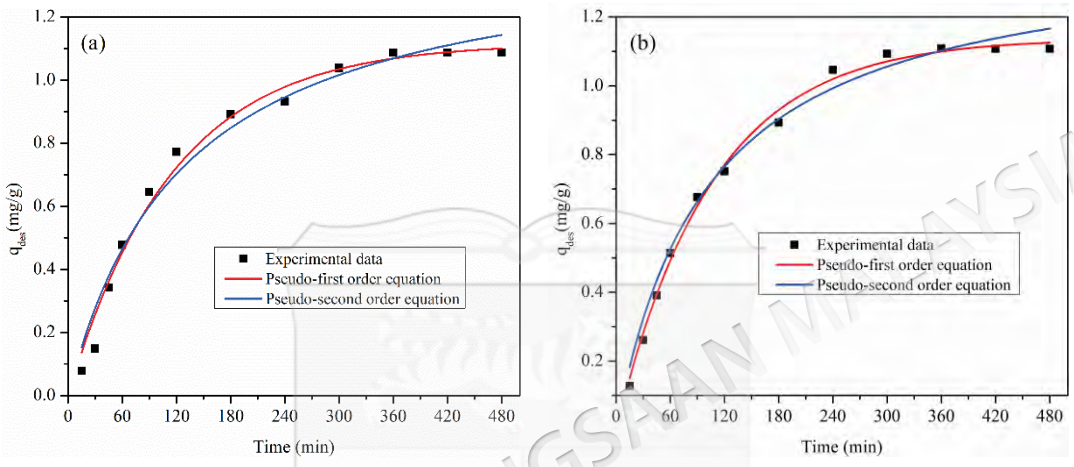

Figure 4.27 Kinetic models for (a) VO-TPP and (b) Ni-TPP desorption onto CHS/ZX composite.

The desorption kinetics studies were essential to better understand the mechanism of the adsorbent's regeneration cycle and the potential rate-controlling step. The pseudo-first order (PFO) and pseudo-second order (PSO) kinetics models were used to study the desorption process of metal porphyrins on prepared CHS/ZX composite using the chloroform as eluent. The non-linear first- and second-order kinetics equations can be written as the following Equations. (4.21) and (4.22):

$$q_t = q_e \left(1 - exp^{(-k_1 t)}\right) \tag{4.21}$$

$$q_t = \frac{q_e^2 k_2 t}{1 + q_e k_2 t} \tag{4.22}$$

where, $q_{e\ des}$ and $q_{t\ des}$ are the amount of metal porphyrins (mg/g) desorbed at equilibrium and time t (min), respectively, while k_1 is the rate constant of the pseudo-first order kinetics (min^{-1}) and k_2 is the rate constant of desorption ($g(mg \cdot min^{-1})$). The non-linearized plots of the pseudo-first order and pseudo-second order kinetics using chloroform as the eluent are presented in Figure 4.27. The determined parameters for

these two models used for the desorption process are summarized in Table 4.16. The fitness of each model was evaluated using the non-linear regression coefficient, R^2, residual root means square error (RMSE), and the sum of squares error (SSE) is calculated from the following Equations (4.23) and (4.24), respectively (El Messaoudi et al. 2023):

$$RMSE = \sqrt{\sum_{i=1}^{n} \frac{\left(q_{e\ des\ exp} - q_{e\ des\ cal}\right)^2 i}{n}} \tag{4.23}$$

$$SSE = \sum_{i=1}^{n} \left(q_{e\ des\ exp} - q_{e\ des\ cal}\right)^2 i \tag{4.24}$$

where, n represents the number of experimental points.

The metal porphyrins desorption process was found to have a better fit with the pseudo-first order kinetics model for nickel and vanadium porphyrins. Meanwhile, the values of RMSE and SSE were lower in the pseudo-first order kinetics model compared pseudo-second order kinetic model. Higher R^2 values and lower RMSE and SSE values, respectively, showed that the pseudo-first order model used chloroform as an eluent. In addition, the $q_{e\ des}$ values of the pseudo-first order model was closer to the experimental $q_{e\ des}$ values compared with the pseudo-second order model. The rate constants of the desorption process were also found to be different using different models. Table 4.16 shows that the values of the desorption rate constant (K_2) for the pseudo-second order model are lower compared to the desorption rate constant (K_1) for pseudo-first order. A low desorption rate constant shows that a shorter time is needed to achieve desorption equilibrium (Ahammad et al. 2021).

Table 4.16 Pseudo-first order and pseudo-second order kinetics studies for desorption of metal porphyrins CHS/ZX composite

Models	Parameters	VO-TPP desorption	Ni-TPP desorption
Pseudo-first order	R^2	0.983	0.995
	q_e	1.117	1.138
	K_1	0.008	0.009
	RMSE	0.354	0.393
	SSE	1.758	1.857
Pseudo-second order	R^2	0.973	0.991
	q_e	1.444	1.412
	K_2	0.005	0.007
	RMSE	0.428	0.459
	SSE	2.568	2.960

The results indicate that the desorption of nickel and vanadium porphyrins from the CHS/ZX composite with chloroform as the eluent follows a physical desorption mechanism controlled by diffusion, as evidenced by its good fit to the pseudo-first-order kinetic model. The desorption rate would, therefore, be essentially determined by the rate of porphyrin transfer from the surface to the solvent and not by any other chemical reactions. The higher R^2 values, along with the lower RMSE and SSE values obtained for the pseudo-first order model, hint at a better fit of the desorption process by the pseudo-second order model. Furthermore, desorption rate constants (K_1) pertaining to the pseudo-first order model are quite high, indicating that the attainment of equilibrium is faster and thus further proving that physical interactions, not chemical bonds, rule the desorption mechanism (Ahammad et al. 2021). In summary, the high linear correlation coefficient obtained between predicted and experimental qe des values confirms the suitability of the pseudo-first order model for interpreting the desorption dynamics within the present system.

Therefore, this study has proven that the metal porphyrins desorption process using chloroform as an eluent followed the pseudo-first order kinetics model.

4.12.6 Effect of initial concentrations of metal porphyrins

Figure 4.28a displays the metal porphyrins desorption rate profiles at six different initial concentrations. At lower initial concentrations (e.g., 10-20 mg/L), the surface of the CHS/ZX composite has more available active sites for the metal porphyrins to attach to. These metal porphyrins are not in high competition for binding, meaning they form weaker, more reversible interactions with the adsorbent. As a result, during desorption, the energy required to release the porphyrins from the surface is relatively low. This leads to higher desorption rates, as the metal porphyrins are less tightly bound and can easily detach from the composite surface. The presence of abundant active sites also contributes to maintaining a high desorption efficiency.

Additionally, at low concentrations, electrostatic repulsion forces between adsorbed species are lower, which allows the desorption process to be more efficient. The physical and chemical interactions between the composite and metal porphyrins at lower concentrations are less intense compared to those at higher concentrations, which justifies the higher desorption rates.

As the concentration of metal porphyrins increases (e.g., 40-60 mg/L), the active sites on the CHS/ZX composite surface become more saturated. At this point, the available sites for adsorption become limited, leading to stronger interactions between the adsorbent and the metal porphyrins. The metal porphyrins, in this case, have to compete for the remaining active sites, which results in tighter binding to the surface. These stronger interactions, which may include van der Waals forces, electrostatic attraction, or coordination bonds, make desorption more challenging. As a result, the desorption rates decrease since more energy is required to overcome these interactions and release the metal porphyrins from the composite surface.

Additionally, at higher concentrations, multilayer adsorption or stronger chemical interactions might occur, reducing the ability of the metal porphyrins to desorb easily. This behavior aligns with the principles of adsorption isotherms, where saturation leads to reduced desorption due to stronger adsorbate-adsorbent interactions.

Figure 4.28b explores the impact of varying initial metal porphyrins concentrations on the desorption capacity. In contrast, the desorption capacity (q_{des}), which represents the amount of metal porphyrins desorbed per unit of composite, increases with the initial concentration. This is because, at higher initial concentrations, more metal porphyrins are adsorbed onto the surface during the adsorption process, leaving a larger quantity available for desorption. Even though the desorption rate decreases at higher concentrations, the overall desorbed amount increases, as indicated by the rising trend in q_{des}. This can be attributed to the fact that a greater total quantity of metal porphyrins was initially adsorbed, resulting in more being desorbed despite the lower percentage desorption.

Additionally, the increased q_{des} at higher concentrations reflects the larger reservoir of metal porphyrins available on the composite surface, which balances the decrease in desorption rate. This outcome suggests that while it becomes harder to desorb individual porphyrins, the total quantity desorbed still increases due to the larger initial adsorption.

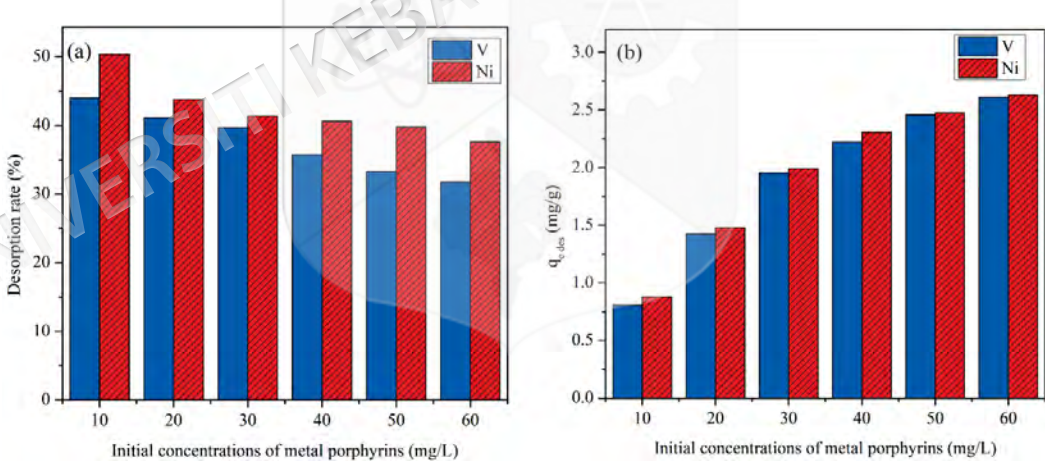

Figure 4.28 Effect of different initial metal porphyrins concentrations in desorption experiment

4.13 ADSORPTION-DESORPTION OF METAL PORPHYRINS CYCLES

The subsequent adsorption-desorption cycles of CHS/ZX facilitated the assessment of this material's capability in the removal and recovery of vanadyl and nickel porphyrins. This evaluation was based on the results of the removal rate ($R\%_{ads}$), removal capacity

($q_{e\ ads}$), desorption rate ($R\%_{\ des}$), and desorption capacity ($q_{\ des}$), which are detailed in Table 4.17.

Based on the information presented in Table 4.17, it is evident that there was a decline in the removal percentage and adsorption capacity of vanadyl and nickel porphyrins on CHS/ZX as the number of cycles increased. The most notable disparity was observed after the fourth cycle, with a reduction of roughly 50.09% and 51.72% for the removal rate of nickel and vanadyl porphyrins, respectively.

Table 4.17 Adsorption-desorption cycles of metal porphyrins in CHS/ZX under optimum experimental desorption conditions

cycle	Ni-TPP porphyrin				VO-TPP porphyrin			
	$q_{e\ ads}$ (mg/g)	$R\%_{\ ads}$	$q_{\ des}$ (mg/g)	$R\%_{\ des}$	$qe_{\ ads}$ (mg/g)	$R\%_{\ ads}$	$q_{\ des}$ (mg/g)	$R\%_{\ des}$
1	7.97	79.79	4.32	54.19	8.81	88.18	3.92	44.54
2	7.23	72.35	4.89	67.67	8.11	81.14	4.89	60.34
3	6.72	67.28	5.31	78.95	7.54	75.42	5.57	73.87
4	6.47	64.77	6.20	95.84	6.98	69.87	6.11	87.47
5	5.00	50.09	7.28	145.41	5.17	51.72	6.56	126.99

Notwithstanding the reduction in the factors related to the adsorption of vanadyl and nickel porphyrins on the CHS/ZX surface, a gradual increase in the percentage of porphyrin desorption rate and desorption capacity was observed with each cycle. Consequently, the desorption of porphyrin molecules previously adsorbed accounts for the R% des values exceeding 100% from the fifth cycle onward. Likely, as the cycles advanced, the strength of the adsorbent-adsorbate interactions diminished, promoting desorption. This phenomenon, referred to as the carry-over effect, is a common issue in HPLC analyses due to its impact on the quantitative results per run (Caetano et al. 2023a). Nevertheless, the outcomes obtained at the conclusion of the regeneration cycles indicated that the carry-over effects were beneficial, leading to an increment in the partial results achieved per cycle. Over the course of the five cycles, approximately 36.63 mg/g and 33.42 mg/g of vanadyl and nickel porphyrins were adsorbed, respectively. Notably, around 73.7 % (27.076 mg/g) of the adsorbed vanadyl porphyrins and 83.8% (28.02 mg/g) of the adsorbed nickel porphyrins were recovered.

Efforts have been made to regenerate the adsorbent utilized for the extraction of nickel and vanadium from petroleum substances. The regeneration process involved soaking the adsorbent in a hydrochloric acid solution to reclaim the nickel ions, as demonstrated in both studies (Shahat et al. 2018; Xu et al. 2018). The recovery was limited to nickel ions, leaving the free porphyrin base on the adsorbent's surface, which possesses considerable value from both laboratory and industrial perspectives.

4.14 SUMMARY

The potential of using a composite material consisting of chitosan and synthetic zeolite-X from coal fly ash (CH/ZX) as a demetallization agent for vanadyl and nickel porphyrin was investigated. The CHS/ZX composite was fabricated by immersing as-synthesized zeolite particles into the chitosan-gelling solution, and the matrix formulation was optimized via response surface methodology (RSM). The model's reliability in predicting the removal of metal porphyrins using the values of the established variables was excitedly validated with a reasonable accuracy error of 0.5%. The synthesized composite was systematically characterized using X-ray Photoelectron Spectroscopy (XPS), SEM, BET, XRD, FTIR, TGA, and CHN analyses. The adsorption and desorption mechanisms of metal porphyrins by the CHS/ZX composite were investigated using a model solution containing vanadyl and nickel tetraphenyl porphyrin (VO-TPP and Ni-TPP) in toluene. The CHS/ZX composite exhibited double the capacity for removing metal porphyrins compared to the individual components CHS and ZX. Several parameters that significantly influenced the capacity of adsorption were studied, including the temperature of adsorption, the initial concentration of metal-porphyrins, and the dose of CHS/ZX composite. The optimal conditions of the adsorption process were found to be 25°C (the lower temperature), 0.006 g of CHS/ZX (minimum of adsorbent dose), and 20 mg/L (maximum of porphyrin concentration). The experimental results consistently demonstrated that the pseudo-second order model provided an excellent fit for the adsorption kinetics. The initial stage of adsorption, particularly within the first hour, was marked by its rapidity, suggesting that physisorption forces primarily govern the interaction between metal-porphyrins and CHS/ZX. Furthermore, vanadyl-porphyrins exhibit a greater affinity for the CHS/ZX composite, as indicated by the q_e values when compared to Ni-porphyrins.

The adsorption processes of VO-TPP and Ni-TPP on CHS/ZX were effectively assessed through various equilibrium models, such as Langmuir, Freundlich, and Dubinin-Radushkevich (D-R). The adsorption process was characterized as exothermic and spontaneous based on the calculated thermodynamic parameters. The XPS analysis provided strong evidence for a multi-interaction adsorption mechanism involving coordination bonds, hydrogen bonding, and π interactions. Different factors influencing the desorption of metal porphyrins from CHS/ZX composite were explored. Chloroform emerged as the most efficient eluent due to its hydrophobic nature, facilitating superior desorption compared to other solvents. Temperature played a crucial role, with increasing temperatures initially enhancing desorption efficiency by promoting solvent agitation and diffusion, yet excessively high temperatures ultimately led to decreased efficiency. Moreover, the mass loading of the CHS/ZX composite inversely affected desorption, as higher loading resulted in decreased desorption percentage due to increased particle interaction and reduced surface area availability. Additionally, the volume of eluent used significantly impacted desorption efficiency, with increasing volumes initially improving efficiency up to an optimal point before further increases yielded diminishing returns. The desorption process exhibited time-dependent behaviour, with rapid desorption initially followed by a slower rate until equilibrium was reached. Finally, higher initial concentrations of metal porphyrins led to decreased desorption efficiency, likely due to increased particle interaction and limited eluent volume. The results regarding adsorption capacity and desorption percentage confirmed that, following five adsorption-desorption cycles, approximately 73.7% and 83.8% of the vanadyl and nickel porphyrins adsorbed by CHS/ZX were successfully recovered. The results obtained from model solutions of synthetic porphyrins indicate the potential of utilizing the prepared materials, which possess diverse active groups and a mesoporous structure, to separate and recover petroleum porphyrins from real petroleum samples.

CHAPTER V

REMOVAL OF NICKEL, VANADIUM, AND IRON FROM CRUDE OIL USING CHS/ZX DEMETALLIZATION AGENT.

5.1 INTRODUCTION

Crude oil is generally defined as a fuel liquid produced through long-time geological activities involving high temperature and pressure in oil reservoirs associated with sedimentary rocks and situated beneath earth's surface piles (Furimsky 2016). This natural resource comprises light and heavy hydrocarbon fractions with other impurities, including oxygenated-, nitrogenated-, and sulphated-compounds, alongside trace metals (Munoz et al. 2019), which must be removed for production of high quality of crude oil containing paraffin (alkanes), naphthenes (cycloalkanes), as well as aromatic compounds (Corma et al. 2017). Notably, oxygenated, nitrogenated, and sulfonated compounds can be effectively removed through absorption and hydrocracking processes (Argyle & Bartholomew 2015). However, trace metals pose a challenge due to their high solubility, making them difficult to eliminate. These unremoved species can poison refinery catalysts and result in poor reaction performance (Jenifer et al. 2015). Indeed, the crude oil electrical desalting process can remove most metals, such as Na, Ca, and Mg, but not for the Ni and V species (Yu et al. 2015). Noteworthy to mention, Ni and V are the most abundant trace metals in petroleum and are present in amounts from about 10 to about 2000 ppm with V, generally, in higher concentration than Ni. Both Ni and V occur in petroleum in two forms, porphyrinic and non-porphyrinic (Fan et al. 2020).

The petroporphyrins are concentrated in the high boiling point residual and often composed of or associated with heavy oil molecules (preferentially for asphaltene or resin) (Castillo et al. 2023). Special attention has been paid to these constituents over the past several years. This is because metal complexes are poisonous and can foul catalysts or cause undesirable side reactions in refinery operations, such as fluid

cracking and hydrodesulfurization (Adanenche et al. 2023). On the other hand, the photochemical and photophysical properties of metal porphyrins have been studied extensively, owing to the importance of the porphyrin ring system in photosynthetic processes and in biological systems (Monteiro et al. 2023).

Metal porphyrins are compounds with a number of unique properties that allow their use in manufacturing of various catalysts, pharmaceuticals, semiconductors, and dyes. To successfully develop these and other areas, a considerable variety of metal porphyrins with various sets of substituents is needed. Along with synthetic methods of obtaining it is possible to obtain natural metal porphyrins from various raw materials of vegetable and animal origin. It is also possible to consider various oil facilities with high content of vanadium and nickel as the sources of natural porphyrins.

Currently, removal of vanadium and nickel is an urgent problem for heavy oil; a variety of methods are used and developed to do this. Deasphalting process is particularly suitable to remove metals and asphaltenes from oil stock. In case of deasphalting, asphaltene concentrate formed as a nontarget product can be regarded as a raw material for crude extracts of metal porphyrins (Yakubov et al. 2016). The extraction of metal porphyrins from asphaltenes is complicated because of the tendency to aggregate with asphaltene aggregates (Castillo et al. 2023). This interaction between asphaltenes and petroporphyrins may reduce the separation efficiency significantly.

Petroporphyrins are constructed with a core of π-electron systems, which tend to be noncovalently associated or adsorbed to polycyclic aromatic compounds in crude oils by physical interactions (Chen et al. 2017). Chen et al. (2013) studied the model of vanadium porphyrin adsorption to C7-asphaltene in the pentane solution. The molecular evidence of adsorption was identified by using TEM, FT-ICR MS, and BET. The thermodynamics calculation showed strong interaction between porphyrin and asphaltene. Yin et al. (2009) reported difficulties in separating the petroporphyrins from asphaltenes by using chemical modification and selective affinity chromatography. The limitations of the approach likely result from the aggregation of asphaltene with vanadium components.

Shiraishi et al.(2000) developed the demetallization process from model metal porphyrins solution and residue oils based on a combination of photochemical reaction and liquid-liquid extraction. It was found that this first process was able to demetalize “free”-type metal porphyrins but had difficulty in the demetallization of “bound”-type metal porphyrins, which are associated strongly with the asphaltenic molecules in residue oil. To weaken this association and thus convert the bound-type metal porphyrins to the free-type ones, a hydrogen-donating polar solvent, 2-propanol, was added to the residue oil and photoirradiated.

Based on the results presented in the fourth chapter, it was confirmed that the chitosan/zeolite X (CHS/ZX) composite, synthesized from coal fly ash, demonstrates remarkable effectiveness as a demetallization agent, particularly for the removal of free metal porphyrins. Nevertheless, the study was limited as the oil stock originated from model solutions, which may not fully demonstrate its effectiveness in real refinery conditions. Therefore, this study explores a new demetallization process for vanadyl and nickel porphyrins using real crude oil from Basrah as an extension to our previous work through the simultaneous release of petroporphyrins and adsorptive removal processes using CHS/ZX composite as a demetallization agent. The study begins with fractionating crude oil samples, and then it uses the solvent method to determine the metallic distribution in saturates, aromatics, resins, and asphaltenes (SARA) fractions. Furthermore, the demetallization process was optimized under different conditions, such as type of proton-donor solvent, adsorbent dosage, contact time, and temperature, to evaluate the adsorbent performance. The study concludes with an assessment of the adsorbent performance after the removal process to determine its reusability, aiming for an economical and sustainable solution.

5.2 EXPERIMENTAL

5.2.1 Chemicals

The demetallization process has been applied to two Iraqi petroleum crudes, Basrah medium and Basrah heavy oils obtained from ONTA company, containing various concentrations of (V) and (Ni). Nitric acid (70%) and hydrochloric acid (37%) were sourced from Sigma-Aldrich. The analytical grade solvents used included toluene

(99.9%), 2-propanol (99.9%), n-heptane (99%), acetone (99.5%), chloroform (99.9%), acetonitrile (99.5%) and 1-hexanol (99.5%) from Sigma-Aldrich; ethanol (99.5%) from Acros Organics; and cyclohexanol (99.9%) from HmbG. Medium molecular weight CHS with a degree of deacetylation between 75–85% and acetic acid were purchased from R&M (Malaysia). The adsorbents, including aluminum oxide neutral, were purchased from Sigma-Aldrich, while zeolite X, derived from Malaysian coal fly ash, was synthesized as described in Section 3.2.3. The adsorbent CHS/ZX used in this study was synthesized in the previous chapter, as detailed in Section 4.2.10.

5.2.2 Distribution of metallic components in fractions of Basrah crude oil samples

Fractionation is essential for analyzing the metallic elements present in the fractions of the studied crude oils. To prevent the loss of metallic components that can occur with the conventional liquid-solid adsorption chromatography (LSAC) method, a solvent-based approach was employed to separate the crude oil fractions including asphaltenes and resins.

a. Deasphalting of the studied crude oils

Based on China's standard test method SH/T 0266-1992 for the determination of asphaltene content in petroleum, the deasphaltization process followed a series of steps that began with the preparation of 50 g of crude oil, which is placed in a 500 ml round-bottom flask equipped with a reflux condenser and a heater. To this, 300 ml of n-heptane was added. The mixture was then thoroughly mixed using a magnetic stir bar on a hotplate stirrer. The mixture was refluxed for 2 h at 98°C (n-heptane boiling point). After refluxing, the mixture was left to settle in a dark place at an ambient temperature for 24 h, allowing the asphaltene fraction to separate. The mixture was then filtered to remove the asphaltenes, which were continuously washed with n-heptane until the solution turned colorless. The yield of asphaltenes was calculated using the following equation:

$$Asphaltene_{yield} = \frac{m_1 - m_0}{m_s} \times 100 \quad (5.1)$$

where $\text{asphaltenes}_{\text{yield}}$ refers to the yield of asphaltenes expressed as a percentage by weight; m_1 represents the weight of the filter with asphaltenes collected on it, in grams; and m_0 denotes the weight of the empty filter, in grams, m_s represents the wight of crude sample in grams.

Finally, the deasphalted oil (maltene) was separated from the n-heptane through distillation to use in the next stage.

b. Isolation of resins from deasphalted oil (maltene) via precipitation

The following steps were involved in the process of isolating resins from deasphalted oil (maltene) using acetone as a solvent. First, 50 g of the deasphalted oil (maltene) was placed into a beaker. Then, 300 ml of acetone was added to the beaker containing the maltene. The mixture was stirred thoroughly using a magnetic stir bar to ensure the maltene was evenly dispersed in the acetone. As the acetone interacted with the maltene, the resins, which are insoluble in acetone, began to precipitate out as solids (sticky solids). Once precipitation was completed, the solid resin fraction was separated by vacuum filtration. The filtered resins were then washed with additional acetone until the filtration was colorless, ensuring that all soluble components were removed. Finally, the resin fraction was air-dried under ambient conditions to remove any residual acetone, completing the isolation process.

5.2.3 Metallic element occurrence in Basrah crude oil

a. Inorganic and organic metallic components

The process began by weighing 50 g of investigated crude oil and transferring it into a 500 ml round-bottom flask. Subsequently, 200 ml of toluene was added to the flask equipped with a reflux condenser. The mixture was refluxed for 2 h at 110 C, ensuring the crude oil was fully dissolved in the toluene before proceeding to the next step. Following the reflux period, the mixture was allowed to cool at room temperature. Equal volumes of deionized water (150 ml) and absolute ethanol (150 ml) were then added to the flask. The mixture was thoroughly stirred for 30 min to enhance the separation process. Subsequently, the mixture was transferred to a separatory funnel, allowing the

phases to separate. The water phase (bottom layer) was carefully decanted from the funnel, while the oil phase (top layer) was retained. This extraction process was repeated twice, with the oil phases from each extraction combined.

The oil phase was subsequently transferred to a clean round-bottom flask and placed in an oil bath maintained at a temperature of 110°C. The toluene was allowed to evaporate completely, leaving behind the oil phase. The residue obtained from the oil phase was then collected for further analysis. The water and oil phase samples underwent inductively coupled plasma mass spectrometer (ICP-MS) analysis to determine the metallic elements present. The concentrations of water-soluble (inorganic) and oil-soluble (organic) metallic elements were recorded.

b. Metal salts of petroleum acids components

In this procedure, we replicated the previous steps with specific modifications: the extraction solvent was replaced by a mixture of 1% acetic acid solution and absolute ethanol. Our focus shifted to analyzing the proportion of ionized and non-ionized metallic elements within an acidic environment. The remaining steps remained consistent, including the dissolution of crude oil in toluene, solvent evaporation, and subsequent ICP-MS analysis of the metallic elements.

c. Metalloporphyrins and non-metalloporphyrins components

The dissolution of crude oil samples was replicated using 200 ml of chloroform under refluxing conditions for 2 h. Subsequently, the mixture was treated with 100 g of aluminum oxide (alumina), ensuring thorough mixing to achieve complete adsorption of the target components. The solid phase was then separated from the liquid phase through vacuum filtration, leaving the alumina with adsorbed materials. The saturated alumina with the adsorbed materials, was transferred to a Soxhlet extractor, where it underwent extraction with acetonitrile. The extraction process continued until the porphyrins were fully extracted into the acetonitrile. Finally, the acetonitrile extract containing the porphyrins was collected, and the abundance of metallic elements within this extract was measured using (ICP-MS).

5.2.4 Measuring the metals content in crude oil

The samples underwent analysis for Ni, V, and Fe concentrations according to the standard test method (ASTM D5708-02). A precise quantity of crude oil is accurately weighed using a ceramic crucible, slowly heated and then ignited. After combustion, the crude oil was calcined in a muffle furnace at 600 ± 25°C to remove carbon residues. After the ash was allowed to cool, a small volume of distilled water was added to wet the ash and nitric acid, and the hydrochloric acid solutions were then added. The crucible was heated slowly to dissolve the ash, and the solution was removed quantitatively into a volumetric flask. The residual metals content of crude oil was analyzed with (ICP-MS).

5.2.5 Demetallization study of Basrah crude oil

A proton-donor solvent was added to the crude oil to facilitate the release of porphyrins, ensuring optimal conditions for metal removal. An ultrasonication treatment of 30 min was employed to ensure the homogeneity of crude oil solutions for petroporphyrin removal experiments. Experimental assessments regarding metal adsorption from Basrah crude oil samples were conducted using CHS/ZX as the adsorbent material in a batch mode system. Specifically, 25 mL of the crude oil solution, with a defined metal concentration, was placed in a 100 mL round-bottom flask equipped with a condenser to prevent the loss of volatile components and solvents. Laboratory experiments were conducted under varied operating conditions, including type and volume of proton-donor solvent, temperature (ranging from 28°C to 160°C), adsorbent amount (50–400 mg/L of CHS/ZX), and contact time (30–300 min). Each experiment was performed in triplicate to enhance precision and minimize experimental discrepancies. Following the completion of each experiment, the samples underwent vacuum filtration to remove any residual adsorbent material in the treated oil. After the phase separation step, the treated samples were subjected to vacuum distillation to separate and recover the proton-donor solvent. The concentrations of both Ni and V in the treated oil samples were estimated based on the method described in Section 5.2.4.

The efficiency of vanadium/nickel removal from the crude oil was determined by ICP-MS; the removal percentage can be calculated using the following equation:

$$R\% = (C_0 - C_t)C_0 \times 100 \quad (5.2)$$

where %R is the percentage removal of vanadium/nickel elements from crude oil, C_0 is the initial concentration of vanadium/nickel in crude oil (mg/L), and C_t is the concentration of metals in crude oil at any time of treatment (mg/L).

5.2.6 Instruments and material characterization

X-ray fluorescence spectroscopy (XRF) was utilized for elemental analysis using a Philips PW2404 wavelength-dispersive spectrometer. The spectrometer, equipped with a rhodium tube, scintillation counter, and LiF 200 crystal, operated at 50 kV and 70 mA. The elemental composition of carbon, hydrogen, and nitrogen (C/H/N) was determined using the Flash EA1112 organic trace element analyzer. A Perkin Elmer Spectrum 100 FT-IR with a resolution of 4 cm^{-1} and a range of 300–4000 cm^{-1} was employed to identify the chemical functional groups in the samples. The concentrations of nickel (Ni) and vanadium (V) ions were measured using a NexION 2000 Perkin Elmer USA inductively coupled plasma atomic emission spectrometer (ICP-MS) before and after treatment with the composite adsorbent.

5.3 RESULTS AND DISCUSSION

5.3.1 General characteristics of the studied crude oil

Table 5.1 presents a comparison of two Basrah crude oil types, Basrah heavy and Basrah medium, highlighting their physical properties and metal content, which are crucial for refining processes. Basrah heavy crude oil, with a density of 0.91 g/mL, is denser than Basrah medium, which has a density of 0.8807 g/mL. This higher density for heavier crude oils was attributed by the existence of rich high molecular weight hydrocarbon species. In contrast, the lower density of Basrah medium indicates a lighter hydrocarbon profile. Previous studies suggest that the complexity of hydrocarbon species in heavy crude oil presents greater challenges for the refining process compared to medium crude oil (Yarranton et al. 2015).

Table 5.1 General characteristics of the studied crude oil samples

Functions	Basrah heavy	Basrah medium
Density (g/mL)	0.91	0.8807
API gravity	23.7	29.1
Ni (ppm)	36.66	11.73
V (ppm)	86.27	69.07
V/Ni	2.35	5.88

API gravity, a measure inversely related to density, and it was found that Basrah heavy crude oil has an API gravity of 23.7°API while 29.1°API for Basrah medium crude oil. Apparently, higher API gravity signifies a greater proportion of desirable lighter hydrocarbons such as gasoline (Demirbas et al. 2015). Indeed, the higher API gravity of medium crude oil offers advantages for easier refining and more efficient conversion into high-value products. A significant difference in metal content is also observed, particularly in terms of Ni and V concentrations. Basrah heavy contains 36.66 ppm of Ni, substantially higher than Basrah medium's 11.73 ppm. Apparently, Ni species may poison the catalyst during catalytic processes such as hydrocracking, and higher Ni levels necessitate additional refining measures, increasing operational costs. Vanadium content follows a similar pattern, with Basrah heavy containing 86.27 ppm, compared to 69.07 ppm in Basrah medium. Both metals pose challenges for refining due to their propensity to deactivate catalysts, and higher concentrations in Basrah heavy suggested that more extensive measures would be required to mitigate their effects (Silva et al. 2017).

The FT–IR technique is commonly utilized for identifying the functional groups in Basrah heavy crude and Basrah medium crude oil. Based on Figure 5.1, analysis of the FT–IR spectra of the oil samples revealed similar characteristics. Various functional groups, belonging to alkanes, aromatic rings, phenyl rings, aldehydes, ketones, and anhydrides appeared in both of crude oils (Adebiyi & Thoss 2014). The FTIR spectra analysis in the wavenumber range of 3570–3700 cm^{-1} indicates the presence of moisture in the heavy oil sample (Ghani et al. 2016). Peaks at 2920 cm^{-1} and 2850 cm^{-1} correspond to the asymmetric and symmetric stretching vibrations of aliphatic C-H bonds in methylene (Smith 2018). The peak at 1700 cm^{-1} is associated with stretching carbonyl (C=O) groups, indicating the presence of aromatic carboxylic acids (Smith

2018). The spectral band near 1455 cm^{-1} reflects the stretching of C=C bonds within aromatic rings, while a band at 1375 cm^{-1} corresponds to the in-plane bending of O-H bonds in phenolic compounds (Smith 2018). A peak near 1154 cm^{-1} suggests the presence of C-C-O in tertiary alcohols, and a peak at 740 cm^{-1} indicates out-of-plane bending of C-H bonds in aromatic structures (Smith 2018). These functional groups, particularly those associated with oxygenated species, align with the metal salt fractions seen in Table 5.2.

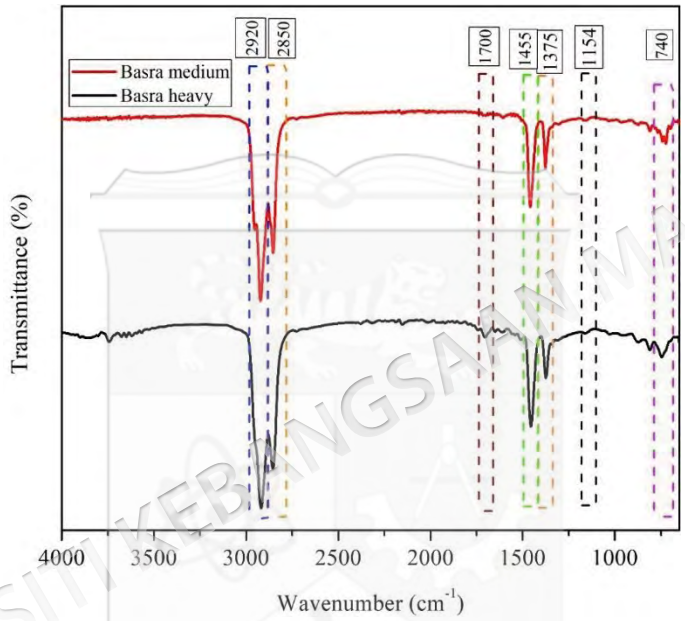

Figure 5.1 FT–IR spectra of Basrah crude oils

5.3.2 Distribution of metallic components in Basrah crude oil fractions

In our study, Basrah crude oil samples underwent precise fractionation into three distinct components: resins, asphaltenes, and aromatics and saturates. The separation procedures, meticulously detailed in Section 5.2.3, ensured that metallic elements were retained despite the absence of a solid adsorbent. Based on Figure 5.2, the composition of fractions in crude oil samples reveals that heavy crude contains 9.7 wt.% resins and 3.5 wt.% asphaltenes, while medium crude contains 6.3 wt.% resins and 3.1 wt.% asphaltenes.

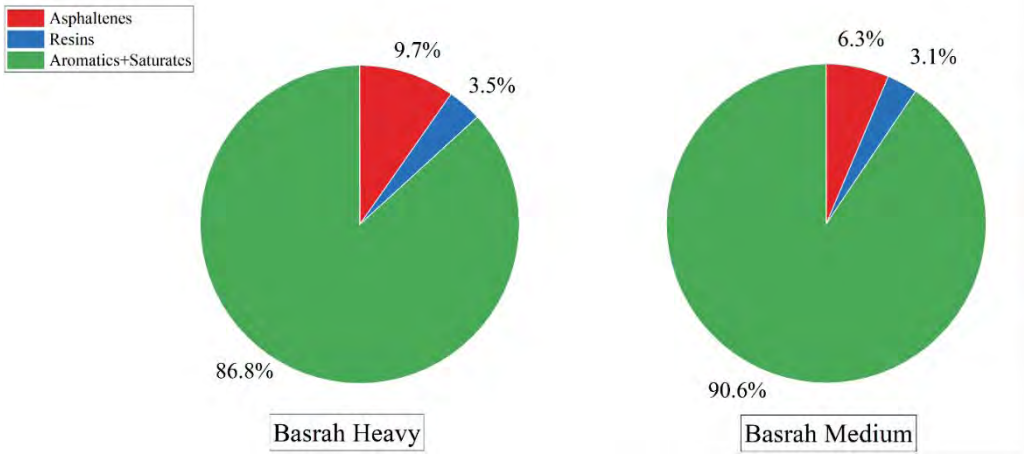

Figure 5.2 Distribution of the fractions of Basrah crude oil.

Indeed, vanadium emerges as the dominant metallic element in both heavy and medium crude oil fractions (Figure 5.3). Specifically, the vanadium content in asphaltenes is around 90% for heavy crude and 89% for medium crude. The total metallic element content is observed in descending order as follows: asphaltenes > resins > aromatics and saturates. These findings are consistent with previous studies (Georgiev et al. 2023; Shishkova et al. 2021).

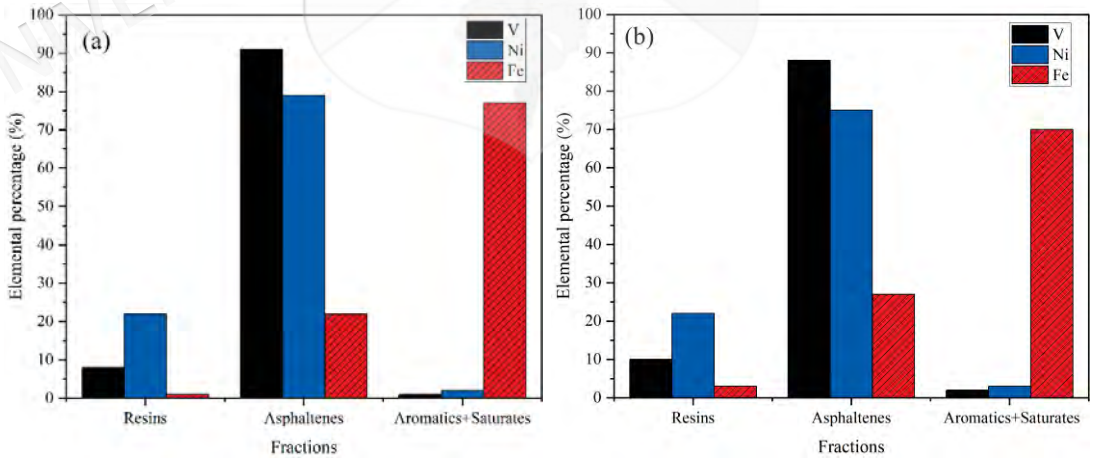

Figure 5.3 The proportion of the metallic components in fractions of Basrah crude oil samples.

Considering the experimental findings from Section 5.2.3 the metallic components V, Ni, and Fe must be standard in Basrah crude oil exhibit distinct forms.

As shown in Table 5.2, those forms include inorganic salts, metal salts of petroleum acids, metalloporphyrins, and non-metalloporphyrins. Notably, deionized water extraction removed only 6.6% (from heavy oil) and 17% (from medium oil) of iron, indicating that most metallic components are oil-soluble compounds. Additionally, a smaller fraction of these metallic elements existed as water-soluble inorganic salts, making their removal via conventional electric desalting challenging. After extraction with a 1% acetic acid solution, the removal rates varied: 1.2% (V, heavy oil), 0.8% (V, medium oil), 8.8% (Ni, heavy oil), 1.6% (Ni, medium oil), 19.4% (Fe, heavy oil), and 27.2% (Fe, medium oil). This phenomenon occurred because some organic compounds of metals in the oil samples were primarily metal salts of petroleum acids, which ionize readily and migrate into an aqueous phase under acidic conditions. Metalloporphyrin constitutes a significant portion of these metals, comprising 98.9% (V), 91.1% (Ni), 74% (Fe) in heavy crude samples, and 99.2% (V), 98.5% (Ni), and 55.6% (Fe) in medium crude samples. The distribution of these metallic elements was notably varied, with Fe exhibiting four distinct types (inorganic, acidic salts, porphyrinc and non-porphyrinc) based on the results of solvent extraction metallic components (see Table 5.2), while V and Ni are predominantly found as metalloporphyrins.

Table 5.2 Abundance percentage of metallic elements in the samples after solution extraction from heavy and medium crude oil

Components	**Basrah Heavy (%)**			**Basrah Medium (%)**		
	V	**Ni**	**Fe**	**V**	**Ni**	**Fe**
Inorganic metallic (water soluble)	-	-	6.6	-	-	17
Metal salts of petroleum acids	1.2	8.8	19.4	0.8	1.6	27.2
Metalloporphyrins	98.9	91.1	74.0	99.2	98.5	55.6

5.3.3 Demetallization of crude oil

As described above, the aim of the study was to explore adsorption technology as a pre-treatment method proposed for Basrah crude oil to remove metals, which was achieved using batch adsorption. Indeed, as preliminary study, the adsorption carried out using untreated crude oil at various of temperature to identify optimal conditions for achieving the highest treatment efficiency. The removal process utilized the CHS/ZX composite

as the adsorbent, which had been previously prepared. Table 5.1 shows that crude oils were highly viscous liquids at room temperature, so they must be diluted to facilitate mixing and phase separation. Figure 5.4 displays the preliminary study results for removing V, Ni, and Fe porphyrins from crude oil samples using the CHS/ZX composite within a temperature range of 30 to 120°C. The preliminary results from the demetallization of crude oils indicated that despite increasing temperatures, the demetallization rate remained negligible. This limited efficiency was attributed to the difficulty in demetalizing bound-type metalloporphyrins, which were strongly associated with asphaltenic molecules (Shiraishi et al. 2000).

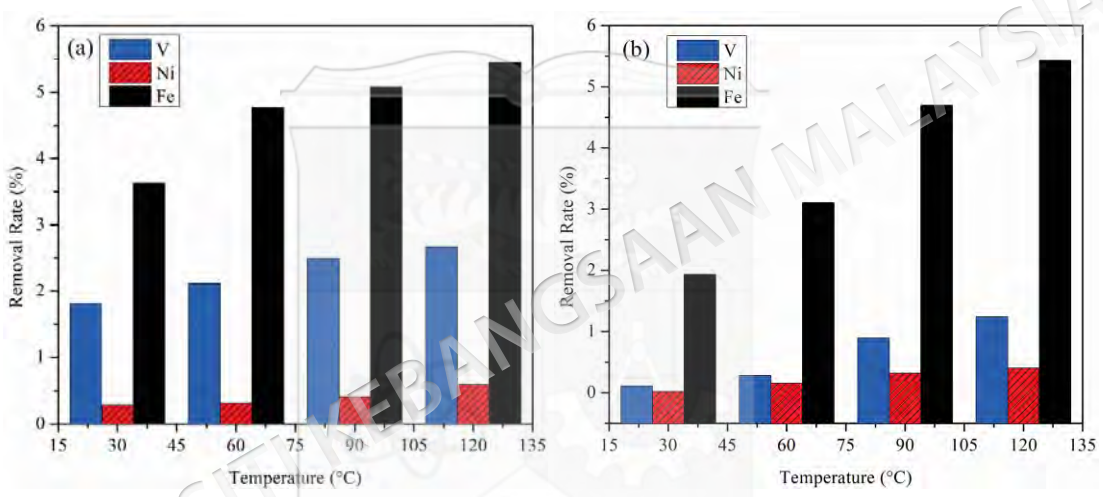

Figure 5.4 Variation in the percentage removal of metals from (a) HB and (b) MB, time (6 h), CHS/ZX dose (100 mg/L)

Further investigation was required to address the limitations observed in previous studies. Several reports have documented that metal porphyrins bound to the asphaltenic fraction of crude oil can be effectively extracted using polar solvents such as THF, pyridine, and isopropanol. These studies suggest bound metal porphyrins are associated with asphaltene molecules via a π-electronic interaction. Therefore, the interaction between the metal porphyrins and asphaltenic molecules must be weakened to enhance the removal of these refractory metal porphyrins (Shiraishi et al. 2000).

a. Effect of the donor solvent

To understand the role of the donor solvent, the removal rates of metals using CHS/ZX without any solvent were first analyzed. The results in Figure 5.5 showed significantly lower removal rates: 20% for V, 15% for Ni, and 30% for Fe. In contrast, the inclusion of a proton-donor solvent, such as 1-hexanol, dramatically improved the removal efficiency, achieving rates of up to 48% for V, 43% for Ni, and 54% for Fe at a volume ratio of 1:0.5 (v/v). These findings highlight the critical role of the donor solvent in enhancing the demetallization process by facilitating the release of porphyrins and improving their interaction with the CHS/ZX adsorbent.

Figure 5.5 illustrates the demetallization results of heavy Basrah crude oil using CHS/ZX in combination with different alcohols 1-hexanol, 2-propanol, ethanol, and cyclohexanol at varying volume ratios. The data reveal a clear relationship between the properties of each alcohol and their effectiveness in the demetallization process. Among the alcohols tested, 1-hexanol consistently achieved the highest removal rates. At a volume ratio of 1:0.5, 1-hexanol resulted in a V removal rate of 48%, Ni of 43% and Fe of 54%. Its superior performance can be attributed to its moderate acidity (pKa ≈ 16.84) and solubility in the non-polar medium, allowing for enhanced interaction with asphaltenes and metal porphyrins (Shiraishi et al. 2000). Although less polar than the other alcohols, 1-hexanol's longer carbon chain likely improves its integration into the non-polar oil environment, contributing to its effectiveness. Noted, 2-propanol, a secondary alcohol, achieved the second-highest removal rates, reaching 40% for V, 43% for Ni and 48% for Fe at 1:0.5 (v/v). This alcohol's moderate polarity and acidity (pKa ≈ 17) enable efficient dissolution of metal porphyrins and effective proton donation (Martins et al. 2018). The lower removal rate for ethanol (38% for V, 41% for Ni and 47% for Fe) is owing to higher polarity and slightly stronger acidity (pKa ≈ 15.9). Apparently, higher polarity and bulkier cycloalkyl structure may reduce compatibility with the non-polar environment. This finding agreed with exhibited the lowest removal rates (30% for V, 35% for Ni and 43% for Fe) by the cyclohexanol, despite having moderate acidity (pKa ≈ 16). Its larger structure likely limits effective interaction with asphaltenes and metal porphyrins within the oil matrix. Notably, these results emphasize the importance of balancing alcohol polarity and molecular structure

to maximize metal removal. Based on the observed removal rates, 1-hexanol is the most effective alcohol for enhancing demetallization in crude oil.

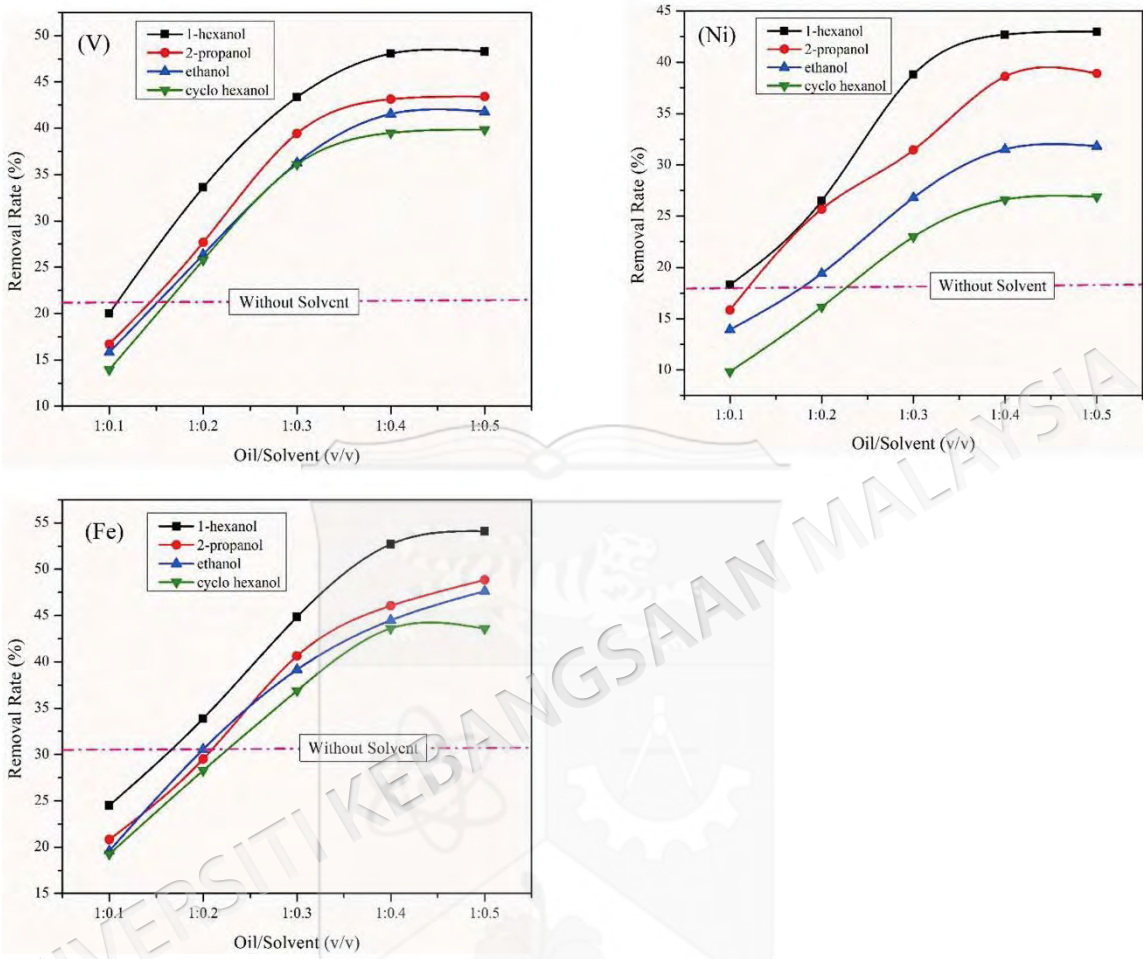

Figure 5.5 Effect of the addition of alcoholic solvents on the rate removal of vanadium, nickel and iron from Basrah heavy.

b. Effect of adsorbent dose

Figure 5.6 illustrates the plotted Ni, V, and Fe removal efficiencies against the CHS/ZX dose. The graph clearly demonstrated that as the adsorbent dose increased while other operational variables remained constant at their optimum values, the removal of metals also increased. This relationship could be attributed to the expanded surface area and the rise in active sites available for metal ion adsorption (Marhoon et al. 2024). Consequently, the functional groups within these active sites had a greater potential to bond with the metal ions present on the surface of the adsorbent material, leading to a reduction in the concentration of Ni ions in crude oil and an increase in removal

efficiency. At a CHS/ZX dose of 100 mg/L, the removal efficiencies of Ni, V, and Fe from heavy Basrah crude oil were 40%, 48%, and 57%, respectively, and for medium Basrah crude oil, the removal efficiencies were 35%, 43%, and 68%, respectively. Upon increasing the CHS/ZX dose to 250 mg/L, the adsorption exhibited enhanced effectiveness, resulting in removal efficiencies for Ni, V, and Fe from heavy Basrah crude oil of 57%, 64%, and 76%, respectively, and removal efficiencies from medium Basrah crude oil of 51%, 61%, and 84%, respectively. However, at doses exceeding 250 mg/L, no further increase in metal removal efficiencies was observed, likely due to a balance between the attractions of metals and the amine and hydroxyl groups of CHS/ZX. This result agreed with (Ali et al. 2021; Wang et al. 2011b).

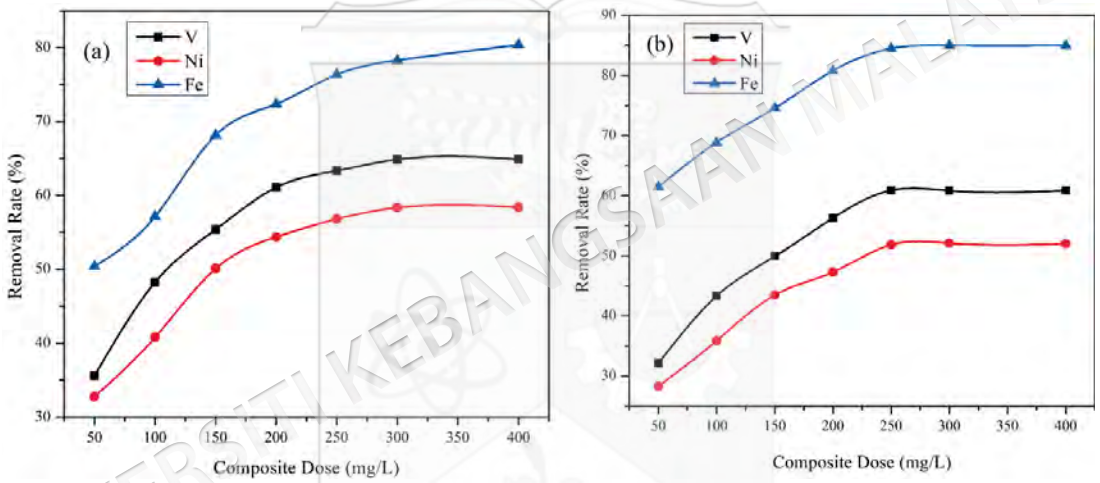

Figure 5.6 Effects of adsorbent dose on demetallization degree for: (a) Basrah heavy; and (b) Basrah medium

c. Effect of contact time

Figure 5.7 a demonstrates the effect of contact time on the efficiency of metal removal from Basrah heavy and Basrah medium crude oil using CHS/ZX as an adsorbent. The data reveal a positive correlation between contact time and the removal efficiency of V, Ni, and Fe, with all other operational parameters held constant at their optimal values. The results indicate that the removal rates for all three metals increase significantly within the first 180 min, after which the rate of increase slows, approaching a plateau. For Basrah heavy crude oil, the removal rates at 300 min were approximately 20% for V, 17% for Ni, and 30% for Fe. Similarly, for Basrah medium crude oil, the removal rates reached approximately 22% for V, 18% for Ni, and 47% for Fe after the same

contact time. These findings suggest that longer contact times promote higher metal removal, although the removal efficiency plateaus after about 270 min. The extended contact time allows for increased interaction between the dissolved metal porphyrins and the available active sites on the adsorbent. Notably, extending the contact time beyond 270 min leads to minimal improvement in removal efficiency, as the active sites on the adsorbent become saturated with metal ions, thereby inhibiting further adsorption activity. The results also show that the optimal contact time for maximum metal removal is approximately 240 min for Basrah heavy crude oil and 210 min for Basrah medium crude oil. This disparity is likely due to the lower initial concentrations of metals in Basrah medium, as observed in the figure. Beyond these optimal contact times, the adsorbent's efficiency stabilizes, and no further significant metal removal is achieved. This plateau effect confirms the saturation of the adsorbent's surface, where all available active sites have been occupied by metal ions (Xu et al. 2018).

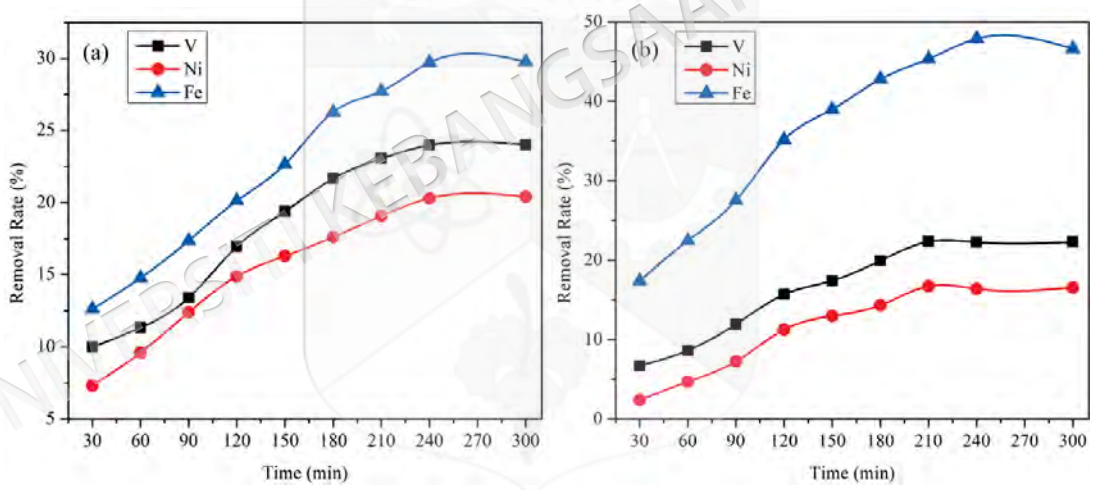

Figure 5.7 Effects of adsorption time on demetallization degree for: (a) Basrah heavy; and (b) Basrah medium

d. Effect of reaction temperature

The experiments were conducted to analyze the impact of reaction temperature on the removal efficiency of metals from both Basrah crude oil samples under constant optimal conditions. As depicted in Figure 5.8, the removal efficiencies of V, Ni, and Fe for heavy Basrah crude oil were 24%, 20%, and 30%, respectively, whereas those for medium Basrah crude were 22%, 17%, and 49% at a reaction temperature of 28°C. However, the removal efficiencies of V, Ni, and Fe for heavy crude oil notably

increased to 57.4%, 50.25%, and 68.22%, respectively, with a temperature elevation to 140°C. Concurrently, the removal efficiencies of V, Ni, and Fe in medium crude oil approached 50%, 43.64%, and 76.86%, respectively, under the same conditions. This observation was attributed to the increased energy and stretching of the polymer at higher temperatures, rendering the active groups more effective and enhancing its demetallization properties (Ma et al. 2016). However, beyond 140°C, a noticeable decline in removal efficiency is observed for both crude oil types. This reduction can be attributed to the difficulty in facilitating the coalescence of water droplets, which is necessary for the separation of dissolved metal compounds from the crude oil-water mixture. At higher temperatures, this separation becomes more challenging, potentially hindering the effective removal of metals (Xu et al. 2018). Temperature has a dual effect on the adsorption process. On one hand, increasing temperature reduces the viscosity of the crude oil, allowing dissolved metal porphyrins to diffuse more easily and enhancing the overall adsorption rate (Caetano et al. 2023a). This is particularly evident in the initial temperature range of 40°C to 140°C, where a steady increase in metal removal rates is observed for both crude oil types. However, at temperatures exceeding 140°C, a decrease in the removal rate was observed, likely due to the increased solubility of metal compounds in crude oil, which resulted in stronger competition between the adsorbate's attraction to the solvent and the adsorbent surface (Caetano et al. 2023a). To better understand the temperature effects on the adsorption process, further investigation through thermodynamic analysis would be beneficial. This approach could help clarify the balance between increased diffusion and the limitations caused by adsorbate solubility at elevated temperatures.

The experimental data indicate that the adsorptive treatment achieved the highest removal rates for iron, with 85% removal from Basrah medium crude and 80% from Basrah heavy crude. For V, the removal rates were 60% for medium crude and 64% for heavy crude, while for Ni, 52% and 58% were removed from medium and heavy crude, respectively. These differences in removal efficiency between the two types of crude oil suggest that the composition and properties of the petroleum feedstock significantly influence the adsorption process due to the diversity of both the nature and concentrations of metallic constituents referred to in Table 5.2. Noted Fe removal shows better than V and Ni which associated by the diverse chemical forms such as inorganic

metallic forms and metallic salts of petroleum acids in which Fe exists within petroleum feedstocks (refer to Table 5.2). Indeed, Fe compounds with tetradentate ligands, exhibit non-aromaticity and are more easily demetalized under appropriate conditions (Kobotaeva & Skorokhodova 2023). In contrast, V and Ni are typically found as metalloporphyrins, combined with alkyl porphyrins that are often integrated into asphaltene aggregates through non-covalent interactions (Ding et al. 2021). These complexes are more structurally stable and less susceptible to adsorption, leading to the observed lower removal efficiencies. Moreover, the higher removal rates of V and Ni from Basrah heavy crude, compared to medium crude, can be attributed to the higher concentrations of these metals in the heavy crude, which provide more opportunities for adsorption (Zhao et al. 2013). These findings align with earlier research, which emphasizes that feedstock composition and the form in which metals occur within crude oil are critical determinants of adsorption efficiency (Yakubov et al. 2016). In this context, Basrah heavy crude demonstrates better adsorption for V and Ni, due to the greater concentration of these metals and their interaction potential with the adsorbent.

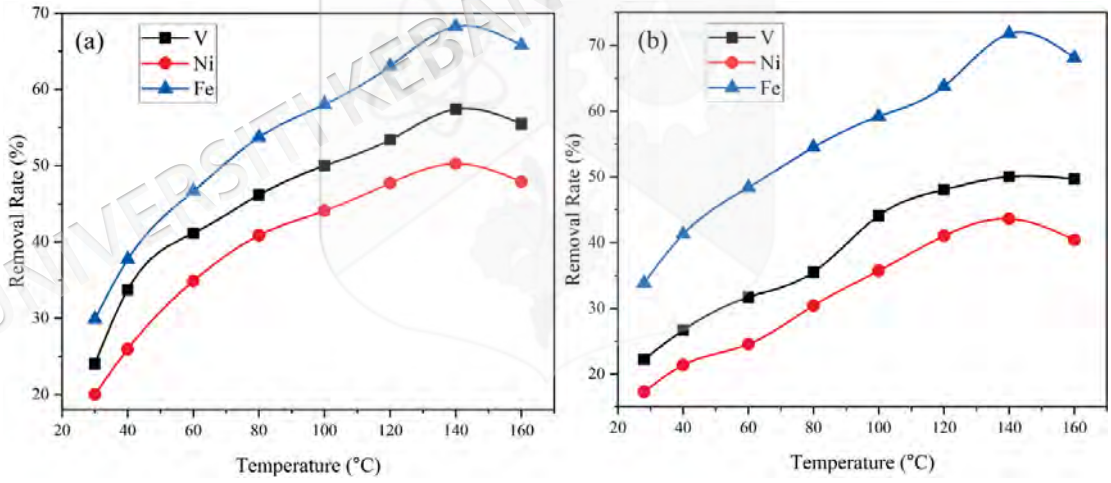

Figure 5.8 Effects of temperature on demetallization degree for: (a) Basrah heavy; and (b) Basrah medium

5.3.4 Characterization of adsorbent after crude oil treatment

a. CHNS analysis results

The comparison of the elemental composition of the adsorbent before and after the treatment of the crude oil is shown in Table 5.3. The results reveal distinct changes

crucial for understanding the demetallization process. The data showd a significant increase in the carbon and hydrogen content from 13.29% to 25.56% and 3.59% to 5.69%, respectively, after the treatment of the crude oil, indicating an accumulation of organic compounds on the adsorbent surface during the demetallization process.

Table 5.3 Results of CHNS analysis of samples

Sample	Elemental composition			
	C%	H%	N%	S%
Basrah medium	85.231	11.242	0.183	3.034
Basrah heavy	87.444	11.863	0.252	4.121
Adsorbent before treatment	13.299	3.598	1.867	-
Adsorbent after treatment	25.568	5.691	1.994	1.322

Increment of carbon which suggests the adsorption of organic compounds, such as hydrocarbons, from the crude oil. The nitrogen content increased from 1.86% to 1.99% after treatment, likely due to the adsorption of nitrogen-containing compounds from the oil by the adsorbent material. Furthermore, sulfur appeared in the composition of the adsorbent after treatment, indicating the adsorbent's significant ability to capture and retain sulfur-containing compounds from the crude oil. This represents an increment in sulfur content in the adsorbent, as sulfur was adsorbed from the crude oil during the treatment process. The presence of sulfur in the adsorbent after treatment highlights its effectiveness in capturing sulfur compounds, contributing to the overall purification of the crude oil. Overall, the increment in the elemental composition of sulfur and other compounds in the adsorbent after treatment demonstrates its ability to adsorb and retain a diverse range of organic and inorganic components from the crude oil, thereby highlighting its efficiency in the demetallization process.

b. XRF analysis results

The results of the XRF analysis, presented in Table 5.4, provide crucial insights into the elemental composition of the adsorbent before and after the demetallization and desulfurization processes. The XRF data reveal significant increases in the metal content of the adsorbent after treatment with Basrah crude oil, including V (from 0% to

0.67%), Ni (from 0% to 0.24%), and Fe (from 0.08% to 0.11%). These results confirm the adsorbent's substantial capacity for metal removal during the treatment process. In addition to metals, the XRF results also show a rise in sulfur content, with an increment from 0% to 1.12%. This increase in sulfur content observed through XRF is further corroborated by the results from the CHNS analysis (Table 5.3), which similarly demonstrates an increase in sulfur content within the adsorbent from 0% to 1.32%. This consistency between the two analyses confirms that sulfur was effectively adsorbed from the crude oil, validating the adsorbent's role in desulfurization. By linking the CHNS and XRF analyses, it is evident that the adsorbent not only captured metal-containing compounds but also effectively removed sulfur-containing compounds and other organic compounds from the crude oil.

Table 5.4 Results of XRF analysis for adsorbent before and after the treatment process

Metals content %	Adsorbent before treatment	Adsorbent after treatment
Al	28.81	28.92
Si	40.28	40.44
V	-	0.67
Ni	-	0.24
Na	20.36	18.11
S	-	1.12
Fe	0.08	0.11
Ca	0.15	0.17
Ti	0.12	0.15
Cl	-	0.03
Mg	0.06	0.062

c. XRD analysis

The XRD patterns of the chitosan/zeolite X (CHS/ZX) composite, shown in Figure 5.9, reveal the structural changes that occurred before and after the demetallization process of crude oil. Prior to demetallization, the XRD pattern displays sharp and well-defined peaks, which correspond to the crystalline structure of zeolite X, confirming the high crystallinity of the CHS/ZX composite. These peaks can be indexed to the zeolite X structure, based on the JCPDS card No. 12–0228 (Shi et al. 2021a). After

demetallization, the XRD pattern of the composite shows a noticeable decrease in peak intensity, particularly in the range of 5° to 30° 2θ. Owing by loss of crystallinity in the CHS/ZX composite, likely due to the strain induced within the crystal lattice during the metal adsorption process (Ji et al. 2020). The interaction of metal ions with the active sites of the zeolite framework may cause distortions in the lattice structure, contributing to the observed reduction in crystallinity. Moreover, no significant shift in the position of the peaks was observed after demetallization, indicating that the bipyramidal structure of the zeolite X remained intact (Li et al. 2020b). This stability is important, as it suggests that while the crystallinity may be slightly reduced, the CHS/ZX composite retains its framework structure, which is crucial for maintaining its adsorption capacity in subsequent cycles. Indeed, minor changes in crystallinity were observed, yet none for the CHS/ZX composite framework, which suggested that the CHS/ZX composite is highly stable during the demetallization process.

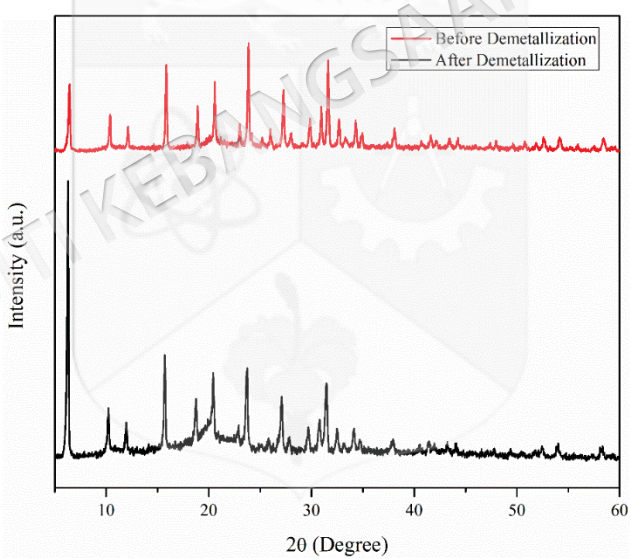

Figure 5.9 XRD pattern of CHS/ZX composite.

d. N_2 adsorption-desorption isotherm

The N_2 adsorption-desorption isotherms and pore size distribution analyses of the CHS/ZX composite, conducted before and after the demetallization process, revealed significant changes in the material's adsorption characteristics. Figure 4.3 illustrate the post-demetallization data, while Figure 5.10 corresponds to the pre-demetallization results. Prior to the demetallization, the CHS/ZX composite exhibited

a high BET surface area of 251 m^2/g, indicative of its robust adsorption capacity. Following the demetallization, this surface area dramatically decreased to 38 m^2/g, owing by the partial blockage of pores by adsorbed metal porphyrins and other crude oil contaminants (Toncón-Leal et al. 2021). This reduction in accessible surface area corresponded directly to the deposition of metal ions and organic residues, which inhibited further adsorption by occupying the active sites on the composite (Ding et al. 2016). Both pre- and post-demetallization isotherms retained the type IV pattern, characteristic of mesoporous materials. Despite the observed decrease in surface area, the mesoporous structure of the CHS/ZX composite remained intact post-demetallization, underscoring the composite's structural resilience. The preservation of this mesoporous framework is critical for maintaining its adsorption efficiency across multiple cycles (Kumar et al. 2023). This structural stability, even in the presence of crude oil contaminants, highlights the material's robustness and adaptability for adsorption applications. Again, based on the pore size distribution result, after demetallization the pore size diameter of CHS/ZX composite reduced remarkably which strongly evinced the pore blockage event (Sheldaisov-Meshcheryakov et al. 2019; Xing et al. 2024). Noteworthy, despite the observed decline in adsorption capacity after demetallization process, the composite's mesoporous structure was preserved, suggesting that with appropriate regeneration techniques, the material could be reused for multiple adsorption cycles. In summary, the CHS/ZX composite presents considerable potential as an adsorbent for demetallization processes, with the possibility of enhancing its operational longevity through suitable regeneration method.

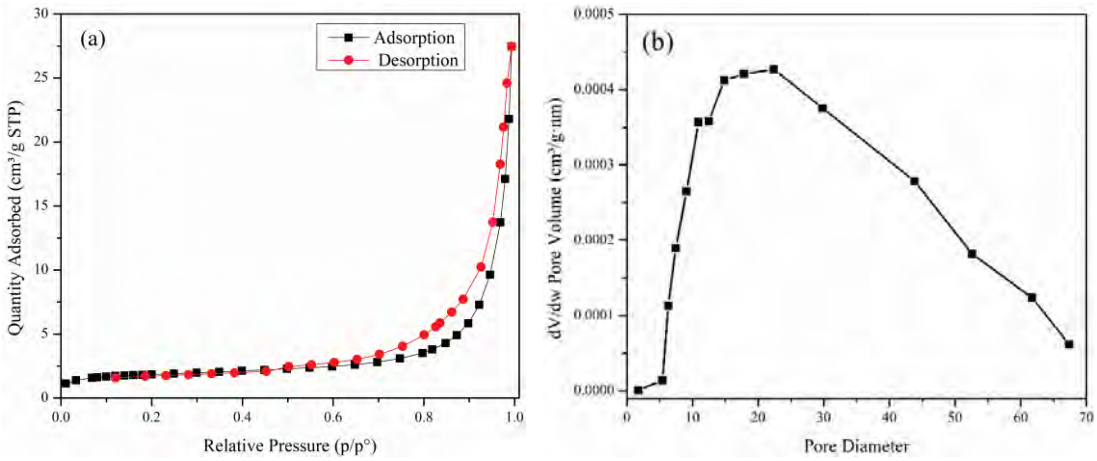

Figure 5.10 (a) N_2 adsorption-desorption isotherms of CHS/ZX, (b) pore size distribution plots of CHS/ZX after crude oil demetallization

5.4 COMPARISON STUDIES

The comparison in Table 5.5 highlights the effectiveness of the CHS/ZX composite relative to other demetallization agents. Notably, CHS/ZX achieved significant removal rates from Basrah heavy crude oil, with 65% of V, 58% of Ni, and 80% of Fe removed. Similarly, the removal rates for Basrah medium were 61% for V, 52% for Ni, and 85% for Fe, showing comparable or superior performance to other adsorbents. For instance, while carboxymethyl chitosan (Wang et al. 2011a) and cationic starch (Wang et al. 2011b) showed relatively higher removal rates for V and Ni, their reliance on microwave irradiation makes them less economically viable for large-scale applications. Conversely, while modified synthetic zeolite (Ongarbayev et al. 2020) and nature zeolite (Rocha Aguilera et al. 2016) were applied under harsh conditions, including high operating temperatures (up to 340°C) and pressure, which elevated energy costs, their efficiency was lower than that observed in our study. Likewise, the CHS/ZX composite proved more effective than methods combining microwave radiation with azomethine-functionalized cellulose (Negi & Singh 2021), as well as spherical polymer brushes with electric desalting (Shen et al. 2023) in removing heavy metal from crude oil samples in removing heavy metal from crude oil samples. In contrast, the CHS/ZX composite operated efficiently at a much lower temperature (140°C), making it more cost-effective while maintaining competitive demetallization performance. Additionally, the zeolite X used in the synthesis of CHS/ZX was derived from coal fly ash, a waste product, further enhancing its economic and sustainable

advantages. The utilization of coal fly ash not only reduces material costs but also promotes environmental sustainability by repurposing industrial waste into an effective adsorbent. This combination of high efficiency, cost-effectiveness, and sustainability makes CHS/ZX a promising alternative for industrial demetallization processes.

Table 5.5 Comparison of demetallization agents and performance of CHS/ZX composite derived from coal fly ash.

Adsorbent	Removal Rate (%)			Remark	References
	Ni	V	Fe		
Carboxymethyl chitosan	69.79	93.66	-	Microwave irradiation	(Wang et al. 2011a)
Zeolite modified 2% V_2O_5 and 10% TiO_2	40.5	35.5	37.3	Temp.= 340°C	(Ongarbayev et al. 2020)
Cationic starch	Iranian crude oil			Microwave irradiation	(Wang et al. 2011b)
	55	76	-		
	Shengli crude oil				
	60	79	-		
Spherical polymer brushes	PAM@PB			Electric desalting	(Rocha Aguilera et al. 2016)
	25	-	-		
	PAA@PB				
	54	-	-		
Chabazite zeolite	-	67.5	-	Temp.= 350°C	(Rocha Aguilera et al. 2016)
Azomethine functionalized cellulose	43.24	50.67	-	Microwave irradiation	(Negi & Singh 2021)
This study	Basrah heavy			-	-
	58	65	80		
	Basrah medium				
	52	61	85		

5.5 SUMMARY

This chapter investigated a new demetallization process for Basrah crude oils, focusing on the dissociation of petroporphyrins from asphaltenes and their adsorption using a CHS/ZX composite adsorbent. While effective for "free"-type metal porphyrins, it struggled with "bound"-type porphyrins strongly associated with asphaltenes. To overcome this, 1-hexanol, a polar solvent, was used to weaken these bonds, converting bound porphyrins to free-type for easier removal. The experimental results demonstrated that this new method successfully removed 65% (7.68 mg/g) of V, 58% of Ni (3.00 mg/g), and 80% of Fe from Basrah heavy crude oil. Similarly, 61% (5.54 mg/g) of V, 52% (0.83 mg/g) of Ni, and 85% of Fe were removed from Basrah medium crude oil. This process, which includes the recovery of 1-hexanol, was presented as an energy-efficient and safe approach for upgrading feedstocks with varying metal concentrations. The study outlined the experimental conditions, including, fractionation of crude oil samples, determination of the nature of metallic components, and key parameters such as temperature, adsorbent dose, and contact time. It emphasized the role of polar solvents in dissociating metal porphyrins from asphaltenes, with 1-hexanol being the most effective solvent. The findings also showed that increasing the CHS/ZX adsorbent dose, along with optimizing contact time and temperature, significantly improved the removal efficiency of Ni, V, and Fe. The study concluded with an evaluation of the adsorbent post-treatment, showing significant increases in the content of metals and sulfur, which confirmed the substantial adsorption capacity of the CHS/ZX composite. Overall, this study provided a comprehensive analysis of a novel and effective method for the removal of heavy metals from crude oil, presenting a viable solution for the purification and upgrading of heavy and medium crude oil feedstocks.

CHAPTER VI

CONCLUSION

6.1 CESSATION

This study successfully achieved the synthesis and characterization of high-purity zeolite X from Malaysian coal fly ash using an alkaline fusion-assisted hydrothermal process. Pretreatment steps, including magnetic separation and acid washing, were critical in enhancing the purity of the fly ash, leading to a single-phase zeolite X with a high specific surface area (452 m^2/g) and excellent crystallinity. The optimized synthesis conditions resulted in a zeolite material superior to untreated fly ash-derived zeolites, as confirmed by comprehensive characterization techniques such as XRD, SEM, BET, and FTIR.

The synthesized zeolite demonstrated effective removal of vanadium (V) and nickel (Ni) ions from aqueous solutions, with adsorption following the pseudo-second-order and Langmuir isotherm models. This indicated strong adsorption affinity and a high degree of surface interaction. The optimized zeolite achieved significant removal efficiencies, establishing its potential as a cost-effective and eco-friendly adsorbent for heavy metal removal in water treatment applications.

In addition, the study synthesized and characterized a novel chitosan-modified zeolite X (CHS/ZX) composite, specifically designed for the efficient removal of vanadyl and nickel porphyrins from model solutions in toluene. The composite outperformed its individual components, demonstrating twice the adsorption capacity. Adsorption followed the Freundlich isotherm model, with vanadyl porphyrins showing greater affinity than nickel porphyrins. The CHS/ZX composite exhibited robust regeneration capabilities, recovering 73.7% of vanadyl porphyrins and 83.8% of nickel porphyrins after five adsorption-desorption cycles.

Finally, the CHS/ZX composite's performance for demetallizing real crude oil samples was evaluated, achieving removal efficiencies of 65% vanadium, 58% nickel, and 80% iron from Basrah heavy crude oil, and slightly lower efficiencies for medium crude oil. The use of 1-hexanol as a hydrogen-donating solvent effectively dissociated bound-type metal porphyrins, improving their removal. These findings demonstrate the composite's capability as a safe, energy-efficient solution for upgrading heavy and medium crude oil feedstocks, with potential for industrial application.

6.2 RECOMMENDATIONS

This study has successfully achieved its objectives; however, several recommendations are proposed for future advancements:

1. Develop a synthesis process for chitosan using biowaste to align with recycling principles and compare the production costs with current market prices.
2. Explore the synthesis of additional chitosan derivatives with more reactive and selective functional groups to enhance the composite's adsorption capabilities.
3. Implement column technology for continuous adsorption processes, which could improve efficiency, automate regeneration, and streamline composite reuse.
4. Conduct preliminary computational studies, such as Density Functional Theory (DFT), to evaluate the potential of the CHS/ZX composite for broader applications in industrial and environmental settings.

REFERENCES

Ababneh, H. & Hameed, B.H. 2023. Chitosan and chitosan composites for oil spills treatment: Review of recent literature. *Journal of Water Process Engineering* 55: 104193.

Abasian, P., Radmansouri, M., Habibi Jouybari, M., Ghasemi, M.V., Mohammadi, A., Irani, M. & Jazi, F.S. 2019. Incorporation of magnetic NaX zeolite/DOX into the PLA/chitosan nanofibers for sustained release of doxorubicin against carcinoma cells death in vitro. *International Journal of Biological Macromolecules* 121: 398–406.

Abdelrahman, E.A., Abou El-Reash, Y.G., Youssef, H.M., Kotp, Y.H. & Hegazey, R.M. 2021. Utilization of rice husk and waste aluminum cans for the synthesis of some nanosized zeolite, zeolite/zeolite, and geopolymer/zeolite products for the efficient removal of Co (II), Cu (II), and Zn (II) ions from aqueous media. *Journal of Hazardous Materials* 401: 123813.

Abdulrasool, M.M., Ruaa, K.M., Mays, A.D., ALsailawi, H.A., Mudhafar, M. & Bashi, A.M. 2021. Regeneration of chitosan-based adsorbents used in heavy metal adsorption. *Journal of Life Sciences* 15: 11–19.

Adanenche, D.E., Aliyu, A., Atta, A.Y. & El-Yakubu, B.J. 2023. Residue fluid catalytic cracking: A review on the mitigation strategies of metal poisoning of RFCC catalyst using metal passivators/traps. *Fuel* 343: 127894.

Adebiyi, F.M. & Thoss, V. 2014. Organic and elemental elucidation of asphaltene fraction of Nigerian crude oils. *Fuel* 118: 426–431.

Adolfo, F.R., Claussen, L.E., Cargnin, R.S., Brudi, L.C., Grasmann, C.S., do Nascimento, P.C., Cravo, M., Nascimento, L.A., Alcantara, A.P.M.P. & Branco, V.T.F.C. 2022. Influence of thermal aging and long term-aging on Ni and V content in asphalt fractions and their determination in air particulate matter from asphalt mixing plants. *Fuel* 324: 124289.

Afkhami, A., Rezaei, M. & Malmiri, H.J. 2021. Effect of chitosan incorporation on crystallinity, mechanical and rheological properties, and photodegradability of PE/TPS blends. *Journal of Thermoplastic Composite Materials* 34(6): 780–800.

Aghahuseynova, M. 2020. Synthesis and Properties of Metal-Complex Catalysts Based on Oil Metalloporphyrins. *EUREKA: Physics and Engineering* 4: 19–28.

Ahammad, N.A., Zulkifli, M.A., Ahmad, M.A., Hameed, B.H. & Mohd Din, A.T. 2021. Desorption of chloramphenicol from ordered mesoporous carbon-alginate beads: Effects of operating parameters, and isotherm, kinetics, and regeneration studies. *Journal of Environmental Chemical Engineering* 9(1): 105015.

Ahmad, W. 2015. Sulfur in Petroleum: Petroleum Desulfurization Techniques. *Applying Nanotechnology to the Desulfurization Process in Petroleum Engineering*, p. 1. IGI Global.

Ahmed, M.J., Hameed, B.H. & Hummadi, E.H. 2020. Review on recent progress in chitosan/chitin-carbonaceous material composites for the adsorption of water pollutants. *Carbohydrate Polymers* 247: 116690.

Aigbe, U.O., Ukhurebor, K.E., Onyancha, R.B., Osibote, O.A., Darmokoesoemo, H. & Kusuma, H.S. 2021. Fly ash-based adsorbent for adsorption of heavy metals and dyes from aqueous solution: a review. *Journal of Materials Research and Technology* 14: 2751–2774.

Akazdam, S., Chafi, M., Yassine, W. & Gourich, B. 2017. Removal of acid orange 7 dye from aqueous solution using the exchange resin amberlite FPA-98 as an efficient adsorbent: kinetics, isotherms, and thermodynamics study. *Journal of Materials and Environmental Sciences* 8(8): 2993–3012.

Aldahri, T., Behin, J., Kazemian, H. & Rohani, S. 2017. Effect of microwave irradiation on crystal growth of zeolitized coal fly ash with different solid/liquid ratios. *Advanced Powder Technology* 28(11): 2865–2874.

Al-Ghouti, M.A. & Da'ana, D.A. 2020. Guidelines for the use and interpretation of adsorption isotherm models: A review. *Journal of hazardous materials* 393: 122383.

Alharthi, F.A., Marghany, A. El, Abduh, N.A.Y. & Hasan, I. 2024. Cerium Vanadate with Nitrogen Doped Reduced Graphene Oxide for Visible Light-Driven Hydrogen Evolution and Dye Degradation. *physica status solidi (a)* 221(4): 2300743.

Ali, G.A.A., Ibrahim, S.A. & Abbas, M.N. 2021. Catalytic adsorptive of nickel metal from Iraqi crude oil using non-conventional catalysts. *Innovative Infrastructure Solutions* 6: 1–9.

Ali, M.F. & Abbas, S. 2006. A review of methods for the demetallization of residual fuel oils.

Aljerf, L. 2018. High-efficiency extraction of bromocresol purple dye and heavy metals as chromium from industrial effluent by adsorption onto a modified surface of zeolite: Kinetics and equilibrium study. *Journal of Environmental Management* 225: 120–132.

Alterary, S.S. & Marei, N.H. 2021. Fly ash properties, characterization, and applications: A review. Elsevier B.V.

Andonegi, M., Las Heras, K., Santos-Vizcaíno, E., Igartua, M., Hernandez, R.M., de la Caba, K. & Guerrero, P. 2020. Structure-properties relationship of chitosan/collagen films with potential for biomedical applications. *Carbohydrate polymers* 237: 116159.

Andrunik, M. & Bajda, T. 2021. Removal of pesticides from waters by adsorption: comparison between synthetic zeolites and mesoporous silica materials. A review. *Materials* 14(13): 3532.

Angaru, G.K.R., Choi, Y.-L., Lingamdinne, L.P., Koduru, J.R., Yang, J.-K., Chang, Y.-Y. & Karri, R.R. 2022. Portable SA/CMC entrapped bimetallic magnetic fly ash zeolite spheres for heavy metals contaminated industrial effluents treatment via batch and column studies. *Scientific Reports* 12(1): 3430.

Argyle, M.D. & Bartholomew, C.H. 2015. Heterogeneous catalyst deactivation and regeneration: a review. *Catalysts* 5(1): 145–269.

Arjoon1, K.K. & Speight, J.G. 2022. Bioupgrading of Crude Oil and Crude Oil Fractions. *Sustainable Solutions for Environmental Pollution: Air, Water and Soil Reclamation*: 457–502.

Ashraf, M.-T., AlHammadi, A.A., El-Sherbeeny, A.M., Alhammadi, S., Al Zoubi, W., Ko, Y.G. & Abukhadra, M.R. 2022. Synthesis of cellulose fibers/Zeolite-A nanocomposite as an environmental adsorbent for organic and inorganic selenium ions; Characterization and advanced equilibrium studies. *Journal of Molecular Liquids* 360: 119573.

Asikin-Mijan, N., Lee, H. V, Taufiq-Yap, Y.H., Abdulkrem-Alsultan, G., Mastuli, M.S. & Ong, H.C. 2017. Optimization study of SiO2-Al2O3 supported bifunctional acid–base NiO-CaO for renewable fuel production using response surface methodology. *Energy Conversion and Management* 141: 325–338.

Attia, M., Farag, S., Jaffer, S.A. & Chaouki, J. 2020. Metal and sulfur removal from petroleum oil using a novel demetallization-desulfurization agent and process. *Journal of Cleaner Production* 275: 124177.

Attia, M.A. 2019. Microwaves-Assisted Demetallization and Desulfurization of Heavy Petroleum Oil Using a Developed Demetallization Agent.

Ayub, A., Raza, Z.A., Majeed, M.I., Tariq, M.R. & Irfan, A. 2020. Development of sustainable magnetic chitosan biosorbent beads for kinetic remediation of arsenic contaminated water. *International Journal of Biological Macromolecules* 163: 603–617.

Bai, P., Etim, U.J., Yan, Z., Mintova, S., Zhang, Z., Zhong, Z. & Gao, X. 2019. Fluid catalytic cracking technology: current status and recent discoveries on catalyst contamination. *Catalysis Reviews* 61(3): 333–405.

Bai, S., Chu, M., Zhou, L., Chang, Z., Zhang, C. & Liu, B. 2022. Removal of heavy metals from aqueous solutions by X-type zeolite prepared from combination of oil shale ash and coal fly ash. *Energy Sources, Part A: Recovery, Utilization, and Environmental Effects* 44(2): 5113–5123.

Bai, S. xia, Zhou, L. mei, Chang, Z. bing, Zhang, C. & Chu, M. 2018. Synthesis of Na-X zeolite from Longkou oil shale ash by alkaline fusion hydrothermal method. *Carbon Resources Conversion* 1(3): 245–250.

Banda-Cruz, E.E., Gallardo-Rivas, N. V, Martínez-Orozco, R.D., Páramo-García, U. & Mendoza-Martínez, A.M. 2021. Derivative UV-Vis Spectroscopy of Crude Oil

and Asphaltene Solutions for Composition Determination. *Journal of Applied Spectroscopy* 87(6): 1157–1162.

Bao, S., Chen, B., Zhang, Y. & Tang, Y. 2018. Synthesis of coated solvent impregnated resins by PVA cross-linked with vapor-phase glutaraldehyde for adsorption of vanadium (IV). *Reactive and Functional Polymers* 128: 58–66.

Baskar, A. V, Bolan, N., Hoang, S.A., Sooriyakumar, P., Kumar, M., Singh, L., Jasemizad, T., Padhye, L.P., Singh, G. & Vinu, A. 2022. Recovery, regeneration and sustainable management of spent adsorbents from wastewater treatment streams: A review. *Science of the Total Environment* 822: 153555.

Bayuo, J., Rwiza, M.J., Choi, J.W., Mtei, K.M., Hosseini-Bandegharaei, A. & Sillanpää, M. 2024. Adsorption and desorption processes of toxic heavy metals, regeneration and reusability of spent adsorbents: Economic and environmental sustainability approach. *Advances in Colloid and Interface Science*: 103196.

Begum, S., Yuhana, N.Y., Saleh, N.M., Kamarudin, N.H.N. & Sulong, A.B. 2021. Review of chitosan composite as a heavy metal adsorbent: Material preparation and properties. *Carbohydrate polymers* 259: 117613.

Belviso, C. 2018. State-of-the-art applications of fly ash from coal and biomass: A focus on zeolite synthesis processes and issues. *Progress in Energy and Combustion Science* 65: 109–135.

Berkgaut, V. & Singer, A. 1996. High capacity cation exchanger by hydrothermal zeolitization of coal fly ash. *Applied clay science* 10(5): 369–378.

Bezerra, M.A., Santelli, R.E., Oliveira, E.P., Villar, L.S. & Escaleira, L.A. 2008. Response surface methodology (RSM) as a tool for optimization in analytical chemistry. *Talanta* 76(5): 965–977.

Bonetto, L.R., Crespo, J.S., Guégan, R., Esteves, V.I. & Giovanela, M. 2021. Removal of methylene blue from aqueous solutions using a solid residue of the apple juice industry: Full factorial design, equilibrium, thermodynamics and kinetics aspects. *Journal of Molecular Structure* 1224: 129296.

Bouazizi, S., Jamoussi, B. & Bousta, D. 2016. Application of response surface methodology for optimization of heavy metals biosorption on natural gum of acacia nilotica. *International Journal of Engineering Research* 5(05).

Butyrskaya, E. 2024. Understanding the mechanism of monolayer adsorption from isotherm. *Adsorption* 30(6): 1395–1406.

Buzukashvili, S., Sommerville, R., Rowson, N.A. & Waters, K.E. 2024. An overview of zeolites synthesised from coal fly ash and their potential for extracting heavy metals from industrial wastewater. *Canadian Metallurgical Quarterly* 63(1): 130–152.

Caetano, G.C., Andrade, L.A.D.E., Martins, P.R. & Ostroski, I.C. 2023a. Optimization of the adsorption and desorption processes of nickel octaethylporphyrin in carbon-based adsorbents. *Anais da Academia Brasileira de Ciências* 95: e20211598.

Caetano, G.C., Franco, D.M.M., Canile, F.M., Vaz, B.G. & Ostroski, I.C. 2023b. Recovery of nickel octaethylporphyrin multilayers from bituminous extracts using low cost adsorbent. *Chemical Engineering Research and Design* 191: 27–37.

Cao, J., Fei, D., Tian, X., Zhu, Y., Wang, S., Zhang, Y., Mao, Q. & Sun, M. 2017. Novel modified microcrystalline cellulose-based porous material for fast and effective heavy-metal removal from aqueous solution. *Cellulose* 24(12): 5565–5577.

Castillo, J., Gonzalez, G., Menta, M., Jimenez-Lamana, J. & Bouyssiere, B. 2023. Biogenic RH-SiO2 Nanoparticles for Vanadium Removal from Asphaltenes via GPC-ICP MS and spICP MS Analysis. *Energy & Fuels* 37(17): 12696–12703.

Castillo, J. & Vargas, V. 2016. Metal porphyrin occlusion: Adsorption during asphaltene aggregation. *Petroleum Science and Technology* 34(10): 873–879.

Castro, P.R. dos S. de, Maia, A.Á.B. & Angélica, R.S. 2020. Study of the thermal stability of faujasite zeolite synthesized from kaolin waste from the Amazon. *Materials Research* 22.

Chacon-Patino, M.L., Nelson, J., Rogel, E., Hench, K., Poirier, L., Lopez-Linares, F. & Ovalles, C. 2021. Vanadium and nickel distributions in Pentane, In-between C5-C7 Asphaltenes, and heptane asphaltenes of heavy crude oils. *Fuel* 292: 120259.

Chacón-Patiño, M.L., Nelson, J., Rogel, E., Hench, K., Poirier, L., Lopez-Linares, F. & Ovalles, C. 2022. Vanadium and nickel distributions in selective-separated n-heptane asphaltenes of heavy crude oils. *Fuel* 312: 122939.

Chauhan, G. & de Klerk, A. 2020. Extraction of Vanadium and Nickel from Diluted Bitumen and Partially Deasphalted Oil Using Ionic Liquids. *Energy & Fuels* 34(9): 10849–10857.

Chen, F., Liu, Q., Xu, Z., Sun, X., Shi, Q. & Zhao, S. 2013. Adsorption kinetics and thermodynamics of vanadyl etioporphyrin on asphaltene in pentane. *Energy and Fuels* 27(11): 6408–6418.

Chen, F., Zhu, Q., Li, S., Xu, Z., Sun, X. & Zhao, S. 2018. The function of poly aromatic nuclei structure for adsorption of vanadyl/nickel etioporphyrin on asphaltene/graphene. *Fuel Processing Technology* 174: 132–141.

Chen, F., Zhu, Q., Xu, Z., Sun, X. & Zhao, S. 2017. Metal Porphyrin Adsorption onto Asphaltene in Pentane Solution: A Comparison between Vanadyl and Nickel Etioporphyrins. *Energy and Fuels* 31(4): 3592–3601.

Chen, M., Nong, S., Zhao, Y., Riaz, M.S., Xiao, Y., Molokeev, M.S. & Huang, F. 2020. Renewable P-type zeolite for superior absorption of heavy metals: Isotherms, kinetics, and mechanism. *Science of the Total Environment* 726: 138535.

Chen, W.-H., Chiu, G.-L., Ong, H.C., Lam, S.S., Lim, S., Ok, Y.S. & Kwon, E.E. 2021. Optimization and analysis of syngas production from methane and CO2 via Taguchi approach, response surface methodology (RSM) and analysis of variance (ANOVA). *Fuel* 296: 120642.

Collins, F., Rozhkovskaya, A., Outram, J.G. & Millar, G.J. 2020. A critical review of waste resources, synthesis, and applications for Zeolite LTA. *Microporous and Mesoporous Materials* 291: 109667.

Coltre, D.S. de C., Cionek, C.A., Meneguin, J.G., Maeda, C.H., Braga, M.U.C., de Araújo, A.C., Gauze, G. de F., de Barros, M.A.S.D. & Arroyo, P.A. 2020. Study of dye desorption mechanism of bone char utilizing different regenerating agents. *SN Applied Sciences* 2: 1–14.

Corma, A., Corresa, E., Mathieu, Y., Sauvanaud, L., Al-Bogami, S., Al-Ghrami, M.S. & Bourane, A. 2017. Crude oil to chemicals: light olefins from crude oil. *Catalysis Science & Technology* 7(1): 12–46.

Curpen, S., Teutsch, N., Kovler, K. & Spatari, S. 2023. Evaluating life cycle environmental impacts of coal fly ash utilization in embankment versus sand and landfilling. *Journal of Cleaner Production* 385: 135402.

Daghooghi-Mobarakeh, H., Campbell, N., Bertrand, W.K., Kumar, P.G., Tiwari, S., Wang, L., Wang, R., Miner, M. & Phelan, P.E. 2020. Ultrasound-assisted regeneration of zeolite/water adsorption pair. *ultrasonics sonochemistry* 64: 105042.

Daneshvar, E., Vazirzadeh, A., Niazi, A., Kousha, M., Naushad, Mu. & Bhatnagar, A. 2017. Desorption of Methylene blue dye from brown macroalga: Effects of operating parameters, isotherm study and kinetic modeling. *Journal of Cleaner Production* 152: 443–453.

de Magalhães, L.F., da Silva, G.R. & Peres, A.E.C. 2022. Zeolite application in wastewater treatment. *Adsorption Science & Technology* 2022: 4544104.

Demirbas, A., Alidrisi, H. & Balubaid, M.A. 2015. API gravity, sulfur content, and desulfurization of crude oil. *Petroleum Science and Technology* 33(1): 93–101.

Dere Ozdemir, O. & Piskin, S. 2019. A Novel Synthesis Method of Zeolite X From Coal Fly Ash: Alkaline Fusion Followed by Ultrasonic-Assisted Synthesis Method. *Waste and Biomass Valorization* 10(1): 143–154.

Díaz-Flores, P.E., Arcibar-Orozco, J.A., Flores-Rojas, A.I. & Rangel-Méndez, J.R. 2021. Synthesis of a chitosan-zeolite composite modified with La (III): characterization and its application in the removal of fluoride from aqueous systems. *Water, Air, & Soil Pollution* 232(6): 235.

Ding, W., Wang, D., Zhao, D. & Ke, M. 2016. A novel self-assembled hierarchical-structured catalyst for the diffusion of macromolecules. *Australian Journal of Chemistry* 69(8): 856–864.

Ding, X., Wei, S., Bian, H., Zhu, L. & Xia, D. 2021. Insights into the Self-Aggregation of Porphyrins and Their Influence on Asphaltene Aggregation. *Energy & Fuels* 35(15): 11848–11857.

Dutta, T., Kim, T., Vellingiri, K., Tsang, D.C.W., Shon, J.R., Kim, K.-H. & Kumar, S. 2019. Recycling and regeneration of carbonaceous and porous materials through thermal or solvent treatment. *Chemical Engineering Journal* 364: 514–529.

El Bojaddayni, I., Küçük, M.E., El Ouardi, Y., Jilal, I., El Barkany, S., Moradi, K., Repo, E., Laatikainen, K. & Ouammou, A. 2023. A review on synthesis of zeolites from natural clay resources and waste ash: Recent approaches and progress. *Minerals Engineering* 198: 108086.

El Kaim Billah, R., Şimşek, S., Majdoubi, H., Kaya, S., Agunaou, M., Soufiane, A. & Katin, K.P. 2023. Removal of lead (II) from aqueous solution using epichlorohydrin cross-linked shrimp waste-derived chitosan based @ calcium phosphates biocomposite: Experimental study and computational approach. *Journal of Molecular Liquids* 389: 122872.

El Messaoudi, N., El Khomri, M., Goodarzvand Chegini, Z., Chlif, N., Dbik, A., Bentahar, S., Iqbal, M., Jada, A. & Lacherai, A. 2023. Desorption study and reusability of raw and H2SO4 modified jujube shells (Zizyphus lotus) for the methylene blue adsorption. *International Journal of Environmental Analytical Chemistry* 103(16): 3762–3778.

Elahi, S.M., Scott, C.E., Chen, Z. & Pereira-Almao, P. 2019. In-situ upgrading and enhanced recovery of heavy oil from carbonate reservoirs using nano-catalysts: Upgrading reactions analysis. *Fuel* 252: 262–271.

Elouahed, S.K., Asikin-Mijan, N., Alsultan, A., Kaddour, O., Yusop, M.R., Mimoun, H., Samidin, S., Mansir, N. & Taufiq-Yap, Y.H. 2024. Optimization of the activity of Mo7-Zn3/CaO catalyst in the transesterification of waste cooking oil into sustainable biodiesel via response surface methodology. *Energy Conversion and Management* 303: 118185.

Fakher, S., Ahdaya, M., Elturki, M. & Imqam, A. 2020. Critical review of asphaltene properties and factors impacting its stability in crude oil. *Journal of Petroleum Exploration and Production Technology* 10: 1183–1200.

Fan, S., Liu, H., Wang, J., Chen, H., Bai, R., Guo, A., Chen, K., Huang, J. & Wang, Z. 2020. Microwave-assisted petroporphyrin release from asphaltene aggregates in polar solvents. *Energy & Fuels* 34(3): 2683–2692.

Fanchi, J.R. & Fanchi, C.J. 2016. *Energy In The 21st Century*. World Scientific Publishing Company.

Fang, J., Zhang, Y., Yan, S., Liu, Z., He, S., Cui, L. & Yin, J. 2014. Poly (L-glutamic acid)/chitosan polyelectrolyte complex porous microspheres as cell microcarriers for cartilage regeneration. *Acta biomaterialia* 10(1): 276–288.

Fathi, P., Sikorski, M., Christodoulides, K., Langan, K., Choi, Y.S., Titcomb, M., Ghodasara, A., Wonodi, O., Thaker, H., Vural, M., Behrens, A. & Kofinas, P. 2018. Zeolite-loaded alginate-chitosan hydrogel beads as a topical hemostat. *Journal of Biomedical Materials Research Part B: Applied Biomaterials* 106(5): 1662–1671.

Freitas, E.D., Moura Jr, C.F., Kerwald, J. & Beppu, M.M. 2020. An overview of current knowledge on the properties, synthesis and applications of quaternary chitosan derivatives. *Polymers* 12(12): 2878.

Fukasawa, T., Karisma, A.D., Shibata, D., Huang, A.-N. & Fukui, K. 2017. Synthesis of zeolite from coal fly ash by microwave hydrothermal treatment with pulverization process. *Advanced Powder Technology* 28(3): 798–804.

Furimsky, E. 2016. On exclusivity of vanadium and nickel porphyrins in crude oil. *Energy & Fuels* 30(11): 9978–9980.

Gagliano, E., Falciglia, P.P., Zaker, Y., Karanfil, T. & Roccaro, P. 2021. Microwave regeneration of granular activated carbon saturated with PFAS. *Water Research* 198: 117121.

Gan, C., Liu, M., Lu, J. & Yang, J. 2020. Adsorption and desorption characteristics of vanadium (V) on silica. *Water, Air, & Soil Pollution* 231: 1–11.

Genç, N., Durna, E. & Kacıra, E. 2022. The preference of the most appropriate radical-based regeneration process for spent activated carbon by the PROMETHEE approach. *Environmental science and pollution research international* 29(4): 5240–5255.

Geng, T., Zhao, D., Xu, J., Ren, M. & Cao, F. 2020. Removal of nickel and calcium from crude oil using core-shell materials grafted with N-substituted pyridines. *Journal of Petroleum Science and Engineering* 195: 107502.

Georgiev, B.E., Stratiev, D.S., Argirov, G.S., Nedelchev, A., Dinkov, R., Shishkova, I.K., Ivanov, M., Atanassov, K., Ribagin, S. & Nikolov Palichev, G. 2023. Commercial ebullated bed vacuum residue hydrocracking performance improvement during processing difficult feeds. *Applied Sciences* 13(6): 3755.

Ghani, S.A., Muhamad, N.A., Chairul, I.S. & Jamri, N. 2016. A study of moisture effects on the breakdown voltage and spectral characteristics of mineral and palm oil-based insulation oils. *ARPN J. Eng. Appl. Sci* 11(8): 5012–5020.

Ghanim, B., Murnane, J.G., O'Donoghue, L., Courtney, R., Pembroke, J.T. & O'Dwyer, T.F. 2020. Removal of vanadium from aqueous solution using a red mud modified saw dust biochar. *Journal of Water Process Engineering* 33: 101076.

Ghassabzadeh, H., Rashidzadeh, M. & Niaei, A. 2020. A novel fast evaluation method for mesoporous NiMo/Al 2 O 3 hydrodemetallization (HDM) catalysts: activity and metal uptake capacity measurements. *Reaction Kinetics, Mechanisms and Catalysis* 130: 381–402.

Ghazali, N., Muthusamy, K. & Ahmad, S.W. 2019. Utilization of Fly Ash in Construction. *Materials Science and Engineering Conference Series*, p. 012023.

Gong, Y., Sun, J., Zhang, Y., Zhang, Y. & Zhang, T. an. 2021. Dependence on the distribution of valuable elements and chemical characterizations based on different particle sizes of high alumina fly ash. *Fuel* 291: 120225.

Groysman, A. 2017. Corrosion problems and solutions in oil, gas, refining and petrochemical industry. *KOM–Corrosion and Material Protection Journal* 61(3): 100–117.

Gu, F., Geng, J., Li, M., Chang, J. & Cui, Y. 2019. Synthesis of Chitosan–Ignosulfonate Composite as an Adsorbent for Dyes and Metal Ions Removal from Wastewater. *ACS Omega* 4(25): 21421–21430.

Gul, K., Sohni, S., Waqar, M., Ahmad, F., Norulaini, N.A.N. & AK, M.O. 2016. Functionalization of magnetic chitosan with graphene oxide for removal of cationic and anionic dyes from aqueous solution. *Carbohydrate Polymers* 152: 520–531.

Guo, R., Yao, W., Ma, H. & Yuan, J. 2020. Two-step hydrothermal synthesis of nano-kaolinite from fly ash: Thermodynamics and mechanism. *Journal of Cleaner Production* 271: 122567.

Habiba, U., Afifi, A.M., Salleh, A. & Ang, B.C. 2017. Chitosan/(polyvinyl alcohol)/zeolite electrospun composite nanofibrous membrane for adsorption of Cr6+, Fe3+ and Ni2+. *Journal of hazardous materials* 322: 182–194.

Habiba, U., Siddique, T.A., Li Lee, J.J., Joo, T.C., Ang, B.C. & Afifi, A.M. 2018. Adsorption study of methyl orange by chitosan/polyvinyl alcohol/zeolite electrospun composite nanofibrous membrane. *Carbohydrate Polymers* 191: 79–85.

Hammadou née Mesdour, S., Boufades, D., Bousak, H., Moussiden, A., Benmabrouka, H., Demim, S., Hamada, B., Hérold, C. & Kaddour, O. 2022. Potential application of carbon nanospheres as adsorbent for the simultaneous desulfurization and demetallization of transportations fuels. *Fullerenes, Nanotubes and Carbon Nanostructures* 30(4): 419–427.

Han, C., Yang, T., Liu, H., Yang, L. & Luo, Y. 2019. Characterizations and mechanisms for synthesis of chitosan-coated Na–X zeolite from fly ash and As (V) adsorption study. *Environmental Science and Pollution Research* 26: 10106–10116.

He, X., Yao, B., Xia, Y., Huang, H., Gan, Y. & Zhang, W. 2020. Coal fly ash derived zeolite for highly efficient removal of Ni2+ inwaste water. *Powder Technology* 367: 40–46.

Hsu, C.S. & Robinson, P.R. 2019a. Cracking. In Hsu, C.S. & Robinson, P.R. (eds.). *Petroleum Science and Technology*, pp. 211–244. Cham: Springer International Publishing.

Hsu, C.S. & Robinson, P.R. 2019b. Midstream Transportation, Storage, and Processing. In Hsu, C.S. & Robinson, P.R. (eds.). *Petroleum Science and Technology*, pp. 385–394. Cham: Springer International Publishing.

Hu, G., Yang, J., Duan, X., Farnood, R., Yang, C., Yang, J., Liu, W. & Liu, Q. 2021. Recent developments and challenges in zeolite-based composite photocatalysts for environmental applications. *Chemical Engineering Journal* 417: 129209.

Hu, Q., Pang, S. & Wang, D. 2022. In-depth insights into mathematical characteristics, selection criteria and common mistakes of adsorption kinetic models: A critical review. *Separation & Purification Reviews* 51(3): 281–299.

Hu, W., Wang, Z., Xiao, Y., Zhang, S. & Wang, J. 2019. Advances in crosslinking strategies of biomedical hydrogels. *Biomaterials science* 7(3): 843–855.

IEA. 2024a. Coal - IEA*IEA*. https://www.iea.org/energy-system/fossil-fuels/coal [1 July 2024].

IEA. 2024b. Statistics - Malaysia Energy Information Hub*IEA*. https://meih.st.gov.my/statistics [1 July 2024].

Iqbal, A., Sattar, H., Haider, R. & Munir, S. 2019. Synthesis and characterization of pure phase zeolite 4A from coal fly ash. *Journal of Cleaner Production* 219: 258–267.

Iqbal, Y., Ahmed, I., Irfan, M.F., Chatha, S.A.S., Zubair, M. & Ullah, A. 2023. Recent advances in chitosan-based materials; The synthesis, modifications and biomedical applications. *Carbohydrate Polymers* 321: 121318.

Iuzmukhametova, R., Boldushevskii, R., Shmelkova, O., Khamzin, Y., Minaev, A. & Nikulshin, P. 2023. Adsorptive Treatment of Residues on Macroporous Adsorbent for Marine Fuel Production Scheme on Refinery. *Journal of Marine Science and Engineering* 11(3): 525.

IZA-SC. 2024. Database of Zeolite Structures. https://www.iza-structure.org/databases/ [19 March 2024].

Jamshaid, F., Dilshad, M.R., Islam, A., Khan, R.U., Ahmad, A., Adrees, M. & Haider, B. 2020. Synthesis, characterization and desalination study of polyvinyl chloride-co-vinyl acetate/cellulose acetate membranes integrated with surface modified zeolites. *Microporous and Mesoporous Materials* 309: 110579.

Jawad, A.H., Abdulhameed, A.S., Reghioua, A. & Yaseen, Z.M. 2020. Zwitterion composite chitosan-epichlorohydrin/zeolite for adsorption of methylene blue and reactive red 120 dyes. *International Journal of Biological Macromolecules* 163: 756–765.

Jenifer, A.C., Sharon, P., Prakash, A. & Sande, P.C. 2015. A Review of the Unconventional Methods Used for the Demetallization of Petroleum Fractions over the Past Decade. *Energy and Fuels* 29(12): 7743–7752.

Jha, B. & Singh, D.N. 2016a. Fly ash zeolites. *Advanced Structured Materials* 78: 5–31.

Jha, B. & Singh, D.N. 2016b. Conventional Methods for Synthesis of Fly Ash Zeolites. In Jha, B. & Singh, D.N. (eds.). *Fly Ash Zeolites: Innovations, Applications, and Directions*, pp. 33–51. Singapore: Springer Singapore.

Ji, Q., Kong, Y., Wang, C., Tan, H., Duan, H., Hu, W., Li, G., Lu, Y., Li, N., Wang, Y., Tian, J., Qi, Z., Sun, Z., Hu, F. & Yan, W. 2020. Lattice Strain Induced by Linker Scission in Metal–Organic Framework Nanosheets for Oxygen Evolution Reaction. *ACS Catalysis* 10(10): 5691–5697.

Jia, J., Chen, X., Zhai, L. & Niu, Y. 2020. Oxidation of toluene to benzoic acid via VOTPP catalyst synthesized with an improved method. *Monatshefte für Chemie-Chemical Monthly* 151: 1549–1555.

Jin, Y., Li, L., Liu, Z., Zhu, S. & Wang, D. 2021. Synthesis and characterization of low-cost zeolite NaA from coal gangue by hydrothermal method. *Advanced Powder Technology* 32(3): 791–801.

Joseph, I. V, Tosheva, L. & Doyle, A.M. 2020. Simultaneous removal of Cd (II), Co (II), Cu (II), Pb (II), and Zn (II) ions from aqueous solutions via adsorption on FAU-type zeolites prepared from coal fly ash. *Journal of Environmental Chemical Engineering* 8(4): 103895.

Julbe, A. & Drobek, M. 2015. Zeolite X: Type. In Drioli, E. & Giorno, L. (eds.). *Encyclopedia of Membranes*, pp. 1–2. Berlin, Heidelberg: Springer Berlin Heidelberg.

Jumina, J., Kurniawan, Y.S., Siswanta, D., Purwono, B., Zulkarnain, A.K., Winarno, A., Waluyo, J. & Ahmad, J.S.M. 2021. The Origin, Physicochemical Properties, and Removal Technology of Metallic Porphyrins from Crude Oils. *Indonesian Journal of Chemistry* 21(4): 1023–1038.

Jurado, J. & Ancheyta, J. 2022. Reactor Model for Heavy Oil Hydrotreating with Catalyst Deactivation Based on Vanadium and Coke Deposition. *Energy & Fuels* 36(18): 11132–11141.

Kandel, D.R., Kim, H.-J., Lim, J.-M., Poudel, M.B., Cho, M., Kim, H.-W., Oh, B.-T., Nah, C., Lee, S.H. & Dahal, B. 2022. Cold plasma-assisted regeneration of biochar for dye adsorption. *Chemosphere* 309: 136638.

Kanimozhi, K., Basha, S.K. & Kumari, V.S. 2016. Processing and characterization of chitosan/PVA and methylcellulose porous scaffolds for tissue engineering. *Materials Science and Engineering: C* 61: 484–491.

Karimi-Maleh, H., Ayati, A., Davoodi, R., Tanhaei, B., Karimi, F., Malekmohammadi, S., Orooji, Y., Fu, L. & Sillanpää, M. 2021. Recent advances in using of chitosan-based adsorbents for removal of pharmaceutical contaminants: A review. *Journal of Cleaner Production* 291: 125880.

Karua, C.S. & Sahoo, A. 2020. Synthesis and characterization of starch/chitosan composites. *Materials Today: Proceedings* 33: 5179–5183.

Kassem, A., Ayoub, G.M. & Malaeb, L. 2019. Antibacterial activity of chitosan nano-composites and carbon nanotubes: A review. *Science of the total environment* 668: 566–576.

Keyhaniyan, M., Shiri, A., Eshghi, H. & Khojastehnezhad, A. 2018. Synthesis, characterization and first application of covalently immobilized nickel-porphyrin on graphene oxide for Suzuki cross-coupling reaction. *New Journal of Chemistry* 42(24): 19433–19441.

Khaleque, A., Alam, M.M., Hoque, M., Mondal, S., Haider, J. Bin, Xu, B., Johir, M.A.H., Karmakar, A.K., Zhou, J.L., Ahmed, M.B. & Moni, M.A. 2020. Zeolite synthesis from low-cost materials and environmental applications: A review. *Environmental Advances* 2: 100019.

Khan, H., Hussain, S., Hussain, S.F., Gul, S., Ahmad, A. & Ullah, S. 2021. Multivariate modeling and optimization of Cr (VI) adsorption onto carbonaceous material via response surface models assisted with multiple regression analysis and particle swarm embedded neural network. *Environmental Technology & Innovation* 24: 101952.

Khnifira, M., Boumya, W., Abdennouri, M., Sadiq, M., Achak, M., Serdaroğlu, G., Kaya, S., Şimşek, S. & Barka, N. 2021. A combined molecular dynamic simulation, DFT calculations, and experimental study of the eriochrome black T dye adsorption onto chitosan in aqueous solutions. *International Journal of Biological Macromolecules* 166: 707–721.

Khorshid, Z.B., Doroodmand, M.M. & Abdollahi, S. 2021. UV–Vis. spectrophotometric method for oil and grease determination in water, soil and different mediates based on emulsion. *Microchemical Journal* 160: 105620.

Kloprogge, J.T. & Wood, B.J. 2020. Oxides and Hydroxides: Oxides. *Handbook of Mineral Spectroscopy*, pp. 81–133. Elsevier.

Kobotaeva, N.S. & Skorohodova, T.S. 2018. Investigation of the process of demetallization of heavy oil stock using chemical reagents and ultrasonic treatment. *Proceedings of the Advanced Materials with Hierarchical Structure for New Technologies and Reliable Structures* 2051(1): 020126.

Kobotaeva, N.S. & Skorokhodova, T.S. 2023. Combined Adsorptive and Ultrasonic Treatment to Remove Metals from Fuel Oil. *Petroleum Chemistry* 63(5): 575–584.

Kohli, K., Prajapati, R., Maity, S.K., Sau, M. & Garg, M.O. 2016. Deactivation of hydrotreating catalyst by metals in resin and asphaltene parts of heavy oil and residues. *Fuel* 175: 264–273.

Konne, L.J., Iheanetu, U.D. & Cookey, A.G. 2017. Demetallization of nickel from crude oil using aluminum oxide (Al2O3) nanoparticles synthesized with sodium dodecyl sulfate (SDS). *J Material Sci Eng* 6(385): 2122–2169.

Koop-Santa, C., Yocupicio-Gaxiola, R.I., Murrieta-Rico, F.N., Avalos-Borja, M., Xiao, M., Petranovskii, V. & Reyes-Serrato, A. 2024. Additive-free synthesis of layer-like Faujasite-type zeolite X. *Journal of Materials Science* 59(23): 10169–10181.

Korpa, A., Teneqja, V., Gjyli, S. & Andoni, A. 2021. Parameters Affecting the Synthesis of X and A Zeolites from Coal Fly Ash. *European Journal of Environment and Earth Sciences* 2(1): 53–59.

Koshlak, H. 2023. Synthesis of zeolites from coal fly ash using alkaline fusion and its applications in removing heavy metals. *Materials* 16(13): 4837.

Król, M. 2019. Hydrothermal synthesis of zeolite aggregate with potential use as a sorbent of heavy metal cations. *Journal of Molecular Structure* 1183: 353–359.

Król, M. 2020. Natural vs. synthetic zeolites. *Crystals* 10(7): 622.

Küçük, M.E., Makarava, I., Kinnarinen, T. & Häkkinen, A. 2023. Simultaneous adsorption of Cu (II), Zn (II), Cd (II) and Pb (II) from synthetic wastewater using NaP and LTA zeolites prepared from biomass fly ash. *Heliyon* 9(10): 20230469854.

Kukwa, R.E. & Dann, S.E. 2019. Grafted zeolites for the removal of metal cations from crude oil hydrotreatment extract. *Desalination and Water Treatment* 153: 136–144.

Kumar, N., Pandey, A., Rosy & Sharma, Y.C. 2023. A review on sustainable mesoporous activated carbon as adsorbent for efficient removal of hazardous dyes from industrial wastewater. *Journal of Water Process Engineering* 54: 104054.

Kumar, S., Prasad, K., Gil, J.M., Sobral, A.J.F.N. & Koh, J. 2018. Mesoporous zeolite-chitosan composite for enhanced capture and catalytic activity in chemical fixation of CO2. *Carbohydrate polymers* 198: 401–406.

Kunecki, P., Wdowin, M. & Hanc, E. 2023. Fly ash-derived zeolites and their sorption abilities in relation to elemental mercury in a simulated gas stream. *Journal of Cleaner Production* 391: 136181.

Kusrini, E., Susanto, B.H., Nasution, D.A., Jonathan, R. & Khairul, W.M. 2017. Removal of mercury in liquid hydrocarbons using zeolites modified with chitosan and magnetic iron oxide nanoparticles. *IOP Conference Series: Earth and Environmental Science*, p. 012010.

Kuzmin, S.M., Chulovskaya, S.A. & Parfenyuk, V.I. 2020. Highly conductive polyporphyrin films obtained by superoxide-assisted electropolymerization of para – aminophenyl porphyrin. *Materials Chemistry and Physics* 241: 122394.

Längauer, D., Čablík, V., Hredzák, S., Zubrik, A., Matik, M. & Danková, Z. 2021. Preparation of synthetic zeolites from coal fly ash by hydrothermal synthesis. *Materials* 14(5): 1267.

Larsen, T.A., Hoffmann, S., Lüthi, C., Truffer, B. & Maurer, M. 2016. Emerging solutions to the water challenges of an urbanizing world. *Science* 352(6288): 928–933.

Lee, K.X. & Valla, J.A. 2019. Adsorptive desulfurization of liquid hydrocarbons using zeolite-based sorbents: a comprehensive review. *Reaction Chemistry & Engineering* 4(8): 1357–1386.

Li, G., Wang, B., Sun, Q., Xu, W.Q. & Han, Y. 2017. Adsorption of lead ion on amino-functionalized fly-ash-based SBA-15 mesoporous molecular sieves prepared via two-step hydrothermal method. *Microporous and Mesoporous Materials* 252: 105–115.

Li, H., Zhao, Z., Xiouras, C., Stefanidis, G.D., Li, X. & Gao, X. 2019a. Fundamentals and applications of microwave heating to chemicals separation processes. *Renewable and Sustainable Energy Reviews* 114: 109316.

Li, J., Ma, S., Ren, K. & Xu, N. 2023. Studies on the preparation of fly ash-derived Fe-SSZ-13 catalysts and their performance in the catalytic oxidation of NO by H2O2. *Molecular Catalysis* 537: 112920.

Li, P., Zhang, M., Zhai, Z., Wang, M., Li, P., Hou, Y. & Niu, Q.J. 2020a. Precise assembly of a zeolite imidazolate framework on polypropylene support for the fabrication of thin film nanocomposite reverse osmosis membrane. *Journal of Membrane Science* 612: 118412.

Li, S., Kong, H. & Zhang, W. 2020b. A Density Functional Theory Modeling on the Framework Stability of Al-Rich Cu-SSZ-13 Zeolite Modified by Metal Ions. *Industrial & Engineering Chemistry Research* 59(13): 5675–5685.

Li, S., Li, J., Dong, M., Fan, S., Zhao, T., Wang, J. & Fan, W. 2019b. Strategies to control zeolite particle morphology. *Chemical Society Reviews* 48(3): 885–907.

Li, X., Han, H., Xu, W., Hwang, S., Lu, P., Bhan, A. & Tsapatsis, M. 2022. Enhanced reactivity of accessible protons in sodalite cages of faujasite zeolite. *Angewandte Chemie International Edition* 61(5): e202111180.

Li, X., Ye, J., Liu, Z., Qiu, Y., Li, L., Mao, S., Wang, X. & Zhang, Q. 2018. Microwave digestion and alkali fusion assisted hydrothermal synthesis of zeolite from coal fly ash for enhanced adsorption of Cd(II) in aqueous solution. *Journal of Central South University* 25(1): 9–20.

Lima, E.C., Hosseini-Bandegharaei, A., Moreno-Piraján, J.C. & Anastopoulos, I. 2019. A critical review of the estimation of the thermodynamic parameters on adsorption equilibria. Wrong use of equilibrium constant in the Van't Hoof equation for calculation of thermodynamic parameters of adsorption. *Journal of Molecular Liquids* 273: 425–434.

Lin, S., Jiang, X., Zhao, Y. & Yan, J. 2022. Zeolite greenly synthesized from fly ash and its resource utilization: A review. *Science of The Total Environment* 851: 158182.

Liu, P., Yuan, N., Xiong, W., Wu, H., Pan, D. & Wu, W. 2017. Removal of nickel (II) from aqueous solutions using synthesized β-zeolite and its ethylenediamine derivative. *Industrial & Engineering Chemistry Research* 56(11): 3067–3076.

Liu, R., Chen, P., Wang, Z., Rong, K., Yan, J., Liu, J. & Deguchi, Y. 2021a. Quantitative analysis of carbon content in fly ash using LIBS based on support vector regression. *Advanced Powder Technology* 32(8): 2978–2987.

Liu, X., Zhao, X., Liu, Y. & Zhang, T. 2022. Review on preparation and adsorption properties of chitosan and chitosan composites. *Polymer Bulletin* 79(4): 2633–2665.

Liu, Y., Huo, Y., Wang, X., Yu, S., Ai, Y., Chen, Z., Zhang, P., Chen, L., Song, G. & Alharbi, N.S. 2021b. Impact of metal ions and organic ligands on uranium removal properties by zeolitic imidazolate framework materials. *Journal of Cleaner Production* 278: 123216.

Liu, Z., Li, S., Li, L., Wang, J., Zhou, Y. & Wang, D. 2019. One-step high efficiency crystallization of zeolite A from ultra-fine circulating fluidized bed fly ash by hydrothermal synthesis method. *Fuel* 257: 116043.

Luo, H., Law, W.W., Wu, Y., Zhu, W. & Yang, E.-H. 2018. Hydrothermal synthesis of needle-like nanocrystalline zeolites from metakaolin and their applications for efficient removal of organic pollutants and heavy metals. *Microporous and Mesoporous Materials* 272: 8–15.

Lv, Y., Ma, B., Liu, Y., Wang, C. & Chen, Y. 2022. Adsorption behavior and mechanism of mixed heavy metal ions by zeolite adsorbent prepared from lithium leach residue. *Microporous and Mesoporous Materials* 329: 111553.

Ma, S., Cai, Z., Zhou, Y., Li, S. & Liang, S. 2016. Preparation of a phosphorous-free terpolymer as a decalcifying agent for removing calcium from crude oil. *RSC advances* 6(63): 58426–58433.

Ma, Y., Cheng, L., Zhang, D., Zhang, F., Zhou, S., Ma, Y., Guo, J., Zhang, Y. & Xing, B. 2022. Stabilization of Pb, Cd, and Zn in soil by modified-zeolite: Mechanisms and evaluation of effectiveness. *Science of the Total Environment* 814: 152746.

Machado, A.A. & Mulky, L. 2024. Reusing waste to save our water: regenerable bioadsorbents for effective oil sequestration. *ChemBioEng Reviews* 11(2): 426–440.

Magomedov, R.N., Popova, A.Z., Maryutina, T.A., Kadiev, K.M. & Khadzhiev, S.N. 2015. Current status and prospects of demetallization of heavy petroleum feedstock (Review). *Petroleum Chemistry* 55(6): 423–443.

Magomedov, R.N., Pripakhaylo, A. V, Dzhumamukhamedov, D.Sh. & Maryutina, T.A. 2020. Solvent deasphalting of vacuum residue using carbon dioxide-toluene binary mixture. *Journal of CO2 Utilization* 40: 101206.

Magomedov, R.N., Pripakhaylo, A. V & Maryutina, T.A. 2017. Solvent demetallization of heavy petroleum feedstock using supercritical carbon dioxide with modifiers. *The Journal of Supercritical Fluids* 119: 150–158.

Mahdavi, E., Haghighi-Yazdi, M., Mashhadi, M.M. & Khaledialidusti, R. 2021. Effects of interlayer density and surfactant on coupled thermal stress and moisture absorption in modified montmorillonite/polypropylene nanocomposite. *Journal of Applied Polymer Science* 138(15).

Mahmodi, G., Zarrintaj, P., Taghizadeh, A., Taghizadeh, M., Manouchehri, S., Dangwal, S., Ronte, A., Ganjali, M.R., Ramsey, J.D., Kim, S.-J. & Saeb, M.R. 2020. From microporous to mesoporous mineral frameworks: An alliance between zeolite and chitosan. *Carbohydrate Research* 489: 107930.

Majchrzak-Kucęba, I. 2013. A simple thermogravimetric method for the evaluation of the degree of fly ash conversion into zeolite material. *Journal of Porous Materials* 20(2): 407–415.

Majdoubi, H., Şimşek, S., El Kaim Billah, R., Koçak, N., Kaya, S., Tamraoui, Y., Katin, K.P., Hannache, H. & Marzouki, R. 2024. Novel geopolymer composite based on oil shale and chitosan for enhanced uranium (VI) adsorption: Experimental and theoretical approaches. *Journal of Molecular Liquids* 395: 123951.

Makgabutlane, B., Nthunya, L.N., Musyoka, N., Dladla, B.S., Nxumalo, E.N. & Mhlanga, S.D. 2020a. Microwave-assisted synthesis of coal fly ash-based zeolites for removal of ammonium from urine. *RSC Advances* 10(4): 2416–2427.

Makgabutlane, B., Nthunya, L.N., Nxumalo, E.N., Musyoka, N.M. & Mhlanga, S.D. 2020b. Microwave Irradiation-Assisted Synthesis of Zeolites from Coal Fly Ash: An Optimization Study for a Sustainable and Efficient Production Process. *ACS Omega* 5(39): 25000–25008.

Mäntele, W. & Deniz, E. 2017. UV–VIS absorption spectroscopy: Lambert-Beer reloaded. Elsevier.

Marhoon, A.A., Hasbullah, S.A., Asikin-Mijan, N. & Mokhtar, W.N.A.W. 2024. Adsorption of metal porphyrins using chitosan/zeolite-X composite as an efficient demetallization agent for crude oil: Isotherm, kinetic, and thermodynamic studies. *International Journal of Biological Macromolecules* 274: 133358.

Márquez, P., Benítez, A., Chica, A.F., Martín, M.A. & Caballero, A. 2022. Evaluating the thermal regeneration process of massively generated granular activated carbons for their reuse in wastewater treatments plants. *Journal of Cleaner Production* 366: 132685.

Marroquin, J.B., Rhee, K.Y. & Park, S.J. 2013. Chitosan nanocomposite films: Enhanced electrical conductivity, thermal stability, and mechanical properties. *Carbohydrate Polymers* 92(2): 1783–1791.

Martins, R.G., Martins, L.S. & Santos, R.G. 2018. Effects of short-chain n-alcohols on the properties of asphaltenes at toluene/air and toluene/water interfaces. *Colloids and Interfaces* 2(2): 13.

Mashhadizadeh, M.H., Amoli-Diva, M. & Pourghazi, K. 2013. Magnetic nanoparticles solid phase extraction for determination of ochratoxin A in cereals using high-performance liquid chromatography with fluorescence detection. *Journal of Chromatography A* 1320: 17–26.

McKenna, A.M., Chacón-Patiño, M.L., Salvato Vallverdu, G., Bouyssiere, B., Giusti, P., Afonso, C., Shi, Q. & Combariza, M.Y. 2021. Advances and challenges in the molecular characterization of petroporphyrins. *Energy & Fuels* 35(22): 18056–18077.

Mechnou, I., Meskini, S., El Ayar, D., Lebrun, L. & Hlaibi, M. 2022. Olive mill wastewater from a liquid biological waste to a carbon/oxocalcium composite for selective and efficient removal of methylene blue and paracetamol from aqueous solution. *Bioresource Technology* 365: 128162.

Medykowska, M., Wiśniewska, M., Szewczuk-Karpisz, K. & Panek, R. 2022. Interaction mechanism of heavy metal ions with the nanostructured zeolites surface–adsorption, electrokinetic and XPS studies. *Journal of Molecular Liquids* 357: 119144.

Meena, A., Singh, N. & Singh, S.P. 2023. High-volume fly ash Self Consolidating Concrete with coal bottom ash and recycled concrete aggregates: Fresh, mechanical and microstructural properties. *Journal of Building Engineering* 63: 105447.

Merrikhpour, H. & Jalali, M. 2013. Comparative and competitive adsorption of cadmium, copper, nickel, and lead ions by Iranian natural zeolite. *Clean Technologies and Environmental Policy* 15: 303–316.

Milordov, D. V, Mironov, N.A., Abilova, G.R., Tazeeva, E.G., Yakubova, S.G. & Yakubov, M.R. 2021. Obtaining pure vanadyl porphyrins from heavy oil residues to form bases of catalysts for different processes. *Catalysis in Industry* 13(2): 105–110.

Mitra, S., Sulakhe, S., Shown, B., Mandal, S. & Das, A.K. 2022. Organic Chlorides in Petroleum Crude Oil: Challenges for Refinery and Mitigations. *ChemBioEng Reviews* 9(3): 319–332.

Moghaddam, N., Oroujzadeh, N. & Salehirad, A. 2022. Fabrication of bioactive glass/chitosan/zeolite bio-nanocomposite: Influence of synthetic route on structural and mechanical properties. *Materials Chemistry and Physics* 278: 125708.

Mohamed, H.S., El-Mageed, H.R.A., Ali, H.S., Mahmoud, T.R., Ahmed, S.A. & Soliman, N.K. 2022. Adsorption of Mn+7 ions on chitosan/cellulose composite: experimentally and theoretically approaches. *Journal of Dispersion Science and Technology* 43(10): 1525–1542.

Mohammad, S. & Suzylawati, I. 2020. Study of the adsorption/desorption of MB dye solution using bentonite adsorbent coating. *Journal of Water Process Engineering* 34: 101155.

Monteiro, C.J.P., Faustino, M.A.F. & Serpa, C. 2023. Porphyrin-Based Compounds: Synthesis and Application. *Molecules* 28(20): 7108.

Morris, R.E. & Nachtigall, P. 2017. *Zeolites in Catalysis: Properties and Applications*. Royal Society of Chemistry.

Mostafa, M., El-Meligy, M.A., Sharaf, M., Soliman, A.T. & AbuKhadra, M.R. 2021. Insight into chitosan/zeolite-A nanocomposite as an advanced carrier for levofloxacin and its anti-inflammatory properties; loading, release, and anti-inflammatory studies. *International Journal of Biological Macromolecules* 179: 206–216.

Mukhopadhyay, M., Lakhotia, S.R., Ghosh, A.K. & Bindal, R.C. 2019. Removal of arsenic from aqueous media using zeolite/chitosan nanocomposite membrane. *Separation science and technology* 54(2): 282–288.

Munagapati, V.S., Yarramuthi, V., Kim, Y., Lee, K.M. & Kim, D.-S. 2018. Removal of anionic dyes (Reactive Black 5 and Congo Red) from aqueous solutions using Banana Peel Powder as an adsorbent. *Ecotoxicology and environmental safety* 148: 601–607.

Munoz, G., Gunessee, B.K., Bégué, D., Bouyssière, B., Baraille, I., Vallverdu, G. & Silva, H.S. 2019. Redox activity of nickel and vanadium porphyrins: a possible mechanism behind petroleum genesis and maturation? *RSC advances* 9(17): 9509–9516.

Murakami, T., Otsuka, K., Fukasawa, T., Ishigami, T. & Fukui, K. 2023. Hierarchical porous zeolite synthesis from coal fly ash via microwave heating. *Colloids and Surfaces A: Physicochemical and Engineering Aspects* 661: 130941.

Murukutti, M.K. & Jena, H. 2022. Synthesis of nano-crystalline zeolite-A and zeolite-X from Indian coal fly ash, its characterization and performance evaluation for the removal of Cs+ and Sr2+ from simulated nuclear waste. *Journal of Hazardous Materials* 423: 127085.

Musah, M., Azeh, Y., Mathew, J.T., Umar, M.T., Abdulhamid, Z. & Muhammad, A.I. 2022. Adsorption kinetics and isotherm models: a review. *CaJoST* 4(1): 20–26.

Musin, L.I., Foss, L.E., Shabalin, K. V, Nagornova, O.A., Borisova, Y.Y., Borisov, D.N. & Yakubov, M.R. 2020. Simple methods for the separation of various subfractions from coal and petroleum asphaltenes. *Energy & Fuels* 34(6): 6523–6543.

Musyoka, N.M., Petrik, L.F., Hums, E., Kuhnt, A. & Schwieger, W. 2015. Thermal stability studies of zeolites A and X synthesized from South African coal fly ash. *Research on Chemical Intermediates* 41(2): 575–582.

Muthurasu, A., Ko, T.H., Kim, T.W., Chhetri, K. & Kim, H.Y. 2024. Interfacial Electronic Modification of Nickel Phosphide via Iron Doping: An Efficient Bifunctional Catalyst for Water/Seawater Splitting. *Advanced Functional Materials* 34: 2404254.

Mutreja, R., Thakur, A. & Goyal, A. 2020. Chapter 13 - Chitin and chitosan: current status and future opportunities. In Gopi, S., Thomas, S., & Pius, A. (eds.). *Handbook of Chitin and Chitosan*, pp. 401–417. Elsevier.

Nagireddi, S., Golder, A.K. & Uppaluri, R. 2019. Role of EDTA on the Pd(II) adsorption characteristics of chitosan cross-linked 3-amino-1,2,4-triazole-5-thiol derivative from synthetic electroless plating solutions. *International Journal of Biological Macromolecules* 127: 320–329.

Najafi, A., Sharifi, F., Mesgari-Abbasi, S. & Khalaj, G. 2022. Influence of pH and temperature parameters on the sol-gel synthesis process of meso porous ZrC nanopowder. *Ceramics International* 48(18): 26725–26731.

Narayanan, S., Tamizhdurai, P., Mangesh, V.L., Ragupathi, C., Santhana krishnan, P. & Ramesh, A. 2020. Recent advances in the synthesis and applications of mordenite zeolite - review. *RSC Advances* 11(1): 250–267.

Nazarova, G., Ivashkina, E., Ivanchina, E., Oreshina, A., Dolganova, I. & Pasyukova, M. 2020. Modeling of the catalytic cracking: Catalyst deactivation by coke and heavy metals. *Fuel Processing Technology* 200: 106318.

Nazir, L.S.M., Yeong, Y.F. & Chew, T.L. 2020. Methods and synthesis parameters affecting the formation of FAU type zeolite membrane and its separation performance: a review. *Journal of Asian Ceramic Societies* 8(3): 553–571.

Negi, H. & Singh, R.K. 2021. Study of azomethine functionalized cellulose with salicylaldehyde as novel demetallization agent for metalloporphyrins in crude oil. *Cellulose* 28(5): 2635–2648.

Negi, H., Verma, P. & Singh, R.K. 2021. A comprehensive review on the applications of functionalized chitosan in petroleum industry. *Carbohydrate Polymers* 266: 118125.

Nguyen, T.-H., Nguyen, Q.-A., Cao, A.N.T., Ernest, T., Nguyen, T.B., Pham, P.T.H. & Nguyen, T.M. 2022. Hydrodemetallization of heavy oil: Recent progress, challenge, and future prospects. *Journal of Petroleum Science and Engineering* 216: 110762.

OA, O., Daramola, O.M., Sunmola, O.P. & Abatan, G.O. 2019. Modelling and simulation of riser reactor of a commercial fluid catalytic cracking unit using 6-lump kinetics of vacuum gas oil. *Chemical Engineering Journal* 3(3): 000194.

Ochedi, F.O., Liu, Y. & Hussain, A. 2020. A review on coal fly ash-based adsorbents for mercury and arsenic removal. *Journal of Cleaner Production* 267: 122143.

Oloruntoba, A., Zhang, Y. & Hsu, C.S. 2022. State-of-the-art review of fluid catalytic cracking (FCC) catalyst regeneration intensification technologies. *Energies* 15(6): 2061.

Ongarbayev, Y., Oteuli, S., Tileuberdi, Y., Maldybaev, G. & Nurzhanova, S. 2020. DEMETALLIZATION OF HEAVY VACUUM RESIDUUM BY TITANIUM-VANADIUM ZEOLITE ADSORBENTS. *Studia Universitatis Babes-Bolyai, Chemia* 65(1): 219–231.

Pal, P., Pal, A., Nakashima, K. & Yadav, B.K. 2021. Applications of chitosan in environmental remediation: A review. *Chemosphere* 266: 128934.

Panitchakarn, P., Laosiripojana, N., Viriya-umpikul, N. & Pavasant, P. 2014. Synthesis of high-purity Na-A and Na-X zeolite from coal fly ash. *Journal of the Air and Waste Management Association* 64(5): 586–596.

Patel, H. 2021. Review on solvent desorption study from exhausted adsorbent. *Journal of Saudi Chemical Society* 25(8): 101302.

Patel, H. 2022. Elution profile of cationic and anionic adsorbate from exhausted adsorbent using solvent desorption. *Scientific Reports* 12(1): 1665.

Patel, P.K., Pandey, L.M. & Uppaluri, R.V.S. 2023. Adsorptive removal of Zn, Fe, and Pb from Zn dominant simulated industrial wastewater solution using polyvinyl alcohol grafted chitosan variant resins. *Chemical Engineering Journal* 459: 141563.

Pei, Y.R., Choi, G., Asahina, S., Yang, J.H., Vinu, A. & Choy, J.H. 2019. A novel geopolymer route to porous carbon: High CO2 adsorption capacity. *Chemical Communications* 55(22): 3266–3269.

Peng, Z., Lin, X., Zhang, Y., Hu, Z., Yang, X., Chen, C., Chen, H., Li, Y. & Wang, J. 2021. Removal of cadmium from wastewater by magnetic zeolite synthesized from natural, low-grade molybdenum. *Science of The Total Environment* 772: 145355.

Petrovic, B., Gorbounov, M., Lahiri, A. & Soltani, S.M. 2021. Biomass Combustion Fly Ash-Derived Nanoporous Zeolites for Post-Combustion Carbon Capture. *2021 IEEE 21st International Conference on Nanotechnology (NANO)*, pp. 233–236.

Qiu, Q., Jiang, X., Lv, G., Chen, Z., Lu, S., Ni, M., Yan, J. & Deng, X. 2018. Adsorption of heavy metal ions using zeolite materials of municipal solid waste incineration fly ash modified by microwave-assisted hydrothermal treatment. *Powder Technology* 335: 156–163.

Rad, L.R. & Anbia, M. 2021. Zeolite-based composites for the adsorption of toxic matters from water: A review. *Journal of Environmental Chemical Engineering* 9(5): 106088.

Rahmani-Azad, M., Najafi, A., Rahmani-Azad, N. & Khalaj, G. 2022. Improvement of ZrB2 nanopowder synthesis by sol-gel method via zirconium alkoxide/boric acid precursors. *Journal of Sol-Gel Science and Technology* 103(1): 87–96.

Rajeswari, A., Gopi, S., Jackcina Stobel Christy, E., Jayaraj, K. & Pius, A. 2020. Chapter 9 - Current research on the blends of chitosan as new biomaterials. In Gopi, S., Thomas, S., & Pius, A. (eds.). *Handbook of Chitin and Chitosan*, pp. 247–283. Elsevier.

Rana, M.S., AlHumaidan, F.S., Bouresli, R. & Navvamani, R. 2021. Guard-bed catalyst: Impact of textural properties on catalyst stability and deactivation rate. *Molecular Catalysis* 502: 111375.

Reiprich, B., Tarach, K.A., Pyra, K., Grzybek, G. & Góra-Marek, K. 2022. High-silica layer-like zeolites Y from seeding-free synthesis and their catalytic performance in low-density polyethylene cracking. *ACS Applied Materials & Interfaces* 14(5): 6667–6679.

Ren, X., Liu, S., Qu, R., Xiao, L., Hu, P., Song, H., Wu, W., Zheng, C., Wu, X. & Gao, X. 2020a. Synthesis and characterization of single-phase submicron zeolite Y from coal fly ash and its potential application for acetone adsorption. *Microporous and Mesoporous Materials* 295: 109940.

Ren, X., Qu, R., Liu, S., Zhao, H., Wu, W., Song, H., Zheng, C., Wu, X. & Gao, X. 2020b. Synthesis of zeolites from coal fly ash for the removal of harmful gaseous pollutants: A review. *Aerosol and Air Quality Research* 20(5): 1127–1144.

Rocha Aguilera, G., Yang, S., Junaid, A.S.M., Kuznicki, S.M. & McCaffrey, W.C. 2016. Ni and V removal from oil and model compounds without hydrogenation: Natural chabazite as solid acid. *Canadian Journal of Chemical Engineering* 94(5): 938–946.

Rodrigues, C., de Mello, J.M.M., Dalcanton, F., Macuvele, D.L.P., Padoin, N., Fiori, M.A., Soares, C. & Riella, H.G. 2020. Mechanical, thermal and antimicrobial properties of chitosan-based-nanocomposite with potential applications for food packaging. *Journal of Polymers and the Environment* 28: 1216–1236.

Rodríguez, E., Félix, G., Ancheyta, J. & Trejo, F. 2018. Modeling of hydrotreating catalyst deactivation for heavy oil hydrocarbons. *Fuel* 225: 118–133.

Sadeghbeigi, R. 2020. *Fluid Catalytic Cracking Handbook: An Expert Guide to the Practical Operation, Design, and Optimization of FCC Units*. Butterworth-Heinemann.

Sadeghi, A., Hassanzadeh, H. & Boustani, A. 2021. The significance of operating parameters on electromagnetic-solvent bitumen recovery process. *Fuel* 304: 121373.

Sahmoune, M.N. 2019. Evaluation of thermodynamic parameters for adsorption of heavy metals by green adsorbents. *Environmental Chemistry Letters* 17(2): 697–704.

Sakthivel, T., L. Reid, D., Goldstein, I., Hench, L. & Seal, S. 2013. Hydrophobic High Surface Area Zeolites Derived from Fly Ash for Oil Spill Remediation. *Environmental Science & Technology* 47(11): 5843–5850.

Saleh, T.A. 2020. Characterization, determination and elimination technologies for sulfur from petroleum: Toward cleaner fuel and a safe environment. *Trends in Environmental Analytical Chemistry* 25: e00080.

Salehi, S., Alijani, S. & Anbia, M. 2020. Enhanced adsorption properties of zirconium modified chitosan-zeolite nanocomposites for vanadium ion removal. *International Journal of Biological Macromolecules* 164: 105–120.

Sama, S.G., Barrère-Mangote, C., Bouyssière, B., Giusti, P. & Lobinski, R. 2018. Recent trends in element speciation analysis of crude oils and heavy petroleum fractions. *TrAC Trends in Analytical Chemistry* 104: 69–76.

Samadi, S., Yazd, S.S., Abdoli, H., Jafari, P. & Aliabadi, M. 2017. Fabrication of novel chitosan/PAN/magnetic ZSM-5 zeolite coated sponges for absorption of oil from water surfaces. *International Journal of Biological Macromolecules* 105: 370–376.

Santos Silva, H., Alfarra, A., Vallverdu, G., Bégué, D., Bouyssiere, B. & Baraille, I. 2018. Impact of H-Bonds and Porphyrins on Asphaltene Aggregation As Revealed by Molecular Dynamics Simulations. *Energy & Fuels* 32(11): 11153–11164.

Sarada, B., Krishna Prasad, M., Kishore Kumar, K. & Murthy, C.V.R. 2017. Biosorption of Cd+ 2 by green plant biomass, Araucaria heterophylla: characterization, kinetic, isotherm and thermodynamic studies. *Applied Water Science* 7: 3483–3496.

Sarkar, S., Datta, D., Deepak, K.S., Mondal, B.K. & Das, B. 2023. Comprehensive investigation of various re-refining technologies of used lubricating oil: a review. *Journal of Material Cycles and Waste Management* 25(4): 1935–1965.

Ściubidło, A. & Majchrzak-Kucęba, I. 2019. Exhaust gas purification process using fly ash-based sorbents. *Fuel* 258: 116126.

Seki, T., Ogawa, Y. & Inoue, C. 2019. Classification of coal fly ash based on pH, CaO content, glassy components, and leachability of toxic elements. *Environmental monitoring and assessment* 191: 1–11.

Sellaoui, L., Hessou, E.P., Badawi, M., Netto, M.S., Dotto, G.L., Silva, L.F.O., Tielens, F., Ifthikar, J., Bonilla-Petriciolet, A. & Chen, Z. 2021. Trapping of Ag+, Cu2+, and Co2+ by faujasite zeolite Y: New interpretations of the adsorption mechanism via DFT and statistical modeling investigation. *Chemical Engineering Journal* 420: 127712.

Senila, M. & Cadar, O. 2024. Modification of natural zeolites and their applications for heavy metal removal from polluted environments: Challenges, recent advances, and perspectives. *Heliyon* 10(3): e25303.

Shabani, J.M., Ameh, A.E., Oyekola, O., Babajide, O.O. & Petrik, L. 2022. Fusion-Assisted Hydrothermal Synthesis and Post-Synthesis Modification of Mesoporous Hydroxy Sodalite Zeolite Prepared from Waste Coal Fly Ash for Biodiesel Production. *Catalysts* 12(12): 1652.

Shahadat, M. & Isamil, S. 2018. Regeneration performance of clay-based adsorbents for the removal of industrial dyes: a review. *RSC advances* 8(43): 24571–24587.

Shahat, A., Hassan, H.M.A., El-Shahat, M.F., El Shahawy, O. & Awual, Md.R. 2018. Visual nickel(II) ions treatment in petroleum samples using a mesoporous composite adsorbent. *Chemical Engineering Journal* 334: 957–967.

Sharma, G., Sharma, S., Kumar, A., Lai, C.W., Naushad, M., Shehnaz, Iqbal, J. & Stadler, F.J. 2022. Activated carbon as superadsorbent and sustainable material for diverse applications. *Adsorption Science & Technology* 2022: 4184809.

Sheldaisov-Meshcheryakov, A.A., Solmanov, P.S., Maximov, N.M., Mozhaev, A. V, Ishutenko, D.I., Nikul'shin, P.A. & Pimerzin, A.A. 2019. Influence of the pore structure of a catalyst for demetallization of petroleum feedstock on the process results. *Russian Journal of Applied Chemistry* 92: 1392–1398.

Shen, K., Cui, L., Yang, L., Wei, X., Liu, X., Ren, M., Cao, F. & Xu, J. 2023. Molecular dynamics simulations of the nickel removal from crude oil by neutral and charged spherical polymer brushes. *Fuel* 345: 128179.

Shi, B., Zhao, J. & Chang, Q. 2021a. Green synthesize of fly ash-based zeolite X: a potential microwave absorbent. *Journal of Materials Science: Materials in Electronics* 32(21): 26097–26104.

Shi, L., Wang, Q., Zhao, X., Che, Y., Liu, H., Zuo, W. & Zhang, Y. 2023. The methyl blue adsorption performance and mechanism of NaX zeolite synthesized from Huadian oil shale ash. *Journal of the Taiwan Institute of Chemical Engineers* 147: 104904.

Shi, Y., Zhang, F. & Linhardt, R.J. 2021b. Porphyrin-based compounds and their applications in materials and medicine. *Dyes and Pigments* 188: 109136.

Shiraishi, Y., Hirai, T. & Komasawa, I. 2000. A novel demetalation process for vanadyl- and nickelporphyrins from petroleum residue by photochemical reaction and liquid− liquid extraction. *Industrial & engineering chemistry research* 39(5): 1345–1355.

Shishkova, I.K., Stratiev, D.S., Tavlieva, M.P., Dinkov, R.K., Yordanov, D., Sotirov, S., Sotirova, E., Atanassova, V., Ribagin, S. & Atanassov, K. 2021. Evaluation of the different compatibility indices to model and predict oil colloidal stability and its relation to crude oil desalting. *Resources* 10(8): 75.

Silas, K., Ghani, W.A.W.A.K., Choong, T.S.Y. & Rashid, U. 2019. Carbonaceous materials modified catalysts for simultaneous SO2/NOx removal from flue gas: A review. *Catalysis Reviews* 61(1): 134–161.

Silva, D.M., Pereira, Á.J., Pierre, T.D.S., Esteves, P.M., Rocha, A.A., Escalfoni, R. & Duyck, C. 2019. Automatized Separation of Fractions from Petroleum Based on Spectrophotometric Signal Derivative Using Open-Source Hardware for the Determination of Ni and V Linked to Porphyrins. *Journal of the Brazilian Chemical Society* 30: 1309–1317.

Silva, H.S., Sodero, A.C.R., Korb, J.-P., Alfarra, A., Giusti, P., Vallverdu, G., Bégué, D., Baraille, I. & Bouyssiere, B. 2017. The role of metalloporphyrins on the physical-chemical properties of petroleum fluids. *Fuel* 188: 374–381.

Silva-Medeiros, F. V, Consolin-Filho, N., Xavier de Lima, M., Bazzo, F.P., Barros, M.A.S.D., Bergamasco, R. & Tavares, C.R.G. 2016. Kinetics and thermodynamics studies of silver ions adsorption onto coconut shell activated carbon. *Environmental technology* 37(24): 3087–3093.

Şimşek, S., Kaya, S. & Jalbani, N.S. 2023. Adsorption properties of amine modified lignin-hydrogel composite for uranyl ions: Theoretical and experimental insights. *Journal of the Indian Chemical Society* 100(2): 100924.

Sivakami, M.S., Gomathi, T., Venkatesan, J., Jeong, H.-S., Kim, S.-K. & Sudha, P.N. 2013. Preparation and characterization of nano chitosan for treatment wastewaters. *International journal of biological macromolecules* 57: 204–212.

Sivalingam, S. & Sen, S. 2018a. Optimization of synthesis parameters and characterization of coal fly ash derived microporous zeolite X. *Applied Surface Science* 455: 903–910.

Sivalingam, S. & Sen, S. 2018b. Rapid ultrasound assisted hydrothermal synthesis of highly pure nanozeolite X from fly ash for efficient treatment of industrial effluent. *Chemosphere* 210: 816–823.

Sivalingam, S. & Sen, S. 2019. Efficient removal of textile dye using nanosized fly ash derived zeolite-x: Kinetics and process optimization study. *Journal of the Taiwan Institute of Chemical Engineers* 96: 305–314.

Smith, B.C. 2018. *Infrared Spectral Interpretation: A Systematic Approach*. CRC press.

Sodha, V., Shahabuddin, S., Gaur, R., Ahmad, I., Bandyopadhyay, R. & Sridewi, N. 2022. Comprehensive review on zeolite-based nanocomposites for treatment of effluents from wastewater. *Nanomaterials* 12(18): 3199.

Solouki, A., Jaffer, S.A. & Chaouki, J. 2022. Process development and techno-economic analysis of microwave-assisted demetallization and desulfurization of crude petroleum oil. *Energy Reports* 8: 4373–4385.

Solouki, A., Monzavi, M. & Chaouki, J. 2023. Microwave-Assisted Nickel and Vanadium Removal from Crude Petroleum Oil Using Bis (2-ethylhexyl) phosphoric Acid: A Kinetic Study. *Industrial & Engineering Chemistry Research* 62(22): 8709–8718.

Song, M.-H., Kim, S., Reddy, D.H.K., Wei, W., Bediako, J.K., Park, S. & Yun, Y.-S. 2017. Development of polyethyleneimine-loaded core-shell chitosan hollow beads and their application for platinum recovery in sequential metal scavenging fill-and-draw process. *Journal of Hazardous Materials* 324: 724–731.

Speight, J.G. 2016. *Handbook of Petroleum Refining*. CRC press.

Sprynskyy, M., Buszewski, B., Terzyk, A.P. & Namieśnik, J. 2006. Study of the selection mechanism of heavy metal (Pb2+, Cu2+, Ni2+, and Cd2+) adsorption on clinoptilolite. *Journal of Colloid and Interface Science* 304(1): 21–28.

Stoleru, E., Hitruc, E.G., Vasile, C. & Oprică, L. 2017. Biodegradation of poly (lactic acid)/chitosan stratified composites in presence of the Phanerochaete chrysosporium fungus. *Polymer Degradation and Stability* 143: 118–129.

Sukthawon, C., Dittanet, P., Saeoui, P., Loykulnant, S. & Prapainainar, P. 2020. Electron beam irradiation crosslinked chitosan/natural rubber-latex film: Preparation and characterization. *Radiation Physics and Chemistry* 177: 109159.

Sun, S., Liu, F., Zhang, L. & Fan, X. 2018. One-step process based on the order of hydrothermal and alkaline treatment for producing lignin with high yield and antioxidant activity. *Industrial Crops and Products* 119: 260–266.

Sun, S. & Meng, F. 2020. Study on solvent deasphalting process for upgrading of hydrocracking unconverted oil. *Industrial & Engineering Chemistry Research* 60(1): 652–658.

Sviridenko, N.N., Iovik, Y.A. & Goncharov, A. V. 2022. Thermal Cracking Processes Up-to-dateness for Oil Vacuum Residual and Bio-Raw Materials: A Perspective for Municipal Solid Waste. In Jacob-Lopes, E., Queiroz Zepka, L., & Costa Deprá, M. (eds.). *Handbook of Waste Biorefinery: Circular Economy of Renewable Energy*, pp. 635–647. Cham: Springer International Publishing.

Szerement, J., Szatanik-Kloc, A., Jarosz, R., Bajda, T. & Mierzwa-Hersztek, M. 2021. Contemporary applications of natural and synthetic zeolites from fly ash in agriculture and environmental protection. *Journal of Cleaner Production* 311: 127461.

Tabatabaeefar, A., Keshtkar, A.R., Talebi, M. & Abolghasemi, H. 2020. Polyvinyl alcohol/alginate/zeolite nanohybrid for removal of metals. *Chemical Engineering & Technology* 43(2): 343–354.

Tahoun, M., Gee, C.T., McCoy, V.E., Sander, P.M. & Müller, C.E. 2021. Chemistry of porphyrins in fossil plants and animals. *RSC Advances* 11(13): 7552–7563.

Tang, X.Q., Pu, J.C., Zheng, H.B., Yu, X. De, Chen, X.F., Yuan, P.Q., Cheng, Z.M. & Yuan, W.K. 2020. Demetallization of Heavy Oils of High Metal Content through Pyrolysis under Supercritical Water Environment. *Energy and Fuels* 34(3): 2861–2869.

Tarekegn, M.M., Balakrishnan, R.M., Hiruy, A.M. & Dekebo, A.H. 2021. Removal of methylene blue dye using nano zerovalent iron, nanoclay and iron impregnated nanoclay–A comparative study. *RSC advances* 11(48): 30109–30131.

Tasneem, N., Ahmed, S. & Hossain, M.M. 2024. Enhancement of Olefins from Fluid Catalytic Cracking Processes: A Review on Effects of Catalysts and Kinetics. *Arabian Journal for Science and Engineering*: 1–22.

Tauanov, Z., Azat, S. & Baibatyrova, A. 2020. A mini-review on coal fly ash properties, utilization and synthesis of zeolites. *International Journal of Coal Preparation and Utilization* 42(7): 1–23.

Tauanov, Z., Shah, D., Inglezakis, V. & Jamwal, P.K. 2018. Hydrothermal synthesis of zeolite production from coal fly ash: A heuristic approach and its optimization for system identification of conversion. *Journal of cleaner production* 182: 616–623.

Tauanov, Z., Tsakiridis, P.E., Shah, D. & Inglezakis, V.J. 2019. Synthetic sodalite doped with silver nanoparticles: Characterization and mercury (II) removal from aqueous solutions. *Journal of Environmental Science and Health, Part A* 54(9): 951–959.

Teimouri, A., Nasab, S.G., Vahdatpoor, N., Habibollahi, S., Salavati, H. & Chermahini, A.N. 2016. Chitosan/Zeolite Y/Nano ZrO2 nanocomposite as an adsorbent for the removal of nitrate from the aqueous solution. *International journal of biological macromolecules* 93: 254–266.

Thacker, B. V, Vadodaria, G.P., Priyadarshi, G. V & Trivedi, M.H. 2023. Biopolymer-based fly ash-activated zeolite for the removal of chromium from acid mine drainage. *The Scientific Temper* 14(04): 1217–1226.

Tirado, A., Félix, G., Trejo, F., Varfolomeev, M.A., Yuan, C., Nurgaliev, D.K., Sámano, V. & Ancheyta, J. 2023. Properties of Heavy and Extra-Heavy Crude Oils. *Catalytic In-Situ Upgrading of Heavy and Extra-Heavy Crude Oils*, pp. 1–38.

Toncón-Leal, C.F., Villarroel-Rocha, J., Silva, M.T.P. da, Braga, T.P. & Sapag, K. 2021. Characterization of mesoporous region by the scanning of the hysteresis loop in adsorption–desorption isotherms. *Adsorption* 27(7): 1109–1122.

Tseng, Y.S., Singhania, R.R., Cheng, A.-C., Chen, C.-W., Dong, C.-D. & Patel, A.K. 2023. Removal of heavy metal vanadium from aqueous solution by nanocellulose produced from Komagataeibacter europaeus employing pineapple waste as carbon source. *Bioresource Technology* 369: 128411.

Ugwu, E.I., Othmani, A. & Nnaji, C.C. 2022. A review on zeolites as cost-effective adsorbents for removal of heavy metals from aqueous environment. *International Journal of Environmental Science and Technology* 19(8): 8061–8084.

Um, N. & Jeon, T.-W. 2021. Pretreatment method for the utilization of the coal ash landfilled in ash ponds. *Process Safety and Environmental Protection* 153: 192–204.

Vakili, M., Deng, S., Cagnetta, G., Wang, W., Meng, P., Liu, D. & Yu, G. 2019a. Regeneration of chitosan-based adsorbents used in heavy metal adsorption: A review. *Separation and Purification Technology* 224: 373–387.

Vakili, M., Deng, S., Shen, L., Shan, D., Liu, D. & Yu, G. 2019b. Regeneration of chitosan-based adsorbents for eliminating dyes from aqueous solutions. *Separation & Purification Reviews* 48(1): 1–13.

Valencia, D. 2023. Chemical bonding and aromaticity analyses of petroporphyrins with vanadium or nickel. *Fuel* 333: 126344.

Visa, M. 2016. Synthesis and characterization of new zeolite materials obtained from fly ash for heavy metals removal in advanced wastewater treatment. *Powder Technology* 294: 338–347.

W. Hipps, K. & Mazur, U. 2017. Kinetic and Thermodynamic Control in Porphyrin and Phthalocyanine Self-Assembled Monolayers. *Langmuir* 34(1): 3–17.

Wang, C., Chang, T., Dong, S., Zhang, D., Ma, C., Chen, S. & Li, H. 2020a. Biopolymer films based on chitosan/potato protein/linseed oil/ZnO NPs to maintain the storage quality of raw meat. *Food chemistry* 332: 127375.

Wang, C., Xu, G., Gu, X., Gao, Y. & Zhao, P. 2021a. High value-added applications of coal fly ash in the form of porous materials: A review. Elsevier Ltd.

Wang, G., Zhang, S., Yao, P., Chen, Y., Xu, X., Li, T. & Gong, G. 2018. Removal of Pb(II) from aqueous solutions by Phytolacca americana L. biomass as a low cost biosorbent. *Arabian Journal of Chemistry* 11(1): 99–110.

Wang, H., Zhao, L. & Hou, W. 2024a. Pseudo-Second-Order Kinetic Equation for Describing the Effect of Sorbent and Sorbate Concentrations. *Langmuir* 40(7): 3559–3568.

Wang, J. & Guo, X. 2020. Adsorption isotherm models: Classification, physical meaning, application and solving method. Elsevier Ltd.

Wang, J. & Zhuang, S. 2022. Chitosan-based materials: Preparation, modification and application. Elsevier Ltd.

Wang, K., Bao, L.-Y., Xing, Y., Yuan, P.-Q., Cheng, Z.-M. & Yuan, W.-K. 2017. Demetalization of Heavy Oil Based on the Preferential Self-assembly of Heavy Aromatics in Supercritical Water. *Industrial & Engineering Chemistry Research* 56(45): 12920–12926.

Wang, L.-T., Hu, Y.-Y., Wang, L.-H., Zhu, Y.-K., Zhang, H.-J., Huang, Z.-B. & Yuan, P.-Q. 2021b. Visbreaking of heavy oil with high metal and asphaltene content. *Journal of Analytical and Applied Pyrolysis* 159: 105336.

Wang, M., Chen, D., Wang, H. & Gao, W. 2024b. A review on fly ash high-value synthesis utilization and its prospect. *Green Energy and Resources* 2(1): 100062.

Wang, N., Sun, X., Zhao, Q., Yang, Y. & Wang, P. 2020b. Leachability and adverse effects of coal fly ash: A review. *Journal of Hazardous Materials* 396: 122725.

Wang, P., Sun, Q., Zhang, Y. & Cao, J. 2020c. Hydrothermal synthesis of magnetic zeolite P from fly ash and its properties. *Materials Research Express* 7(1): 016104.

Wang, S., Xu, X., Yang, J. & Gao, J. 2011a. Effect of the carboxymethyl chitosan on removal of nickel and vanadium from crude oil in the presence of microwave irradiation. *Fuel Processing Technology* 92(3): 486–492.

Wang, S., Yang, J. & Xu, X. 2011b. Effect of the cationic starch on removal of Ni and v from crude oils under microwave irradiation. *Fuel* 90(3): 987–991.

Wang, X., Cheng, H., Chai, P., Bian, J., Wang, X., Liu, Y., Yin, X., Pan, S. & Pan, Z. 2020d. Pore characterization of different clay minerals and its impact on methane adsorption capacity. *Energy & Fuels* 34(10): 12204–12214.

Wang, Y., Acarturk, B.C., Burris, L., Hooton, R.D., Shearer, C.R. & Suraneni, P. 2022. Physicochemical characterization of unconventional fly ashes. *Fuel* 316.

Wang, Y., Sun, Y., Chen, H., Wu, Q. & Chi, D. 2021c. Assessing the performance of clinoptilolite for controlling and releasing ammonium in agricultural applications. *Energy Reports* 7: 887–895.

Wanyonyi, W.C., Onyari, J.M. & Shiundu, P.M. 2014. Adsorption of Congo red dye from aqueous solutions using roots of Eichhornia crassipes: kinetic and equilibrium studies. *Energy Procedia* 50: 862–869.

Xie, W.-M., Zhou, F.-P., Bi, X.-L., Chen, D.-D., Li, J., Sun, S.-Y., Liu, J.-Y. & Chen, X.-Q. 2018. Accelerated crystallization of magnetic 4A-zeolite synthesized from red mud for application in removal of mixed heavy metal ions. *Journal of hazardous materials* 358: 441–449.

Xie, Y., Zhang, Y., He, L., Jia, C.Q., Yao, Q., Sun, M. & Ma, X. 2023. Anti-deactivation of zeolite catalysts for residue fluid catalytic cracking. *Applied Catalysis A: General* 657: 119159.

Xing, G., Li, S., Wang, Y., Zhang, Y., Wang, W. & Qi, L. 2024. Experimental study on the preparation of desulfurizer for low temperature dry desulfurization by digesting CaO in urea solution. *Journal of Environmental Chemical Engineering* 12(5): 113865.

Xu, J., Chen, L., Geng, T., Ren, M., Wang, S., Song, Z. & Cao, F. 2018. Spherical polymer brushes bearing imidazole groups as novel nickel remover for crude oil. *Fuel* 226: 47–53.

Yadav, V.K., Suriyaprabha, R., Inwati, G.K., Gupta, N., Singh, B., Lal, C., Kumar, P., Godha, M. & Kalasariya, H. 2021. A Noble and Economical Method for the Synthesis of Low Cost Zeolites From Coal Fly Ash Waste. *Advances in Materials and Processing Technologies*.

Yadav, V.K., Suriyaprabha, R., Inwati, G.K., Gupta, N., Singh, B., Lal, C., Kumar, P., Godha, M. & Kalasariya, H. 2022. A noble and economical method for the synthesis of low cost zeolites from coal fly ash waste. *Advances in Materials and Processing Technologies* 8(sup2): 301–319.

Yakubov, M., Abilova, G., Tazeeva, E., Yakubova, S., Tazeev, D., Mironov, N. & Milordov, D. 2021. A comparative analysis of vanadyl porphyrins isolated from resins of heavy oils with high and low vanadium content. *Processes* 9(12): 2235.

Yakubov, M.R., Milordov, D. V, Yakubova, S.G., Borisov, D.N., Gryaznov, P.I., Mironov, N.A., Abilova, G.R., Borisova, Y.Y. & Tazeeva, E.G. 2016. Features of the composition of vanadyl porphyrins in the crude extract of asphaltenes of heavy oil with high vanadium content. *Petroleum science and technology* 34(2): 177–183.

Yang, G. & Park, S.-J. 2019. Conventional and microwave hydrothermal synthesis and application of functional materials: A review. *Materials* 12(7): 1177.

Yang, L., Qian, X., Yuan, P., Bai, H., Miki, T., Men, F., Li, H. & Nagasaka, T. 2019a. Green synthesis of zeolite 4A using fly ash fused with synergism of NaOH and Na2CO3. *Journal of Cleaner Production* 212: 250–260.

Yang, L., Shen, K., Xu, J., Ren, M. & Cao, F. 2022. Comprehensive demetallization of crude oil using spherical polyelectrolyte brushes with submicron polybutadiene latex as a core. *Journal of Applied Polymer Science* 139(31): e52709.

Yang, T., Han, C., Liu, H., Yang, L., Liu, D., Tang, J. & Luo, Y. 2019b. Synthesis of Na-X zeolite from low aluminum coal fly ash: characterization and high efficient As (V) removal. *Advanced Powder Technology* 30(1): 199–206.

Yarranton, H.W., Okafor, J.C., Ortiz, D.P. & Van Den Berg, F.G.A. 2015. Density and refractive index of petroleum, cuts, and mixtures. *Energy & Fuels* 29(9): 5723–5736.

Yi, N., Wu, Y., Fan, L. & Hu, S. 2019. Remediating Cd-contaminated soils using natural and chitosan-introduced zeolite, bentonite, and activated carbon. *Polish Journal of Environmental Studies* 28(3): 1461–1468.

Yin, C.-X., Stryker, J.M. & Gray, M.R. 2009. Separation of petroporphyrins from asphaltenes by chemical modification and selective affinity chromatography. *Energy & fuels* 23(5): 2600–2605.

Yoldi, M., Fuentes-Ordoñez, E.G., Korili, S.A. & Gil, A. 2019. Zeolite synthesis from industrial wastes. Elsevier B.V.

Yu, C., Zhang, L., Guo, X., Xu, Z., Sun, X., Xu, C. & Zhao, S. 2015. Association model for nickel and vanadium with asphaltene during solvent deasphalting. *Energy & Fuels* 29(3): 1534–1542.

Yu, Y., Liu, M. & Yang, J. 2018. Characteristics of vanadium adsorption on and desorption from humic acid. *https://doi.org/10.1080/02757540.2018.1452915* 34(6): 548–564.

Yuna, Z. 2016. Review of the natural, modified, and synthetic zeolites for heavy metals removal from wastewater. Mary Ann Liebert Inc.

Zambare, A.S., Ou, J., Hill Wong, D.S., Yao, C.W. & Jang, S.S. 2019. Controlling the product selectivity in the conversion of methanol to the feedstock for phenol production. *RSC Advances* 9(41): 23864–23875.

Zeidan, H., Çufadar, F., Karakaya, N., Karakaya, M.Ç. & Marti, M.E. 2024. Remediation of an aqueous solution contaminated with an anionic diazo dye using natural chabazite. *Desalination and Water Treatment* 317: 100277.

Zhang, H., Luo, C. & Yan, Y. 2017. Adsorption dynamics of isopropanol in structured fixed bed with microfibrous ZSM-5 zeolite structured composite. *Journal of the Taiwan Institute of Chemical Engineers* 80: 779–786.

Zhang, R., Leiviskä, T., Tanskanen, J., Gao, B. & Yue, Q. 2019. Utilization of ferric groundwater treatment residuals for inorganic-organic hybrid biosorbent preparation and its use for vanadium removal. *Chemical Engineering Journal* 361: 680–689.

Zhang, X., Li, C., Zheng, S., Di, Y. & Sun, Z. 2022a. A review of the synthesis and application of zeolites from coal-based solid wastes. *International Journal of Minerals, Metallurgy and Materials* 29(1): 1–21.

Zhang, Y., Dong, J., Guo, F., Shao, Z. & Wu, J. 2018. Zeolite synthesized from coal fly ash produced by a gasification process for Ni2+ removal from water. *Minerals* 8(3): 116.

Zhang, Y., Schuler, B., Liu, F. & Fingas, M. 2022b. The Chemistry of Oil and Petroleum Products.

Zhang, Y.S., Lu, X., Owen, R.E., Manos, G., Xu, R., Wang, F.R., Maskell, W.C., Shearing, P.R. & Brett, D.J.L. 2020a. Fine structural changes of fluid catalytic catalysts and characterization of coke formed resulting from heavy oil devolatilization. *Applied Catalysis B: Environmental* 263: 118329.

Zhang, Z., Li, L., Sun, D., Wang, M., Shi, J., Yang, D., Wang, L. & Zou, S. 2020b. Preparation and properties of chitosan-based microspheres by spray drying. *Food Science & Nutrition* 8(4): 1933–1941.

Zhao, C., Zhang, L., Wang, Q., Zhang, L., Zhu, P., Yu, J. & Zhang, Y. 2021. Porphyrin-based covalent organic framework thin films as cathodic materials for "on–off–on" photoelectrochemical sensing of lead ions. *ACS Applied Materials & Interfaces* 13(17): 20397–20404.

Zhao, X., Liu, Y., Xu, C., Yan, Y., Zhang, Y., Zhang, Q., Zhao, S., Chung, K., Gray, M.R. & Shi, Q. 2013. Separation and characterization of vanadyl porphyrins in Venezuela Orinoco heavy crude oil. *Energy & Fuels* 27(6): 2874–2882.

Zheng, R., Bao, S., Zhang, Y. & Chen, B. 2018. Synthesis of di-(2-ethylhexyl) phosphoric acid (D2EHPA)-tributyl phosphate (TBP) impregnated resin and application in adsorption of vanadium (IV). *Minerals* 8(5): 206.

Zhou, C.-G., Gao, Q., Wang, S., Gong, Y.-S., Xia, K.-S., Han, B., Li, M. & Ling, Y. 2016. Remarkable performance of magnetized chitosan-decorated lignocellulose fiber towards biosorptive removal of acidic azo colorant from aqueous environment. *Reactive and Functional Polymers* 100: 97–106.

Zhou, H., Bhattarai, R., Li, Y., Si, B., Dong, X., Wang, T. & Yao, Z. 2022. Towards sustainable coal industry: Turning coal bottom ash into wealth. *Science of the Total Environment* 804: 149985.

Zhu, X., Li, W., Zhang, Q., Zhang, C. & Chen, L. 2018. Separation characteristics of vanadium from leach liquor of red mud by ion exchange with different resins. *Hydrometallurgy* 176: 42–48.

Zhu, X., Zhang, Z. & Yan, G. 2016. Methylene blue adsorption by novel magnetic chitosan nanoadsorbent. *Journal of Water and Environment Technology* 14(2): 96–105.

Zhuang, S. & Wang, J. 2019. Removal of cobalt ion from aqueous solution using magnetic graphene oxide/chitosan composite. *Environmental Progress & Sustainable Energy* 38(s1): S32–S41.

APPENDIX A

List of Publications and Conferences

Journal Publications

1. **Marhoon, A.A**., Hasbullah, S.A., Asikin-Mijan, N. & Mokhtar, W.N.A.W. 2024. Adsorption of metal porphyrins using chitosan/zeolite-X composite as an efficient demetallization agent for crude oil: Isotherm, kinetic, and thermodynamic studies. International Journal of Biological Macromolecules 274: 133358.

2. **Marhoon, A.A**., Hasbullah, S.A., Asikin-Mijan, N. & Mokhtar, W.N.A.W. 2023. Hydrothermal synthesis of high-purity zeolite X from coal fly ash for heavy metal removal: Kinetic and isotherm analysis. Advanced Powder Technology 34(12): 104242.

Conferences

The 35th International Conference of Analytical Sciences (SKAM35). Influence of Acid-Washing Treatment on the Adsorption Efficiency of Malaysian Fly Ash for Congo Red Dye Removal: A Comparative study. Langkawi, Malaysia. 28-30th August 2023. Presenter (oral).